





P a l a c k ý   U n i v e r s i t y   O l o m o u c

Faculty of Science

Department of Physical Chemistry



## **Chemical functionalization of graphene**

Doctoral Thesis

Author: Mgr. Veronika Šedajová

Supervisor: Aristeidis Bakandritsos, Ph.D.

Study programme:

Field of study:

Form of study:

P 1417 Chemistry

Physical Chemistry

Full-time study

Olomouc 2022



I declare that I have written this doctoral thesis under the supervision of Aristeidis Bakandritsos, Ph.D. It is based on research activities in which I was the first author or contributed as a co-author unless stated otherwise. All used information sources in this thesis have been referenced in the list of references.

This thesis was designed and carried out in the Czech Advanced Technologies and Research Institute, Regional Centre of Advanced Technologies and Materials (CATRIN-RCPTM) and the Department of Physical Chemistry, Palacký University Olomouc.

In Olomouc .....

.....  
Veronika Šedajová



## **Acknowledgment**

I would like to greatly thank my supervisor, Aristeidis Bakandritsos, Ph.D., for his beneficial advice, motivation, patience, and help with working and writing this thesis. I would like to express my sincere gratitude to prof. RNDr. Michal Otyepka, Ph.D., for his continuous support, involving me in exciting research directions, and all advices during my Ph.D.

My thanks belong to all Regional Centre of Advanced Technologies and Materials employees who answered my questions, helped me during Ph.D. studies and measured my samples. Special thanks belong to Mgr. Petr Jakubec, Ph.D. for his valuable help throughout my Ph.D. studies.

Moc bych chtěla poděkovat své rodině za jejich stálou podporu a pochopení. Velmi děkuji svému partnerovi za veškeré kompromisy, motivaci, pomoc a Oskara.

Poděkování patří také mým nejbližším přátelům za jejich trpělivost a podporu a kolegům z kanceláře 2.25 za vzájemnou motivaci.

Merci beaucoup mes amis.

## Bibliografická identifikace

Jméno a příjmení autora:	Veronika Šedajová
Název práce:	Chemická funkcionalizace grafenu
Typ práce:	Doktorská
Pracoviště:	Katedra fyzikální chemie
Vedoucí práce:	Aristeidis Bakandritsos, Ph.D.
Rok obhajoby práce:	2022
Abstrakt:	Tato dizertační práce se zabývá syntézou, charakterizací a aplikací kovalentně funkcionalizovaných grafenových derivátů připravených chemií fluorografenu. Uplatnění těchto derivátů je zejména na poli ukládání energie, specificky v superkondenzátorech.
Klíčová slova:	grafen, fluorografen, deriváty, ukládání energie, superkondenzátory
Počet stran:	83
Počet příloh:	3
Jazyk:	Angličtina



## **Bibliographical identification:**

Author's first name and surname:	Veronika Šedajová
Title:	Chemical functionalization of graphene
Type of thesis:	Doctoral
Department:	Department of Physical Chemistry
Supervisor:	Aristeidis Bakandritsos, Ph.D.
Defense year:	2022
Abstract:	This thesis focuses on the synthesis, characterization and application of covalently functionalized graphene derivatives prepared via fluorographene chemistry. The prepared graphene derivatives are used in energy storage applications, especially in supercapacitors.
Key words:	graphene, fluorographene, derivatives, energy storage, supercapacitors
Number of pages:	83
Number of appendices:	3
Language:	English

**List of publications to which the author of this doctoral thesis has contributed as main author or co-author during her doctoral studies (2018 - 2022):**

- (1) Petr, M.; Jakubec, P.; Ranc, V.; Šedajová, V.; Langer, R.; Medved', M.; Bloński, P.; Kašlík, J.; Kupka, V.; Otyepka, M.; Zbořil, R. Thermally Reduced Fluorographenes as Efficient Electrode Materials for Supercapacitors. **Nanoscale** 2019, 11 (44), 21364–21375. <https://doi.org/10.1039/C9NR07255A>.  
a. IF=7.8
- (2) Zaoralová, D.; Hrubý, V.; Šedajová, V.; Mach, R.; Kupka, V.; Ugolotti, J.; Bakandritsos, A.; Medved', M.; Otyepka, M. Tunable Synthesis of Nitrogen Doped Graphene from Fluorographene under Mild Conditions. **ACS Sustain. Chem. Eng.** 2020, 8 (12), 4764–4772. <https://doi.org/10.1021/acssuschemeng.9b07161>.  
a. IF=8.2, back cover
- (3) Šedajová, V.; Jakubec, P.; Bakandritsos, A.; Ranc, V.; Otyepka, M. New Limits for Stability of Supercapacitor Electrode Material Based on Graphene Derivative. **Nanomaterials** 2020, 10 (9), 1731. <https://doi.org/10.3390/nano10091731>.  
a. IF=5
- (4) Chalmpes, N.; Bourlinos, A. B.; Šedajová, V.; Kupka, V.; Moschovas, D.; Avgeropoulos, A.; Karakassides, M. A.; Gournis, D. Hypergolic Materials Synthesis through Reaction of Fuming Nitric Acid with Certain Cyclopentadienyl Compounds. **C** 2020, 6 (4), 61. <https://doi.org/10.3390/c6040061>.
- (5) Jakubec, P.; Bartusek, S.; Dvořáček, J. J.; Šedajová, V.; Kupka, V.; Otyepka, M. Flax-Derived Carbon: A Highly Durable Electrode Material for Electrochemical Double-Layer Supercapacitors. **Nanomaterials** 2021, 11 (9), 2229. <https://doi.org/10.3390/nano11092229>.  
a. IF=5
- (6) Chalmpes, N.; Asimakopoulos, G.; Baikousi, M.; Moschovas, D.; Avgeropoulos, A.; Bourlinos, AB; Šedajová, V.; Bakandritsos, A.; Gournis, D.; Karakassides, MA. Fast and Direct Microwave Synthesis of Carbon from Bovine Blood Waste: A Feedstock Material for Extractive Metallurgy, Carbon Dots Production and Graphite Synthesis. **J. Nanotechnol. Res.** 2021, 3, 011-028. <https://doi.org/10.26502/jnr.2688-85210021>
- (7) Vermisoglou, E. C.; Jakubec, P.; Bakandritsos, A.; Kupka, V.; Pykal, M.; Šedajová, V.; Vlček, J.; Tomanec, O.; Scheibe, M.; Zbořil, R.; Otyepka, M. Graphene with Covalently Grafted Amino Acid as a Route Toward Eco-Friendly and Sustainable Supercapacitors. **ChemSusChem** 2021, 14 (18), 3904–3914. <https://doi.org/10.1002/cssc.202101039>.  
a. IF=8.9

- (8) Saini, H.; Srinivasan, N.; Šedajová, V.; Majumder, M.; Dubal, D. P.; Otyepka, M.; Zbořil, R.; Kurra, N.; Fischer, R. A.; Jayaramulu, K. Emerging MXene@Metal–Organic Framework Hybrids: Design Strategies toward Versatile Applications. **ACS Nano** 2021, 15 (12), 18742–18776. <https://doi.org/10.1021/acsnano.1c06402>.  
a. IF=15.9, cover
- (9) Obratsov, I.; Bakandritsos, A.; Šedajová, V.; Langer, R.; Jakubec, P.; Zoppellaro, G.; Pykal, M.; Presser, V.; Otyepka, M.; Zbořil, R. Graphene Acid for Lithium-Ion Batteries—Carboxylation Boosts Storage Capacity in Graphene. **Adv. Energy Mater.** 2022, 12 (5), 2103010. <https://doi.org/10.1002/aenm.202103010>.  
a. IF=29.4
- (10) Dědek, I.; Kupka, V.; Jakubec, P.; Šedajová, V.; Jayaramulu, K.; Otyepka, M. Metal-Organic Framework/Conductive Polymer Hybrid Materials for Supercapacitors. **Appl. Mater. Today** 2022, 26, 101387. <https://doi.org/10.1016/j.apmt.2022.101387>.  
a. IF=10
- (11) Šedajová, V.; Bakandritsos, A.; Błoński, P.; Medved', M.; Langer, R.; Zaoralová, D.; Ugolotti, J.; Dzibelová, J.; Jakubec, P.; Kupka, V.; Otyepka, M. Nitrogen Doped Graphene with Diamond-like Bonds Achieves Unprecedented Energy Density at High Power in a Symmetric Sustainable Supercapacitor. **Energy Environ. Sci.** 2022, 15 (2), 740–748. <https://doi.org/10.1039/D1EE02234B>.  
a. IF=38.5
- (12) Hrubý, V.; Zdražil, L.; Dzibelová, J.; Šedajová, V.; Bakandritsos, A.; Lazar, P.; Otyepka, M. Unveiling the True Band Gap of Fluorographene and Its Origins by Teaming Theory and Experiment. **Appl. Surf. Sci.** 2022, 587, 152839. <https://doi.org/10.1016/j.apsusc.2022.152839>.  
a. IF=6.7
- (13) Asimakopoulos, G.; Moschovas, D.; Avgeropoulos, A.; Bourlinos, A.B.; Tantis, I.; Šedajová, V.; Tomanec, O.; Salmas, C.E.; Gournis, D.; Karakassides, M.A. From Waste Tea to Carbon Rocket Fuels through a Piranha Solution-Mediated Carbonization Treatment **J. Nanotechnol. Res.** 2022, 4, 31. <https://doi.org/10.26502/jnr.2688-85210029>
- (14) Chaloupková, Z.; Medříková, Z.; Král, M.; Šedajová, V.; Ranc, V.; Label-free determination of PSA and freePSA using MA-SERS. **Front. Anal. Sci.** 2022, 2, 847730. <https://doi.org/10.3389/frans.2022.847730>

- (15) Panáček, D.; Zdražil, L.; Langer, M.; Šedajová, V.; Baďura, Z.; Zoppellaro, G.; Yang, Q.; Nguyen, P.E.; Álvarez, R.; Hrubý, V.; Kolařík, J.; Chalmes, N.; Bourlinos, A.B.; Zbořil, R.; Merkoçi, A.; Bakandritsos, A.; Otyepka, M. Graphene Nanobeacons with High-Affinity Pockets for Combined, Selective, and Effective Decontamination and Reagentless Detection of Heavy Metals **Small** 2022, 18, 2201003. <https://doi.org/10.1002/sml.202201003>  
a. IF=13.3
- (16) A. Inman, V. Šedajová, K. Matthews, J. Gravlin, J. Busa, C. E. Shuck, A. VahidMohammadi, A. Bakandritsos, M. Shekhirev, M. Otyepka and Y. Gogotsi, **J. Mater. Res.** Shear delamination of multilayer MXenes. Just accepted. <https://doi.org/10.1557/s43578-022-00690-3>.  
a. IF=2.9

## **Conferences and other achievements:**

2017

Graphene Study School – Electronic and photonic devices and their applications, poster presentation

2018

Graphene Study School – Structural characterization of graphene-based materials, poster presentation

2019

Graphene Study School – Science and technologies of 2D materials

2020

WORKSHOP on Low Dimensional Materials 2020 – oral presentation

2020

NanoCon Conference 2020 – poster presentation

2021

School of Catalysis – oral presentation, award for TOP 3 presentations

2021

NanoCon Conference 2021 – poster presentation, poster award

2022

Jean-Marie Lehn Prize for Chemistry 2022 – first place

## List of figures

Figure 1 The schematic representation of a graphene's structure. Adapted from ref <sup>9</sup> ....	22
Figure 2 a) The schematic showing $p_z$ -orbitals of graphene with $\sigma$ - and $\pi$ - bonds. Adapted from ref <sup>11</sup> . b) Crystallographic sublattices A (red atoms) and B (blue atoms). Adapted from ref <sup>12</sup> .....	23
Figure 3 a), b) Calculated band structure for single-layer graphene. The valence and conduction band touch at K and K' points. Adapted from ref <sup>12</sup> and ref <sup>30</sup> .....	24
Figure 4 Schematic representation of the broad portfolio of the possible application utilizing functionalized graphene derivatives. Adapted from ref <sup>9</sup> .....	26
Figure 5 Idealized representation of $\pi$ - $\pi$ -interaction of graphene with aromatic molecules like benzene or naphthalene. Adapted from ref <sup>32</sup> . .....	27
Figure 6 Schematic representation of a non-covalent functionalization of graphene and graphene oxide. Adapted from ref <sup>32</sup> .....	28
Figure 7 General mechanism of a) nucleophilic addition and b) cycloaddition via aziridine adduct onto graphene. Adapted from ref <sup>24</sup> .....	29
Figure 8 General mechanism of a) Diels-Alder reaction where graphene acts both as dien and dienophile, b) free radical addition of phenyl and c) Friedl-Crafts acylation on graphene. Adapted from ref <sup>24</sup> .....	31
Figure 9 Examples of possible graphene derivatives synthesized via fluorographene chemistry. Adapted from ref <sup>35</sup> .....	32
Figure 10 Overview of possible functionalization of graphene, such as a) on edge, b) – d) on the basal plane, and e) stacked into a layered structure. Adapted from ref <sup>36</sup> .	33
Figure 11 (a) Schematic depiction of the synthesis of GN3. (b)-(d) XPS characterization and deconvolutions. (e) CP MAS <sup>13</sup> C solid-state NMR and (f) FT-IR spectra of starting product, byproducts, and final material.....	46
Figure 12 The formation of GN3 structures via the reaction of FG with sodium azide in DMF modeled at the $\omega$ B97X-D/6-31++G(d,p)/SMD(solvent=DMF) level of theory <sup>100,101</sup> , showing the formation of different nitrogen configurations. The energies are given in kcal mol <sup>-1</sup> .....	48
Figure 13 HR-TEM images of the GN3 material alongside the EDS mapping of carbon and nitrogen.....	49
Figure 14 (a) Theoretical model of GN3 fragment by DFT calculations. (b) TGA-MS analysis of GN3 product in the air atmosphere.....	50

Figure 15 Photos of a digital micrometer with GN3 electrodes before and after pressing at 80 kN for 1 minute. ....	50
Figure 16 (a) Adsorption and desorption N <sub>2</sub> isotherms of the GN3 material, recorded at 77 K. (b) Pore width distribution for GN3 material. ....	51
Figure 17 Cyclic voltammograms of GN3 material in a symmetric full cell system. ....	52
Figure 18 Comparison of (a) GCD curves and (b) energy storage values at 2 A g <sup>-1</sup> of the GN3 material with porous carbons. ....	53
Figure 19 State-of-the-art comparison of the previously published report and this work's results. ....	54
Figure 20 Scheme illustrating FG reaction with Boc-Arg-OH, followed by removal of the Boc protecting group, resulting in the FG/Arg product. Color coding is as follows: carbon – grey; fluorine – green; nitrogen – blue; oxygen – red. ....	56
Figure 21 TGA graphs of Arg, FG/Arg-48h, and FG/Arg-48h_K .....	58
Figure 22 (a) FTIR spectra of GrF, FG/Boc-48h and FG/Arg-48h. (b) High resolution C1s XPS spectra of the parent material GrF and final product FG/Arg-48h. (c) Raman spectra of FG/Arg-48h and FG/Arg-48h_K samples. ....	59
Figure 23 (a) ζ-potential curve of an FG/Arg-48h aqueous dispersion versus pH, (b) water droplet contact angle measurements of parent material and FG/Arg-48h ....	60
Figure 24 (a) N <sub>2</sub> adsorption/desorption isotherms obtained at -196 °C for FG/Arg-48h and FG/Arg-48h_K samples. (b) Pore size distributions of FG/Arg-48h and FG/Arg-48h_K samples. ....	60
Figure 25 SEM images of (a) the FG/Arg-48h and (b) FG/Arg-48h_K samples. ....	61
Figure 26 (a) TEM and (b) HRTEM images of a FG/Arg-48h_K sample. (c) Dark field HRTEM image of FG/Arg-48h_K and corresponding chemical mapping: (d) carbon map, (e) nitrogen map, (f) oxygen map, (g) fluorine map, (h) carbon-fluorine map, and (i) carbon-nitrogen-oxygen combined map. ....	62
Figure 27 (a) CVs of graphene derivatives with Arg groups at different reaction times. (b) GCD profiles of the prepared materials. (c) GCD profiles of FG/Arg-48h_K, at current densities from 0.25 A g <sup>-1</sup> to 5 A g <sup>-1</sup> , and (d) the specific capacitance vs. current density profile. ....	63
Figure 28 (a), (b) GCD profiles of FG/Arg-48h_K recorded at different current densities. (c) Stability of FG/Arg-48h_K after 30,000 GCD cycles. ....	64
Figure 29 Structural characterization of GA material, (a) XRD and (b) Raman spectra. (c)-(e) XPS evaluation of GA. ....	67

Figure 30 (a), (b) HRTEM images of GA. (c)-(d) HAADF image and corresponding elemental mapping of carbon and oxygen. (e) Structural GA model.....	68
Figure 31 (a) Raman and (b) XPS spectra comparing three different syntheses of GA. ....	69
Figure 32 (a) GCD profiles of GA in a two-electrode system, (b) the dependence of capacitance vs current density. (c) Rate and (d) cycling stability test. (e),(f) Supercapacitors with GA electrodes connected in parallel and series, showing increased values as well as lighted up 2V LED diode. ....	70



## List of abbreviations

Arginine – Arg

Brunauer–Emmett–Teller – BET

Capacitance –  $C_g/C_v$

Cyanographene – GCN

Cyclic voltammetry – CV

Density functional theory – DFT

Energy density –  $E_g/E_v$

Energy-dispersive X-ray spectroscopy – EDS

Electrochemical impedance spectroscopy – EIS

Fluorographene – FG / GrF

Fourier transformed infrared spectroscopy – FTIR

Functionalization degree – FD

Galvanostatic charge / discharge – GCD

Graphene acid – GA

Graphene oxide – GO

Graphite fluoride – GF

High angle annular dark field – HAADF

High-resolution transmission electron microscopy – HR-TEM

Kuraray carbon – KC

Mass spectroscopy – MS

N-doped graphene ref<sup>1</sup> – GN3

Nuclear magnetic resonance – NMR

Porous carbon – PC

Power density –  $P_g/P_v$

Scanning electron microscopy – SEM

Specific surface area – SSA

Tert-butoxycarbonyl – Boc

Thermogravimetric analysis – TGA

Transmission electron microscopy – TEM

X-ray diffraction – XRD

X-ray photoelectron spectroscopy – XPS

## Table of contents

1	INTRODUCTION .....	21
1.1	Graphene .....	22
1.1	Functionalization of graphene.....	25
1.1.1	Non-covalent approaches.....	26
1.1.2	Covalent approaches .....	29
1.2	Fluorographene .....	31
1.3	Graphene derivatives in electrochemical applications - supercapacitors.....	32
2	AIM OF THE THESIS .....	35
3	EXPERIMENTAL PART.....	36
3.1	Methods of characterization.....	36
3.1.1	Fourier transformed infrared spectroscopy.....	36
3.1.2	X-ray photoelectron spectroscopy .....	36
3.1.3	Microscopy techniques .....	36
3.1.4	Raman spectroscopy .....	37
3.1.5	X-ray diffraction spectroscopy .....	37
3.1.6	Thermogravimetric analysis .....	37
3.1.7	Surface area analysis.....	38
3.1.8	Nuclear magnetic resonance .....	38
3.1.9	Electrochemical testing.....	38
3.2	Syntheses of graphene derivatives featured in the thesis.....	41
3.2.1	Synthesis of nitrogen superdoped graphene, denoted as GN3, adapted from ref <sup>1</sup> .....	41
3.2.2	Synthesis of amino acid functionalized graphene, denoted as FG/Arg_48h, adapted from ref <sup>92</sup> .....	41
3.2.3	Synthesis of carboxyl-functionalized graphene derivatives, denoted as GA, adapted from ref <sup>93-95</sup> .....	42
4	RESULTS AND DISCUSSION .....	44
4.1	Nitrogen Doped Graphene with Diamond-like Bonds Achieves Unprecedented Energy Density at High Power in a Symmetric Sustainable Supercapacitor .....	44
	Introduction.....	44
	Results.....	45
	Conclusions.....	54
4.2	Graphene with Covalently Grafted Amino Acid as a Route Toward Eco-Friendly and Sustainable Supercapacitors .....	55
	Introduction.....	55
	Results.....	56
	Conclusions.....	64

4.3	New Limits for Stability of Supercapacitor Electrode Material Based on Graphene Derivative .....	65
	Introduction .....	65
	Results .....	66
	Conclusions .....	70
5	SUMMARY .....	71
6	ZÁVĚR.....	72
7	REFERENCES.....	73
8	LIST OF APPENDICES .....	83





# 1 INTRODUCTION

It has been almost twenty years since the discovery of graphene. Nevertheless, graphene and its derivatives are still being intensively studied and investigated throughout the scientific world. With such promising properties, a broad portfolio of synthetic procedures, applications and/or theoretical studies was already published. However, there are still many possible ways to expand knowledge in this exciting field.

Graphene, as one atom thick carbon layer with  $sp^2$  hybridization, honeycomb lattice, and aromatic network, comes with relatively low reactivity of graphene itself. Moreover, combined with graphene's zero band gap and hydrophobicity, these facts spurred the research directions towards graphene derivatives with non-zero band gap with tunable functional groups.

Fluorographene (exfoliated graphite fluoride) is a graphene derivative having a fluorine atom bonded on every carbon. Its rich chemistry provides an easy pathway to prepare homogeneously and highly chemically functionalized graphene derivatives because the fluorographene's reactivity is much higher than graphene's.

Within this work, new ways of chemical functionalization of graphene were pursued with a focus on tuning the materials' properties toward energy storage applications. The aim was to yield highly conductive functionalized graphene derivatives, which will preferably have redox-active groups grafted or nitrogen atoms introduced into the graphenic lattice to improve their properties.

Firstly, nitrogen superdoped graphene was synthesized with diamond-like interlayer bonds with exceptionally high mass density. Secondly, amino-acid functionalized, as well as carboxyl group functionalized, graphene derivatives were prepared via the intense study and tailored synthetic protocols utilizing the fluorographene chemistry.

In the frame of this thesis, all materials were utilized in the energy storage field application as highly stable and exceptionally performing supercapacitor active electrode materials.

## 1.1 Graphene

Graphene, a two-dimensional carbon-based material, is a one-atom thin single layer of graphite. It was first predicted theoretically in 1947<sup>2</sup> and experimentally prepared during the next 50 years<sup>3,4</sup>. In 2004, Geim and Novoselov published their breakthrough re-discovery and characterization of graphene<sup>5</sup>. It disproved the long-standing claim that strictly 2D crystals can not be thermodynamically stable – therefore exist<sup>6,7</sup>. Alongside graphene, the boron nitride was another example of stable 2D material<sup>8</sup>. The years of 2004 and 2005 started incredible research interest in novel low-dimensional materials due to their very intriguing properties and promising applicability.

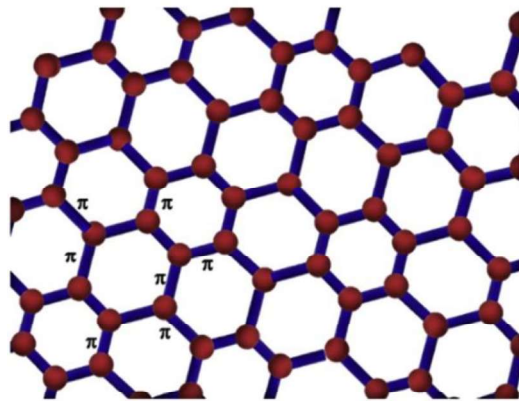


Figure 1 The schematic representation of a graphene's structure. Adapted from ref<sup>9</sup>

Graphene consists of units of six  $sp^2$ -carbon atoms tightly bonded in hexagonal, honeycomb-like rings, forming a conductive network thanks to the delocalized electrons in  $\pi$ - orbitals (Figure 1). This electron cloud, perpendicular to the graphene layer, is the reason behind the exceptional electrical conductivity but also the chemical inertness of the graphene<sup>10</sup>. Such properties offer a possibility of multiple applications in the fields of electronics, sensors, biosystems, or as protective layers against corrosions. The crystallographic studies revealed two sublattices, A and B, in the graphene structure, as shown in Figure 2.



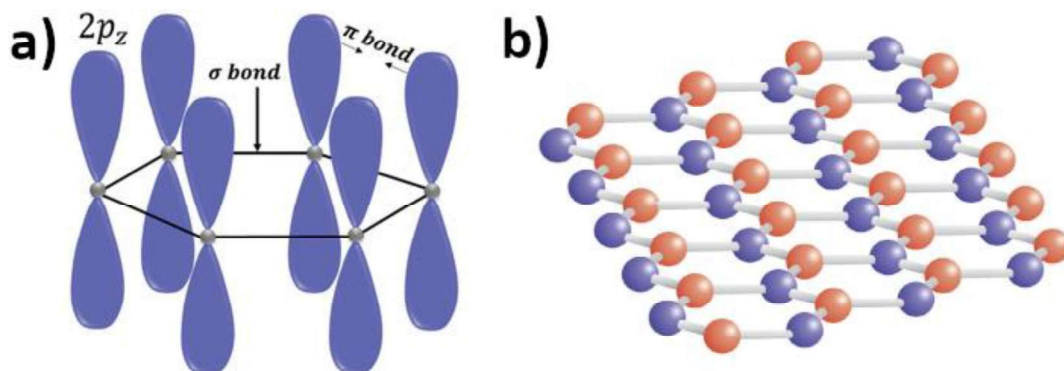


Figure 2 a) The schematic showing  $p_z$ -orbitals of graphene with  $\sigma$ - and  $\pi$ - bonds. Adapted from ref<sup>11</sup>. b) Crystallographic sublattices A (red atoms) and B (blue atoms). Adapted from ref<sup>12</sup>

Most of the materials have some defects: including graphene. During synthesis and preparation of graphene, there are always defects, such as vacancies, different edge configurations, or impurities, which all alter its properties. Defects change graphene's chemical and electronic properties since they act as centres of activity. Targeted interactions on the defects can lead to the proper identification of the defects<sup>13</sup> and toward the modification of the electronic structure of graphene.<sup>9,13-27</sup>

The electronic structure of graphene is particularly unique. Usually, the Schrödinger equation is enough to describe the properties of materials. Nevertheless, graphene is special – its charge carriers behave like relativistic particles and can be described by the Dirac equation, resulting in a commonly shared fact that Dirac massless fermions are graphene's charge carriers.<sup>28</sup> This uniqueness is yet another proof of why graphene caused such a spur of attention in the world of two-dimensional materials research. Another property, related to graphene's electronic applications, is that graphene is classified as a zero-band gap semiconductor; its valence band and conduction band touch in so-called Dirac points (Figure 3). As a result, high-quality graphene exhibits high Fermi velocity<sup>29</sup>.

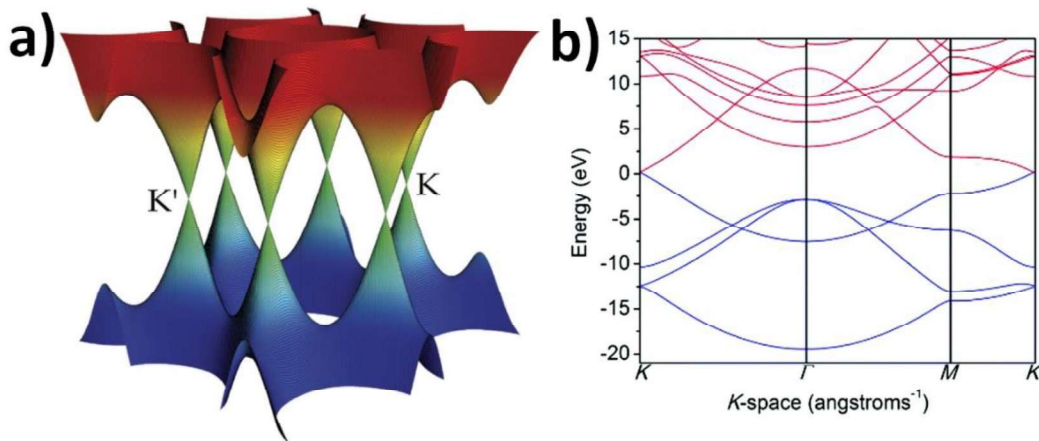


Figure 3 a) The 3D view schematic of a band structure for single-layer graphene. b) The calculated valence and conduction band touch at K and K' points. Adapted from ref<sup>30</sup> and ref<sup>31</sup>.

The strong sigma bonding of the carbon atoms in the graphene layer results in exciting mechanical properties, such as high Young's modulus (approx. 1 TPa) and an insignificant drop of electrical conductivity when strained. Apart from electrical conductivity, its thermal conductivity is theoretically predicted to reach up to 6000 W mK<sup>-1</sup>, opening the application window also as a heat exchanger. Moreover, the optical properties, such as 2.3 % maximum absorbance by the graphene monolayer, gradually increasing with the number of layers, and non-linear behaviour, especially at the region around ~250 nm, are worth mentioning for potential optical utilizations.

All the above-listed properties suggest that graphene is a two-dimensional material with extraordinary properties. However, a few obstructive properties have an immense negative impact on the direct application potential. Zero band-gap, dispersibility and self-aggregation are all among these undesirable properties. The direct use of graphene in semiconductor passive parts is disallowed due to the zero band gap, a significant flaw in the electronics world. Pristine graphene is hydrophobic and can be dispersed only in solvents with high surface tension<sup>32</sup>, insoluble in most traditional solvents and self-aggregating due to  $\pi$ - $\pi$  interactions, disrupting the ease of processing dispersions of graphene mainly for scale-up synthesis and usage.

Identifying tailored procedures to overcome these bottlenecks of pure graphene monolayers is a crucial step toward wide graphene use in daily life. The facilitation of multifunctional applications of graphene is of immense interest due to its exciting properties and potential to replace some of the critical elements, environmentally non-friendly elements and compounds or to replace current technologies already at their

fundamental limit (like Si-based technology). Functionalization of graphene is a solution to graphene's issues.

## 1.1 Functionalization of graphene

Functionalization of graphene or its derivatives via different methods and approaches is a vital way to increase the competitive strength of graphene in many applications since functionalization causes the opening of a band-gap, better dispersibility, reduces the re-stacking of graphene sheets. Moreover, functionalization is a way of imprinting desired properties in the graphene based materials.

Covalent attachment or non-covalent interactions of various foreign compounds, atoms or molecules lead to a precisely controlled functionalization of a graphene single or multi-layers. Because the functionalized derivatives overcome the pristine graphene's struggles, they are widely used and precisely designed and synthesized in order to fit perfectly and exhibit extraordinary performance in the desired application, preferably better than current technologies.

This theoretical introduction will focus on the chemical functionalization of pure graphene and fluorographene, the latter as the main subject of the experimental part, excluding the functionalization of graphene oxide. The graphene oxide is a non-stoichiometric graphene derivative with various oxygen-bearing moieties, enabling a wide window of possible functionalities. However, the major disadvantage of graphene oxide is the presence of many different functional groups, including peroxides, carboxyls, hydroxyls, and epoxy groups. Such a variety causes low selectivity and non-specific interactions for any possible compounds used for functionalization because they can react with the different types of functionalities. Moreover, the functionalization of graphene oxide yields low conducting materials because the many moieties already disrupt the  $sp^2$  conductive network of the parent graphene oxide. Thus, the functionalization of graphene oxide will not be discussed in detail.<sup>25</sup>

Thanks to their unique and tunable properties, functionalized graphene derivatives are utilized in various applications (Figure 4), including catalysis<sup>33</sup>, water remediation<sup>34,35</sup>, bio-applications<sup>36</sup>, sensing<sup>37-39</sup>, hydrogen storage<sup>40</sup> or the field of energy storage<sup>41,42</sup>, closely related to the research done within this thesis.

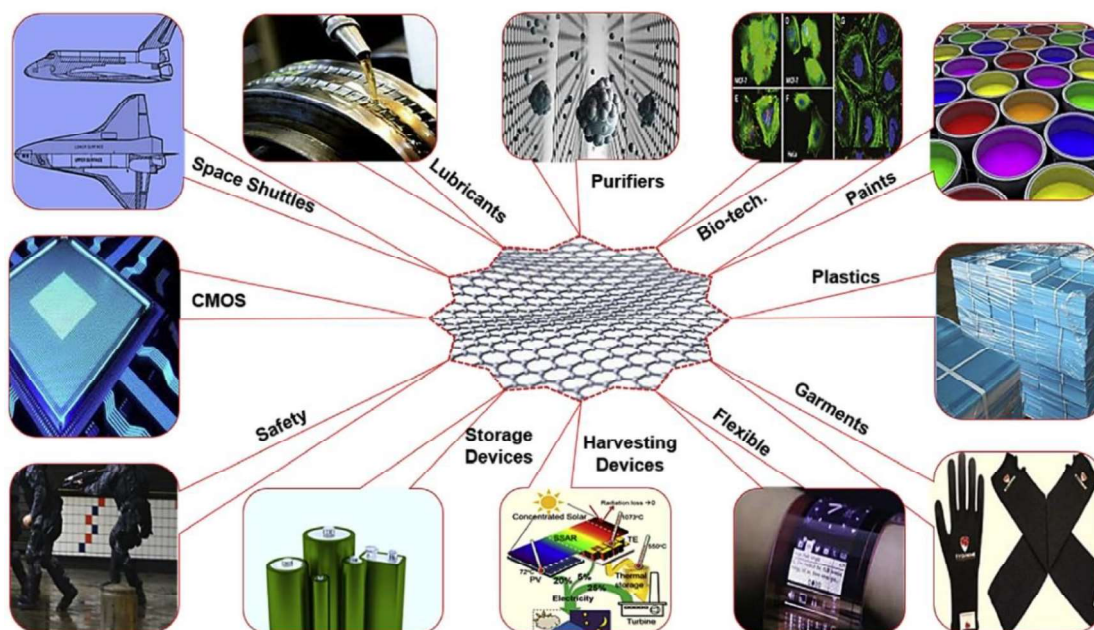


Figure 4 Schematic representation of the broad portfolio of the possible application utilizing functionalized graphene derivatives. Adapted from ref<sup>9</sup>

### 1.1.1 Non-covalent approaches

Non-covalent functionalization is an elegant way to improve graphene's intrinsic properties while retaining most features like pristine structure. It usually utilizes different types of non-covalent interactions, such as electrostatic or  $\pi$ -interactions, which offer effective synthetic methods for attaching functional groups without disrupting the conducting electronic network. The  $\pi$ -interaction term encapsulates various attractive forces and also repulsive forces. Understanding which of them would prevail and would be beneficial during the preparation of non-covalently functionalized materials is crucial for designing synthetic pathways.

- **Hydrogen- $\pi$ -interaction:** As a type of hydrogen bond, this interaction largely depends on the polarizability of the  $\pi$ -system, driving the nature and geometry of the interaction. Moreover, large  $\pi$ -systems with multiple hydrogen bonding need stabilization from dispersion energy.

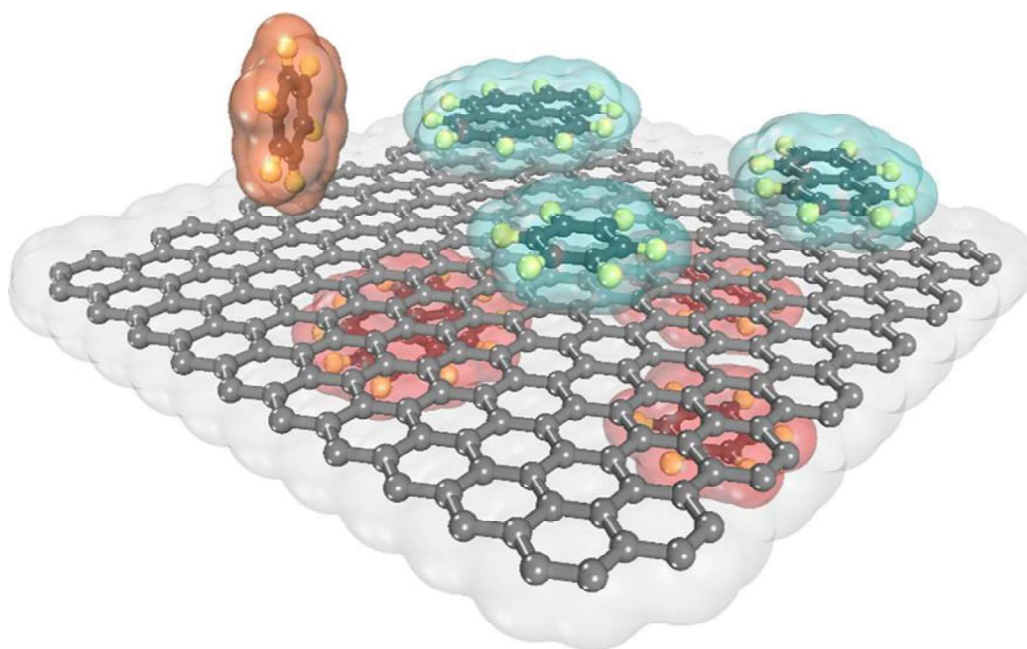


Figure 5 Idealized representation of  $\pi$ - $\pi$ -interaction of graphene with aromatic molecules like benzene or naphthalene. Adapted from ref<sup>43</sup>.

- $\pi$ - $\pi$ -interaction: The  $\pi$ - $\pi$ -interaction is of high interest because the  $\pi$ -systems, having similar electron densities, the attractive forces are driven by dispersion interactions. Depending on the other functional groups attached to the  $\pi$ -system, one will be the electron-donating and one electron-attracting part of the interaction. The behaviour of two benzene rings (Figure 5) was profoundly studied,<sup>44-46</sup> estimating the interaction energy to  $\sim 2 \text{ kcal mol}^{-1}$ , which is considered favourable. However, the  $\pi$ - $\pi$ -interaction also heavily depends on the position and orientation in space because the electrostatic energies and exchange interactions are significant energetic contributions. The  $\pi$ - $\pi$ -interaction is critical in supramolecular self-assembly due to the favourable energy exchanges while forming ordered structures or designing mechanosensitive molecules<sup>47</sup>.
- Cation- $\pi$ -interaction: When the cation is of metallic nature, the prevailing dominant interaction energies are induction and electrostatic, while when an organic cation counter molecule is part of the  $\pi$ -interaction, a certain degree of the polarizability of the electron cloud of the graphene is necessary. Moreover, the interaction energies are much higher for metallic cations. For any cation type, also conformation, geometry, and space arrangement play a crucial role in the interaction, which is needed to be taken into consideration while designing the

functionalized derivatives. Another interaction, which is very closely related to cation- $\pi$ -interaction, is  $\pi_{\text{cation}}-\pi$ -interaction, which differs in the binding energy - being weaker than the actual cation- $\pi$  interaction, but still being significantly stronger than the  $\pi$ - $\pi$ -interaction itself.

- Anion- $\pi$ -interaction: Considered as a base for possible anion recognition or anion host designed materials, the anion- $\pi$ -interaction is driven by the dispersion and donor-acceptor exchanges between the anion and the graphene. As a type of physisorption, the dielectric constant of the solvent needs to support the electron distribution on the graphene flakes.<sup>48</sup>
- Other graphene-ligand interactions: Many reports show the non-covalent interaction of graphene with other molecules, materials or chemical compounds (Figure 6). Some of the most promising are the interaction involving biologically essential molecules like the DNA or RNA, the influence of the substrate under the graphene sheet or the interaction of metallic atoms with pure graphene.

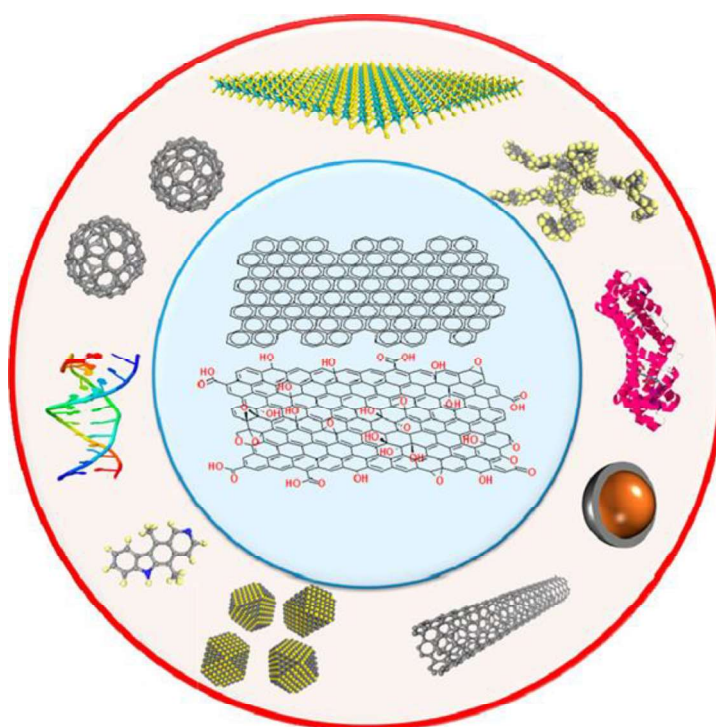


Figure 6 Schematic representation of a non-covalent functionalization of graphene and graphene oxide. Adapted from ref<sup>43</sup>.

### 1.1.2 Covalent approaches

Covalently grafted electron-donating or electron-withdrawing groups significantly alter graphene's electronic structure,  $\pi$ - $\pi$  conjugation system, and open its band gap. Moreover, the attachment considerably increases the dispersibility in commonly used solvents which is also connected to less re-stacking. The advantage of the covalently functionalized graphene derivatives is their stability in different environments since the covalent bond is hardly broken and the possibility of the solid attachment of various functional groups.<sup>12,49</sup> Since several mechanisms allow for covalent attachment of groups onto the graphenic surface, the suitable one for every possible group can be chosen, each with its unique application potential. In order to covalently graft moieties on the low-reactive graphene flakes, there are synthetic pathways for preparing the derivatives directly from pristine graphene:<sup>13,20,21,24,50</sup>

- Nucleophilic addition: Originating from the fullerene chemistry, a Bingel reaction utilizes nucleophilic addition. The mild reaction conditions resulted in the use for the synthesis of functionalized graphene derivatives. In situ produced enolate ion from halocarbon nucleophilically attacks the C=C bond in the graphene system, followed by a second attack of carbanion (Figure 7). The final moiety is formed by the closing of the ring.<sup>51</sup>

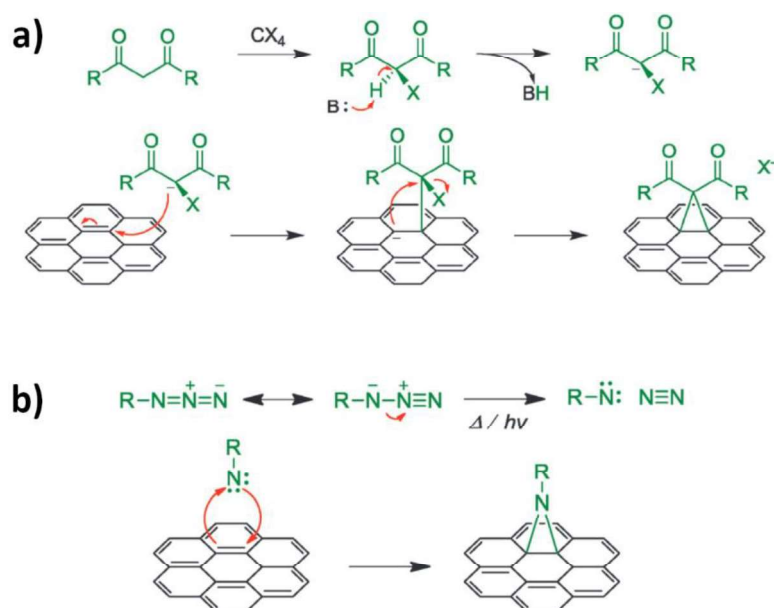


Figure 7 General mechanism of a) nucleophilic addition and b) cycloaddition via aziridine adduct onto graphene. Adapted from ref<sup>24</sup>

- Cycloaddition: This type of reaction is very common because of its versatility and the usual absence of intermediate formation. There are different types of cycloaddition, determined by the number of atoms of the grafting molecule and the number of atoms from the graphenic layer.
  - [2+1] cycloaddition is performed by attachment of cyclopropane ring with attached moieties through cyclopropane (via dichlorocarbene) or aziridine (via nitrene) adducts (Figure 7).
  - [2+2] cycloaddition involving four electrons propagates via the elimination-addition mechanism.
  - [3+2] cycloaddition yields a five-membered ring, mainly utilizing decarboxylation initiated formation of unstable azomethine ylides, which consequently reacts with the  $sp^2$  graphene network (known from fullerene chemistry as Prato reaction).<sup>52,53</sup>
  - [4+2], mostly known as Diels-Alder, cycloaddition is a well-known reaction in the addition mechanism (Figure 8), resulting in a six-membered ring. For example, the reaction of a dienophile (grafting molecule) and a conjugated diene in cis conformation ( $sp^2$  graphene network) is a one-step process while being heat-treated.<sup>21</sup>
  
- Radical reactions: The most widely used grafting of an aryl group on the graphene plane using radical addition is accomplished by employing the aryl diazonium salts (Figure 8). Accompanied by the release of an  $N_2$ , a reaction in both acidic and base/neutral environments produces reactive radical aryl moiety, responsible for the covalent grafting onto the graphene network.<sup>54,55</sup>
  
- Substitution reaction utilizes the electron-rich graphene structure. In an electrophilic substitution, the Friedel-Crafts acylation (Figure 8) or a hydrogen-lithium exchange can benefit from the high affinity of graphene towards electrophilic compounds.<sup>56,57</sup>



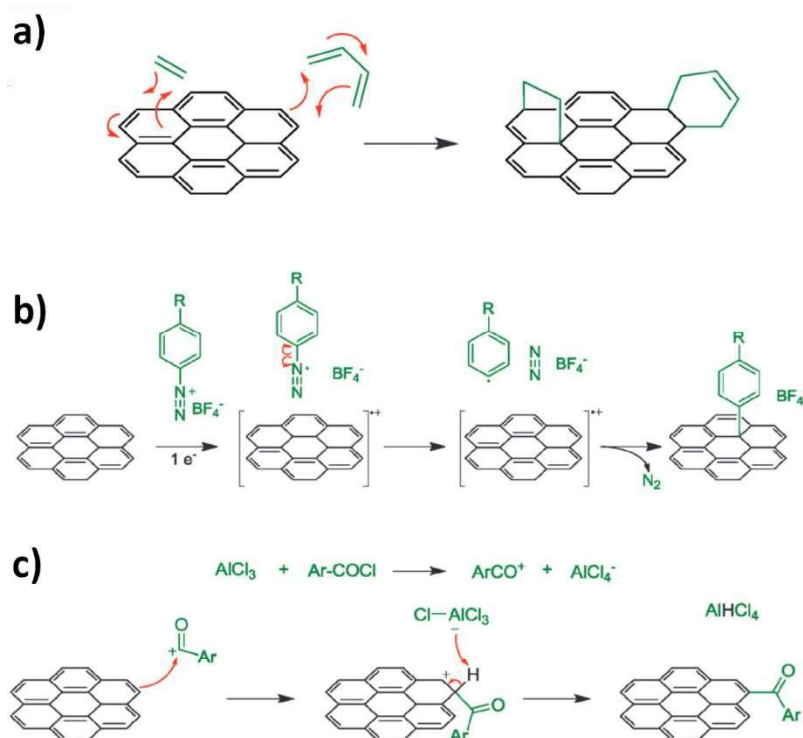


Figure 8 General mechanism of a) Diels-Alder reaction where graphene acts both as dien and dienophile, b) free radical addition of phenyl and c) Friedl-Crafts acylation on graphene. Adapted from ref<sup>24</sup>

- Rearrangement is a rarely used approach to covalently graft moieties onto e.g. graphene oxide, where it is possible with the rearrangement reaction the “exchange” of a -hydroxyl group for a carbonyl group.

## 1.2 Fluorographene

Fluorographene, sometimes so-called “2D-teflon”, is a stoichiometric graphene derivative with a fluorine atom bonded to every carbon atom in a graphene-like structure. With a  $\text{C}_1\text{F}_1$  composition, it can exist in four different conformations – the most stable chair, followed by armchair, boat, and zig-zag. Both top-bottom and bottom-up synthetic approaches yield different compositions of fluorographene, resulting in varying properties depending on the coverage of fluorine ad-atoms.

Because the covalent attachment of fluorine atoms to the carbon atoms disrupts the  $\pi$ -conjugated system, fluorographene is the thinnest known insulator with a recently

accurately theoretically calculated and experimentally verified (by means of DRIFT) bandgap of 5.7 eV.<sup>58</sup>

One of the properties that fluorographene inherited from its parent material, graphene, is its high hydrophobicity, preventing its direct easy processability. Same like graphene, it can be dispersed in some organic solvents, from which some of them propagate defluorination of the FG, such as DMF.<sup>59–61</sup>

Moreover, the exceptional strength of the C-F bond is usually beneficial in the means of thermal stability and chemical inertness – therefore, the “nickname” 2D-Teflon. However, contrary to Teflon, fluorographene offers a plethora of possible reactions (Figure 9) thanks to the fluorine vacancies, partial positive charge on the carbanion and resulting nucleophilic substitution on such region in the fluorographene’s structure.<sup>62–64</sup>

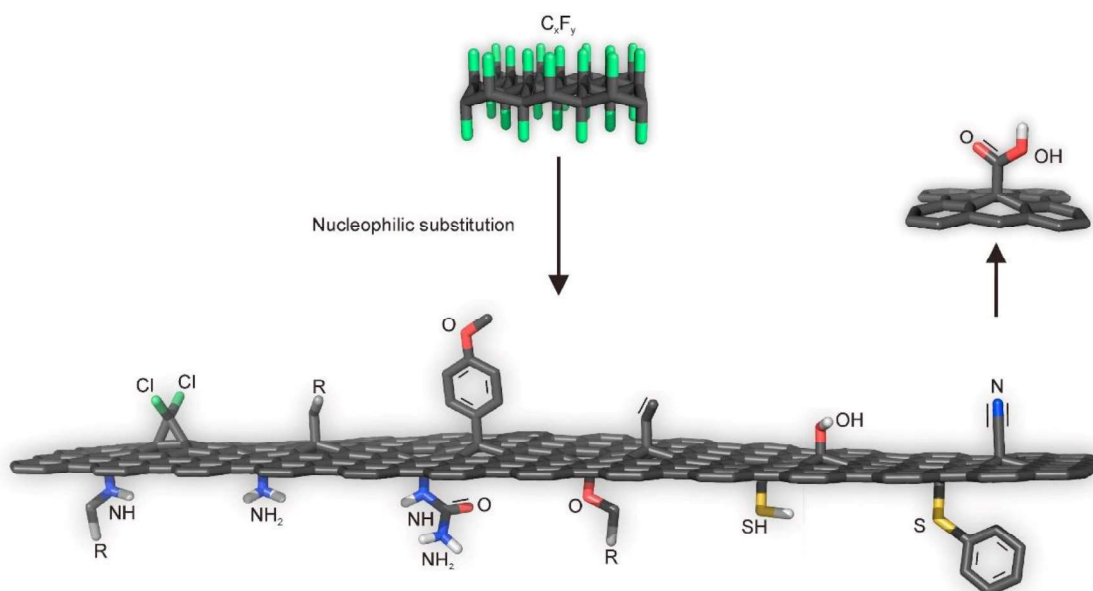


Figure 9 Examples of possible graphene derivatives synthesized via fluorographene chemistry. Adapted from ref<sup>61</sup>.

### 1.3 Graphene derivatives in electrochemical applications - supercapacitors

Graphene derivatives, thanks to their exceptional properties, found an application in many fields, as described thoroughly in many reports in the literature. One of the most promising fields is energy storage because carbon-based materials present a

lightweight, conductive, cheap, stable and eco-friendly alternative to currently widely used technologies.

Inherent from graphene itself, graphene derivatives usually possess a large surface area and, depending on the degree of functionalization, also a substantial conductivity. The theoretical capacitance of graphene should reach up to  $550 \text{ F g}^{-1}$ .<sup>65</sup> However, most of the reports utilizing pure graphene/reduced graphene oxide do not exhibit such a high value, probably due to the restacking of the sheets and low wettability by the electrolyte. Therefore, both in-plane (heteroatom doping) and out-of-plane (functional groups) functionalization of graphene is very beneficial for increasing the surface area available for contact with electrolytes, as shown in Figure 10. Moreover, a possible introduction of redox-active molecules can boost the performance with pseudocapacitance contribution for the already inherent double-layer capacitance.

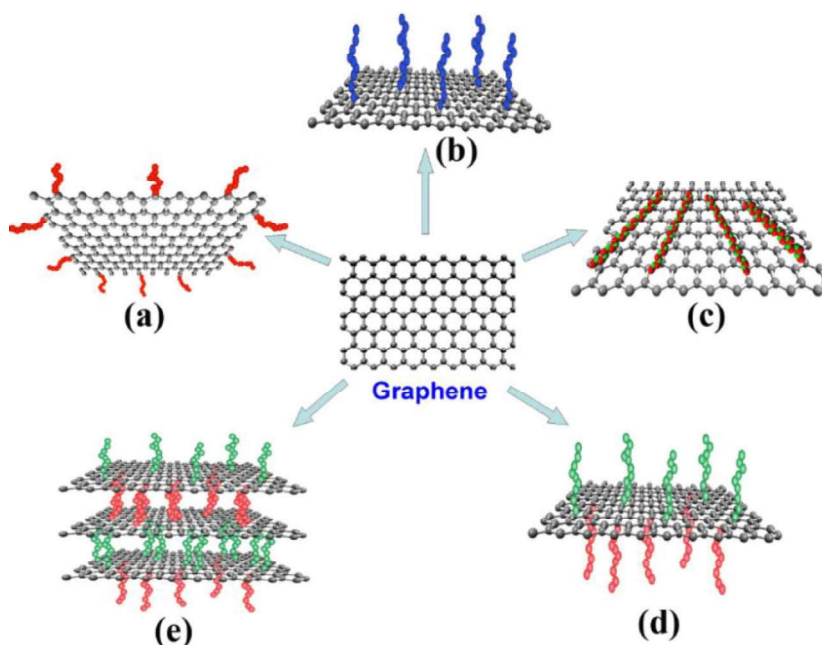


Figure 10 Overview of possible functionalization of graphene, such as a) on edge, b) – d) on the basal plane, and e) stacked into a layered structure. Adapted from ref<sup>66</sup>.

Fluorographene offers rich chemistry, yielding well-defined graphene derivatives with a low amount of residual fluorine and high functionalization degree. Since these derivatives contain both conductive  $sp^2$  conjugated network and  $sp^3$  carbon bearing the functional groups, they offer precise tweaking of their conductivity.<sup>42,59,62,63</sup> Therefore, we can assume that fluorographene is a perfect precursor for synthesizing a broad portfolio of conductive, precisely tailored, functionalized derivatives with controlled properties and structure. These derivatives are forming a potentially large emerging new

class of covalently functionalized graphene-based materials that offer very promising properties and performance for their application in the energy storage field.

## 2 AIM OF THE THESIS

This doctoral thesis aims to develop new covalently functionalized graphene derivatives, via fluorographene chemistry, with tailored properties targeting specific applications. As described previously, fluorographene offers higher reactivity than graphene. Thus, it enables a broad portfolio of possible reactions, yielding different graphene derivatives. Exploiting this chemistry, nitrogen-doped graphene, amino acid functionalized graphene, and graphene acid were prepared, characterized, and studied as active electrode materials in electrochemical energy storage applications, especially supercapacitors.

The aims of this thesis involve the in-depth description of the pathways to yield the three different graphene derivatives, their characterization, and their physicochemical and electrochemical properties:

- Firstly, a highly nitrogen doped graphene derivative (GN3) was prepared, further characterized, and used in energy storage application.
- Secondly, a new amino acid functionalized material was prepared and used as active electrode material in a sustainable supercapacitor.
- Lastly, an application study of highly functionalized graphene derivatives, graphene acid, was conducted to evaluate its performance as a supercapacitor focusing on the intrinsically good properties of graphene acid for utilization in energy storage.

This thesis provides an example of two strategies for precise designing and preparing chemically functionalized graphene derivatives for targeted use in the energy storage field. The tunable and efficient grafting of carefully selected moieties enabled a better performance than state-of-the-art in terms of energy content, power density or stability upon charging/discharging.

## **3 EXPERIMENTAL PART**

### **3.1 Methods of characterization**

The prepared materials were characterized using various methods, such as different spectroscopies, thermal and surface area analysis, or microscopy techniques. Their application potential in the energy storage field was optionally evaluated using a battery tester and potentiostat, featuring generally used cyclic voltammetry, galvanostatic charge/discharge, and electrochemical impedance spectroscopy.

#### **3.1.1 Fourier transformed infrared spectroscopy**

Infrared spectroscopy is a spectroscopic method based on the interaction of electromagnetic radiation with molecules when radiation passes through a sample. An essential condition is changing the dipole moment during absorption (dipole moment can be induced by vibration or permanent).

Spectral lines (bands) in region  $500 - 1500 \text{ cm}^{-1}$  represent skeletal vibrations of molecules; this region is the so-called fingerprint region – according to these bands, there is a possibility to identify unknown substances from libraries.

FT-IR can be used for qualitative analysis of materials, especially for resolving different functional groups, which other techniques can not easily differentiate.

#### **3.1.2 X-ray photoelectron spectroscopy**

X-ray photoelectron spectroscopy (XPS) is a spectroscopic method using the interaction of x-ray radiation with atoms in the sample. Roentgen rays are highly energetic electromagnetic radiation with wavelengths  $0,1 - 10 \text{ nm}$ , making them very penetrating.

The principle of XPS is based on the photoelectron effect (the process of photoelectron emission from a sample due to the interaction with electromagnetic radiation of suitable energy). The analysis depth is around  $10 \text{ nm}$ .

#### **3.1.3 Microscopy techniques**

Transmission electron microscopy (TEM) and scanning electron microscopy (SEM) are crucial methods for imaging nanosized objects and structures. These

techniques provide insights into the structure and physiochemical properties of studied materials.

The microscopy techniques use an electron beam source to inflict collision of the electrons with a sample to obtain information from the detected signals after collisions. The obtained resolution can be as low as 0.05 nm (the case of High Resolution (H.R.) TEM).

### **3.1.4 Raman spectroscopy**

Raman spectroscopy is a fast, sensitive and non-destructive spectroscopic method. It determines the vibrational (optionally also rotational) modes of a molecule. The principle is based on a Raman scattering of photons interacting with the measured sample.

The yielded spectrum is a fingerprint of the studied material, providing quantitative and qualitative information. Raman is a beneficial technique for studying graphene-based materials primarily because of graphene's distinct features in the spectrum.

### **3.1.5 X-ray diffraction spectroscopy**

X-ray diffraction spectroscopy is a non-destructive technique based on the interaction of X-ray with the material's crystal lattice. According to Bragg's law of diffraction, the yielded spectrum provides a characteristic pattern for all crystalline substances. There are no sharp observed peaks for mainly amorphous materials, like graphene and its derivatives; however, the layer distance can be calculated from the broad measured peaks.

### **3.1.6 Thermogravimetric analysis**

The thermogravimetric analysis serves as a very useful tool to experimentally probe the thermal stability of prepared materials. The sample is heated up in various atmospheres and the mass loss is recorded. Based on this TGA "spectrum", the information about leaving functional groups and overall decompositions can be extracted.

This technique is a powerful tool for confirming the presence of covalently attached functional groups on the graphene lattice.

### 3.1.7 Surface area analysis

The measurement technique for analysis of surface area (usually abbreviated as BET based on the common adsorption model equation used for final calculations of surface area) is a valuable method to obtain a surface area of a sample in dried form.

During the measurement, the machine monitors gas pressure in a temperature-controlled cell/cuvette with a sample, where sorption/desorption of the used gas occurs. The amount of adsorbed/desorbed gas is then calculated and using different adsorption models (Langmuir, Brunauer-Emmett-Teller, etc.), the surface area and pore distribution are obtained.

### 3.1.8 Nuclear magnetic resonance

Nuclear magnetic resonance is a powerful technique to study the atomic levels of nuclei in a magnetic field. A solid-state probe is used for solid samples, like powders, and the resonance frequency of a nuclear spin is recorded. It is affected by the magnetic field and the nuclei's interactions with their chemical surroundings.

The obtained spectra can give information on the different nature of the bonds, structure, conformation or functionalization.

### 3.1.9 Electrochemical testing

The supercapacitor charge storage mechanism can be divided into two groups<sup>67</sup>:

- 1) EDLC - electric double-layer supercapacitors, electrostatically stored charge arises from a double-layer interaction of ions at the interface of an electrode/electrolyte), typical in carbon-based materials<sup>68</sup>,
- 2) Pseudocapacitive - charge stored in the electrochemical faradaic reaction of redox-active materials such as metal oxides<sup>69,70</sup>, MOFs<sup>71,72</sup>, MXenes<sup>73</sup>.

The three-electrode testing system consists of a working electrode, a reference electrode, and a counter electrode. The working electrode is the one being tested. The studied material is in the form of a drop-casted film, thick paste, ink, or in any other form conductively attached to the electrode. The electrode material must be inert such as various metals, glassy carbon electrodes, or carbonaceous materials<sup>74</sup>. The reference electrode is an electrode with constant standard electrode potential; it is used for the determination of applied potential on a working electrode<sup>75</sup>, the most common ones are



standardized electrodes such as saturated calomel electrode or silver chloride electrode. The counter electrode often utilizes inert metals like gold, platinum, or stainless steel<sup>76</sup>, but new electrode materials have lately emerged, as well<sup>77,78</sup>. A sufficiently large surface area of the counter electrode is crucial to counterbalance the surface area of the active material deposited on the working electrode.

The two-electrode system is built using two current collectors with conductively attached active material; these two electrodes are separated by an insulating separator. The whole system is immersed in a conductive electrolyte and sealed<sup>79</sup>. The current collectors collect electrons and provide support for most of the materials (except for materials that are very conductive by themselves). The separator prevents electrical shortcuts and enables the storage of the electrolyte within its pores<sup>80</sup>, such as any insulating material, e.g. paper, glass fibers or polypropylene membrane (Celgard)<sup>81</sup>. Electrodes with the active material under study are usually prepared by drop-casting or by the Dr. Blade technique. The casting paste comprises an active material, an optimal binder, and a conductive additive, usually dispersed in an organic solvent.

### 3.1.9.1 Cycling voltammetry

During the measurements, the potential is applied to the working electrode with a respect to the fixed potential of the reference electrode (in the three-electrode setup), or it is applied between the positive and the negative electrode in the two-electrode configuration. The speed of the potential sweep is called the scan rate ( $\text{V s}^{-1}$ ), while the range of scanned potential is known as the potential window. The resulting current ( $I$ ) vs. potential ( $E$ ) CV voltammogram enables a diagnosis of the tested material both from the quantitative and qualitative points of view<sup>82</sup>. The shape of the CV can be used for distinguishing between the EDLC and pseudocapacitive (PC) behaviours, where the CV curve of EDLC is mostly rectangular in shape, compared to PC where there is the presence of redox peaks<sup>83</sup>. From different scan rates, it is also possible to extract information about the contribution of the EDLC and PC mechanisms separately, as described by Trassati<sup>84,85</sup> or Dunn<sup>86,87</sup>.

### 3.1.9.2 Galvanostatic charge and discharge

A GCD technique is the most common method for the evaluation of a supercapacitor performance under the controlled current conditions<sup>88</sup>, such as

capacitance results, energy density, power density, *etc.* The desired values can be easily calculated from fundamental indicators while performing the testing in both three and two-electrode setup. Repetitive charging and discharging of the tested material at a constant current result in the plot where the potential (V) is plotted against the time (s). Moreover, this method is beneficial for evaluating the active material in rate and life-time stability testing.

### **3.1.9.3 Electrochemical impedance spectroscopy**

The ground principle of EIS is the measurement of impedance as the function of the frequency where the low amplitude alternating voltage (usually lower than 10 mV) is superimposed on a steady-state potential. The output is drawn as the frequency dependence on a phase angle (Bode plot) or impedance's real and imaginary part on a complex plane (Nyquist plot) <sup>89-91</sup>. Therefore, EIS is a powerful tool for determining charge transfer resistance, ESR, mass transport characteristics, or charge storage mechanism. It can also be used for cross-checking the obtained values of capacitance from the testing system.

## **3.2 Syntheses of graphene derivatives featured in the thesis**

### **3.2.1 Synthesis of nitrogen superdoped graphene, denoted as GN3, adapted from ref<sup>1</sup>**

1 g of graphite fluoride was dispersed in 60 ml DMF in a round bottom glass flask under an inert atmosphere and stirred with a Teflon coated magnetic stirrer for 3 days at 500 rpm. Then, the dispersion was sonicated for 4 hours in a sonication bath (Bandelin Sonorex, frequency 35 kHz, effective power 160 W), then left for stirring overnight. The next day, 3 g of NaN<sub>3</sub> were added to the flask and the mixture was heated for 72 hours at 130 °C in an oil bath for 72 h with a condenser on top while stirring at 800 rpm. After the reaction, the reaction mixture was left to cool down, collected to plastic falcons, and washed using centrifugation (Sigma 4-16K at 13 000 rcf) as follows: the dispersion was centrifuged, the supernatant was discarded, and the black solids were redispersed in a same amount of fresh solvent using vigorous shaking and brief mild sonication. The solvents for washing were used as follows: 3x DMF, acetone, ethanol, hot water (80 °C), water, and acidified water (3% solution of HCl). Finally, washing with water was performed until the material stopped precipitating with the centrifuge. The dispersion was then subjected to dialysis against ultrapure water for 3 weeks.

Product denoted as GN3.

### **3.2.2 Synthesis of amino acid functionalized graphene, denoted as FG/Arg\_48h, adapted from ref<sup>92</sup>**

The synthesis of amino acid functionalized graphene can be performed with or without a presence of potassium carbonate, which acts as a pore-forming agent, further boosting the electrochemical performance. For clarity in the following discussion, both synthetic protocols are provided:

#### **a) Synthesis of Boc- and Arg-functionalized graphene**

200 mg of graphite fluoride was dispersed in 10 mL of DMF and subjected to probe sonication (Bandelin Sonoplus, type UW 3200, probe VS70T). The mixture was transferred to a glass flask and the flask was sonicated for 2.5h in a sonication bath (Bandelin Sonorex, DT255H type, effective power 160 W). Then, 1.76 g of Boc-Arg-

OH was added to the flask and the mixture was sonicated for another 1 h. Afterward, the complete dispersion was heated at 125 °C for varying times (24, 48, or 72 h) while stirring in an oil bath. When the reaction finished, the mixture was separated and washed by centrifugation, using DMF, water and ethanol as washing steps. The purified product was moved to a round bottom flask with 20 mL hydrochloric acid (5.7 M) and 3.75 mL acetone. The mixture was heated at 100 °C for 1h while stirring. Finally, the black product was separated from the solvent and purified by centrifugation steps with water, acetone, and ethanol.

Product denoted as FG/Arg\_ number of hours of synthesis.

#### **b) Synthesis of Boc- and Arg-functionalized FG in the presence of potassium carbonate**

200 mg of graphite fluoride was dispersed in 10 mL of DMF and subjected to probe sonication (Bandelin Sonoplus, type UW 3200, probe VS70T). The mixture was transferred to a glass flask and the flask was sonicated for 2.5h in a sonication bath (Bandelin Sonorex, DT255H type, effective power 160 W). Then, 1.76 g of Boc-Arg-OH was added to the flask, and the mixture was sonicated for another 1 h. Afterwards, 0.44 g of potassium carbonate dissolved in 2 mL of water was added to the mixture, and the system was sonicated for another 15 min. Afterwards, the complete dispersion was heated at 125 °C for 48 h while stirring in an oil bath. When the reaction finished, the mixture was separated and washed by centrifugation, using DMF, water and ethanol as washing steps. The purified product was moved to a round bottom flask with 20 mL hydrochloric acid (5.7 M) and 3.75 mL acetone. The mixture was heated at 100 °C for 1h while stirring. Finally, the black product was separated from the solvent and purified by centrifugation steps with water, acetone, and ethanol.

Product denoted as FG/Arg\_48\_K

### **3.2.3 Synthesis of carboxyl-functionalized graphene derivatives, denoted as GA, adapted from ref<sup>93-95</sup>.**

Graphene acid is synthesized from another graphene derivative, the cyanographene. The synthesis of graphene acid is similar to the first published protocol<sup>95</sup>. Graphite fluoride (120 mg) was dispersed in 15 mL of DMF and left for stirring for 2 days under a nitrogen atmosphere. Then, the mixture was sonicated for 4 h in a sonication bath

(Bandelin Sonorex) and left for stirring overnight. Afterwards, 800 mg of NaCN was added and the mixture was heated at 130 °C in an oil bath for 72 h with a condenser on top while stirring at 500 rpm. After the reaction, the reaction mixture was left to cool down, collected to plastic falcons, and washed using centrifugation (Sigma 4-16K at 13 000 rcf) as follows: the dispersion was centrifuged, the supernatant was discarded, and the black solids were redispersed in a new amount of the solvent using vigorous shaking and brief mild sonication. The solvents for washing were used as follows: 3x DMF, acetone, ethanol, hot water (80 °C), water, and acidified water (3% solution of HCl). Finally, washing with water was performed until the material stopped precipitating with the centrifuge. The final (pure) cyanographene was subjected to hydrolysis to obtain graphene acid. Concentrated nitric acid (65%) was added to a suspension of cyanographene in deionized water in a ratio to obtain a 25% concentration while stirring. The mixture was heated for 24 h at 100 °C with a condenser while stirring at 400 rpm. After the reaction, the reaction mixture was left to cool down and washed with cold water, hot water, and acidified water until precipitation of the product ceased in the centrifuge.

## 4 RESULTS AND DISCUSSION

This thesis's discussion comprises four publications dealing with functionalized graphene derivatives utilized in energy storage applications. The author of this thesis contributed as a first author in two of those publications<sup>1,94</sup> and as a co-author in the third one<sup>92</sup>.

### 4.1 Nitrogen Doped Graphene with Diamond-like Bonds Achieves Unprecedented Energy Density at High Power in a Symmetric Sustainable Supercapacitor

*Text adapted from*

- Šedajová, V.; Bakandritsos, A.; Błoński, P.; Medved', M.; Langer, R.; Zaoralová, D.; Ugolotti, J.; Džibelová, J.; Jakubec, P.; Kupka, V.; Otyepka, M. Nitrogen Doped Graphene with Diamond-like Bonds Achieves Unprecedented Energy Density at High Power in a Symmetric Sustainable Supercapacitor. *Energy Environ. Sci.* 2022, 15 (2), 740–748. <https://doi.org/10.1039/D1EE02234B>.

#### Introduction

Supercapacitors belong to the portfolio of energy storage devices with their extraordinary qualities, like fast charging/discharging and very long cycle-life.<sup>96</sup> Unfortunately, the energy density of the best existing supercapacitors (their amount of stored energy) is at low values. Commercial supercapacitors have cell-level specific energies (and energy densities) of 10 Wh kg<sup>-1</sup> (5-8 Wh L<sup>-1</sup>)<sup>97,98</sup>. In comparison, lead-acid batteries offer 20-35 Wh kg<sup>-1</sup> (40-80 Wh L<sup>-1</sup>)<sup>99</sup>, with the state-of-the-art Li-ion batteries achieving ~150 Wh kg<sup>-1</sup> (~250 Wh L<sup>-1</sup>).<sup>100,101</sup> However, the disadvantages of Li-ion batteries are well known, such as long charging/discharging times and short life cycle due to the irreversible processes during cycling. Identification of electrode materials with substantially improved energy densities combined with long life and high power is necessary to utilize the benefits of supercapacitors in a broader range of applications. Moreover, reducing our dependence on critical resources, increasing sustainability, and decreasing our carbon footprint are widely discussed targets. The replacement of metal atoms in electrode materials with earth-abundant, non-metallic elements, such as carbon, fits perfectly within the goals of the Green Deal.

Energy density is a crucial parameter in energy storage devices, making it a high priority target to improve<sup>97–99,102–105</sup>. The highest energy density reported to date was obtained using electrodes consisting of bilayers of exfoliated graphene-mediated hydrogen iodide-reduced graphene oxide (EGM-GO)<sup>106</sup> with a mass density of *ca.* 1 g cm<sup>-3</sup> exhibiting capacitance 203 F cm<sup>-3</sup> and, at that time, the record energy density of 113 Wh L<sup>-1</sup> at 0.9 kW L<sup>-1</sup> (current density 1 A g<sup>-1</sup>). Within this work, we reported a novel carbon-based electrode material, GN3, with an unprecedented mass density of 2.8 g cm<sup>-3</sup>. Its excellent ability to host ions surpasses commercially used porous materials (S.A. > 2000 m<sup>2</sup> g<sup>-1</sup>). GN3, with its extraordinary properties, achieved an energy density of 200 Wh L<sup>-1</sup> at a power density of 2.6 kW L<sup>-1</sup>, corresponding to improvements of 74% and 190%, respectively, over the previous record.<sup>106</sup>

Based on our knowledge and experience in utilizing fluorographene chemistry, we predicted that it could produce carbon derivatives with high mass densities. Based on previously published reports of the synthesis of *sp*<sup>3</sup>-rich carbon materials,<sup>107–109</sup> via fluorine and radical chemistry<sup>110,111</sup>, and by the high density of such materials,<sup>112</sup> The carbon atoms in between fluorine atoms in FCCF manner in (C<sub>2</sub>F)<sub>n</sub> are adopting a diamond-like structure,<sup>113,114</sup> giving rise to the high mass density.<sup>114</sup> Theoretical and experimental verifications of similar *sp*<sup>3</sup>-rich systems were observed for bilayer graphene.<sup>115,116</sup> Fluorocarbons are large band-gap insulators<sup>117</sup> with intrinsic high mass density. However, the lack of sites for solid interaction with ionic species hinders ionic transport. The radical reactions propagated by fluorine elimination<sup>118,119</sup> are known to trigger the defluorination and functionalization of fluorographene, potentially being the driving force of *sp*<sup>3</sup> C-C bond formation, creating graphene-based materials with high mass density.

## Results

Therefore, we experimentally and theoretically investigated a reaction of few-layered fluorographene with sodium azide. Sodium azide has a double role as a defluorinating and doping agent (introducing different configurations of nitrogen atoms inside the graphenic lattice). The functionalization increases the polarity and hydrophilicity of the carbon surface and creates vacancies, as previously studied through reactions of fluorographene with other nitrogen-containing nucleophiles.<sup>119–121</sup> Exfoliated fluorographene was subjected to a reaction with NaN<sub>3</sub> in dimethylformamide

at 130 °C, yielding nitrogen-superdoped graphene (Figure 11). XPS revealed a significant decrease in the atomic content of 4h byproduct, followed by almost complete defluorination after 72h. Moreover, the GN3 material's N content reached 16.1 at.% after the reaction also reflected in the C1s deconvolutions. The carbon atoms, initially bonded with fluorine (binding energies above 289.5 eV), were transformed during the synthesis into aromatic  $sp^2$  carbons (284.7 eV, 45%), non-functionalized  $sp^3$  carbons (285.5 eV, 25%), and nitrogen bonded carbons (286.6 eV, 19%), respectively. The other components are related to the residual amounts of fluorine (the non-reactive  $CF_2$  species on the edges) and carbon atoms bonded to oxygen (coming from the environment).

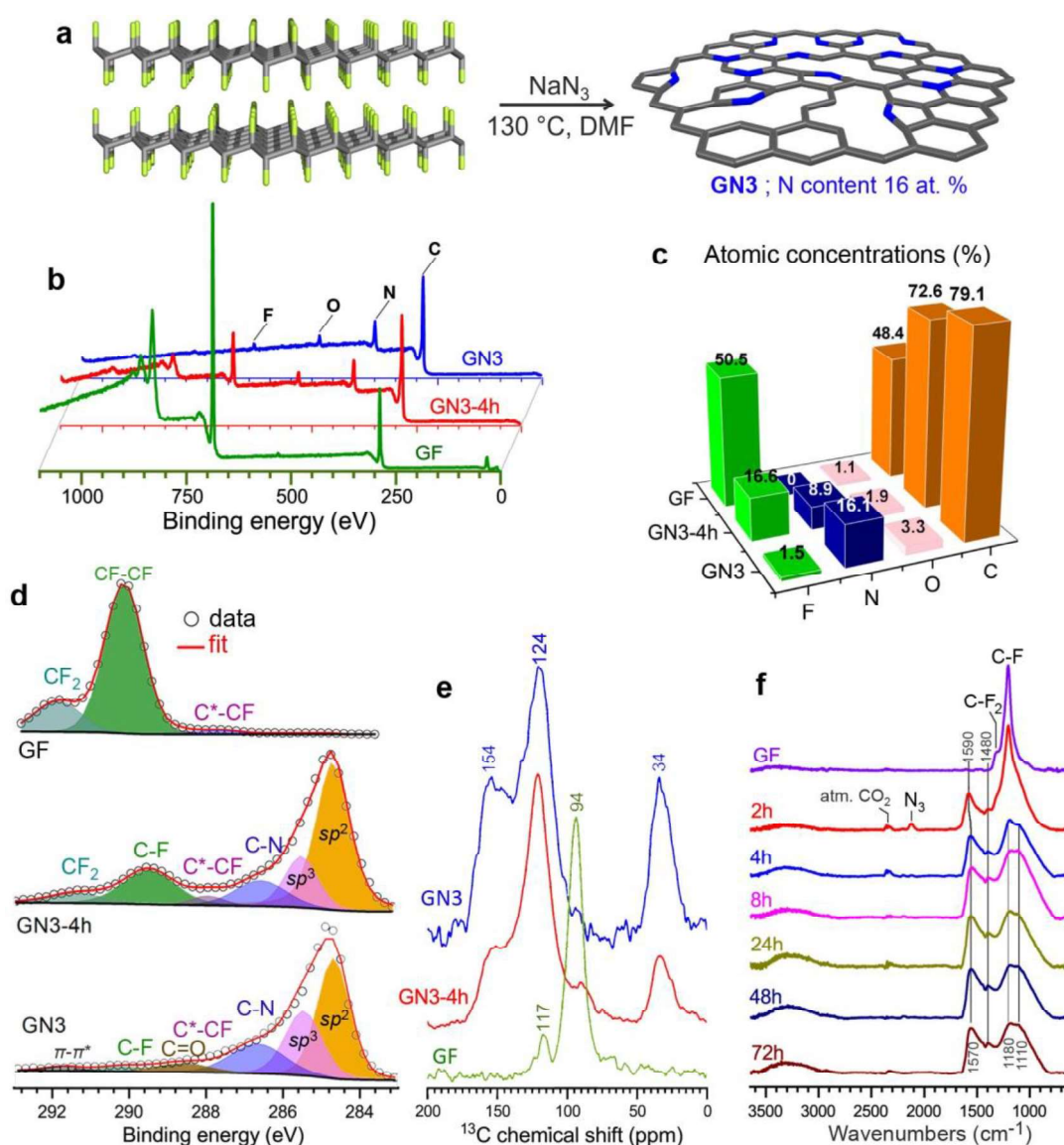


Figure 11 (a) Schematic depiction of the synthesis of GN3. (b)-(d) XPS characterization and deconvolutions. (e) CP MAS  $^{13}C$  solid-state NMR and (f) FT-IR spectra of starting product, byproducts, and final material.



The  $^1\text{H}\rightarrow^{13}\text{C}$  CP MAS solid-state NMR spectra (Figure 11) showed peaks at 34 ppm typical for non-functionalized and non-nitrogen bonded  $sp^3$  carbons in diamond and diamond-like carbon materials.<sup>122</sup> This peak was more intense in the spectrum of GN3 final material than in the GN3-4h intermediate, indicating that these  $sp^3$  carbons were formed as the reaction progressed. Moreover, the presence of a  $\pi$ -conjugated aromatic network and aromatic  $>\text{C}=\text{N}$  moieties (pyridinic and pyrrolic)<sup>122,123</sup> was confirmed by the peaks centered at 124 and 154 ppm, respectively.  $^{19}\text{F}\rightarrow^{13}\text{C}$  CP MAS of the starting material showed peaks corresponding to  $\text{CF}_2$  (117 ppm) and  $\text{CF}$  (94 ppm) groups, respectively, which are typical in graphite fluoride.<sup>124</sup>

The FTIR technique provided thorough insights into the reaction mechanism; specifically, the bands of the  $\text{CF}$  and  $\text{CF}_2$  groups of GF (1200 and 1305  $\text{cm}^{-1}$ , respectively) were progressively replaced with bands at 1580 and 1210  $\text{cm}^{-1}$  (characteristic of aromatic carbon rings<sup>125</sup>), indicating the defluorination and formation of an  $sp^2$  network (Figure 11). Additional aromatic-ring vibrations, corresponding to the band at 1400  $\text{cm}^{-1}$ , can be assigned to a heteroatom substitution (e.g., with pyridinic nitrogens<sup>125,126</sup>), as suggested using theoretical calculations.<sup>127,128</sup> Interestingly, the initial attachment of azide groups in the first hours of the reaction was confirmed by the infra-red spectrum of the 2h intermediate, corroborating the theoretical results explaining the reaction mechanism.

Further insights into the N-doping of fluorographene with  $\text{NaN}_3$  were obtained through DFT calculations. The  $\text{N}_3^-$  anion initiated the reaction by nucleophilic attack on carbon radical defects, leading to  $\text{N}_2$  release and fluorine elimination (Figure 12). The formation of graphitic nitrogen configuration by a nucleophilic attack of the azide anion on the single vacancy (SV) and double vacancy (DV) was calculated. The general reaction mechanism is in line with the recent reports on the mechanisms underlying the chemistry of fluorographene.<sup>64,110,111,119</sup>

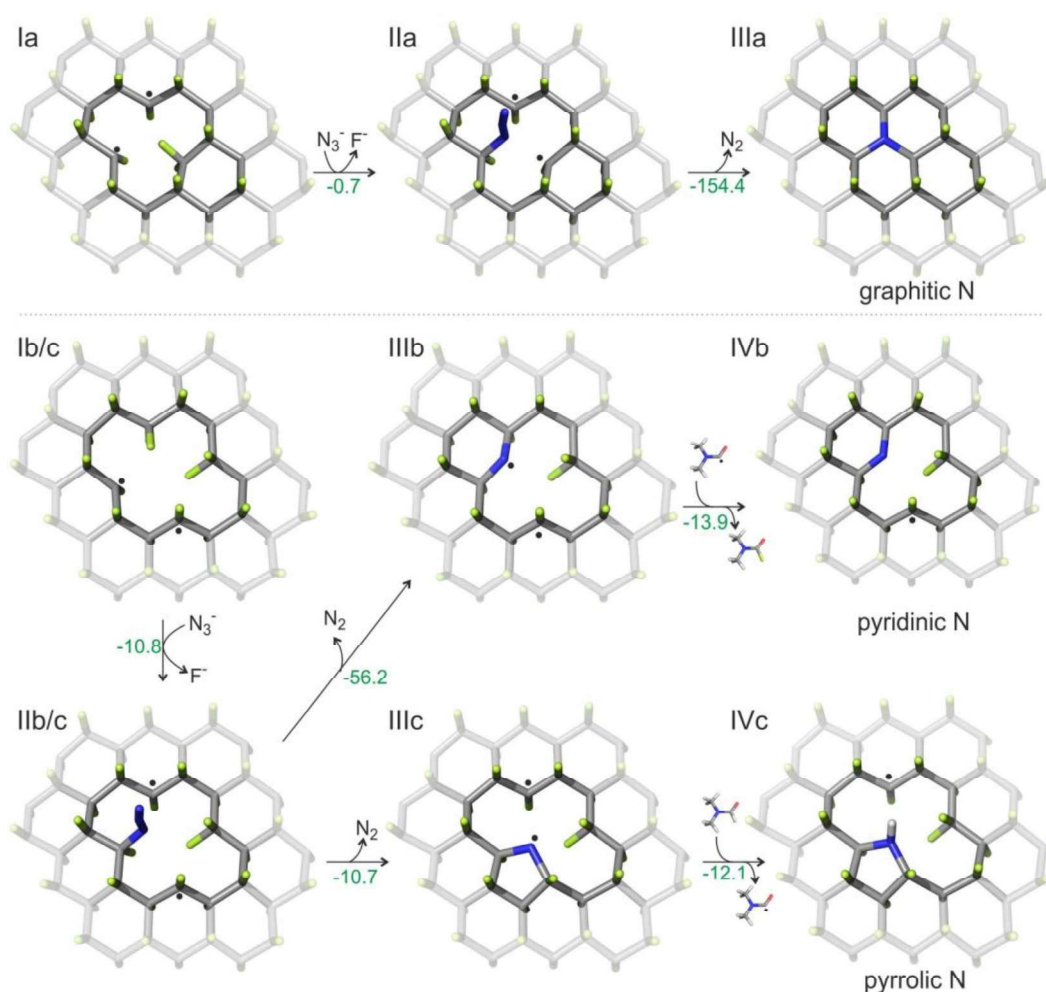


Figure 12 The formation of GN3 structures via the reaction of FG with sodium azide in DMF modeled at the  $\omega$ B97X-D/6-31++G(d,p)/SMD(solvent=DMF) level of theory<sup>129,130</sup>, showing the formation of different nitrogen configurations. The energies are given in kcal mol $^{-1}$ .

The high-resolution transmission electron microscopy (HR-TEM) revealed that the nature of the GN3 structure is indeed 2D sheets with a very holey design, as shown in Figure 13. EDXS elemental mapping with high-angle annular dark-field scanning transmission electron microscopy (HAADF-STEM, Figure 13) showed that the GN3 sheets are densely and homogeneously doped with nitrogen atoms inside the graphenic lattice.

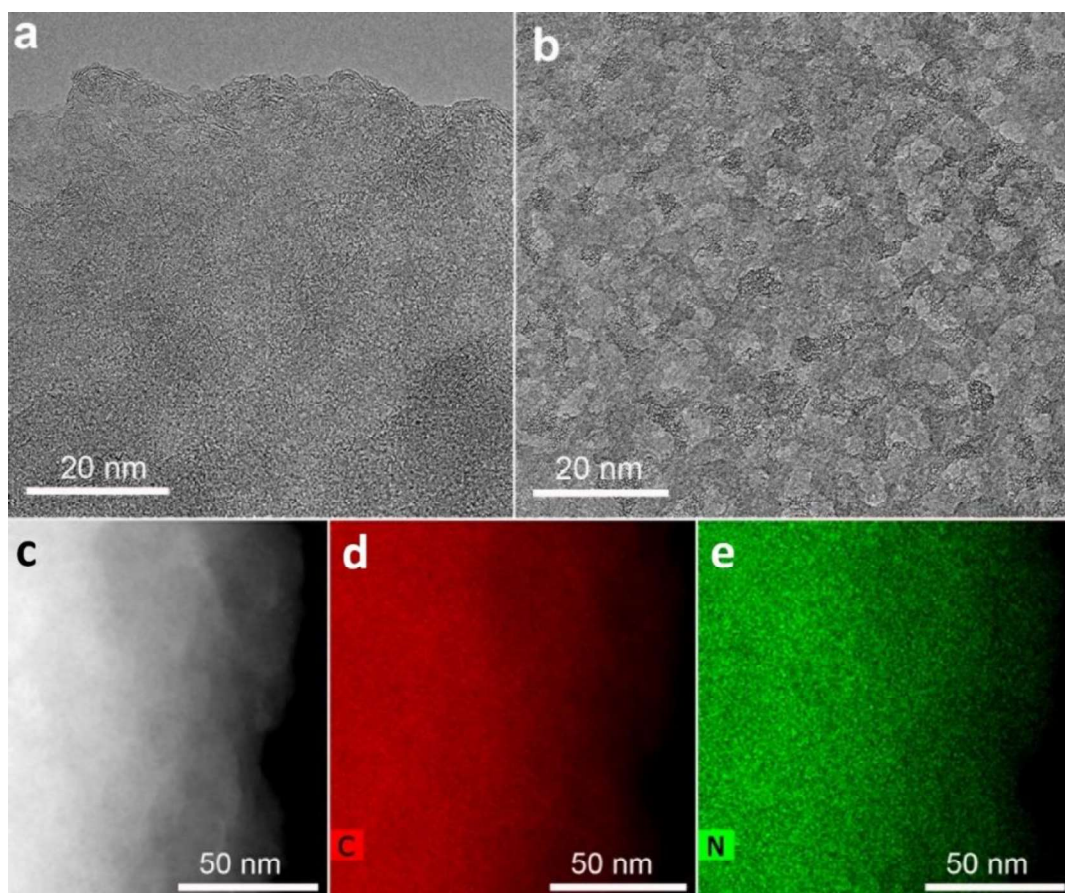


Figure 13 HR-TEM images of the GN3 material alongside the EDS mapping of carbon and nitrogen.

In order to understand better the formation of the tetrahedral C-C bonds, using spin-polarized DFT was employed to investigate the theoretical models of the GN3 sheet fragment. The sheets were designed to contain vacancies and nitrogen dopants, mainly in pyridinic and pyrrolic configurations) to simulate the experimental findings. The GN3 system relaxed into a thermodynamically stable structure, spontaneously forming tetrahedral  $sp^3$  C-C bonds, thoroughly verifying the experimental NMR results. The tetrahedral bonds were formed between the carbons in the vacancies related to pyridinic nitrogens, where radicals were centered (highlighted spheres in Figure 14 (a) Theoretical model of GN3 fragment by DFT calculations. (b) TGA-MS analysis of GN3 product in the air atmosphere.). Similar  $sp^3$  bonding was suggested to form after introducing atomic vacancies and pyrrolic N atoms by N-ion beam irradiation of graphene sheets, which creates carbon atoms with dangling bonds (radicals) around the vacancies.<sup>131</sup> Moreover, the TGA-MS analysis in the air atmosphere (Figure 14) proved that the nitrogen atoms are indeed incorporated in the graphenic structure because the

NO emission ( $m/z=30$ ) peaked at the same high temperature of 675 °C as CO<sub>2</sub> ( $m/z=40$ ), which corresponds to the graphene lattice decomposition.

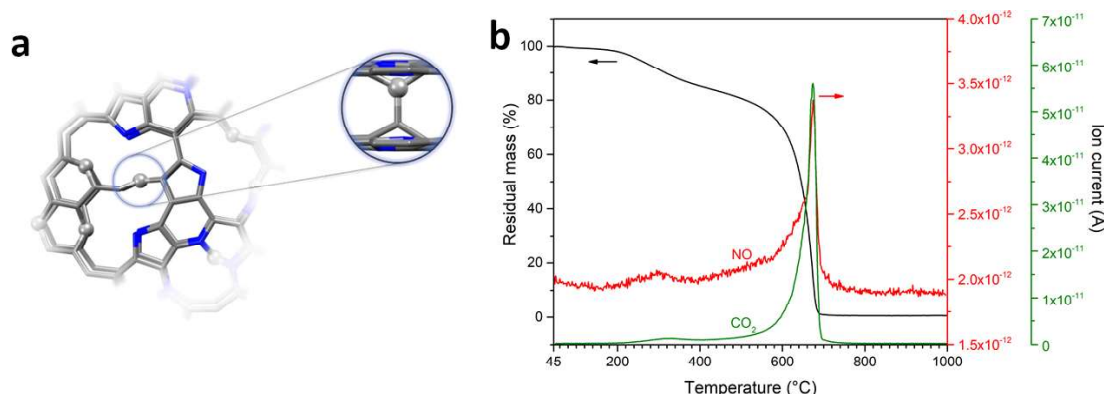


Figure 14 (a) Theoretical model of GN3 fragment by DFT calculations. (b) TGA-MS analysis of GN3 product in the air atmosphere.

Pasted films of GN3 material with additives (polymer binder PTFE at 10%wt; conductive additive TimCal at 5%wt.) were prepared via the Dr. Blade technique by pasting homogeneous slurries on Al foil for density measurements and preparation of supercapacitor electrodes. Thickness measurements using SEM<sup>1</sup> and digital micrometer (Figure 15) showed that pressing the film between two metallic plates for 1 min at 80 kN caused bed consolidation of the material, increasing the mass density of the material to 2.75 g cm<sup>-3</sup> compared to 0.5 g cm<sup>-3</sup> before pressing.

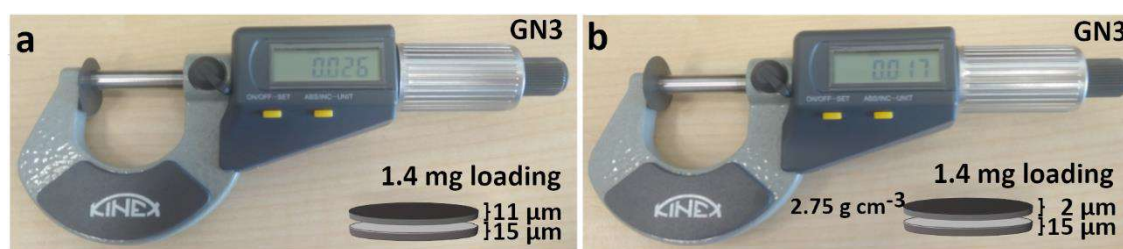


Figure 15 Photos of a digital micrometer with GN3 electrodes before and after pressing at 80 kN for 1 minute.

Ten different batches of GN3 material were prepared, all consistently reached that high mass density. Control tests were performed with Al foil alone and commercial carbons of high surface area, specifically porous carbon (PC) from ACS Material (mass density of 0.3 g cm<sup>-3</sup>) and YP-80F Kuraray carbon (KC) (mass density of 0.6 g cm<sup>-3</sup>).

Results verified that Al foil did not change its thickness during pressing and that values of the mass density for the porous carbons matched those given by the providers. The surface area of GN3 determined from the N<sub>2</sub> sorption isotherm using the BET equation (Figure 16) was 128 m<sup>2</sup> g<sup>-1</sup>, while the surface area determined by methylene blue sorption was 300 m<sup>2</sup> g<sup>-1</sup>. This result indicated that the GN3 material structure is far more open in solvated conditions, allowing charged species/molecules to penetrate the network. The low-pressure hysteresis observed for GN3 (despite the 40 s equilibration time allowed during sorption/desorption) constitutes the pore size analysis relatively unsafe. It can be related to various reasons, including changes in the pore size or strong sorbent/adsorbate interactions,<sup>132</sup> or it can probably be due to the requirement of a very long equilibration time during the desorption.<sup>133</sup> The isotherm shape with the minimal knee at the low-pressure regions suggests an absence of micropores. The pore width distribution curve shows relatively uniform pore-size for GN3 material (Figure 16).

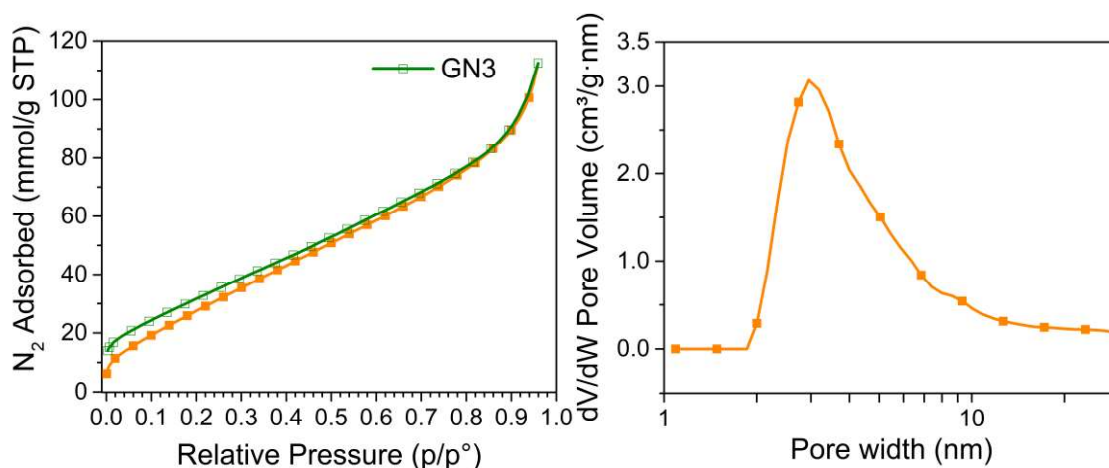


Figure 16 (a) Adsorption and desorption N<sub>2</sub> isotherms of the GN3 material, recorded at 77 K. (b) Pore width distribution for GN3 material.

All the above-mentioned properties predetermined the GN3 material to be superior in energy storage applications, especially in supercapacitors. Briefly, the electrochemical properties of GN3 were studied in a symmetric system in an organic electrolyte (1-ethyl-3-methylimidazolium tetrafluoroborate EMIM-BF<sub>4</sub> with 1,1,2,2-tetrafluoroethyl-2,2,3,3-tetrafluoropropyl ether TTE in a 9:1 ratio). The cyclic voltammograms (Figure 17) were quasi-rectangular featuring minor redox peaks

associated with the nitrogen atoms embedded in the lattice of the GN3 material<sup>134</sup>, retaining the same shape even at a high scan rate.

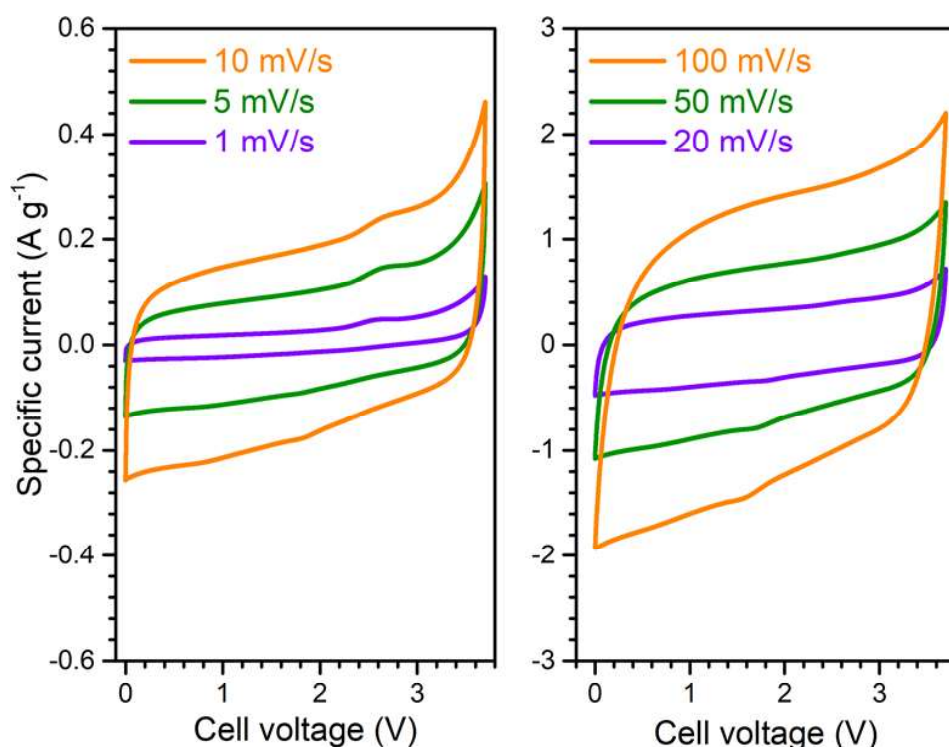


Figure 17 Cyclic voltammograms of GN3 material in a symmetric full cell system.

The galvanostatic charge/discharge measurements (Figure 18) showed linear and symmetric profiles (124 s charging, 118 s discharging at  $2 \text{ A g}^{-1}$ , 95% energy efficiency), resulting from predominantly capacitive behaviour<sup>135</sup>, accompanied by a fast charge transport in the material and at the interfaces.<sup>104</sup>

Moreover, as proper benchmark materials, the carbons PC and KC<sup>136</sup> were tested under identical conditions. GN3 material had a significantly better discharging time (Figure 18) than PC and KC. Despite the dramatic difference in the BET surface area of the GN3 materials and the very porous carbon materials, GN3 exhibited superior performance in both volumetric and gravimetric terms, dominating mainly the volumetric values owing to its high mass density.

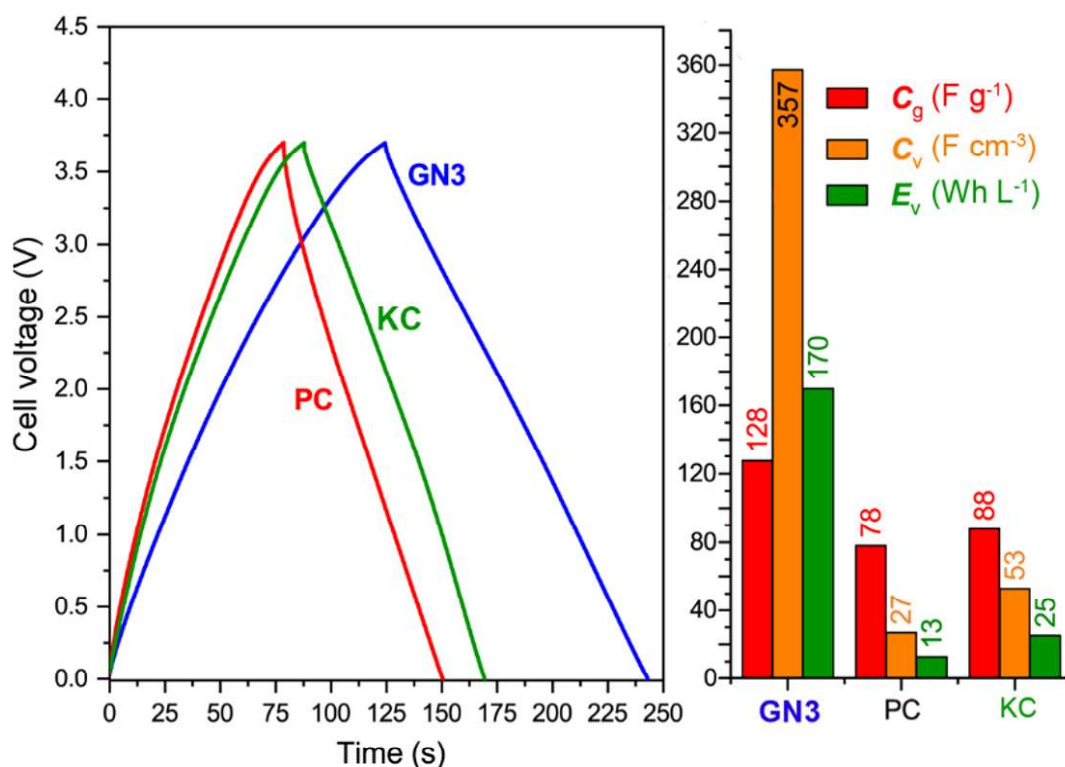


Figure 18 Comparison of (a) GCD curves and (b) energy storage values at 2 A g<sup>-1</sup> of the GN3 material with porous carbons.

Volumetric performance is crucial for devices in the portable energy storage landscape;<sup>97,99,102,103,106,137</sup> when both high energy and high power density are desirable at the same time. The former directly affects the amount of energy that can be stored, while the latter allows for fast charging and discharging. Energy density is the usual weak point of supercapacitors, whereas high power densities are one of their benefits, which must be preserved. The GN3 cell (Figure 19) demonstrated ground-breaking performance by delivering simultaneously ultrahigh energy density and power density, especially when its energy density was *ca.* 200 Wh L<sup>-1</sup> at a power of 2.6 kW L<sup>-1</sup> and 143 Wh L<sup>-1</sup> at 52 kW L<sup>-1</sup>. In order to compare our results with the current state of the art, we had selected top-performing materials from the field, as can be found in Figure 19 (when the same sets of equations and metrics were used in all cases<sup>106</sup>).

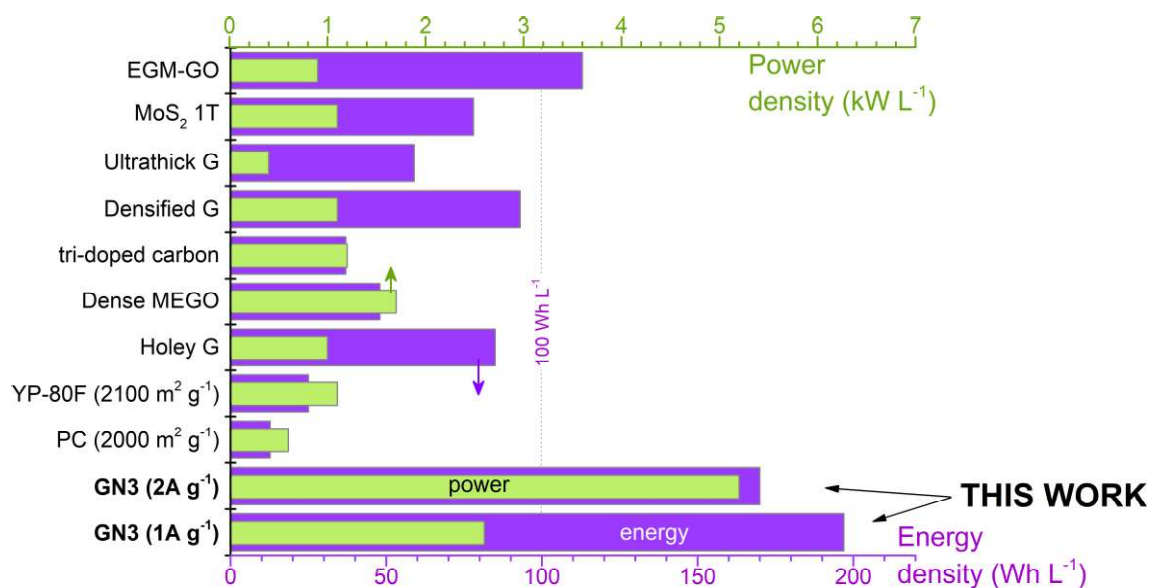


Figure 19 State-of-the-art comparison of the previously published report and this work's results.

Lastly, the GN3 cell could also be operated at commercially relevant mass loadings of up to  $10 \text{ mg cm}^{-2}$ , demonstrating 99% retention of low-mass loading capacitance at a temperature of  $38 \text{ }^\circ\text{C}$ , which is in the range typically used to evaluate energy storage devices,<sup>138–141</sup>.

## Conclusions

In the frame of this work, we have reported a new class of carbon-based materials featuring nitrogen-doped graphene with diamond tetrahedral bonds for high energy density supercapacitor electrodes. The new materials are prepared by utilizing radical-based FG chemistry, allowing the beneficial combination of  $\text{sp}^2$  and  $\text{sp}^3$  carbon bonds in the same network alongside very high nitrogen doping and vacancies. This hybrid carbon achieves a mass density of  $2.8 \text{ g cm}^{-3}$  while maintaining efficient charge transport, ion penetration, diffusion, and storage, even at commercial level mass loading. Specifically, its energy density was approximately  $200 \text{ Wh L}^{-1}$  at  $2.6 \text{ kW L}^{-1}$  and  $143 \text{ Wh L}^{-1}$  at  $52 \text{ kW L}^{-1}$ , well above the state-of-the-art literature reports.



## 4.2 Graphene with Covalently Grafted Amino Acid as a Route Toward Eco-Friendly and Sustainable Supercapacitors

*Text adapted from*

- Vermisoglou, E. C.; Jakubec, P.; Bakandritsos, A.; Kupka, V.; Pykal, M.; Šedajová, V.; Vlček, J.; Tomanec, O.; Scheibe, M.; Zbořil, R.; Otyepka, M. *Graphene with Covalently Grafted Amino Acid as a Route Toward Eco-Friendly and Sustainable Supercapacitors. ChemSusChem* 2021, 14 (18), 3904–3914. <https://doi.org/10.1002/cssc.202101039>.

### Introduction

As mentioned above, direct covalent functionalization of graphene is hard to achieve. Fluorographene chemistry circumvents this obstacle, enabling a broad portfolio of graphene derivatives to be synthesized with covalently attached functional groups. The starting material, graphite fluoride, is well abundant (production in tons) because of its use industrially as a lubricant.

This presented work reported a synthesis of zwitterionic arginine-functionalized FG (FG/Arg). The guanidino functional group on arginine acted as a nucleophile and caused grafting on FG through the nucleophilic attack. The initiation is known to be caused by the electrophilic radical centres at the defect sites of FG.<sup>118,142</sup> Employment of tert-butoxycarbonyl (Boc) protected Arg was necessary in order to protect the amino acid from the random attachment of the arginine onto FG. Afterwards, the arginine already covalently grafted on the FG was deprotected from the Boc group.

For complete optimization of the reaction conditions in terms of the defluorination (increasing the conductivity) and functionalization degree (FD, increasing the zwitterionic character benefiting the capacitance<sup>143</sup>), different times of the synthesis were investigated. As expected, the prepared graphene derivative with optimal porosity exhibited the maximum capacitive performance. It was improved further by adding potassium carbonate (K<sub>2</sub>CO<sub>3</sub>) as a pore-forming agent, causing an increase by a factor of 3 of the surface area, as well as the development of micropores during the reaction. The final highly porous graphene derivative had higher capacitance by 30 % in comparison to the derivative without K<sub>2</sub>CO<sub>3</sub> treatment.

These presented findings showed that this strategy of covalent functionalization of graphene tuned three key factors important in energy storage application - conductivity, FD, and porosity.<sup>144</sup> The synthesized material represents eco-friendly Arg-

functionalized graphene that could be used as an efficient supercapacitor in aqueous electrolytes.

## Results

The reaction leading to the covalent functionalization of FG with Arg is shown in Figure 20. First, the FG reacted through nucleophilic attack with the primary guanidino amine of Boc-Arg-OH, followed by the deprotection of FG/Boc with hydrochloric acid under heating.

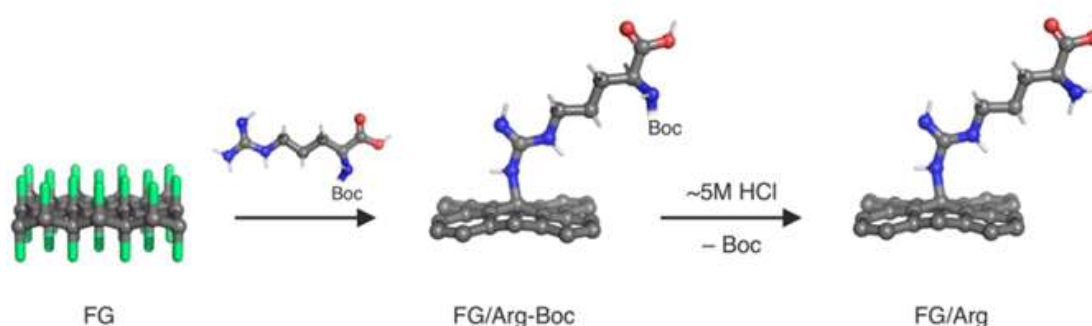


Figure 20 Scheme illustrating FG reaction with Boc-Arg-OH, followed by removal of the Boc protecting group, resulting in the FG/Arg product. Colour coding is as follows: carbon – grey; fluorine – green; nitrogen – blue; oxygen – red.

FTIR measurements confirmed the successful removal of the Boc-protecting group and the presence of a free out-of-plane amino group in the final product (Figure 2), as well as provided direct evidence for the functionalization of FG with Arg. The spectrum of the starting material showed characteristic bands at  $1204\text{ cm}^{-1}$  and  $1307\text{ cm}^{-1}$  assigned to stretching vibrations of C-F bonds.<sup>144,145</sup> The spectrum of FG/Boc-48h shows the distinctive band of N-H stretching vibrations at  $3187\text{ cm}^{-1}$ , attributed to the secondary amine. The FG/Arg-48h product exhibited the O-H vibration (broad band below  $3500\text{ cm}^{-1}$ ), directly overlapping with a second N-H stretching vibration band attributed to the deprotected primary amine.<sup>146,147</sup> Boc protecting group in the deprotected product was proved by the two weak bands at  $\sim 2800\text{--}2950\text{ cm}^{-1}$ , attributed to C-H stretching vibrations of present methyls.<sup>146</sup> Moreover, a missing stretching vibration of the C=O group in the Boc protecting group at  $\sim 1670\text{ cm}^{-1}$  is absent in the FG/Arg-48h spectrum, further indicating effective deprotection of the Arg.<sup>147</sup> An absorption band at  $\sim 1571\text{ cm}^{-1}$  is related to C=C skeleton vibrations in aromatic graphene regions in FG/Boc-48h, also –N-H bending vibration of the primary amine in FG/Arg-48h.<sup>145,147</sup>

The byproducts and final products were evaluated by XPS to compare the atomic ratios. The results showed a significant loss of F atoms with time up to 48 h (decrease from 55.7 at.% of fluorine to 3.2 at.%), which was further reduced by adding the potassium carbonate (2 at.% of fluorine). The complete atomic composition of the FG/Arg-48h product is 76.4 at.% of carbon, 13.7 at.% of nitrogen, 6.6 at.% of oxygen and 3.3 at.% of fluorine, respectively. The atomic composition changed very slightly in the more porous product, resulting from the fluorine elimination, causing a slight increase in the ratio of other elements by 0.7 at.% at maximum.

High-resolution C 1s XPS spectra of the parent material and the covalently functionalized graphene derivative FG/Arg-48h are presented in Figure 22. The deconvolution the C1s region of both materials resulted in the evident differences of the deconvoluted components: C-C ( $sp^2$ ), C-C ( $sp^3$ ), C-N, C\*-C-F, O=C-O, C-F and  $CF_2$ . As the reaction time increased, the area percentage of C-F decreased, reaching a value of 4.3% in the C 1s area in sample treated for 48 h, before remaining constant with further time increases.

The FD of the prepared graphene derivatives was estimated by combining the results from TGA and XPS techniques. The TGA of the FG/Arg and FG/Arg\_K are presented in Figure 21. Via the following calculation, the FD reached 3.7 and 3.5, respectively. Shortly, considering the mass losses after the TGA analysis and the XPS atomic composition, we calculated the formula of the material, and the mass of the product accounted for the functionalities. After subtraction of fluorine content from complete functionalities loss, in order to calculate only the FD of arginine groups, we receive that there is 3.7 mol of functional groups per 100 of graphene carbon atoms for the FG/Arg-48h sample. Thus, the FD is  $\sim 3.7$ . The functionalization degree for the FG/Arg-48h\_K was calculated using the same procedure.

The FD, low content of F atoms, and high content of  $sp^2$  C atoms clearly explain the resulting conductivity of the graphene with grafted Arg, hence its high performance in energy storage devices.

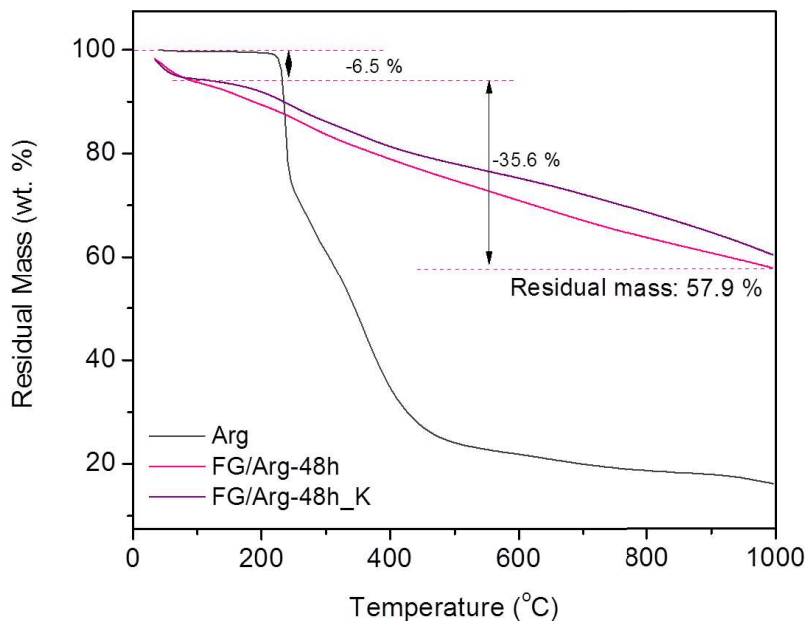


Figure 21 TGA graphs of Arg, FG/Arg-48h, and FG/Arg-48h\_K

The formation of the functionalized graphene derivative was further proved by means of Raman spectroscopy. Two characteristic bands D ( $1332\text{ cm}^{-1}$ ) and G ( $1595\text{ cm}^{-1}$ ) bands were present in the spectra of both prepared samples. The FG/Arg-48h exhibited a ratio  $I_D/I_G$  of 1.32 ( $>1$ ), reflecting the high FD as well as the presence of  $sp^3$  hybridized carbon atoms.<sup>143,144</sup> However, the present carbon  $sp^2$  hybridized atoms are a dominant fraction in the material, giving rise to a high-intensity G peak. It should be noted that the parent material GrF is a Raman silent material.<sup>148</sup> The sample FG/Arg-48h had the highest FD (3.7) and the highest  $I_D/I_G$  ratio (1.32). The slightly lower  $I_D/I_G$  ratio for the FG/Arg-48h\_K sample could be explained by the lower amount of the  $sp^3$  less ordered carbon configuration, which increased the  $sp^2$  content in the sample, caused by etching of this phase by the pore-forming agent.

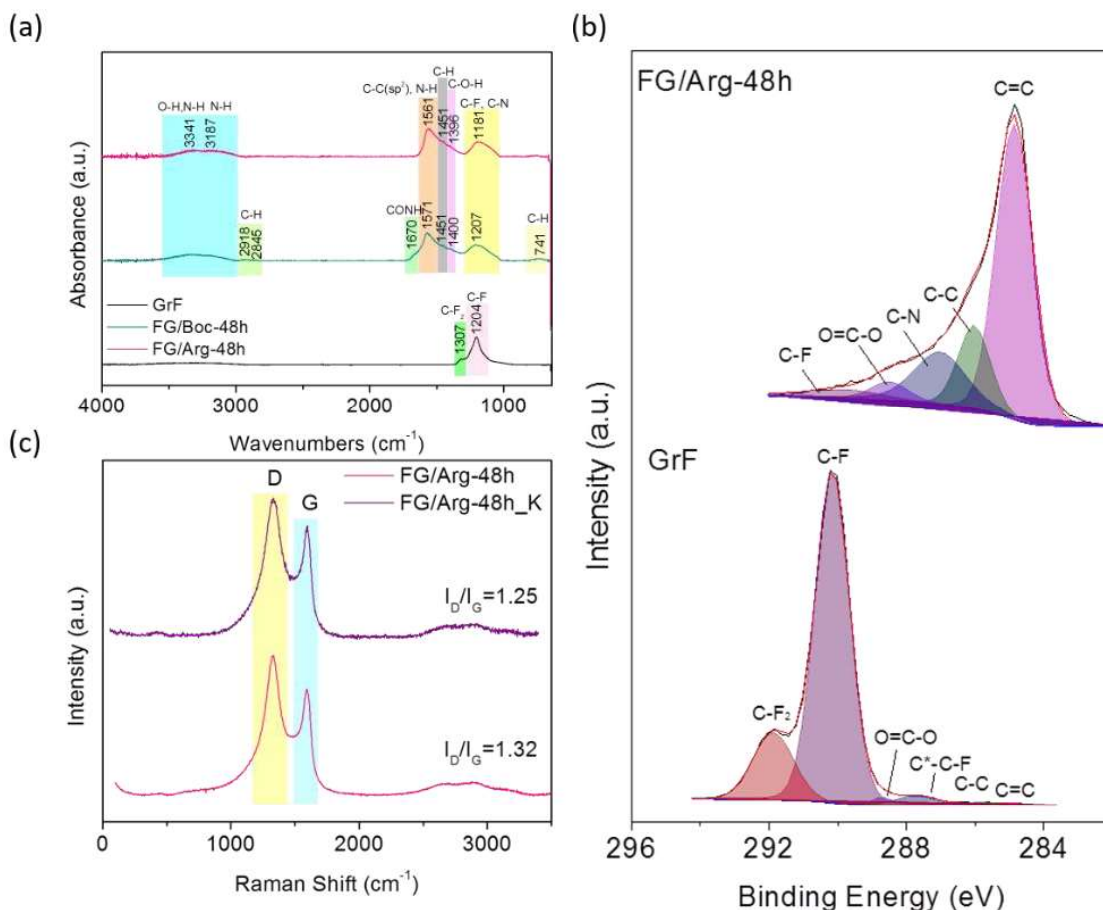


Figure 22 (a) FTIR spectra of GrF, FG/Boc-48h and FG/Arg-48h. (b) High resolution C1s XPS spectra of the parent material GrF and final product FG/Arg-48h. (c) Raman spectra of FG/Arg-48h and FG/Arg-48h\_K samples.

Zeta potential  $\zeta$  measurements as a function of pH were measured (Figure 23) to investigate the behaviour of the zwitterionic network grafted on the graphene. The FG/Arg-48h sheets exhibited positive values (up to +36.8 mV) due to protonation of the amino groups (pH 3.0-6.0). The isoelectric point (IEP) was estimated to be at pH=7.9, which is a notable shift compared to the isoelectric point of Arg (at pH=10.8). This shift can be taken as (indirect) proof of Arg attacking the FG via the guanidine group during the synthesis.

Both FG and graphene are hydrophobic materials, whereas our FG/Arg are hydrophilic and highly water dispersible. Water droplet contact angle measurements were used to study the hydrophilicity of the graphene derivatives. Figure 23 shows a change in the hydrophilicity upon Arg functionalization of the hydrophobic parent, with a decrease in the water droplet contact angle from 142.5° to 10.7° and 15.2° for FG/Arg-

48h. The high wettability of our covalently functionalized graphene verifies the successful grafting of groups.

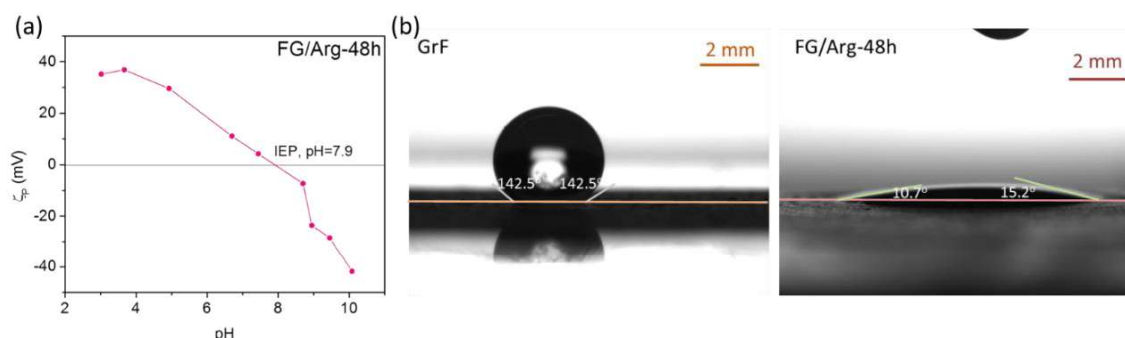


Figure 23 (a)  $\zeta$ -potential curve of an FG/Arg-48h aqueous dispersion versus pH, (b) water droplet contact angle measurements of parent material and FG/Arg-48h

The surface area of FG/Arg-48h and FG/Arg-48h\_K was measured by N<sub>2</sub> adsorption-desorption measurements (Figure 24) and their corresponding pore size distribution (PSD) characteristics were calculated. The Brunauer–Emmett–Teller (BET) surface areas of FG/Arg-48h and FG/Arg-48h\_K were 29 and 100 m<sup>2</sup>/g, respectively. The relatively low surface areas of the graphene derivatives are caused by the restacking of the graphene sheets in the dried samples (used for surface area measurements), contrary to the behaviour in water dispersions.<sup>144,149</sup> The open isotherm of FG/Arg-48h\_K indicates slow desorption kinetics of this sample. The size of the micropores (~1.5 nm) enabled the accommodation of electrolyte ions, therefore predetermined the material to be efficient as supercapacitor electrode materials.

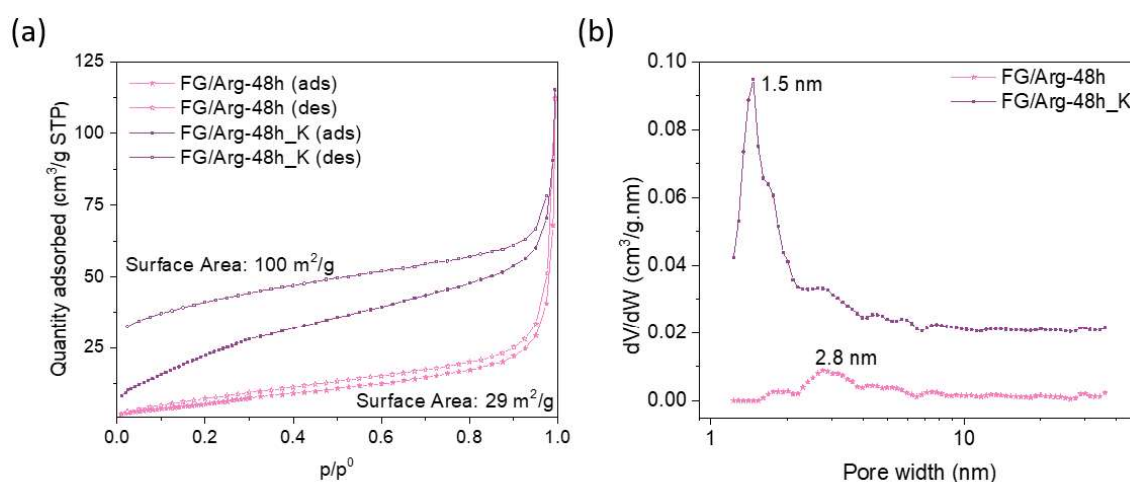


Figure 24 (a) N<sub>2</sub> adsorption/desorption isotherms obtained at -196 °C for FG/Arg-48h and FG/Arg-48h\_K samples. (b) Pore size distributions of FG/Arg-48h and FG/Arg-48h\_K samples.

Microscopy techniques were utilized to investigate the morphology and size of the graphene derivatives prepared at different reaction times and with/without potassium carbonate. SEM images (Figure 25) of FG/Arg-48h and FG/Arg-48h\_K showed thin, few-layered flakes of functionalized graphene with lateral sizes around 1  $\mu\text{m}$ . These images provide evidence of successful implementation of exfoliation during the initial steps of the synthesis.

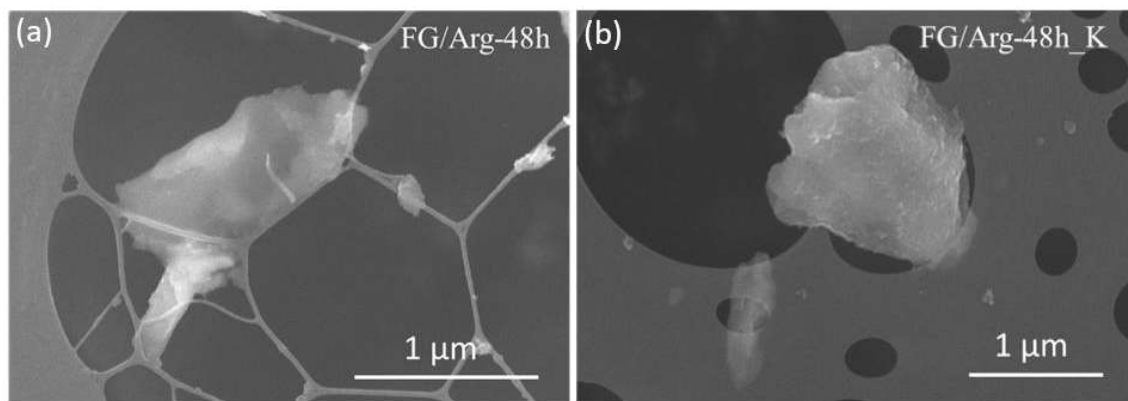


Figure 25 SEM images of (a) the FG/Arg-48h and (b) FG/Arg-48h\_K samples.

TEM techniques (Figure 26) revealed thin flakes, indicative of exfoliated materials, of FG/Arg-48h\_K sample. The edges of the FG/Arg-48h\_K sheets in HR-TEM images were almost transparent, indicating that this material's thickness is only a few graphenic layers. Elemental mapping of FG/Arg-48h\_K (Figure 26d-i) revealed homogeneous grafting of functional groups throughout the flake's surface. Potassium was removed entirely during thermal treatment with hydrochloric acid. As evident, a high density of functional groups was distributed uniformly across the surface of the graphene flakes. This homogeneity in distribution and the precise type of covalently grafted functional groups are significant advantages of FG chemistry compared to GO chemistry.

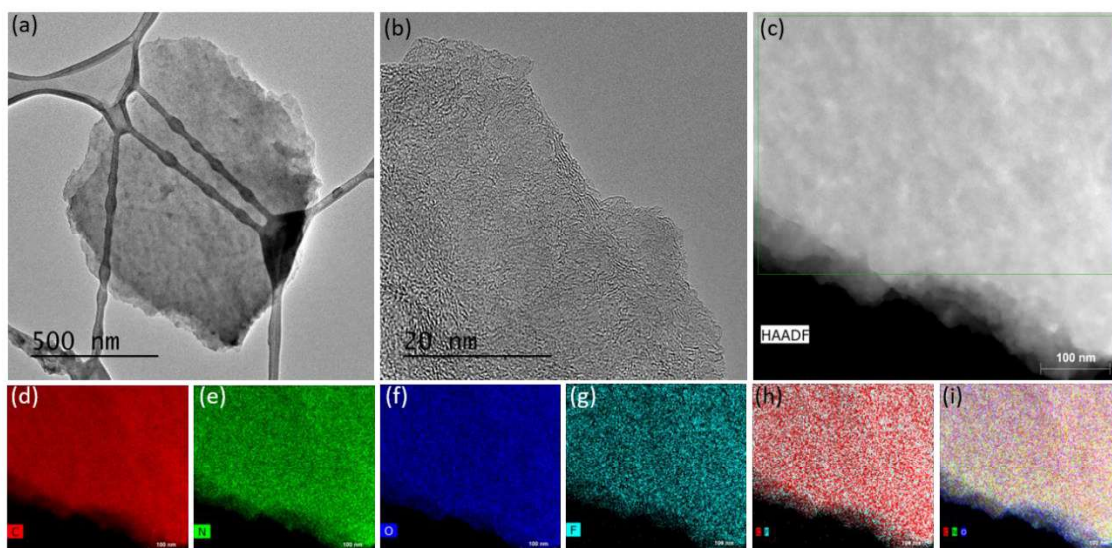


Figure 26 (a) TEM and (b) HRTEM images of a FG/Arg-48h\_K sample. (c) Dark field HRTEM image of FG/Arg-48h\_K and corresponding chemical mapping: (d) carbon map, (e) nitrogen map, (f) oxygen map, (g) fluorine map, (h) carbon-fluorine map, and (i) carbon-nitrogen-oxygen combined map.

Figure 27 shows CV profiles recorded in 1 M H<sub>2</sub>SO<sub>4</sub> (at a constant scan rate of 50 mV s<sup>-1</sup>) for samples prepared at different reaction times. The CV curves feature quasi rectangular profiles with small broad redox peaks centred at ~0.45 V. The deviation from the ideal rectangular shape can be explained by the occurrence of ESR (finite resistance of the electrode material) and EPR (ohmic conduction across the capacitor *via* the electrolyte).<sup>150</sup> The redox response of the system comes from the presence of oxygen-containing groups<sup>151,152</sup> as previously discussed and experimentally verified by the XPS and FTIR analysis. The CV results showed that the highest current response was obtained with the sample prepared for 48 h of synthesis, which is in agreement with the higher FD calculated. The presence of amino groups from Arg can significantly improve the electrochemical performance, especially the conductivity and redox activity.<sup>153,154</sup>

In order to enhance the double-layer capacitance component of the FG/Arg-48h sample, the sample with increased SSA and a microporous structure was prepared using potassium carbonate, as described in the previous section. As expected, such surface size enhancement decreased the FD (from 3.7 to 3.5) and affected the CV current response of the FG/Arg-48h\_K sample. However, a high SSA and a high level of surface functionalization were at a trade-off threshold since the capacitive performance



of the FG/Arg-48h\_K sample as evident from GCD records (Figure 27) increased significantly. The GCD profiles of the more porous sample recorded at current densities ranging from 0.25 to 5 A g<sup>-1</sup> revealed the highest value of specific capacitance at 0.25 A g<sup>-1</sup> (391 F g<sup>-1</sup>). The pore size of ~1.5 nm in the FG/Arg-48h\_K sample enabled sulfate ions to interact with the surface and pores of the material, especially at a low current density, resulting in high capacitance values.

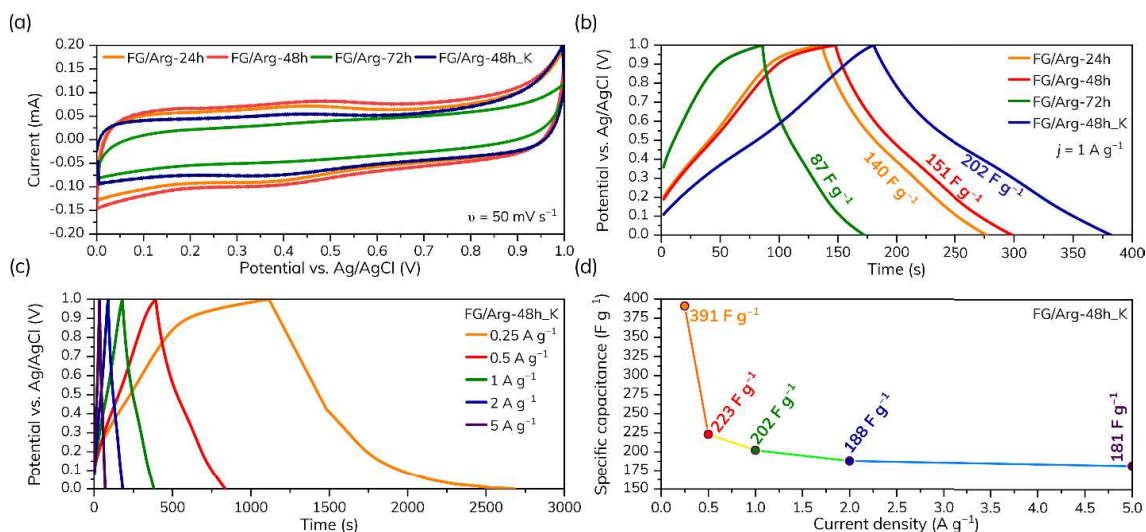


Figure 27 (a) CVs of graphene derivatives with Arg groups at different reaction times. (b) GCD profiles of the prepared materials. (c) GCD profiles of FG/Arg-48h\_K, at current densities from 0.25 A g<sup>-1</sup> to 5 A g<sup>-1</sup>, and (d) the specific capacitance vs current density profile.

A symmetric supercapacitor in a two-electrode setup with 1 M H<sub>2</sub>SO<sub>4</sub> as an electrolyte was assembled to evaluate the performance of the FG/Arg-48h\_K sample. Figure 28 shows the GCD profiles of FG/Arg-48h\_K using current densities from 0.1 A g<sup>-1</sup> to 5 A g<sup>-1</sup>. It can be seen that the shape of the GCD curves is significantly more symmetrical, suggesting enhanced diffusion of the ions inside the electrochemical cell. The rate test revealed outstanding stability of the capacitive response across the wide range of current densities. Moreover, the life-time stability test confirmed the stability of the FG/Arg-48\_K sample, resulting in capacitance retention of 82.3 % after 30,000 GCD cycles.

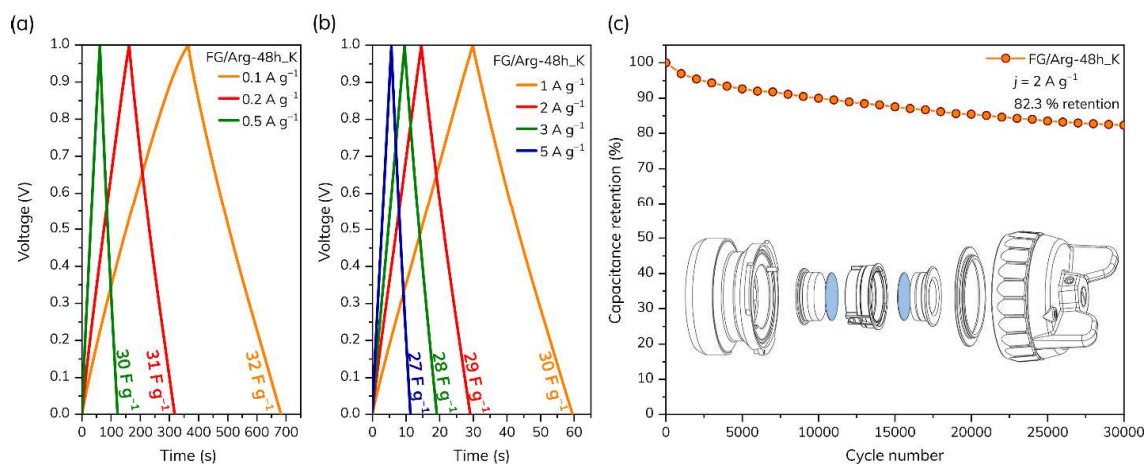


Figure 28 (a), (b) GCD profiles of FG/Arg-48h\_K recorded at different current densities. (c) Stability of FG/Arg-48h\_K after 30,000 GCD cycles.

## Conclusions

This presented work reported a successful synthesis of covalently functionalized graphene derivative with arginine to a graphene surface by reacting arginine was grafted via its guanidine group homogeneously on both sides of graphene (3.7 % functionalization degree). The best performing sample in supercapacitor application was treated with a pore-forming agent, potassium carbonate, directly boosting the capacitive performance ( $\sim 390 \text{ F g}^{-1}$  at a current density of  $0.25 \text{ A g}^{-1}$ ). After 30,000 charging/discharging cycles at a current density of  $2 \text{ A g}^{-1}$ , the capacitance retained over 80 %. Therefore, as well as being eco-friendly, the material exhibited outstanding sustainability with promising properties for supercapacitor materials. Moreover, adopting the strategy of successful covalent grafting of particular functional groups on the surface of graphene paves the way for the development of energy storage devices with significantly improved electrochemical performance and stability.

## 4.3 New Limits for Stability of Supercapacitor Electrode Material Based on Graphene Derivative

*Text adapted from*

- Šedajová, V.; Jakubec, P.; Bakandritsos, A.; Ranc, V.; Otyepka, M. *New Limits for Stability of Supercapacitor Electrode Material Based on Graphene Derivative. Nanomaterials* 2020, 10 (9), 1731. <https://doi.org/10.3390/nano10091731>.

### Introduction

Carbon-based materials' surface is prone to be functionalized via different routes to graft various functional groups, as discussed previously in this thesis. Our group reported that such modifications boost electrochemical stability, capacitive performance, and rate performance<sup>155,156</sup>. As oxygen-containing groups are present in most carbon-based materials due to the reactions in the air atmosphere, targeted utilization would offer a promising strategy for improving the capacitive performance. The insertion of oxygen-containing groups positively affects a material's wettability, hydrophilicity, and pseudocapacitive behaviour. Thanks to the oxygen functionalities, the material is less restacked due to electrostatic interactions; increased wettability enhances the contact between the active material and electrolyte<sup>157</sup>. Oxygen-containing functionalities are usually involved in fast redox reactions, increasing the pseudocapacitance contribution<sup>158</sup>. However, it is of high importance that the oxygen-containing groups would be covalently attached in a stable form, such as carboxylic groups, to prevent possible decomposition, high self-discharge rates, or increased leakage current<sup>159</sup>.

The presented studies investigated the pseudocapacitive behaviour of graphene acid (GA)<sup>149</sup> as a supercapacitor electrode material<sup>94</sup>. GA is a highly conductive, hydrophilic graphene derivative, functionalized with carboxyl groups, which are homogeneously dispersed among the graphene surface<sup>149</sup>. GA was already employed with excellent results in electrochemical sensing<sup>160</sup>, catalysis<sup>161–163</sup> and electrocatalysis<sup>164</sup>.

This paper focused on describing the pseudocapacitive behaviour of GA in an acidic electrolyte in supercapacitor application. Contrary to most published reports, we showed the excellent reproducibility of the synthesis, with variations in the individual measurements. The graphene acid was tremendously stable, exhibiting 95% specific

capacitance retention after 60,000 cycles in a two-electrode cell and high rate stability. These findings again show that covalently functionalized graphene derivatives provide a solution for supercapacitor metal-free electrode materials.

## Results

Graphene acid was synthesized based on an already published report<sup>95</sup>. However, we decided to repeat the synthesis three times and perform a thorough characterization, focusing on the reproducibility of the synthesis. The XRD showed two broad peaks at 29° and 50°, corresponding to the (0 0 2) and (1 0 1) planes, respectively, characteristic for stacked sheets with short-range order in amorphous structure<sup>165</sup>. The d-space value of 0.3579 nm, calculated from the 29° peak, is slightly higher than the one of graphite (inset of Figure 29 (a)). A Raman spectrum of GA revealed two well-known peaks, D-band related to defects and vacancies and G-band related to the aromatic sp<sup>2</sup> structure.<sup>166,167</sup> The I<sub>D</sub>/I<sub>G</sub> ratio of 1.69 confirms the suggested structure of GA, with out-of-plane functionalities, but retaining the sp<sup>2</sup> structure responsible for the conductivity, which was noted in previously highly functionalized graphene derivatives.<sup>42,92,155,156,168</sup>

An XPS survey spectrum (Figure 29) revealed the atomic composition as follows: carbon (76.7 at. %), oxygen (18.0 at. %), followed by N (3.5 at. %) and F (1.8 at. %). The fluorine content is caused by the non-reactive CF<sub>2</sub> species remaining in the cyanographene, while the N content is caused by the intrinsic N-doping of cyanographene from the synthesis in DMF<sup>64,95</sup>. The deconvolution of C 1s HR-XPS of GA (Figure 29) yielded six different configurations of carbons in the GA structure, most dominant ones are sp<sup>2</sup> (C=C), sp<sup>3</sup> (C-C), and -COOH bonds, respectively. The deconvoluted O 1s XPS spectrum was deconvoluted using two peaks, attributed to oxygen in C=O and C-OH chemical environments, respectively. Both carbon and oxygen deconvolution confirmed the presence of the carboxylic groups, as well as the FT-IR spectrum with a band located at around 1600 cm<sup>-1</sup>, usually attributed to the carbon-oxygen vibration in carboxylic groups.<sup>94,95</sup>

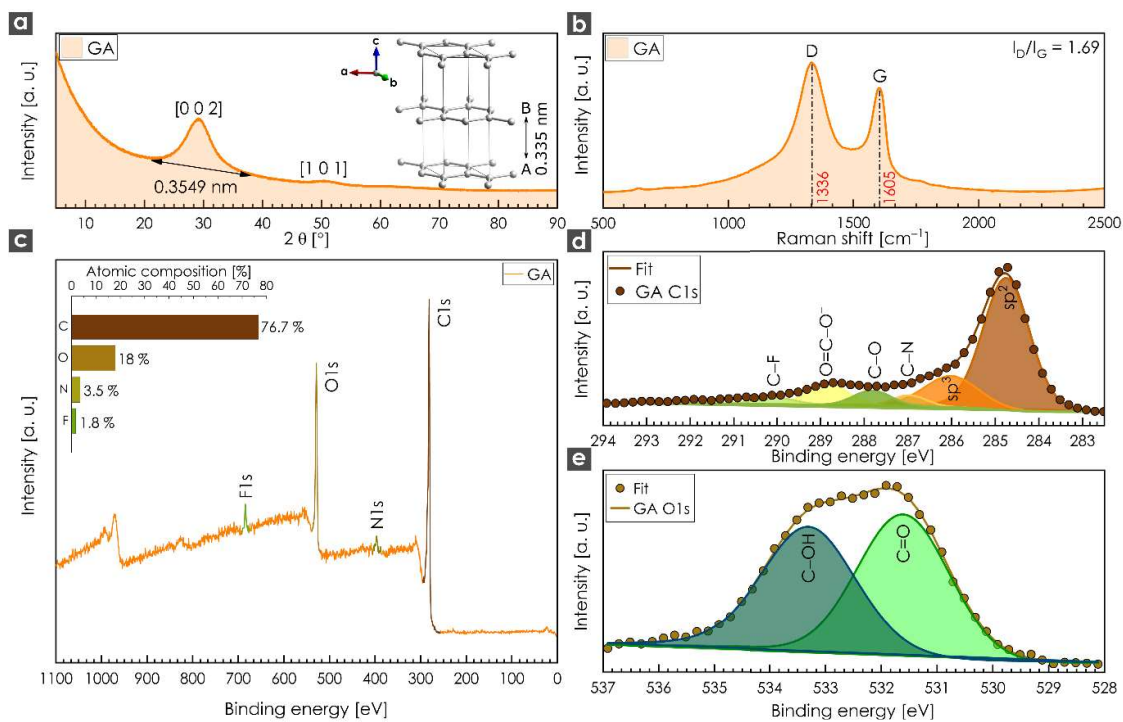


Figure 29 Structural characterization of GA material, (a) XRD and (b) Raman spectra. (c)-(e) XPS evaluation of GA.

Microscopic methods further evaluated the structural properties and composition of GA (Figure 30), showing the layered structure of GA, with thin graphenic sheets and lateral size of units of a micrometre. HAADF-HRTEM was used to investigate the elemental distribution of the graphene derivative, showing that the oxygen functional groups are homogeneously dispersed across the surface, further confirming GA well-defined nature. Based on the characterization techniques, the optimized GA structure model was designed.

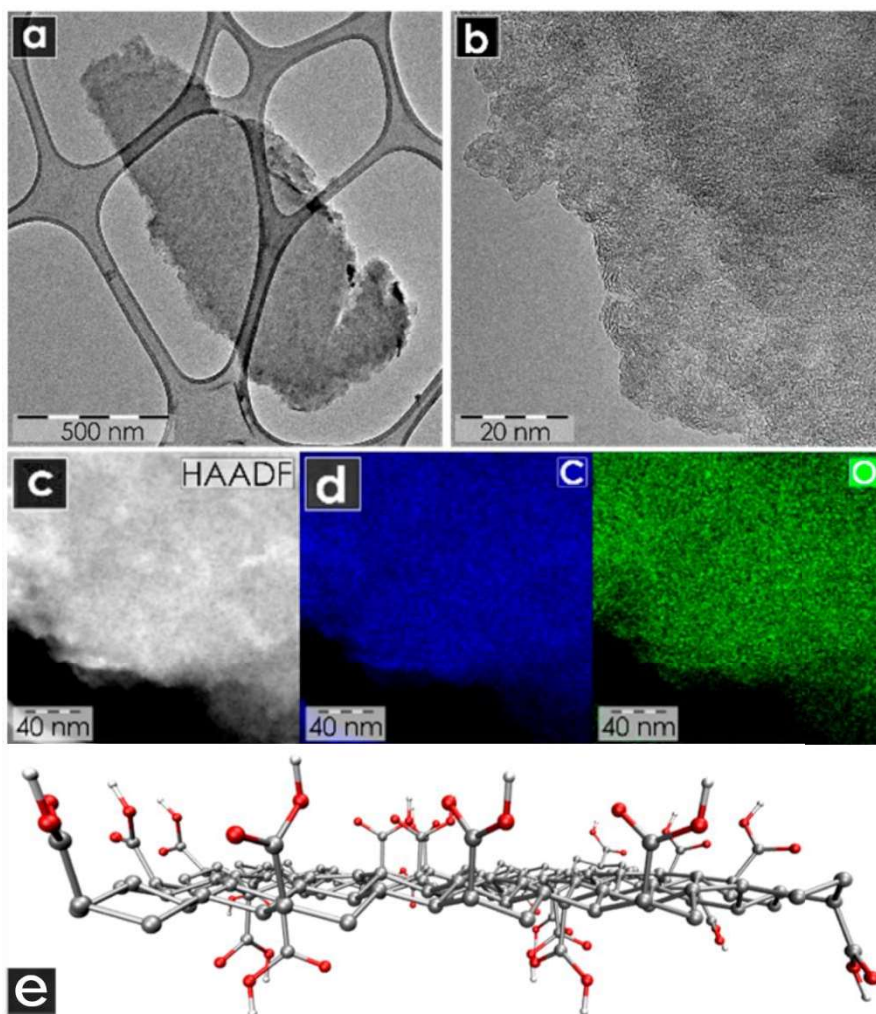


Figure 30 (a), (b) HRTEM images of GA. (c)-(d) HAADF image and corresponding elemental mapping of carbon and oxygen. (e) Structural GA model.

In order to highlight the importance of the chemical syntheses' reproducibility, we conducted an in-depth characterization of three individual batches of GA (Figure 31). Both Raman and XPS spectroscopy revealed minimal changes in the elemental composition and structure, as well as the following electrochemical testing.

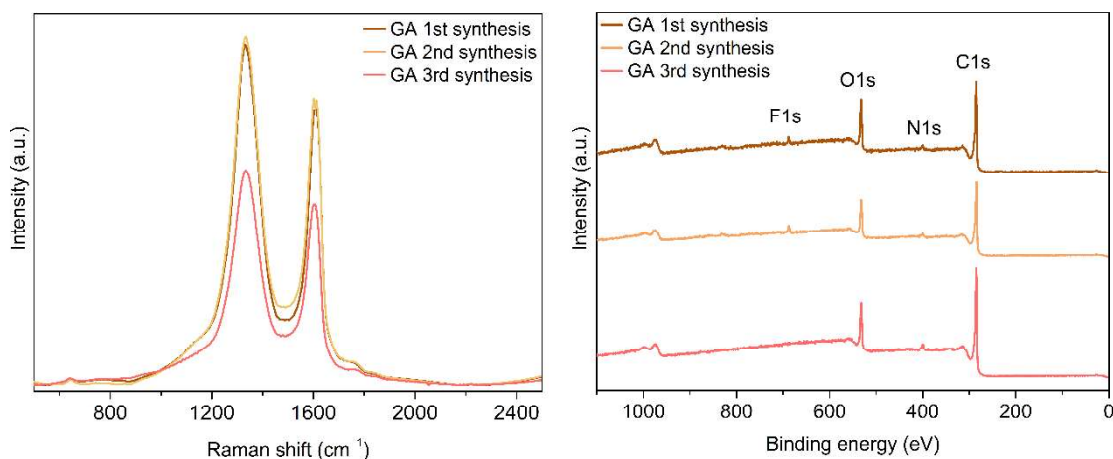


Figure 31 (a) Raman and (b) XPS spectra comparing three different syntheses of GA.

Electrochemical testing of a material can be performed in a three- or two-electrode system, whereas the two electrode system is much closer to the real operational conditions of commercial supercapacitors. We first evaluated the GA in a three-electrode system; however, more importantly, we tested its performance in a two-electrode symmetric system to assess the feasibility of GA.

We have assembled a symmetric supercapacitor with  $1 \text{ mol L}^{-1} \text{ H}_2\text{SO}_4$  as the electrolyte. Additive-free, drop-casted electrodes were used, further highlighting the high conductivity of GA and the simplicity of the electrode preparation. The charging and discharging responses of GA were recorded at a range of 1 to  $20 \text{ A g}^{-1}$ , showing linear response (contrary to the three-electrode system) since the two electrode system operates differently with the voltage<sup>169</sup>. The GA exhibited excellent rate stability, as well as remarkable cycling stability at  $3 \text{ A g}^{-1}$  current density (Figure 32). Such stability for a carbon-based material is significantly important precedence for its wide use since commercial supercapacitors endure many charge/discharge cycles. In real-life applications, supercapacitors are usually connected in parallel (to increase the capacitance – alias the amount of stored energy) or in series (to increase the voltage window). Two supercapacitors with GA as electrode material were successfully tested in both configurations, exhibiting the expected electrochemical behaviour. Moreover, we conducted the LED test, where the two cells assembled with GA electrodes and sulphuric acid electrolyte lighted up 2V LED without fast fading.

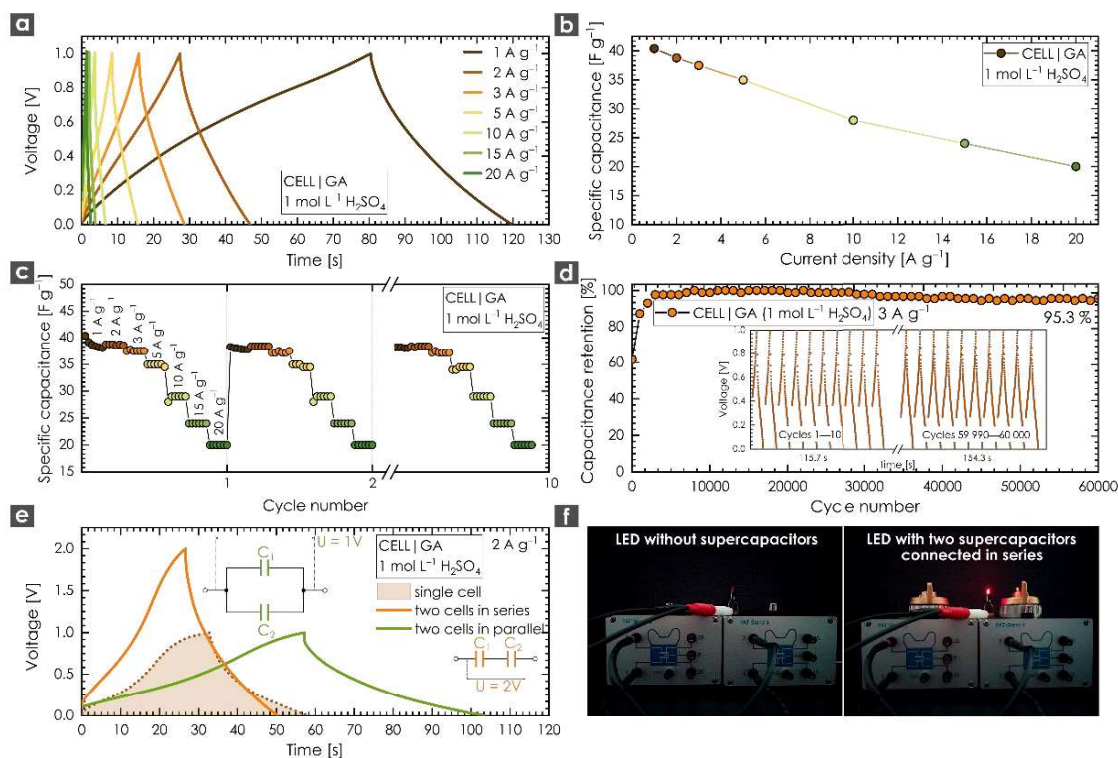


Figure 32 (a) GCD profiles of GA in a two-electrode system, (b) the dependence of capacitance vs current density. (c) Rate and (d) cycling stability test. (e),(f) Supercapacitors with GA electrodes connected in parallel and series, showing increased values as well as lighted up 2V LED diode.

## Conclusions

Graphene acid is a covalently functionalized graphene derivative prepared from fluorographene, offering a very stable electrode material for supercapacitors with promising performance. The oxygen-containing functional groups offer a high pseudocapacitive response in a sulphuric acid electrolyte without compromising the stability of the system. Both rate and cycling stability tests revealed the extraordinary performance of GA, demonstrating the high feasibility of GA for supercapacitor applications.



## 5 SUMMARY

This doctoral thesis focused on the synthesis and characterization of covalently functionalized graphene derivatives, using fluorographene as starting material. The physicochemical and electrochemical properties of the developed materials were evaluated in order to understand their function as electrode materials in electric double-layer capacitors (supercapacitors). The type of the covalently attached functional groups and/or nitrogen doping critically affects their overall properties, enabling their efficient use in supercapacitors and improving their operation.

Within the frame of this thesis, fluorographene chemistry was used to circumvent graphene's low reactivity during direct functionalization. The pathways using exfoliated graphite fluoride yielded chemically functionalized graphene derivatives, with nitrogen doping and with covalently attached amino acid and carboxylic groups.

Firstly, nitrogen superdoped (16 at.%) graphene was synthesized with diamond-like interlayer bonds with exceptionally high mass density. This material, when used as electrode in a symmetric supercapacitor device operating with an ionic liquid, presented a ground-breaking volumetric energy density compared to the state-of-the-art materials and commercially used high surface area carbons.

Secondly, amino-acid functionalized graphene derivatives were prepared with optimized porous structure using a pore-forming agent and applied as supercapacitor electrodes. The final device benefited from the covalently grafted functional groups, which provided redox processes during charging and discharging. Moreover, the use of eco-friendly electrolyte further increased the feasibility of the whole device.

Lastly, the highly carboxylated graphene derivative was subjected to an in-depth characterization, emphasizing the synthesis reproducibility in terms of stability of the electrochemical properties. Remarkably, the graphene acid exhibited exceptional life-cycle stability in an acidic electrolyte in supercapacitor application.

The materials and the synthetic procedures reported in this thesis show new ways to develop covalent graphene derivatives, which can offer interesting properties in technologically important areas, as in electrochemical energy storage and in particular in supercapacitors. These reported designs pave the way for new, specifically tailored properties of graphene derivatives for desired applications.

## 6 ZÁVĚR

Tato disertační práce byla zaměřena na syntézu a charakterizaci kovalentně funkcionalizovaných derivátů grafenu s využitím fluorografenu jako výchozího materiálu. Vlastnosti a benefity prezentovaných materiálů byly zkoumány a testovány pro jejich aplikaci jako elektrodových materiálů na poli ukládání energie v superkondenzátorech. Functionalizace a dusíkový doping kladně ovlivňují jejich chování, a proto zlepšují jejich výkon v zařízeních.

V rámci této práce byla využita fluorografenová chemie k překonání nízké reaktivity grafenu při jeho přímé funkcionalizaci. Syntetické procesy využily exfoliovaný grafit fluorid pro přípravu chemicky funkcionalizovaných derivátů grafenu s dopováním dusíkem a s kovalentně připojenými aminokyselinami a karboxylovými skupinami.

Prvně byl syntetizován dusíkem superdopovaný (16 at.%) grafen s mezivrstevnými vazbami podobnými diamantu s mimořádně vysokou hustotou. Tento materiál, v symetrickém zařízení za použití iontové kapaliny jako elektrolytu, představuje průlom v objemovém ukládání energie ve srovnání s dříve publikovanými výsledky.

Následně byly připraveny deriváty grafenu funkcionalizované aminokyselinami, které byly dále optimalizovány pomocí pórotvorného činidla a využity jako aktivní materiál v superkondenzátorech. Finální zařízení benefitovalo právě z kovalentně navázaných funkčních skupin, které zajišťovaly redoxní procesy v superkondenzátoru. Použití ekologického elektrolytu navíc dále zvýšilo relevantnost, udržitelnost a možnost komerčního využití celého zařízení.

Jako poslední byl v rámci práce charakterizován vysoce karboxylovaný derivát grafenu s důrazem na reprodukovatelnost syntézy. Grafenová kyselina vykazovala výjimečnou cyklickou stabilitu v kyselém elektrolytu a našla opět využití v superkondenzátorech.

Materiály a syntetické postupy uvedené v této práci ukazují nové cesty pro vývoj kovalentních derivátů grafenu. Ty byly přesně navrženy tak, aby poskytovaly výjimečné a excelentní vlastnosti v technologicky důležitých oblastech, s důrazem na použití v aplikacích pro ukládání energie, zejména v superkondenzátorech.

## 7 REFERENCES

- 1 V. Šedajová, A. Bakandritsos, P. Błoński, M. Medved', R. Langer, D. Zaoralová, J. Ugolotti, J. Dzibelová, P. Jakubec, V. Kupka and M. Otyepka, *Energy Environ. Sci.*, 2022, **15**, 740–748.
- 2 P. R. Wallace, *Phys. Rev.*, 1947, **71**, 622–634.
- 3 C. Oshima and A. Nagashima, *J. Phys. Condens. Matter*, 1997, **9**, 1–20.
- 4 A. E. Karu and M. Beer, *J. Appl. Phys.*, 1966, **37**, 2179–2181.
- 5 K. S. Novoselov, A. K. Geim, S. V. Morozov, D. Jiang, Y. Zhang, S. V. Dubonos, I. V. Grigorieva and A. A. Firsov, *Science*, 2004, **306**, 666–669.
- 6 L. D. Landau, *Phys. Z. Sowjetunion*, 1937, **11**, 26–35.
- 7 R. Peierls, *Ann. Inst. Henri Poincaré*, 1935, **5**, 177–222.
- 8 K. S. Novoselov, D. Jiang, F. Schedin, T. J. Booth, V. V. Khotkevich, S. V. Morozov and A. K. Geim, *Proc. Natl. Acad. Sci.*, 2005, **102**, 10451–10453.
- 9 K. R. Nandanapalli, D. Mudusu and S. Lee, *Carbon*, 2019, **152**, 954–985.
- 10 Y. Gogotsi and V. Presser, *Carbon Nanomaterials*, CRC Press, 2013th edn., 2013.
- 11 H. A. Hafez, S. Kovalev, K.-J. Tielrooij, M. Bonn, M. Gensch and D. Turchinovich, *Adv. Opt. Mater.*, 2020, **8**, 1900771.
- 12 M. I. Katsnelson, *Mater. Today*, 2007, **10**, 20–27.
- 13 D. W. Boukhvalov and M. I. Katsnelson, *Nano Lett.*, 2008, **8**, 4373–4379.
- 14 G. Yang, D. Bao, H. Liu, D. Zhang, N. Wang and H. Li, *J. Inorg. Organomet. Polym. Mater.*, 2017, **27**, 1129–1141.
- 15 G. Bottari, M. Ángeles Herranz, L. Wibmer, M. Volland, L. Rodríguez-Pérez, D. M. Guldi, A. Hirsch, N. Martín, F. D'Souza and T. Torres, *Chem. Soc. Rev.*, 2017, **46**, 4464–4500.
- 16 M. S. Chang, Y. S. Kim, J. H. Kang, J. Park, S. J. Sung, S. H. So, K. T. Park, S. J. Yang, T. Kim and C. R. Park, *Chem. Mater.*, 2017, **29**, 307–318.
- 17 V. Georgakilas, M. Otyepka, A. B. Bourlinos, V. Chandra, N. Kim, K. C. Kemp, P. Hobza, R. Zboril and K. S. Kim, *Chem. Rev.*, 2012, **112**, 6156–6214.
- 18 A. Hirsch, J. M. Englert and F. Hauke, *Acc. Chem. Res.*, 2013, **46**, 87–96.
- 19 P. Arranz-Mascarós, M. L. Godino-Salido, R. López-Garzón, C. García-Gallarín, I. Chamorro-Mena, F. J. López-Garzón, E. Fernández-García and M. D. Gutiérrez-Valero, *ACS Omega*, 2020, **5**, 18849.

- 20 T. Kuila, S. Bose, A. K. Mishra, P. Khanra, N. H. Kim and J. H. Lee, *Prog. Mater. Sci.*, 2012, **57**, 1061–1105.
- 21 J. Zhang, K. Hu, Q. Ouyang, Q. Gui and X. Chen, *Front. Mater. Sci.*, 2020, **14**, 198–210.
- 22 P. Arranz-Mascarós, M. L. Godino-Salido, R. López-Garzón, C. García-Gallarín, I. Chamorro-Mena, F. J. López-Garzón, E. Fernández-García and M. D. Gutiérrez-Valero, *ACS Omega*, 2020, **5**, 18849–18861.
- 23 J. Park and M. Yan, *Acc. Chem. Res.*, 2013, **46**, 181–189.
- 24 C. K. Chua and M. Pumera, *Chem. Soc. Rev.*, 2013, **42**, 3222–3233.
- 25 W. Yu, L. Sisi, Y. Haiyan and L. Jie, *RSC Adv.*, 2020, **10**, 15328–15345.
- 26 G. Bottari, M. Á. Herranz, L. Wibmer, M. Volland, L. Rodríguez-Pérez, D. M. Guldi, A. Hirsch, N. Martín, F. D'Souza and T. Torres, *Chem. Soc. Rev.*, 2017, **46**, 4464–4500.
- 27 V. V. Shnitov, M. K. Rabchinskii, M. Brzhezinskaya, D. Yu. Stolyarova, S. V. Pavlov, M. V. Baidakova, A. V. Shvidchenko, V. A. Kislenko, S. A. Kislenko and P. N. Brunkov, *Small*, 2021, **17**, 2104316.
- 28 K. S. Novoselov, A. K. Geim, S. V. Morozov, D. Jiang, M. I. Katsnelson, I. V. Grigorieva, S. V. Dubonos and A. A. Firsov, *Nature*, 2005, **438**, 197–200.
- 29 W. A. Gómez-Arias and G. G. Naumis, *Int. J. Mod. Phys. B*, 2016, **30**, 1550263.
- 30 M. I. Katsnelson, *Mater. Today*, 2007, **10**, 20–27.
- 31 B. J. Schultz, R. V. Dennis, V. Lee and S. Banerjee, *Nanoscale*, 2014, **6**, 3444–3466.
- 32 Y. Hernandez, V. Nicolosi, M. Lotya, F. M. Blighe, Z. Sun, S. De, I. T. McGovern, B. Holland, M. Byrne, Y. K. Gun'Ko, J. J. Boland, P. Niraj, G. Duesberg, S. Krishnamurthy, R. Goodhue, J. Hutchison, V. Scardaci, A. C. Ferrari and J. N. Coleman, *Nat. Nanotechnol.*, 2008, **3**, 563–568.
- 33 D. Haag and H. H. Kung, *Top. Catal.*, 2014, **57**, 762–773.
- 34 K. Christian Kemp, H. Seema, M. Saleh, N. H. Le, K. Mahesh, V. Chandra and K. S. Kim, *Nanoscale*, 2013, **5**, 3149–3171.
- 35 N. Baig, Ihsanullah, M. Sajid and T. A. Saleh, *J. Environ. Manage.*, 2019, **244**, 370–382.
- 36 S. Kumar and K. Chatterjee, *ACS Appl. Mater. Interfaces*, 2016, **8**, 26431–26457.
- 37 N. M. Nurazzi, N. Abdullah, S. Z. N. Demon, N. A. Halim, A. F. M. Azmi, V. F. Knight and I. S. Mohamad, *Nanotechnol. Rev.*, 2021, **10**, 330–369.
- 38 X. Tang, M. Debliqy, D. Lahem, Y. Yan and J.-P. Raskin, *Sensors*, 2021, **21**, 1443.

- 39N. Alzate-Carvajal and A. Luican-Mayer, *ACS Omega*, 2020, **5**, 21320–21329.
- 40V. Jain and B. Kandasubramanian, *J. Mater. Sci.*, 2020, **55**, 1865–1903.
- 41H. Huang, H. Shi, P. Das, J. Qin, Y. Li, X. Wang, F. Su, P. Wen, S. Li, P. Lu, F. Liu, Y. Li, Y. Zhang, Y. Wang, Z.-S. Wu and H.-M. Cheng, *Adv. Funct. Mater.*, 2020, **30**, 1909035.
- 42A. Bakandritsos, P. Jakubec, M. Pykal and M. Otyepka, *FlatChem*, 2019, **13**, 25–33.
- 43V. Georgakilas, J. N. Tiwari, K. C. Kemp, J. A. Perman, A. B. Bourlinos, K. S. Kim and R. Zboril, *Chem. Rev.*, 2016, **116**, 5464–5519.
- 44W. Wang and P. Hobza, *ChemPhysChem*, 2008, **9**, 1003–1009.
- 45W. L. Jorgensen and D. L. Severance, *J. Am. Chem. Soc.*, 1990, **112**, 4768–4774.
- 46D. A. Dougherty and D. A. Stauffer, *Science*, 1990, **250**, 1558–1560.
- 47H. G. Kim, C.-W. Lee, S. Yun, B. H. Hong, Y.-O. Kim, D. Kim, H. Ihm, J. W. Lee, E. C. Lee, P. Tarakeshwar, S.-M. Park and K. S. Kim, *Org. Lett.*, 2003, **5**, 961–961.
- 48B. Saha and P. Kr. Bhattacharyya, *Comput. Theor. Chem.*, 2019, **1147**, 62–71.
- 49K. P. Loh, Q. Bao, P. K. Ang and J. Yang, *J. Mater. Chem.*, 2010, **20**, 2277–2289.
- 50D. W. Boukhvalov and M. I. Katsnelson, 2009.
- 51S. P. Economopoulos, G. Rotas, Y. Miyata, H. Shinohara and N. Tagmatarchis, *ACS Nano*, 2010, **4**, 7499–7507.
- 52T. Da Ros, M. Prato, M. Carano, P. Ceroni, F. Paolucci and S. Roffia, *J. Am. Chem. Soc.*, 1998, **120**, 11645–11648.
- 53M. Prato and M. Maggini, *Acc. Chem. Res.*, 1998, **31**, 519–526.
- 54G. L. C. Paulus, Q. H. Wang and M. S. Strano, *Acc. Chem. Res.*, 2013, **46**, 160–170.
- 55Z. Jin, T. P. McNicholas, C.-J. Shih, Q. H. Wang, G. L. C. Paulus, A. J. Hilmer, S. Shimizu and M. S. Strano, *Chem. Mater.*, 2011, **23**, 3362–3370.
- 56C. Yuan, W. Chen and L. Yan, *J. Mater. Chem.*, 2012, **22**, 7456–7460.
- 57C. K. Chua and M. Pumera, *Chem. – Asian J.*, 2012, **7**, 1009–1012.
- 58V. Hrubý, L. Zdražil, J. Dzibelová, V. Šedajová, A. Bakandritsos, P. Lazar and M. Otyepka, *Appl. Surf. Sci.*, 2022, **587**, 152839.
- 59R. A. Borse, M. B. Kale, S. H. Sonawane and Y. Wang, *Adv. Funct. Mater.*, 2022, **32**, 2202570.
- 60R. Zbořil, F. Karlický, A. B. Bourlinos, T. A. Steriotis, A. K. Stubos, V. Georgakilas, K. Šafářová, D. Jančík, C. Trapalis and M. Otyepka, *Small*, 2010, **6**, 2885–2891.
- 61D. D. Chronopoulos, A. Bakandritsos, M. Pykal, R. Zbořil and M. Otyepka, *Appl. Mater. Today*, 2017, **9**, 60–70.

- 62 R. Langer, D. Zaoralová, M. Medved', P. Banáš, P. Błoński and M. Otyepka, *J. Phys. Chem. C*, 2019, **123**, 27896–27903.
- 63 M. Dubecký, E. Otyepková, P. Lazar, F. Karlický, M. Petr, K. Čépe, P. Banáš, R. Zbořil and M. Otyepka, *J. Phys. Chem. Lett.*, 2015, **6**, 1430–1434.
- 64 M. Medved', G. Zoppellaro, J. Ugolotti, D. Matochová, P. Lazar, T. Pospíšil, A. Bakandritsos, J. Tuček, R. Zbořil and M. Otyepka, *Nanoscale*, 2018, **10**, 4696–4707.
- 65 J. Xia, F. Chen, J. Li and N. Tao, *Nat. Nanotechnol.*, 2009, **4**, 505–509.
- 66 L. Dai, *Acc. Chem. Res.*, 2013, **46**, 31–42.
- 67 L. L. Zhang and X. S. Zhao, *Chem. Soc. Rev.*, 2009, **38**, 2520.
- 68 E. Frackowiak and F. Béguin, *Carbon*, 2001, **39**, 937–950.
- 69 C. An, Y. Zhang, H. Guo and Y. Wang, *Nanoscale Adv.*, 2019, **1**, 4644–4658.
- 70 V. Augustyn, P. Simon and B. Dunn, *Energy Environ. Sci.*, 2014, **7**, 1597.
- 71 R. R. Salunkhe, Y. V. Kaneti and Y. Yamauchi, *ACS Nano*, 2017, **11**, 5293–5308.
- 72 R. R. Salunkhe, Y. V. Kaneti, J. Kim, J. H. Kim and Y. Yamauchi, *Acc. Chem. Res.*, 2016, **49**, 2796–2806.
- 73 Z. Ling, C. E. Ren, M.-Q. Zhao, J. Yang, J. M. Giammarco, J. Qiu, M. W. Barsoum and Y. Gogotsi, *Proc. Natl. Acad. Sci.*, 2014, **111**, 16676–16681.
- 74 D. M. Heard and A. J. J. Lennox, *Angew. Chem. Int. Ed.*, 2020, **59**, 18866–18884.
- 75 G. Inzelt, A. Lewenstam and F. Scholz, Eds., *Handbook of Reference Electrodes*, Springer Berlin Heidelberg, Berlin, Heidelberg, 2013.
- 76 C. G. Zoski, *Handbook of electrochemistry*, Elsevier, Amsterdam; Boston, 2007.
- 77 S. Prasad, G. Durai, D. Devaraj, M. S. AlSalhi, J. Theerthagiri, P. Arunachalam, M. Gurulakshmi, M. Raghavender and P. Kuppasami, *RSC Adv.*, 2018, **8**, 8828–8835.
- 78 E. Zhang, N. Fulik, G. Hao, H. Zhang, K. Kaneko, L. Borchardt, E. Brunner and S. Kaskel, *Angew. Chem. Int. Ed.*, 2019, **58**, 13060–13065.
- 79 A. Yu, V. Chabot and J. Zhang, *Electrochemical Supercapacitors for Energy Storage and Delivery: Fundamentals and Applications*, CRC Press, 1st edn., 2017.
- 80 K. K. Kar, Ed., *Handbook of Nanocomposite Supercapacitor Materials I: Characteristics*, Springer International Publishing, 2020.
- 81 K. K. Kar, Ed., *Handbook of Nanocomposite Supercapacitor Materials II: Performance*, Springer International Publishing, 2020.
- 82 S. Zhang and N. Pan, *Adv. Energy Mater.*, 2015, **5**, 1401401.
- 83 Y. Gogotsi and R. M. Penner, *ACS Nano*, 2018, **12**, 2081–2083.
- 84 S. Ardizzone, G. Fregonara and S. Trasatti, *Electrochimica Acta*, 1990, **35**, 263–267.

- 85 J. Shao, X. Zhou, Q. Liu, R. Zou, W. Li, J. Yang and J. Hu, *J. Mater. Chem. A*, 2015, **3**, 6168–6176.
- 86 V. Augustyn, J. Come, M. A. Lowe, J. W. Kim, P.-L. Taberna, S. H. Tolbert, H. D. Abruña, P. Simon and B. Dunn, *Nat. Mater.*, 2013, **12**, 518–522.
- 87 H.-S. Kim, J. B. Cook, H. Lin, J. S. Ko, S. H. Tolbert, V. Ozolins and B. Dunn, *Nat. Mater.*, 2017, **16**, 9.
- 88 M. A. Scibioh and B. Viswanathan, *Materials for supercapacitor applications*, Elsevier, Cambridge, 1st edn., 2020.
- 89 P. L. Taberna, P. Simon and J. F. Fauvarque, *J. Electrochem. Soc.*, 2003, **150**, A292.
- 90 R. Negroiu, P. Svasta, C. Pirvu, Al. Vasile and C. Marghescu, in *2017 40th International Spring Seminar on Electronics Technology (ISSE)*, IEEE, Sofia, Bulgaria, 2017, pp. 1–4.
- 91 D. Zhao, K. Jiang, J. Li, X. Zhu, C. Ke, S. Han, E. Kymakis and X. Zhuang, *BMC Mater.*, 2020, **2**, 3.
- 92 E. C. Vermisoglou, P. Jakubec, A. Bakandritsos, V. Kupka, M. Pykal, V. Šedajová, J. Vlček, O. Tomanec, M. Scheibe, R. Zbořil and M. Otyepka, *ChemSusChem*, 2021, **14**, 3904–3914.
- 93 I. Obraztsov, A. Bakandritsos, V. Šedajová, R. Langer, P. Jakubec, G. Zoppellaro, M. Pykal, V. Presser, M. Otyepka and R. Zbořil, *Adv. Energy Mater.*, 2022, **12**, 2103010.
- 94 V. Šedajová, P. Jakubec, A. Bakandritsos, V. Ranc and M. Otyepka, *Nanomaterials*, 2020, **10**, 1731.
- 95 A. Bakandritsos, M. Pykal, P. Błoński, P. Jakubec, D. D. Chronopoulos, K. Poláková, V. Georgakilas, K. Čépe, O. Tomanec, V. Ranc, A. B. Bourlinos, R. Zbořil and M. Otyepka, *ACS Nano*, 2017, **11**, 2982–2991.
- 96 A. S. Aricò, P. Bruce, B. Scrosati, J.-M. Tarascon and W. van Schalkwijk, *Nat. Mater.*, 2005, **4**, 366–377.
- 97 W. Gu and G. Yushin, *Wiley Interdiscip. Rev. Energy Environ.*, 2014, **3**, 424–473.
- 98 Q. Wang, J. Yan and Z. Fan, *Energy Environ. Sci.*, 2016, **9**, 729–762.
- 99 Y. Gogotsi and P. Simon, *Science*, 2011, **334**, 917–918.
- 100 J. W. Choi and D. Aurbach, *Nat. Rev. Mater.*, 2016, **1**, 16013.
- 101 P. Albertus, S. Babinec, S. Litzelman and A. Newman, *Nat. Energy*, 2018, **3**, 16–21.
- 102 P. Simon and Y. Gogotsi, *Acc. Chem. Res.*, 2013, **46**, 1094–1103.

- 103 H. Li, Y. Tao, X. Zheng, J. Luo, F. Kang, H.-M. Cheng and Q.-H. Yang, *Energy Environ. Sci.*, 2016, **9**, 3135–3142.
- 104 D. Yu, K. Goh, H. Wang, L. Wei, W. Jiang, Q. Zhang, L. Dai and Y. Chen, *Nat. Nanotechnol.*, 2014, **9**, 555–562.
- 105 R. Weber, M. Genovese, A. J. Louli, S. Hames, C. Martin, I. G. Hill and J. R. Dahn, *Nat. Energy*, 2019, **4**, 683–689.
- 106 Z. Li, S. Gadipelli, H. Li, C. A. Howard, D. J. L. Brett, P. R. Shearing, Z. Guo, I. P. Parkin and F. Li, *Nat. Energy*, 2020, **5**, 160–168.
- 107 W. A. Yarbrough, *J. Am. Ceram. Soc.*, 1992, **75**, 3179–3200.
- 108 Z.-J. Liu, S.-J. Ding, P.-F. Wang, D. W. Zhang, J.-Y. Zhang, J.-T. Wang and K. Kohse-Hoinghaus, *Thin Solid Films*, 2000, **368**, 208–210.
- 109 I. Schmidt and C. Benndorf, *Diam. Relat. Mater.*, 1997, **6**, 964–969.
- 110 W. Lai, D. Xu, X. Wang, Z. Wang, Y. Liu, X. Zhang, Y. Li and X. Liu, *Phys. Chem. Chem. Phys.*, 2017, **19**, 24076–24081.
- 111 U. Rajeena, P. Raveendran and R. M. Ramakrishnan, *J. Fluor. Chem.*, 2020, **235**, 109555.
- 112 J. Robertson, *Mater. Sci. Eng. R Rep.*, 2002, **37**, 129–281.
- 113 V. Pischedda, S. Radescu, M. Dubois, N. Batische, F. Balima, C. Cavallari and L. Cardenas, *Carbon*, 2017, **114**, 690–699.
- 114 H. Touhara, K. Kadono, Y. Fujii and N. Watanabe, *Z. Für Anorg. Allg. Chem.*, 1987, **544**, 7–20.
- 115 P. V. Bakharev, M. Huang, M. Saxena, S. W. Lee, S. H. Joo, S. O. Park, J. Dong, D. C. Camacho-Mojica, S. Jin, Y. Kwon, M. Biswal, F. Ding, S. K. Kwak, Z. Lee and R. S. Ruoff, *Nat. Nanotechnol.*, 2020, **15**, 59–66.
- 116 J. Sivek, O. Leenaerts, B. Partoens and F. M. Peeters, *J. Phys. Chem. C*, 2012, **116**, 19240–19245.
- 117 F. Karlický, R. D. Kumara, M. Otyepka and R. Zbořil, *ACS Nano*, 2013, **7**, 6434–6464.
- 118 M. Medved', G. Zoppellaro, J. Ugolotti, D. Matochová, P. Lazar, T. Pospíšil, A. Bakandritsos, J. Tuček, R. Zbořil and M. Otyepka, *Nanoscale*, 2018, **10**, 4696–4707.
- 119 D. Zaoralová, V. Hrubý, V. Šedajová, R. Mach, V. Kupka, J. Ugolotti, A. Bakandritsos, M. Medved' and M. Otyepka, *ACS Sustain. Chem. Eng.*, 2020, **8**, 4764–4772.



- 120 G. Zoppellaro, A. Bakandritsos, J. Tuček, P. Błoński, T. Susi, P. Lazar, Z. Bad'ura, T. Steklý, A. Opletalová, M. Otyepka and R. Zbořil, *Adv. Mater.*, 2019, **31**, 1902587.
- 121 Y. Liu, Y. Shen, L. Sun, J. Li, C. Liu, W. Ren, F. Li, L. Gao, J. Chen, F. Liu, Y. Sun, N. Tang, H.-M. Cheng and Y. Du, *Nat. Commun.*, 2016, **7**, 1–9.
- 122 A. S. Mazur, M. A. Vovk and P. M. Tolstoy, *Fuller. Nanotub. Carbon Nanostructures*, 2020, **28**, 202–213.
- 123 R. L. Johnson, J. M. Anderson, B. H. Shanks and K. Schmidt-Rohr, *Chem. Mater.*, 2014, **26**, 5523–5532.
- 124 J. Giraudet, M. Dubois, A. Hamwi, W. E. E. Stone, P. Pirotte and F. Masin, *J. Phys. Chem. B*, 2005, **109**, 175–181.
- 125 D. W. Mayo, in *Course Notes on the Interpretation of Infrared and Raman Spectra*, eds. D. W. Mayo, F. A. Miller and R. W. Hannah, John Wiley & Sons, Inc., 2004, pp. 101–140.
- 126 J. Senthilnathan, C.-C. Weng, J.-D. Liao and M. Yoshimura, *Sci. Rep.*, 2013, **3**, srep02414.
- 127 A. Bakandritsos, R. G. Kadam, P. Kumar, G. Zoppellaro, M. Medved', J. Tuček, T. Montini, O. Tomanec, P. Andrášková, B. Drahoš, R. S. Varma, M. Otyepka, M. B. Gawande, P. Fornasiero and R. Zbořil, *Adv. Mater.*, 2019, **31**, 1900323.
- 128 P. Lazar, R. Mach and M. Otyepka, *J. Phys. Chem. C*, 2019, **123**, 10695–10702.
- 129 J.-D. Chai and M. Head-Gordon, *Phys. Chem. Chem. Phys.*, 2008, **10**, 6615–6620.
- 130 R. Ditchfield, W. J. Hehre and J. A. Pople, *J. Chem. Phys.*, 1971, **54**, 724–728.
- 131 X. Wu, H. Zhao, J. Pei and D. Yan, *Appl. Phys. Lett.*, 2017, **110**, 133102.
- 132 K. S. W. Sing, *Pure Appl. Chem.*, 1985, **57**, 603–619.
- 133 A. M. Silvestre-Albero, J. M. Juárez-Galán, J. Silvestre-Albero and F. Rodríguez-Reinoso, *J. Phys. Chem. C*, 2012, **116**, 16652–16655.
- 134 D. Hulicova-Jurcakova, M. Seredych, G. Q. Lu and T. J. Bandosz, *Adv. Funct. Mater.*, 2009, **19**, 438–447.
- 135 Y. Zhu, S. Murali, M. D. Stoller, K. J. Ganesh, W. Cai, P. J. Ferreira, A. Pirkle, R. M. Wallace, K. A. Cychosz, M. Thommes, D. Su, E. A. Stach and R. S. Ruoff, *Science*, 2011, **332**, 1537–1541.
- 136 L. Weinstein and R. Dash, *Mater. Today*, 2013, **16**, 356–357.

- 137 H. Jin, X. Feng, J. Li, M. Li, Y. Xia, Y. Yuan, C. Yang, B. Dai, Z. Lin, J. Wang, J. Lu and S. Wang, *Angew. Chem. Int. Ed.*, 2019, **58**, 2397–2401.
- 138 R. Weber, M. Genovese, A. J. Louli, S. Hames, C. Martin, I. G. Hill and J. R. Dahn, *Nat. Energy*, 2019, **4**, 683–689.
- 139 X. Lin, M. Salari, L. M. R. Arava, P. M. Ajayan and M. W. Grinstaff, *Chem. Soc. Rev.*, 2016, **45**, 5848–5887.
- 140 L. Timperman, H. Galiano, D. Lemordant and M. Anouti, *Electrochem. Commun.*, 2011, **13**, 1112–1115.
- 141 J. Alvarado, M. A. Schroeder, M. Zhang, O. Borodin, E. Gobrogge, M. Olguin, M. S. Ding, M. Gobet, S. Greenbaum, Y. S. Meng and K. Xu, *Mater. Today*, 2018, **21**, 341–353.
- 142 D. Matochová, M. Medved', A. Bakandritsos, T. Steklý, R. Zbořil and M. Otyepka, *J. Phys. Chem. Lett.*, 2018, **9**, 3580–3585.
- 143 A. Bakandritsos, D. D. Chronopoulos, P. Jakubec, M. Pykal, K. Čépe, T. Steriotis, S. Kalytchuk, M. Petr, R. Zbořil and M. Otyepka, *Adv. Funct. Mater.*, 2018, **28**, 1801111.
- 144 E. C. Vermisoglou, P. Jakubec, A. Bakandritsos, M. Pykal, S. Talande, V. Kupka, R. Zbořil and M. Otyepka, *Chem. Mater.*, 2019, **31**, 4698–4709.
- 145 K. Hou, P. Gong, J. Wang, Z. Yang, Z. Wang and S. Yang, *RSC Adv*, 2014, **4**, 56543–56551.
- 146 A. R. Rafieerad, A. R. Bushroa, A. Amiri, K. Kalaiselvam, K. Vellasamy and J. Vadivelu, *J. Hazard. Mater.*, 2018, **360**, 132–140.
- 147 D. Chen, Q. Chen, T. Liu, J. Kang, R. Xu, Y. Cao and M. Xiang, *RSC Adv.*, 2019, **9**, 20149–20160.
- 148 M. Zhang, Y. Ma, Y. Zhu, J. Che and Y. Xiao, *Carbon*, 2013, **63**, 149–156.
- 149 A. Bakandritsos, M. Pykal, P. Błoński, P. Jakubec, D. D. Chronopoulos, K. Poláková, V. Georgakilas, K. Čépe, O. Tomanec, V. Ranc, A. B. Bourlinos, R. Zbořil and M. Otyepka, *ACS Nano*, 2017, **11**, 2982–2991.
- 150 D. Boonpakdee, C. F. Guajardo Yévenes, W. Surareungchai and C. La-ovorakiat, *J. Mater. Chem. A*, 2018, **6**, 7162–7167.
- 151 Y. J. Oh, J. J. Yoo, Y. I. Kim, J. K. Yoon, H. N. Yoon, J.-H. Kim and S. B. Park, *Electrochimica Acta*, 2014, **116**, 118–128.
- 152 Y.-H. Lee, K.-H. Chang and C.-C. Hu, *J. Power Sources*, 2013, **227**, 300–308.

- 153 M. Yu, Z. Wang, H. Zhang, P. Zhang, T. Zhang, X. Lu and X. Feng, *Nano Energy*, 2019, **65**, 103987.
- 154 M. Yang and Z. Zhou, *Adv Sci*, 2017, 10.
- 155 K. Jayaramulu, M. Horn, A. Schneemann, H. Saini, A. Bakandritsos, V. Ranc, M. Petr, V. Stavila, C. Narayana, B. Scheibe, Š. Kment, M. Otyepka, N. Motta, D. Dubal, R. Zbořil and R. A. Fischer, *Adv. Mater.*, 2021, **33**, 2004560.
- 156 E. C. Vermisoglou, P. Jakubec, A. Bakandritsos, M. Pykal, S. Talande, V. Kupka, R. Zbořil and M. Otyepka, *Chem. Mater.*, 2019, **31**, 4698–4709.
- 157 J. Yan, Q. Wang, T. Wei and Z. Fan, *Adv. Energy Mater.*, 2014, **4**, 1300816.
- 158 E. G. Calvo, N. Rey-Raap, A. Arenillas and J. A. Menéndez, *RSC Adv*, 2014, **4**, 32398–32404.
- 159 A. G. Pandolfo and A. F. Hollenkamp, *J. Power Sources*, 2006, **157**, 11–27.
- 160 Y. Heng Cheong, M. Z. M. Nasir, A. Bakandritsos, M. Pykal, P. Jakubec, R. Zbořil, M. Otyepka and M. Pumera, *ChemElectroChem*, 2019, **6**, 229–234.
- 161 M. Blanco, D. Mosconi, C. Tubaro, A. Biffis, D. Badocco, P. Pastore, M. Otyepka, A. Bakandritsos, Z. Liu, W. Ren, S. Agnoli and G. Granozzi, *Green Chem.*, 2019, **21**, 5238–5247.
- 162 M. Blanco, D. Mosconi, M. Otyepka, M. Medved', A. Bakandritsos, S. Agnoli and G. Granozzi, *Chem. Sci.*, 2019, **10**, 9438–9445.
- 163 B. Reuillard, M. Blanco, L. Calvillo, N. Coutard, A. Ghedjatti, P. Chenevier, S. Agnoli, M. Otyepka, G. Granozzi and V. Artero, *ACS Appl. Mater. Interfaces*, 2020, **12**, 5805–5811.
- 164 H. Seelajaroen, A. Bakandritsos, M. Otyepka, R. Zbořil and N. S. Sariciftci, *ACS Appl. Mater. Interfaces*, 2020, **12**, 250–259.
- 165 Y. Si and E. T. Samulski, *Chem. Mater.*, 2008, **20**, 6792–6797.
- 166 A. Eckmann, A. Felten, A. Mishchenko, L. Britnell, R. Krupke, K. S. Novoselov and C. Casiraghi, *Nano Lett.*, 2012, **12**, 3925–3930.
- 167 F. T. Johra, J.-W. Lee and W.-G. Jung, *J. Ind. Eng. Chem.*, 2014, **20**, 2883–2887.
- 168 A. Bakandritsos, D. D. Chronopoulos, P. Jakubec, M. Pykal, K. Čépe, T. Steriotis, S. Kalytchuk, M. Petr, R. Zbořil and M. Otyepka, *Adv. Funct. Mater.*, 2018, **28**, 1801111–1801111.
- 169 Y. Gogotsi and P. Simon, *Science*, 2011, **334**, 917–918.



## 8 LIST OF APPENDICES

### Appendix A

Full text of a publication: Šedajová, V.; Bakandritsos, A.; Błoński, P.; Medved', M.; Langer, R.; Zaoralová, D.; Ugolotti, J.; Džíbelová, J.; Jakubec, P.; Kupka, V.; Otyepka, M. Nitrogen Doped Graphene with Diamond-like Bonds Achieves Unprecedented Energy Density at High Power in a Symmetric Sustainable Supercapacitor. **Energy Environ. Sci.** 2022, 15 (2), 740–748. <https://doi.org/10.1039/D1EE02234B>

### Appendix B

Full text of a publication: Vermisoglou, E. C.; Jakubec, P.; Bakandritsos, A.; Kupka, V.; Pykal, M.; Šedajová, V.; Vlček, J.; Tomanec, O.; Scheibe, M.; Zbořil, R.; Otyepka, M. Graphene with Covalently Grafted Amino Acid as a Route Toward Eco-Friendly and Sustainable Supercapacitors. **ChemSusChem** 2021, 14 (18), 3904–3914. <https://doi.org/10.1002/cssc.202101039>

### Appendix C

Full text of a publication: Šedajová, V.; Jakubec, P.; Bakandritsos, A.; Ranc, V.; Otyepka, M. New Limits for Stability of Supercapacitor Electrode Material Based on Graphene Derivative. **Nanomaterials** 2020, 10 (9), 1731. <https://doi.org/10.3390/nano10091731>

## APPENDIX A

Šedajová, V.; Bakandritsos, A.; Błoński, P.; Medved', M.; Langer, R.; Zaoralová, D.; Ugolotti, J.; Dzibelová, J.; Jakubec, P.; Kupka, V.; Otyepka, M. Nitrogen Doped Graphene with Diamond-like Bonds Achieves Unprecedented Energy Density at High Power in a Symmetric Sustainable Supercapacitor. **Energy Environ. Sci.** 2022, 15 (2), 740–748. <https://doi.org/10.1039/D1EE02234B>

## APPENDIX B

Vermisoglou, E. C.; Jakubec, P.; Bakandritsos, A.; Kupka, V.; Pykal, M.; Šedajová, V.; Vlček, J.; Tomanec, O.; Scheibe, M.; Zbořil, R.; Otyepka, M. Graphene with Covalently Grafted Amino Acid as a Route Toward Eco-Friendly and Sustainable Supercapacitors. **ChemSusChem** 2021, 14 (18), 3904–3914. <https://doi.org/10.1002/cssc.202101039>

## APPENDIX C

Šedajová, V.; Jakubec, P.; Bakandritsos, A.; Ranc, V.; Otyepka, M. New Limits for Stability of Supercapacitor Electrode Material Based on Graphene Derivative. **Nanomaterials** 2020, 10 (9), 1731. <https://doi.org/10.3390/nano10091731>





Cite this: *Energy Environ. Sci.*, 2022, 15, 740

## Nitrogen doped graphene with diamond-like bonds achieves unprecedented energy density at high power in a symmetric sustainable supercapacitor†

Veronika Šedajová,<sup>ab</sup> Aristides Bakandritsos,<sup>id \*ac</sup> Piotr Błoński,<sup>id a</sup> Miroslav Medveď,<sup>a</sup> Rostislav Langer,<sup>ab</sup> Dagmar Zaoralová,<sup>ab</sup> Juri Ugolotti,<sup>a</sup> Jana Dzibelová,<sup>ad</sup> Petr Jakubec,<sup>a</sup> Vojtěch Kupka<sup>a</sup> and Michal Otyepka<sup>id \*ae</sup>

Supercapacitors have attracted great interest because of their fast, reversible operation and sustainability. However, their energy densities remain lower than those of batteries. In the last decade, supercapacitors with an energy content of  $\sim 110 \text{ W h L}^{-1}$  at a power of  $\sim 1 \text{ kW L}^{-1}$  were developed by leveraging the open framework structure of graphene-related architectures. Here, we report that the reaction of fluorographene with azide anions enables the preparation of a material combining graphene-type  $\text{sp}^2$  layers with tetrahedral carbon-carbon bonds and nitrogen (pyridinic and pyrrolic) superdoping (16%). Theoretical investigations showed that the C-C bonds develop between carbon-centered radicals, which emerge in the vicinity of the nitrogen dopants. This material, with diamond-like bonds and an ultra-high mass density of  $2.8 \text{ g cm}^{-3}$ , is an excellent host for the ions, delivering unprecedented energy densities of  $200 \text{ W h L}^{-1}$  at a power of  $2.6 \text{ kW L}^{-1}$  and  $143 \text{ W h L}^{-1}$  at  $52 \text{ kW L}^{-1}$ . These findings open a route to materials whose properties may enable a transformative improvement in the performance of supercapacitor components.

Received 19th July 2021,  
Accepted 17th December 2021

DOI: 10.1039/d1ee02234b

rsc.li/ees

### Broader context

Modern society relies on electricity. The demand is bound to grow due to the increasing electromobility, the number of mobile devices, and extending the networks for the internet of things. The depleting reserves of fossil-based energy resulted in efforts to support renewable resources, which are, however, intermittent in their production. These facts call for the development of electrochemical energy storage devices with improved performance, safety, eco-friendliness, and lower cost in order to contribute to the goal of the United Nations for affordable, reliable, and sustainable energy. Lithium-ion batteries have matured and currently dominate the field. Nevertheless, carbon-based supercapacitors offer independence of critical elements, alongside safety, long life-cycle, and ultrafast charging-discharging. Here, we present a nitrogen superdoped graphene material with diamond-like interlayer bonds that dramatically increases the energy content, which can be stored per volumetric unit of the electrode—the Achilles heel of contemporary supercapacitors. The electrode displays an ultrahigh mass density compared to porous carbons, keeping intact its ability to host the electrolyte ions—the energy carriers. Consequently, a supercapacitor device made from this electrode delivers energy density twice as high as that of top-rated materials and several-fold higher than commercial supercapacitor carbons, thus enhancing the performance of supercapacitor components.

<sup>a</sup> Regional Centre of Advanced Technologies and Materials, Czech Advanced Technology and Research Institute (CATRIN), Palacký University, Šlechtitelů 27, 783 71, Olomouc, Czech Republic. E-mail: [michal.otyepka@upol.cz](mailto:michal.otyepka@upol.cz), [a.bakandritsos@upol.cz](mailto:a.bakandritsos@upol.cz)

<sup>b</sup> Department of Physical Chemistry, Faculty of Science, Palacký University, 17. listopadu 1192/12, 779 00 Olomouc, Czech Republic

<sup>c</sup> Nanotechnology Centre, Centre of Energy and Environmental Technologies, VŠB-Technical University of Ostrava, 17. listopadu 2172/15, Poruba, 708 00 Ostrava, Czech Republic

<sup>d</sup> Department of Experimental Physics, Faculty of Science, Palacký University Olomouc, 17. listopadu 1192/12, Olomouc, 77900, Czech Republic

<sup>e</sup> IT4Innovations, VŠB-Technical University of Ostrava, 17. listopadu 2172/15, 708 00 Ostrava-Poruba, Czech Republic

† Electronic supplementary information (ESI) available. See DOI: 10.1039/d1ee02234b

## 1. Introduction

Supercapacitors are energy storage devices with remarkable qualities including fast charging/discharging (*i.e.* high power) and extralong cycle-life.<sup>1</sup> Unfortunately, the energy density of the best existing supercapacitors (*i.e.* their ability to store charge/energy) is low. Commercial supercapacitors have cell-level specific energies (and energy densities) of  $10 \text{ W h kg}^{-1}$  ( $5\text{--}8 \text{ W h L}^{-1}$ ),<sup>2,3</sup> while lead-acid batteries offer  $20\text{--}35 \text{ W h kg}^{-1}$  ( $40\text{--}80 \text{ W h L}^{-1}$ )<sup>4</sup> and state-of-the-art Li-ion batteries achieve  $\sim 150 \text{ W h kg}^{-1}$  ( $\sim 250 \text{ W h L}^{-1}$ ).<sup>5,6</sup> However, Li-ion batteries



suffer from long charging times and, unlike supercapacitors, undergo irreversible processes during cycling that gradually reduce their energy density and thus their cycle-life. To exploit the benefits of supercapacitors in a broader range of applications, it will be necessary to identify electrode materials that have substantially improved energy densities combined with long life and high power. In addition, replacing metal atoms in electrode materials with non-metal and earth-abundant elements, such as carbon, would have significant environmental advantages, reducing our reliance on critical natural resources and increasing sustainability.

Due to the importance of the electrode material/electrolyte interface for charge storage,<sup>7</sup> intense efforts have been focused on lightweight materials with high surface areas such as nitrogen-doped mesoporous carbon<sup>8</sup> (2000 m<sup>2</sup> g<sup>-1</sup>), carbon nanosheets<sup>9</sup> (2500 m<sup>2</sup> g<sup>-1</sup>), activated graphene<sup>10</sup> (3100 m<sup>2</sup> g<sup>-1</sup>), and carbon nanotubes<sup>11</sup> (1300 m<sup>2</sup> g<sup>-1</sup>). The specific energies of these materials range from *ca.* 10 to 90 W h kg<sup>-1</sup>, with the highest values being reported for activated graphene,<sup>10</sup> carbon nanosheets,<sup>9</sup> and nanotubes<sup>11</sup> in ionic liquid (IL)-based electrolytes. Unfortunately, like most commercial electrodes,<sup>12</sup> these carbon materials have very low mass densities (*ca.* 0.3–0.7 g cm<sup>-3</sup>).<sup>8,10</sup> Consequently, the energy densities achieved with mesoporous carbon,<sup>8</sup> activated graphene,<sup>10</sup> and carbon nanosheets<sup>9</sup> (or single wall carbon nanotubes<sup>11</sup>) are only 22, 26, and 45 W h L<sup>-1</sup>, respectively.

To achieve higher energy densities, which is a key performance parameter,<sup>2–4,13–16</sup> efforts have been made to increase the mass density of electrode materials. Compressing a graphene electrode increased its mass density from 0.34 to 0.75 g cm<sup>-3</sup> and its energy density from 26<sup>10</sup> to 48 W h L<sup>-1</sup> (ref. 17) without adversely affecting the interactions between the electrolyte ions and the carbon surface. Capillary densification of a chemically reduced graphene gel in the presence of an IL led to an even higher density of 1.3 g cm<sup>-3</sup>, resulting in a material that delivered 90 W h L<sup>-1</sup> at a power density of 1.1 kW L<sup>-1</sup> (1 A g<sup>-1</sup>).<sup>18</sup> It was deduced that densification in the presence of the non-evaporating IL prevented the restacking of the graphene sheets and helped preserve the material's charge transport properties. Mechanical compression of a H<sub>2</sub>O<sub>2</sub>-treated reduced graphene oxide<sup>19</sup> yielded a material with a density of 0.7 g cm<sup>-3</sup> and a holey structure (beneficial for ion diffusion) that very effectively promoted three-dimensional ionic transport, delivering 85 W h L<sup>-1</sup> at 1.75 kW L<sup>-1</sup> (1 A g<sup>-1</sup>). In 2016, capillary drying was combined with a different pore-forming agent (ZnCl<sub>2</sub>), to afford a monolithic dense (0.9 g cm<sup>-3</sup>) graphene electrode<sup>14</sup> exhibiting 60 W h L<sup>-1</sup> at 0.4 kW L<sup>-1</sup> (0.6 A g<sup>-1</sup>). Further attempts to increase the energy density by heteroatom tri-doping<sup>20</sup> and densification<sup>21</sup> were not more effective, resulting in energy densities of 40 and 65 W h L<sup>-1</sup>, respectively. Even high mass density inorganic phases such as 1T-MoS<sub>2</sub> did not exceed 80 W h L<sup>-1</sup> at 1.12 kW L<sup>-1</sup> (0.5 A g<sup>-1</sup>).<sup>22</sup> The highest energy density reported to date was obtained using electrodes consisting of interdigitated bilayers of exfoliated graphene-mediated hydrogen iodide-reduced graphene oxide (EGM-GO)<sup>23</sup> with a mass density of *ca.* 1 g cm<sup>-3</sup> and a capacitance of 203 F cm<sup>-3</sup>. These

electrodes offered an energy density of 113 W h L<sup>-1</sup> at 0.9 kW L<sup>-1</sup> (1 A g<sup>-1</sup>) (see the experimental section for information on the metrics used). Thus, over the last decade there have been small improvements in materials design for higher energy contents, and power densities have remained relatively low.

Here we report a carbon-based electrode material, GN3, with an unprecedented density of 2.8 g cm<sup>-3</sup> and an N<sub>2</sub> sorption-based surface area of 128 m<sup>2</sup> g<sup>-1</sup> that can host ions even more efficiently than carbon materials with surface areas exceeding 2000 m<sup>2</sup> g<sup>-1</sup>. GN3, which is prepared by reacting graphite fluoride with sodium azide, has tetrahedral (sp<sup>3</sup>) C–C bonds, which were identified by solid-state nuclear magnetic resonance in the same region as the C–C bonds in diamond. However, it retains a 2-D structure with a very high content of aromatic (and thus conductive) regions, together with nitrogen superdoping in the vacancies and holes of the aromatic lattice. The ultrahigh mass density of GN3 combined with its polar nitrogen moieties and vacancies facilitated an energy density of 200 W h L<sup>-1</sup> at a power density of 2.6 kW L<sup>-1</sup>, corresponding to improvements of 74% and 190%, respectively, over the previous record.<sup>23</sup>

## 2. Results and discussion

Motivated by the importance of fluorine and radical chemistry<sup>24,25</sup> in the synthesis of sp<sup>3</sup>-rich carbon materials,<sup>26–28</sup> and by the high density of such materials,<sup>29</sup> we hypothesized that fluorographene chemistry could produce carbon derivatives with high mass densities. This hypothesis was strengthened by the fact that in (C<sub>2</sub>F)<sub>*n*</sub>, whereby fluorine atoms occupy one side of every other carbon sheet in an FCCF manner, the carbon atoms in between adopt a diamond-like structure,<sup>30,31</sup> ascribing high mass density.<sup>31</sup> The formation of similar sp<sup>3</sup>-rich structures was also verified theoretically and experimentally for bilayer graphene.<sup>32,33</sup> Despite their high mass density, fluorocarbons are large band-gap insulators<sup>34</sup> and lack sites capable of interacting strongly with ionic species and facilitating their transport. However, because the defluorination and functionalization of fluorographene is known to occur *via* radical reactions propagated by fluorine elimination,<sup>35,36</sup> these processes could potentially be exploited to drive sp<sup>3</sup> C–C bond formation and create graphene-based materials with high mass density.

To investigate this hypothesis, we experimentally and theoretically probed the reaction of few-layered fluorographene with sodium azide as a defluorinating agent that could at the same time introduce nitrogen atoms into the formed structure. This would increase the polarity of the carbon surface and create vacancies, as previously observed following reactions of fluorographene with various nitrogen-containing nucleophiles.<sup>36–38</sup> Sonicated bulk graphite fluoride reacted very efficiently with NaN<sub>3</sub> in dimethylformamide at 130 °C, resulting in nitrogen superdoping (Fig. 1a). X-ray photoelectron spectroscopy (XPS) revealed a decrease in the material's content of F atoms after a reaction time of 4 h and almost complete elimination of F after 72 h, at which point the material's N content reached 16.1 at% (Fig. 1b and c). This change was reflected in the C 1s regions of the materials' XPS spectra (Fig. 1c): the initially



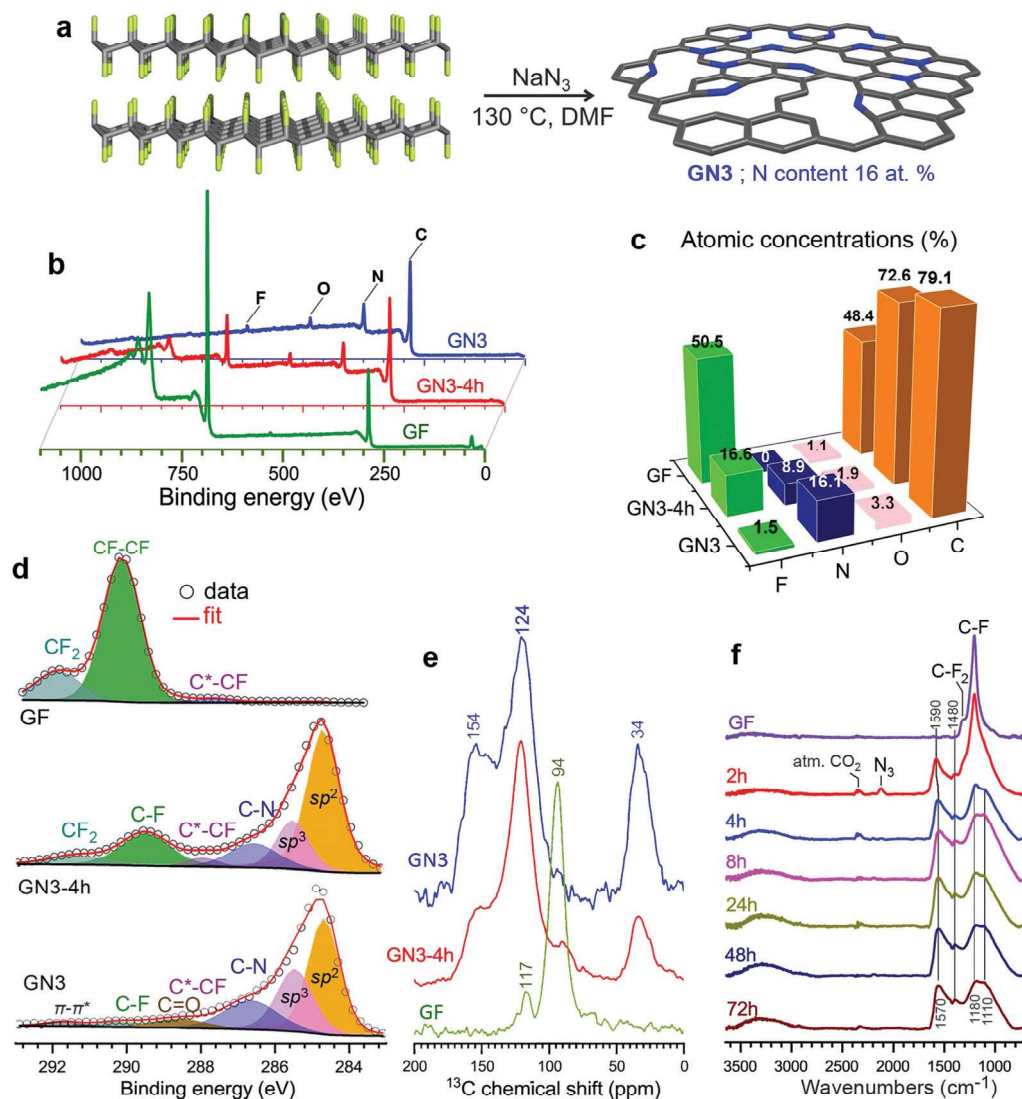


**Fig. 1** Synthesis and characterization of the GN3 material. (a) Schematic depiction of the synthesis of GN3 from sonicated graphite fluoride (GF). (b) XPS survey spectra of the starting GF and the N-doped derivative after reaction times of 4 h and 72 h (GN3). (c) Elemental compositions of the same materials determined by XPS. (d) Deconvoluted HR-XPS spectra for the C 1s regions. (e) CP MAS  $^{13}\text{C}$  solid state NMR spectra and (f) IR spectra of GF, reaction intermediates at various time points, and the final GN3 product.

F-bonded carbon atoms of fluorographene, with binding energies above 289.5 eV, were transformed into (i) aromatic  $\text{sp}^2$  carbons (284.7 eV, 45%), (ii) non-functionalized  $\text{sp}^3$  carbons (285.5 eV, 25%), and (iii) nitrogen bonded carbons (286.6 eV, 19%). The other components in this spectral region were attributed to small amounts of residual fluorine and oxygen from the environment. The HR-XPS spectra of the N 1s envelope (Fig. S1, ESI<sup>†</sup>) revealed the presence of nitrogen atoms in pyridinic and pyrrolic configurations (or protonated and non-protonated N centres), as well as a very small number of graphitic nitrogens (44, 49, and 7 at%, respectively). The dominance of pyridinic and pyrrolic nitrogens is consistent with the vacancies present in the parent material<sup>36</sup> and with the extensive development of such vacancies during defluorination.<sup>36–38</sup>

The  $^1\text{H} \rightarrow ^{13}\text{C}$  CP MAS solid-state NMR spectra of the GN3-4 h intermediate and GN3 show peaks at 34 ppm (Fig. 1e).

Chemical shifts in this range are typical for non-functionalized and non-nitrogen bonded  $\text{sp}^3$  carbons in diamond and diamond-like carbon materials.<sup>39</sup> This peak was stronger in the spectrum of GN3 than the GN3-4 h intermediate, indicating that these  $\text{sp}^3$  carbons formed gradually as the reaction progressed. Furthermore, the peaks centred at 124 and 154 ppm indicate the presence of a  $\pi$ -conjugated aromatic network and aromatic  $>\text{C}=\text{N}$  moieties (pyridinic and pyrrolic),<sup>39,40</sup> respectively.  $^{19}\text{F} \rightarrow ^{13}\text{C}$  CP MAS of the starting GF revealed peaks corresponding to  $\text{CF}_2$  (117 ppm) and CF (94 ppm) groups, typical for FG.<sup>41</sup> Such non-functionalized tetrahedral carbons at 34 ppm are not detected in graphene oxide, reduced graphene oxide, or graphene.<sup>42,43</sup> The reaction's progress was also verified by infra-red spectroscopy (Fig. 1f). Specifically, the bands of the CF and  $\text{CF}_2$  groups of GF (1200 and 1305  $\text{cm}^{-1}$ , respectively) were progressively replaced with



bands at 1580 and 1210  $\text{cm}^{-1}$  (characteristic of aromatic carbon rings<sup>44</sup>), indicating the formation of an  $\text{sp}^2$  network. Additional aromatic-ring vibrations, appearing at 1400  $\text{cm}^{-1}$ , could be ascribed to heteroatom substitution (*e.g.* with pyridinic nitrogens<sup>44,45</sup>), as suggested by theoretical calculations.<sup>46,47</sup> The Raman spectrum of GN3 featured broad D and G bands at 1300 and 1590  $\text{cm}^{-1}$ , respectively, and an  $I_{\text{D}}/I_{\text{G}}$  ratio of 1.3, which remained unchanged even after heating at 1000 °C in an argon atmosphere (Fig. S2, ESI<sup>†</sup>), indicating the presence of a large number of non heat-susceptible  $\text{sp}^3$  carbons and non-healable defects (*i.e.* vacancies). Raman bands and X-ray diffraction peaks (XRD) deconvolution performed on GN3, and on the commercial porous carbon for comparison (Fig. S3 and S4, ESI<sup>†</sup>), showed that the GN3 displays a disordered structure with randomly developed tetrahedral C–C bonds. Results also highlighted the very small planarity of the aromatic areas, with a lateral size ( $L_{\text{a}}$ ) of *ca.* 4 nm (Fig. S3 and S4 (ESI<sup>†</sup>), and comments in the caption). Further insights into the N-doping of fluorographene with  $\text{NaN}_3$  were obtained through density functional theory (DFT) calculations. The  $\text{N}_3^-$  anion initiated the reaction by nucleophilic attack on carbon radical defects, leading to  $\text{N}_2$  release and fluorine elimination (Fig. S5, ESI<sup>†</sup>). The attachment of azide groups in the initial stages of the reaction was confirmed by the infra-red spectrum of the 2 h intermediate (Fig. 1f). High-resolution transmission electron microscopy (HR-TEM, Fig. 2a and b) revealed that GN3 indeed exists as sheets with patches and holes.

Energy dispersive X-ray spectroscopy (EDXS) elemental mapping with high-angle annular dark-field scanning transmission electron microscopy (HAADF-STEM, Fig. 2c) showed that the GN3 sheets (Fig. 2d) are densely and homogeneously covered with nitrogen (Fig. 2e). Thermogravimetric and evolved gas analyses in air (Fig. S6, ESI<sup>†</sup>) indicated that these nitrogen atoms were embedded in the lattice rather than being out-of-plane functionalities, because emission of NO gas ( $m/z = 30$ ) peaked at very high temperature (675 °C), at which  $\text{CO}_2$  emission also took place due to carbon lattice decomposition.

To better understand the formation of the tetrahedral C–C bonds, theoretical models of GN3 sheet fragments were studied using spin-polarized DFT (Fig. 3), consistent with the experimental findings (*i.e.* containing vacancies and nitrogen dopants mainly in pyridinic and pyrrolic configurations, Fig. 3). Remarkably, the system relaxed into a thermodynamically stable structure with spontaneously formed tetrahedral  $\text{sp}^3$  C–C bonds, verifying the experimental NMR findings. The bonds were formed between the carbons in the pyridinic vacancies, where radicals were centred (highlighted by spheres in Fig. 3). Similar  $\text{sp}^3$  bonding was suggested to form after the introduction of atomic vacancies and pyrrolic N atoms by N-ion beam irradiation of graphene sheets, which creates carbon atoms with dangling bonds (radicals) around the vacancies.<sup>48</sup>

Films of GN3 or GN3 with additives (polymer binder 10%; conductive additive 5%) were formed by pasting slurries onto 15  $\mu\text{m}$ -thick Al foils for density measurements and preparation

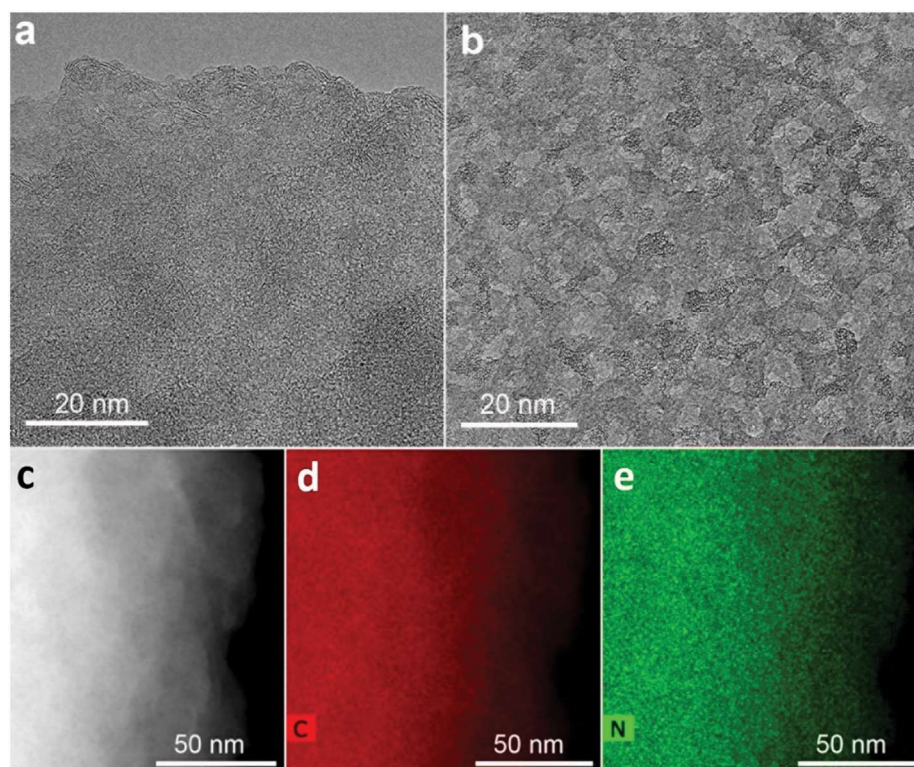


Fig. 2 (a) and (b) High-resolution transmission electron microscopy images of GN3 flakes; several areas had extensively holey structure, as shown in (b), and in Fig. S1b (ESI<sup>†</sup>). (c) HAADF image of a GN3 flake used for EDXS mapping, along with the corresponding (d) carbon and (e) nitrogen map.



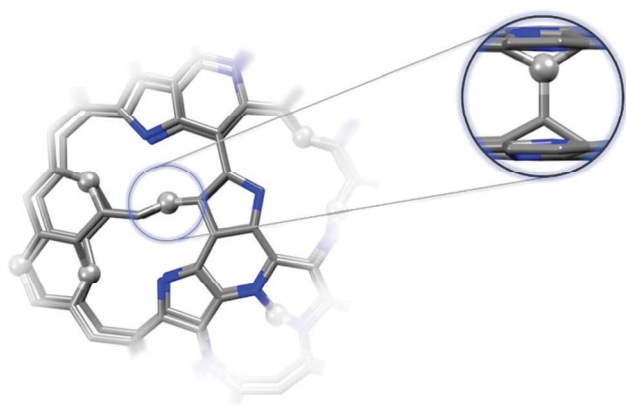


Fig. 3 Theoretical model of GN3 structural fragment (C : N atomic ratio of ca. 84 : 16) optimized by first-principles spin-polarized DFT calculations. Top view of this structure with the carbons bearing radicals and forming interlayer bonds highlighted as spheres (zoomed side-view). The model simulates the structure locally (few-atom level) and does not (and cannot) provide macroscopic structural information.

of supercapacitor electrodes (ESI† Methods). Scanning electron microscopy (SEM, Fig. 4a–c) showed that compression at 80 kN for 1 minute ( $\sim 65$  MPa) reduced a ca. 10  $\mu\text{m}$  thick film of GN3 to a thickness of 2  $\mu\text{m}$  (Fig. 4d–f). From thickness measurements performed using SEM and a digital micrometer (Fig. S7c and d, ESI†), the density of these films consistently reached values of 2.7–2.8  $\text{g cm}^{-3}$ , compared to  $\sim 0.5$   $\text{g cm}^{-3}$  before pressing. The same mass density was also attained for a high-mass loading electrode (8.3  $\text{mg cm}^{-2}$ , Fig. S7i and j, ESI†). The NMR spectrum of the pressed material was identical to that before pressing, indicating that pressing caused only bed consolidation, and not formation of bonds. Five GN3 batches

from different reactions were measured to determine the mass density; it should be noted that densities were only measured after dialysis of GN3. Control tests were performed using the same procedure with Al foil alone (Fig. S7a and b, ESI†) and with commercial carbons of high surface area (Fig. S7e–h, ESI†), namely porous carbon (PC) from ACS Material (0.3  $\text{g cm}^{-3}$ , 2000  $\text{m}^2 \text{g}^{-1}$  according to  $\text{N}_2$  BET) and YP-80F Kuraray carbon (KC) (0.6  $\text{g cm}^{-3}$ , 2363  $\text{m}^2 \text{g}^{-1}$  according to  $\text{N}_2$  BET; also measured in-house, Fig. S8b and d, ESI†). The thickness measurements for the PC carbon were cross-checked by SEM (Fig. S9, ESI†). Results verified that no compression took place for Al foil, and that all mass density calculations for the commercial carbons after their pressing matched those given by the provider. Moreover, we performed elemental analysis for Na showing that 0.02 mass% of sodium remained in GN3, and therefore, the respective contribution in mass density of the material is negligible. The surface area of GN3 determined from the  $\text{N}_2$  sorption isotherm using BET equation was only 128  $\text{m}^2 \text{g}^{-1}$ , (Fig. S8a and c, ESI†). The surface area determined by methylene blue sorption was 300  $\text{m}^2 \text{g}^{-1}$  (Fig. S10, ESI†), suggesting that under solvated conditions (as in an electrolytic supercapacitor cell), charged species/molecules, like methylene blue in this case, may penetrate into the structure of GN3. Interestingly, preliminary electrochemical testing of GN3 showed that pressing did not affect its charge storage properties; in fact, pressing increased the capacitance relative to the non-pressed electrode (Fig. S11, ESI†).

The electrochemical properties of GN3 were studied in a symmetric full cell using as the electrolyte the IL 1-ethyl-3-methylimidazolium tetrafluoroborate (EMIM- $\text{BF}_4$ ) with 1,1,2,2-tetrafluoroethyl-2,2,3,3-tetrafluoropropyl ether (TTE) in a 9 : 1

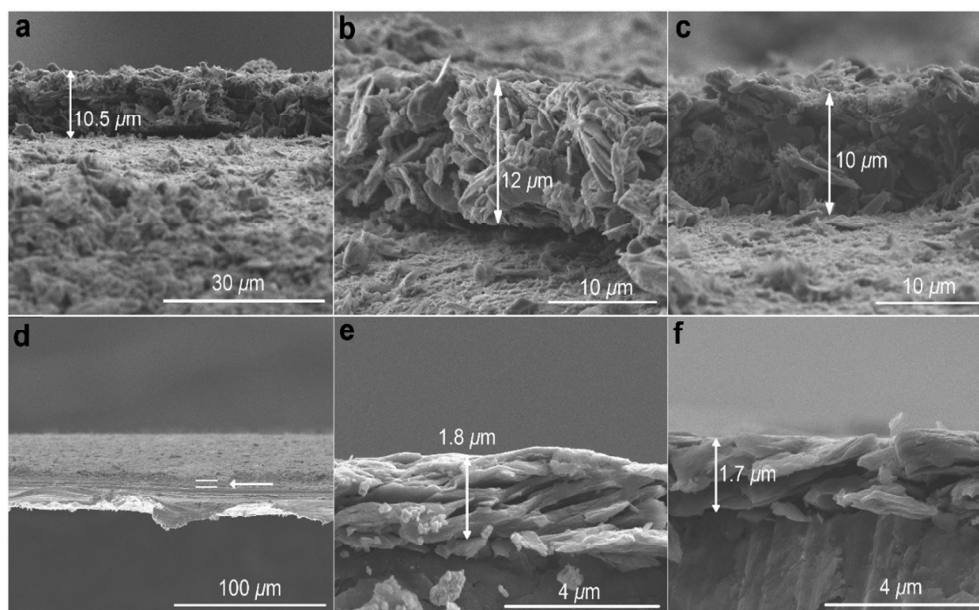


Fig. 4 SEM images of GN3 with 10 mass% additives pasted on Al foil. (a)–(c) Before pressing and (d)–(f) after pressing. Pressing the Al foil itself did not affect its thickness (Fig. S7a and b, ESI†).



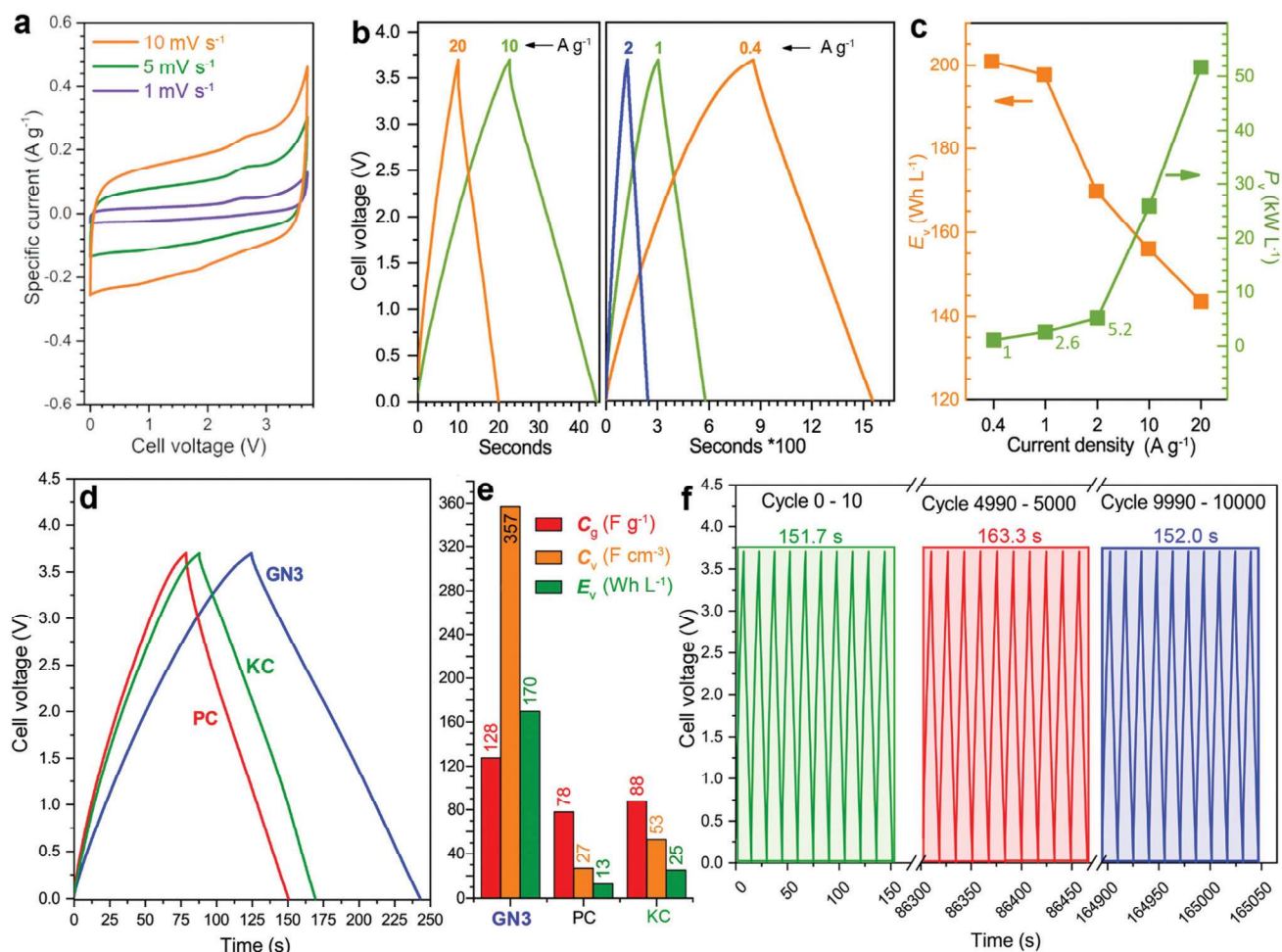


Fig. 5 Electrochemical characterization of a symmetric supercapacitor cell with GN3 electrodes. (a) CV curves in the EMIM-BF<sub>4</sub> and TTE (9 : 1) electrolyte at low scan rates. (b) GCD profiles at different specific currents. (c) Energy and power density of GN3 at increasing specific currents. (d) Comparison of the GN3 cell with symmetric cells made using commercial high surface area (2000 m<sup>2</sup> g<sup>-1</sup>) porous carbons (PC and KC) at 2 A g<sup>-1</sup> and (e) the performance of these cells. (f) Cyclic stability of GN3 showing the GCD profiles at the beginning, mid-point, and end of a 10 000 cycle test at 20 A g<sup>-1</sup> current density.

ratio. The cyclic voltammograms (CVs, Fig. 5a) were quasi-rectangular in shape with minor redox peaks, probably due to the nitrogen lattice atoms of the GN3 material.<sup>49</sup> This shape was preserved even at very high scan rates (Fig. S12, ESI<sup>†</sup>), indicating that the system exhibits predominantly capacitive behaviour<sup>10</sup> with fast charge transport in the material and at the interfaces.<sup>15</sup> These features were verified by galvanostatic charge/discharge measurements (GCD, Fig. 5b), which yielded linear and symmetric profiles (124 s charging, 118 s discharging at 2 A g<sup>-1</sup>, 95% energy efficiency). The efficiency improved to 100% at 20 A g<sup>-1</sup> (22 s charging, 22 s discharging). At 1 A g<sup>-1</sup>, the GN3 cell achieved an ultrahigh energy density of 197.6 Wh L<sup>-1</sup> at a power of 2.6 kW L<sup>-1</sup>. At 20 A g<sup>-1</sup>, the energy density remained high at 143.5 Wh L<sup>-1</sup>, while the power density jumped to 51.8 kW L<sup>-1</sup> (Fig. 5c).

For benchmarking, the carbons PC and KC (the latter widely used in commercial supercapacitors<sup>50</sup>) were evaluated under identical conditions. GN3 had a significantly better discharging time (Fig. 5d) than PC and KC, and its performance was

superior in both volumetric and gravimetric terms (Fig. 5e), which is impressive given the dramatic differences in the materials' BET surface areas. The cycling stability test of the GN3 material showed capacitance retention of 100% after 10 000 cycles at 20 A g<sup>-1</sup> (Fig. 5f) and 98% after 14 000 cycles at 5 A g<sup>-1</sup> (Fig. S15, ESI<sup>†</sup>). Rate testing of the GN3 cell showed that 76% retention of its capacitance at 40 A g<sup>-1</sup> (Fig. 6a). A similar (70%) capacitance retention was achieved at 40 A g<sup>-1</sup> for a cell made with exfoliated graphene-mediated HI-reduced graphene oxide (EGM-GO), which contained 50% exfoliated graphene.<sup>23</sup>

For comparative purposes, reported capacitance retention values for other high-performance graphene-based electrodes are *ca.* 65% at 40 A g<sup>-1</sup> for liquid-mediated densified graphene,<sup>18</sup> 70% at 40 A g<sup>-1</sup> for holey graphene,<sup>19</sup> 57% at 10 A g<sup>-1</sup> for capillary-densified graphene,<sup>21</sup> and 77% at 20 A g<sup>-1</sup> for vertically aligned graphene electrodes<sup>51</sup> (a much more conductive aqueous electrolyte was used in the latter case, which unfortunately keeps energy content low). These

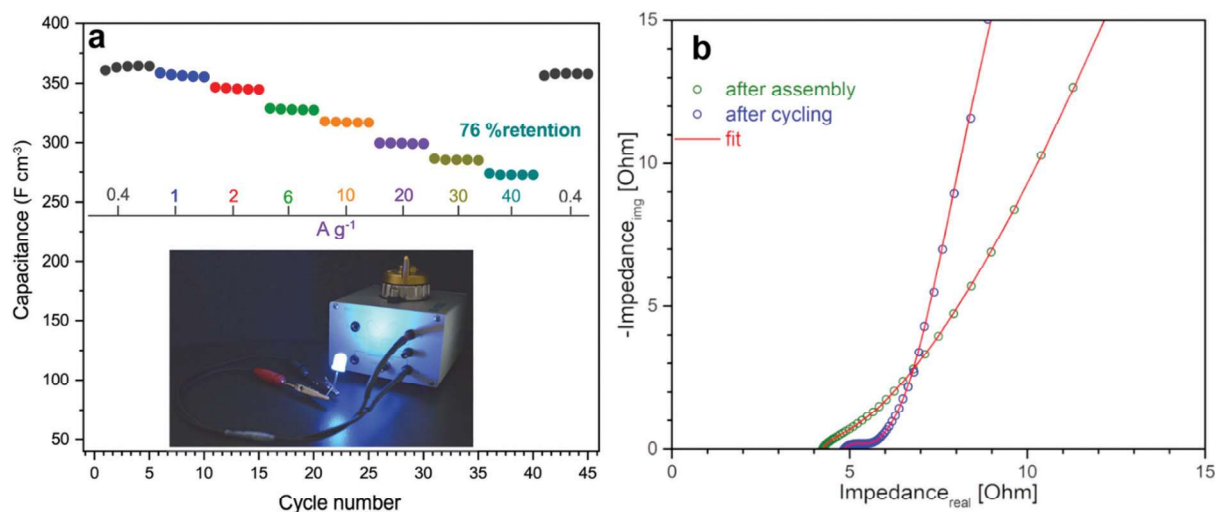


Fig. 6 Electrochemical properties of a symmetric supercapacitor cell with GN3 electrodes. (a) Rate test at increasing specific currents. (b) Nyquist plots of GN3 after cell assembly and after cycling in EMIM-BF<sub>4</sub> and TTE electrolyte (9 : 1 ratio).

comparisons highlight the excellent charge transport properties of GN3, which are also reflected in its electrochemical impedance spectroscopic features before and after cycling (Fig. 6b). Based on the modified Frumkin–Melik–Gaykazyan circuit (Fig. S17, ESI<sup>†</sup>), the intersection of the Nyquist plot with the real axis at the start of the high frequency region corresponded to an equivalent series resistance ( $R_s$ ) of 3.9  $\Omega$  before cycling, which was only marginally increased to 4.4  $\Omega$  after 10 000 cycles.

Furthermore, the total absence of semicircles in the high frequency region indicated a very low charge transfer resistivity ( $R_{ct}$ ) in the bulk material and at the interfaces.<sup>19,52</sup> The almost vertical slope of the spectrum in the low frequency region

(on the right of the x-axis) suggested a highly capacitive behaviour and effective ionic charge transport in the bulk of the electrode material.

Volumetric performance is particularly important for devices in the modern portable energy storage landscape;<sup>2,4,13,14,20,23</sup> both energy and power density are desired. The former directly affects the amount of energy that can be stored, while high power density enables fast charging and discharging. Energy density is the Achilles heel of supercapacitors, whereas high power densities are one of their greatest strengths, which must be preserved. The GN3 cell (Fig. 5c and Fig. S18, ESI<sup>†</sup>) demonstrated ground-breaking performance by delivering both ultrahigh energy density and power density. Specifically, its energy density was *ca.* 200 W h L<sup>-1</sup> at a

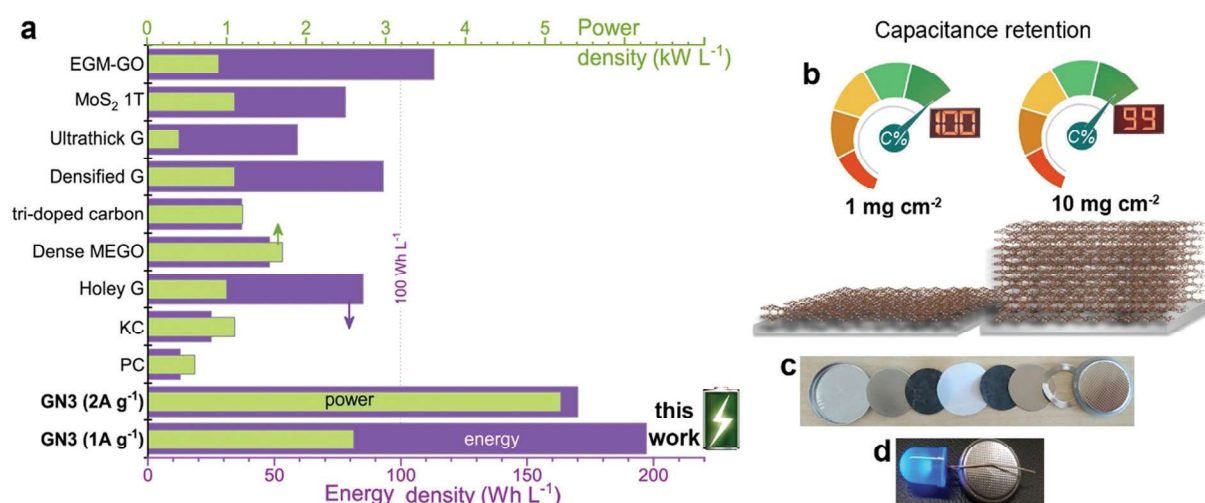


Fig. 7 (a) The energy and power density output achieved with GN3 electrodes compared to electrodes made with commercial 2000 m<sup>2</sup> g<sup>-1</sup> active carbon and prominent analogues selected from the literature, chosen for their promising features; (holey G: holey graphene;<sup>19</sup> dense MEGO: compressed, microwave expanded and activated reduced graphene oxide;<sup>17</sup> tri-doped carbon;<sup>20</sup> densified G: capillary densified graphene;<sup>18</sup> ultrathick graphene;<sup>14</sup> 1T-MoS<sub>2</sub> (ref. 22) and EGM-GO: exfoliated graphene-mediated graphene oxide<sup>23</sup>). (b) Specific capacitance in symmetric full cell at high (10 mg cm<sup>-2</sup>) mass loading of GN3 was 99% of the recorded capacitance of the low-mass-loading (1 mg cm<sup>-2</sup>) symmetric full cell. (c),(d) Coin cell GN3 electrodes on aluminium foils before (c) and after assembly (d); the assembled cell was used to operate a 4 V LED diode.



power of  $2.6 \text{ kW L}^{-1}$ ,  $170 \text{ W h L}^{-1}$  at  $5.2 \text{ kW L}^{-1}$ , and  $143 \text{ W h L}^{-1}$  at  $52 \text{ kW L}^{-1}$ . To set these results into the context of the current state of the art, they are presented alongside literature data on top-performing materials in Fig. 7a. When making these comparisons, care was taken to ensure that the same set of equations and metrics were used in all cases.<sup>53–55</sup> The equations from ref. 23 were used, as described in the experimental section. The comparisons highlight the transformative performance of GN3: not only does it have a higher energy density than the previously best-in-class EGM-GO electrode ( $170 \text{ W h L}^{-1}$  for GN3 vs.  $113 \text{ W h L}^{-1}$  for EGM-GO<sup>23</sup>), but this energy could be delivered at a power of  $5.2 \text{ kW L}^{-1}$  compared to  $0.9 \text{ kW L}^{-1}$ . Importantly, the GN3 cell could also be operated at mass loadings of up to  $10 \text{ mg cm}^{-2}$ , demonstrating almost identical capacitance (Fig. 7b) at a temperature of  $38 \text{ }^\circ\text{C}$ , which is in the range typically used to evaluate energy storage devices,<sup>56–59</sup> and 81% retention at the same testing conditions as the low mass-loading supercapacitor cell (see experimental part, ESI†). The coin cell shown in Fig. 7c and d, was constructed with a commercial ultrathin  $25 \text{ }\mu\text{m}$  membrane operating a  $4 \text{ V}$  LED lamp. Successful operation of carbon materials with such highly attractive features lays the ground for the fabrication of competitive, commercially relevant cells.

### 3. Conclusions

We have discovered a new class of carbon-based materials comprising nitrogen doped graphene with diamond-like tetrahedral bonds for high energy density supercapacitor electrodes that are significantly more dense than comparable materials prepared by mechanical compression,<sup>17</sup> capillary densification,<sup>18</sup> and other methods.<sup>19,23</sup> The new materials are prepared by leveraging the radical-based chemistry of fluorographene, which enables the fruitful combination of  $\text{sp}^2$  and  $\text{sp}^3$  carbon bonds in the same network, along with very high nitrogen doping and vacancies. This hybrid carbon achieves mass densities of  $2.8 \text{ g cm}^{-3}$ , while retaining efficient charge transport, ion penetration, diffusion, and storage. Therefore, cells with electrodes made from these materials offer ground-breaking energy storage capability at very high charging/discharging rates. The discovery of this class of materials will spur intense research on other high-density conductive carbon materials with different functionalities, with the aim of further increasing the competitiveness of supercapacitors in the portable energy storage landscape.

### Conflicts of interest

A European patent with the number EP 3907184 has been published.

### Acknowledgements

M. O. acknowledges support from the ERC in the form of a Consolidator Grant (H2020, No. 683024), V. Š., R. L. and J. D. acknowledge support from the Internal Student Grant Agency

of the Palacký University in Olomouc, Czech Republic (IGA\_PrF\_2021\_031, IGA\_PrF\_2021\_003). A. B. acknowledges funding from the Czech Science Foundation, project GA CR – EXPRO, 19-27454X. P. J. acknowledges the Research Infrastructure NanoEnviCz, supported by the Ministry of Education, Youth and Sports of the Czech Republic under Project No. LM2018124. We also acknowledge support from the Operational Programme Research, Development and Education – European Regional Development Fund, Project No. CZ.02.1.01/0.0/0.0/16\_019/0000754 of the Ministry of Education, Youth and Sports of the Czech Republic. The authors gratefully thank O. Tomanec (HR-TEM); C. Perez, E. Ioannou (SEM); K. Roháčová (Raman); Tomáš Steklý (synthesis, MB measurements); Jan Kolařík (AAS) and J. Pauswang (part of electrochemical testing).

### Notes and references

- 1 A. S. Aricò, P. Bruce, B. Scrosati, J.-M. Tarascon and W. van Schalkwijk, *Nat. Mater.*, 2005, **4**, 366–377.
- 2 W. Gu and G. Yushin, *Wiley Interdiscip. Rev.: Energy Environ.*, 2014, **3**, 424–473.
- 3 Q. Wang, J. Yan and Z. Fan, *Energy Environ. Sci.*, 2016, **9**, 729–762.
- 4 Y. Gogotsi and P. Simon, *Science*, 2011, **334**, 917–918.
- 5 J. W. Choi and D. Aurbach, *Nat. Rev. Mater.*, 2016, **1**, 16013.
- 6 P. Albertus, S. Babinec, S. Litzelman and A. Newman, *Nat. Energy*, 2018, **3**, 16–21.
- 7 M. Salanne, B. Rotenberg, K. Naoi, K. Kaneko, P.-L. Taberna, C. P. Grey, B. Dunn and P. Simon, *Nat. Energy*, 2016, **1**, 16070.
- 8 T. Lin, I.-W. Chen, F. Liu, C. Yang, H. Bi, F. Xu and F. Huang, *Science*, 2015, **350**, 1508–1513.
- 9 J. Hou, C. Cao, F. Idrees and X. Ma, *ACS Nano*, 2015, **9**, 2556–2564.
- 10 Y. Zhu, S. Murali, M. D. Stoller, K. J. Ganesh, W. Cai, P. J. Ferreira, A. Pirkle, R. M. Wallace, K. A. Cychosz, M. Thommes, D. Su, E. A. Stach and R. S. Ruoff, *Science*, 2011, **332**, 1537–1541.
- 11 A. Izadi-Najafabadi, S. Yasuda, K. Kobashi, T. Yamada, D. N. Futaba, H. Hatori, M. Yumura, S. Iijima and K. Hata, *Adv. Mater.*, 2010, **22**, E235–E241.
- 12 EP2357046B1, 2013.
- 13 P. Simon and Y. Gogotsi, *Acc. Chem. Res.*, 2013, **46**, 1094–1103.
- 14 H. Li, Y. Tao, X. Zheng, J. Luo, F. Kang, H.-M. Cheng and Q.-H. Yang, *Energy Environ. Sci.*, 2016, **9**, 3135–3142.
- 15 D. Yu, K. Goh, H. Wang, L. Wei, W. Jiang, Q. Zhang, L. Dai and Y. Chen, *Nat. Nanotechnol.*, 2014, **9**, 555–562.
- 16 R. Weber, M. Genovese, A. J. Louli, S. Hames, C. Martin, I. G. Hill and J. R. Dahn, *Nat. Energy*, 2019, **4**, 683–689.
- 17 S. Murali, N. Quarles, L. L. Zhang, J. R. Potts, Z. Tan, Y. Lu, Y. Zhu and R. S. Ruoff, *Nano Energy*, 2013, **2**, 764–768.
- 18 X. Yang, C. Cheng, Y. Wang, L. Qiu and D. Li, *Science*, 2013, **341**, 534–537.





- 19 Y. Xu, Z. Lin, X. Zhong, X. Huang, N. O. Weiss, Y. Huang and X. Duan, *Nat. Commun.*, 2014, **5**, 5554.
- 20 H. Jin, X. Feng, J. Li, M. Li, Y. Xia, Y. Yuan, C. Yang, B. Dai, Z. Lin, J. Wang, J. Lu and S. Wang, *Angew. Chem., Int. Ed.*, 2019, **58**, 2397–2401.
- 21 P. Li, H. Li, D. Han, T. Shang, Y. Deng, Y. Tao, W. Lv and Q.-H. Yang, *Adv. Sci.*, 2019, **6**, 1802355.
- 22 M. Acerce, D. Voiry and M. Chhowalla, *Nat. Nanotechnol.*, 2015, **10**, 313–318.
- 23 Z. Li, S. Gadipelli, H. Li, C. A. Howard, D. J. L. Brett, P. R. Shearing, Z. Guo, I. P. Parkin and F. Li, *Nat. Energy*, 2020, **5**, 160–168.
- 24 W. Lai, D. Xu, X. Wang, Z. Wang, Y. Liu, X. Zhang, Y. Li and X. Liu, *Phys. Chem. Chem. Phys.*, 2017, **19**, 24076–24081.
- 25 U. Rajeena, P. Raveendran and R. M. Ramakrishnan, *J. Fluorine Chem.*, 2020, **235**, 109555.
- 26 W. A. Yarbrough, *J. Am. Ceram. Soc.*, 1992, **75**, 3179–3200.
- 27 Z.-J. Liu, S.-J. Ding, P.-F. Wang, D. W. Zhang, J.-Y. Zhang, J.-T. Wang and K. Kohse-Hoinghaus, *Thin Solid Films*, 2000, **368**, 208–210.
- 28 I. Schmidt and C. Benndorf, *Diamond Relat. Mater.*, 1997, **6**, 964–969.
- 29 J. Robertson, *Mater. Sci. Eng., R*, 2002, **37**, 129–281.
- 30 V. Pischedda, S. Radescu, M. Dubois, N. Batisse, F. Balima, C. Cavallari and L. Cardenas, *Carbon*, 2017, **114**, 690–699.
- 31 H. Touhara, K. Kadono, Y. Fujii and N. Watanabe, *Z. Anorg. Allg. Chem.*, 1987, **544**, 7–20.
- 32 P. V. Bakharev, M. Huang, M. Saxena, S. W. Lee, S. H. Joo, S. O. Park, J. Dong, D. C. Camacho-Mojica, S. Jin, Y. Kwon, M. Biswal, F. Ding, S. K. Kwak, Z. Lee and R. S. Ruoff, *Nat. Nanotechnol.*, 2020, **15**, 59–66.
- 33 J. Sivek, O. Leenaerts, B. Partoens and F. M. Peeters, *J. Phys. Chem. C*, 2012, **116**, 19240–19245.
- 34 F. Karlický, R. D. Kumara, M. Otyepka and R. Zbořil, *ACS Nano*, 2013, **7**, 6434–6464.
- 35 M. Medved', G. Zoppellaro, J. Ugolotti, D. Matochová, P. Lazar, T. Pospíšil, A. Bakandritsos, J. Tuček, R. Zbořil and M. Otyepka, *Nanoscale*, 2018, **10**, 4696–4707.
- 36 D. Zaoralová, V. Hrubý, V. Šedajová, R. Mach, V. Kupka, J. Ugolotti, A. Bakandritsos, M. Medved and M. Otyepka, *ACS Sustainable Chem. Eng.*, 2020, **8**, 4764–4772.
- 37 G. Zoppellaro, A. Bakandritsos, J. Tuček, P. Błoński, T. Susi, P. Lazar, Z. Bad'ura, T. Steklý, A. Opletalová, M. Otyepka and R. Zbořil, *Adv. Mater.*, 2019, **31**, 1902587.
- 38 Y. Liu, Y. Shen, L. Sun, J. Li, C. Liu, W. Ren, F. Li, L. Gao, J. Chen, F. Liu, Y. Sun, N. Tang, H.-M. Cheng and Y. Du, *Nat. Commun.*, 2016, **7**, 1–9.
- 39 A. S. Mazur, M. A. Vovk and P. M. Tolstoy, *Fullerenes, Nanotubes, Carbon Nanostruct.*, 2020, **28**, 202–213.
- 40 R. L. Johnson, J. M. Anderson, B. H. Shanks and K. Schmidt-Rohr, *Chem. Mater.*, 2014, **26**, 5523–5532.
- 41 J. Giraudet, M. Dubois, A. Hamwi, W. E. E. Stone, P. Pirotte and F. Masin, *J. Phys. Chem. B*, 2005, **109**, 175–181.
- 42 S. Stankovich, D. A. Dikin, R. D. Piner, K. A. Kohlhaas, A. Kleinhammes, Y. Jia, Y. Wu, S. T. Nguyen and R. S. Ruoff, *Carbon*, 2007, **45**, 1558–1565.
- 43 W. Gao, L. B. Alemany, L. Ci and P. M. Ajayan, *Nat. Chem.*, 2009, **1**, 403–408.
- 44 D. W. Mayo, in *Course Notes on the Interpretation of Infrared and Raman Spectra*, eds. D. W. Mayo, F. A. Miller and R. W. Hannah, John Wiley & Sons, Inc., 2004, pp. 101–140.
- 45 J. Senthilnathan, C.-C. Weng, J.-D. Liao and M. Yoshimura, *Sci. Rep.*, 2013, **3**, srep02414.
- 46 A. Bakandritsos, R. G. Kadam, P. Kumar, G. Zoppellaro, M. Medved', J. Tuček, T. Montini, O. Tomanec, P. Andrášková, B. Drahoš, R. S. Varma, M. Otyepka, M. B. Gawande, P. Fornasiero and R. Zbořil, *Adv. Mater.*, 2019, **31**, 1900323.
- 47 P. Lazar, R. Mach and M. Otyepka, *J. Phys. Chem. C*, 2019, **123**, 10695–10702.
- 48 X. Wu, H. Zhao, J. Pei and D. Yan, *Appl. Phys. Lett.*, 2017, **110**, 133102.
- 49 D. Hulicova-Jurcakova, M. Seredych, G. Q. Lu and T. J. Bando, *Adv. Funct. Mater.*, 2009, **19**, 438–447.
- 50 L. Weinstein and R. Dash, *Mater. Today*, 2013, **16**, 356–357.
- 51 Y. Yoon, K. Lee, S. Kwon, S. Seo, H. Yoo, S. Kim, Y. Shin, Y. Park, D. Kim, J.-Y. Choi and H. Lee, *ACS Nano*, 2014, **8**, 4580–4590.
- 52 J. Wang, J. Tang, B. Ding, V. Malgras, Z. Chang, X. Hao, Y. Wang, H. Dou, X. Zhang and Y. Yamauchi, *Nat. Commun.*, 2017, **8**, 15717.
- 53 M. D. Stoller and R. S. Ruoff, *Energy Environ. Sci.*, 2010, **3**, 1294–1301.
- 54 S. Zhang and N. Pan, *Adv. Energy Mater.*, 2015, **5**, 1401401.
- 55 A. Noori, M. F. El-Kady, M. S. Rahmanifar, R. B. Kaner and M. F. Mousavi, *Chem. Soc. Rev.*, 2019, **48**, 1272–1341.
- 56 R. Weber, M. Genovese, A. J. Louli, S. Hames, C. Martin, I. G. Hill and J. R. Dahn, *Nat. Energy*, 2019, **4**, 683–689.
- 57 X. Lin, M. Salari, L. M. R. Arava, P. M. Ajayan and M. W. Grinstaff, *Chem. Soc. Rev.*, 2016, **45**, 5848–5887.
- 58 L. Timperman, H. Galiano, D. Lemordant and M. Anouti, *Electrochem. Commun.*, 2011, **13**, 1112–1115.
- 59 J. Alvarado, M. A. Schroeder, M. Zhang, O. Borodin, E. Gobrogge, M. Olguin, M. S. Ding, M. Gobet, S. Greenbaum, Y. S. Meng and K. Xu, *Mater. Today*, 2018, **21**, 341–353.



# Graphene with Covalently Grafted Amino Acid as a Route Toward Eco-Friendly and Sustainable Supercapacitors

Eleni C. Vermisoglou,<sup>[a]</sup> Petr Jakubec,<sup>[a]</sup> Aristides Bakandritsos,<sup>[a, b]</sup> Vojtěch Kupka,<sup>[a]</sup> Martin Pykal,<sup>[a]</sup> Veronika Šedajová,<sup>[a, c]</sup> Jakub Vlček,<sup>[c]</sup> Ondřej Tomanec,<sup>[a]</sup> Magdalena Scheibe,<sup>[a]</sup> Radek Zbořil,<sup>[a, b]</sup> and Michal Otyepka<sup>\*,[a, d]</sup>

Eco-friendly, electrochemically active electrode materials based on covalent graphene derivatives offer enormous potential for energy storage applications. However, covalent grafting of functional groups onto the graphene surface is challenging due to its low reactivity. Here, fluorographene chemistry was employed to graft an arginine moiety via its guanidine group homogeneously on both sides of graphene. By tuning the reaction conditions and adding a non-toxic pore-forming agent, an optimum degree of functionalization and hierarchical porosity was achieved in the material. This tripled the specific

surface area and yielded a high capacitance value of approximately  $390 \text{ F g}^{-1}$  at a current density of  $0.25 \text{ A g}^{-1}$ . The applicability of the electrode material was investigated under typical operating conditions by testing an assembled supercapacitor device for up to 30000 charging/discharging cycles, revealing capacitance retention of 82.3%. This work enables the preparation of graphene derivatives with covalently grafted amino acids for technologically important applications, such as supercapacitor-based energy storage.

## Introduction

Depleted natural resources, such as fossil fuels, and severe environmental pollution problems related to the greenhouse effect and global warming as well as ever-growing energy consumption have prompted the search for clean energy sources and renewable energy storage technologies.<sup>[1]</sup> Electrochemical energy storage devices utilize physical-chemical processes to store electricity. Rechargeable batteries and supercapacitors have attracted great attention in applications

concerning hybrid electric vehicles, mobile electronics, and smart displays.<sup>[2,3]</sup> Even though rechargeable batteries can store large amounts of energy (i.e., enable a high energy density) they provide a low power density due to long charge/discharge times. Moreover, they often suffer from poor lifecycle stability, which restricts their versatility. In contrast, supercapacitors achieve a high power density and long cycle lifetimes, and significant efforts to improve their relatively low energy density have been made worldwide.<sup>[4,5]</sup> Ultra-long electrochemical stability and slow aging are fundamental requirements for cutting-edge technology products.<sup>[6]</sup>

Graphene, an allotrope of carbon in the form of a monolayer, appears to be excellent candidate for supercapacitor electrode material due to its huge theoretical specific surface area (SSA,  $2675 \text{ m}^2 \text{ g}^{-1}$ ), high conductivity, and intrinsic mechanical strength, giving rise to a specific capacitance of  $550 \text{ F g}^{-1}$ .<sup>[7–9]</sup> This lightweight and flexible material may exhibit much lower values of specific capacitance due to irreversible restacking and agglomeration upon preparation processes as a result of graphene interlayer van der Waals forces. Consequently, the active surface area accessible to electrolyte ions is significantly reduced.<sup>[10]</sup> Functionalization of graphene with small biocompatible organic molecules that can act as spacer materials prevents the aggregation of graphene sheets, facilitating ion transfer. Furthermore, bio-organic functionalities are renewable, typically low cost, allow rational design synthesis, and generate minimum waste.<sup>[11]</sup> These low-molecular units afford extra redox sites, contributing pseudocapacitance to the overall capacitance. So far, only a few electrode materials have been prepared by functionalization of graphene with biocompatible organic molecules (Table S1 in the Supporting Information). In 2017, El-Gendy et al. reported the covalent functionalization of spongy graphene with biocompatible adenine, where the labile oxygen groups of graphite oxide (GO) were covalently

[a] Dr. E. C. Vermisoglou, Dr. P. Jakubec, Dr. A. Bakandritsos, Dr. V. Kupka, Dr. M. Pykal, V. Šedajová, O. Tomanec, Dr. M. Scheibe, Prof. Dr. R. Zbořil, Prof. Dr. M. Otyepka  
Czech Advanced Technology and Research Institute (CATRIN)  
Regional Centre of Advanced Technologies and Materials (RCPTM)  
Palacký University Olomouc  
Šlechtitelů 27, 779 00 Olomouc (Czech Republic)  
E-mail: Michal.Otyepka@upol.cz

[b] Dr. A. Bakandritsos, Prof. Dr. R. Zbořil  
Nanotechnology Centre,  
Centre of Energy and Environmental Technologies  
VŠB–Technical University of Ostrava  
17. listopadu 2172/15, 708 00 Ostrava-Poruba (Czech Republic)

[c] V. Šedajová, Dr. J. Vlček  
Department of Physical Chemistry,  
Faculty of Science  
Palacký University Olomouc  
17. listopadu 12, 771 46 Olomouc (Czech Republic)

[d] Prof. Dr. M. Otyepka  
IT4Innovations,  
VSB–Technical University of Ostrava  
17. listopadu 2172/15, 708 00 Ostrava-Poruba (Czech Republic)

Supporting information for this article is available on the WWW under <https://doi.org/10.1002/cssc.202101039>

© 2021 The Authors. ChemSusChem published by Wiley-VCH GmbH. This is an open access article under the terms of the Creative Commons Attribution Non-Commercial License, which permits use, distribution and reproduction in any medium, provided the original work is properly cited and is not used for commercial purposes.

bound to the amino groups of adenine, for preparing green and high-performance supercapacitors. A capacitance of  $322.1 \text{ F g}^{-1}$  at a current density of  $1 \text{ A g}^{-1}$  was achieved using aqueous  $0.5 \text{ M H}_2\text{SO}_4$  as an electrolyte in a three-electrode system. The material was tested for 1000 charging/discharging cycles and exhibited capacitance retention of 102%.<sup>[12]</sup> However, tests in a two-electrode setup corresponding more closely to real capacitor devices have not yet been performed. In 2020, Deng et al. presented the non-covalent functionalization of graphene with methylene blue as a binder-free electrode for solid-state supercapacitors. The material had an outstanding capacitance of  $517 \text{ F g}^{-1}$  at a current density of  $0.5 \text{ A g}^{-1}$  using aqueous  $0.5 \text{ M H}_2\text{SO}_4$  as an electrolyte in a three-electrode setup. The corresponding device showed capacitance retention of 72% in 10000 charging/discharging cycles in  $\text{H}_2\text{SO}_4$ /polyvinyl alcohol (PVA) electrolyte.<sup>[13]</sup> Zhou et al. confined methylene blue in three-dimensional reduced graphene oxide, and the prepared electrode material displayed a capacitance of  $311 \text{ F g}^{-1}$  at a current density of  $1 \text{ A g}^{-1}$  using  $1 \text{ M H}_2\text{SO}_4$  as an electrolyte in a three-electrode setup. The capacitance retention for 10000 cycles was 96%. The material in a device exhibited capacitance retention of 81% for 10000 cycles using PVA/ $\text{H}_2\text{SO}_4$  as an electrolyte.<sup>[14]</sup> However, non-covalently functionalized materials are susceptible to spontaneous disintegration. Therefore, it is desirable to prepare covalently functionalized graphene using biocompatible organic molecules. Covalent functionalization compared to non-covalent functionalization has the benefits of stability and controllability of the structure, enabling better processability.<sup>[15]</sup> The functionality is fixed on graphene and cannot easily be detached into the electrolyte solution. Therefore, the integrity of the material is preserved for a longer time.<sup>[16]</sup>

Direct covalent functionalization of graphene is hard to achieve. However, the use of fluorographene (FG) chemistry bypasses this obstacle, enabling a wide portfolio of graphene derivatives to be synthesized with grafted functional groups. The source of FG (i.e., graphite fluoride) is abundant since it is produced in tons industrially to be used as a lubricant. Further, FG has a well-defined structure, that is, a hexagonal lattice of  $\text{sp}^3$  carbons homogeneously bonded to fluorine atoms. FG is easily susceptible to nucleophilic attack, reacting readily with amines, alcohols, thiols, and others.<sup>[17–19]</sup>

In the present work, the synthesis of zwitterionic arginine-functionalized FG (FG/Arg) is reported. Owing to the guanidino functional group, Arg can act as a nucleophile and can be grafted onto FG through nucleophilic attack, initiated on the electrophilic radical centers at the defect sites of FG.<sup>[20,21]</sup> To avoid random grafting of Arg on FG, the functionalization initially employed *tert*-butoxycarbonyl (Boc)-protected Arg, which was afterwards deprotected. Different reaction times were investigated to optimize the reaction conditions in terms of the defluorination (increasing the conductivity) and functionalization degree (FD, increasing the zwitterionic character benefiting the capacitance<sup>[22]</sup>). The derivative with the optimum porosity exhibited the maximum capacitive performance, which was further improved by adding potassium carbonate ( $\text{K}_2\text{CO}_3$ ). The surface area was increased by a factor of around 3, and (in addition to the existing mesoporosity) micropores (centered at  $\approx 1.5 \text{ nm}$ ) were developed in situ during the reaction, yielding a hierarchically porous derivative. The impact of hierarchical porosity was profound, increasing the capacitance by 30% in comparison to the derivative without  $\text{K}_2\text{CO}_3$  treatment, reaching  $390 \text{ F g}^{-1}$  at a current density of  $0.25 \text{ A g}^{-1}$ . These findings show that the present strategy can tune three key features of graphene derivatives (conductivity, FD, and porosity), significantly enhancing the capacitance of the products.<sup>[23]</sup> The synthesized material represents an eco-friendly Arg-functionalized graphene that could be used as an efficient supercapacitor in aqueous electrolytes. This work opens new avenues for grafting amino acids onto a graphene surface. Owing to the N- and C-termini, such graphenes could be useful in many applications, including biosensing, analytical chemistry, and others.

## Results and Discussion

The strategy used for the specific covalent functionalization of FG with Arg is summarized in Figure 1a. First, the available primary guanidino amine of Boc-Arg-OH was reacted with FG through nucleophilic attack and then de-protection was carried out by treatment of FG/Boc-48 h with hydrochloric acid under heating. The successful removal of the Boc protecting group and presence of a free  $\alpha$ -amino group in the produced FG/Arg-48 h were confirmed by the Kaiser test and Fourier-transform

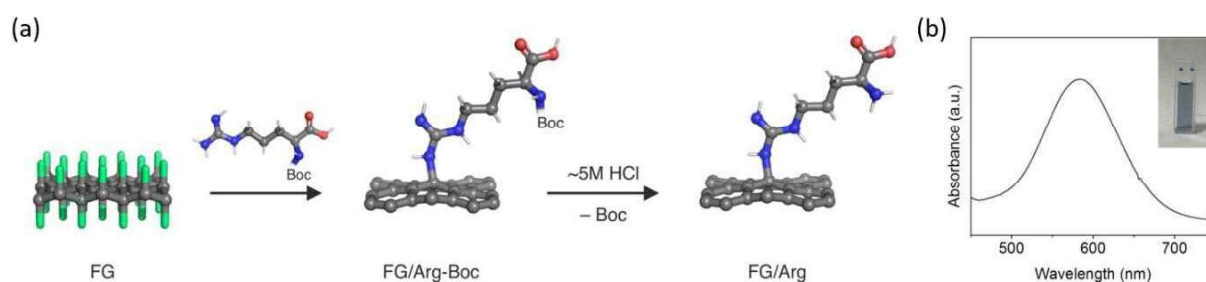


**Figure 1.** (a) Scheme illustrating FG reaction with Boc-Arg-OH and subsequent removal of the Boc protecting group to generate the FG/Arg product (hydrogens are not shown). Color of important elements in 3D visualization of molecules is coded as follows: carbon = grey; fluorine = green; nitrogen = blue; oxygen = red. (b) Kaiser test of FG/Arg-48 h sample.

(FT)IR measurements. Reaction with ninhydrin generated a deep blue solution (with absorption maximum at  $\approx 583$  nm, Figure 1b), whereas in the absence of FG/Arg-48 h, both FG/Boc-48 h and the blank solutions were colorless (Figure S1).

Direct evidence for the functionalization of GrF with Arg was obtained from FTIR measurements of GrF, FG/Boc-48 h, and FG/Arg-48 h samples. The FTIR spectrum of GrF (Figure 2a) showed a characteristic strong band at  $1204\text{ cm}^{-1}$  and weaker band at  $1307\text{ cm}^{-1}$  assigned to stretching vibrations of covalent C–F bonds and peripheral C–F<sub>2</sub> bonds, respectively.<sup>[23,24]</sup> The spectrum of FG/Boc-48 h showed the characteristic band of N–H stretching vibrations at around  $3187\text{ cm}^{-1}$ , which was attributed to the secondary amine, and a band at around  $3341\text{ cm}^{-1}$ , which was assigned to O–H stretching vibrations. In the case of FG/Arg-48 h, the O–H stretching vibration overlapped with a second N–H stretching vibration band attributed to the deprotected primary amine.<sup>[25,26]</sup> Two weak bands at around  $2800\text{--}2950\text{ cm}^{-1}$  in the FG/Boc-48 h spectrum were attributed to C–H stretching vibrations of methyls present in the Boc protecting group.<sup>[25]</sup> A stretching vibration of the C=O group in the Boc protecting group was detected in the FG/Boc-48 h spectrum at around  $1670\text{ cm}^{-1}$  but was absent in the FG/Arg-48 h spectrum, indicating effective de-protection of the Arg primary amine.<sup>[26]</sup> An absorption band at approximately  $1571\text{ cm}^{-1}$  was suggested to be related to C=C skeleton

vibrations in aromatic graphene regions in FG/Boc-48 h and also N–H bending vibration of the primary amine in FG/Arg-48 h.<sup>[24,26]</sup> A band at around  $1400\text{ cm}^{-1}$  was assigned to either C–O–H bending due to a carboxylic group and/or C–N stretching vibration and  $-\text{CH}_2$  deformation.<sup>[27–29]</sup> A band at approximately  $1451\text{ cm}^{-1}$  was also attributed to  $-\text{CH}_2$  bending vibration.<sup>[25]</sup> Broad strong bands centered at around  $1207\text{ cm}^{-1}$  for FG/Boc-48 h and  $1181\text{ cm}^{-1}$  for FG/Arg-48 h were assigned to C–F stretching vibration ( $\approx 1200\text{ cm}^{-1}$ ) and C–N vibration ( $1000\text{--}1250\text{ cm}^{-1}$ ).<sup>[30,31]</sup> The intensity ratio ( $> 1.5$ ) of the bands attributed to aromatic graphene and C–F stretching vibration in FG/Arg-48 h\_K and FG/Arg-48 h indicated extensive graphitization and effective defluorination of the functionalized FG (Figure S2a). All the FTIR spectra are presented in Figure S2b.

Changes in the surface chemistry of graphene derivatives as a function of reaction time and upon addition of potassium carbonate to the reaction were elucidated by X-ray photoelectron spectroscopy (XPS). The results showed a significant loss of F atoms with time up to 48 h and greater elimination of F atoms for the sample prepared under alkaline conditions (FG/Arg-48\_K) (Table 1).

High-resolution C 1 s XPS spectra of the parent material GrF and the covalently functionalized graphene derivative FG/Arg-48 h are presented in Figure 2b. The C 1 s peak was deconvoluted into six components in the case of GrF and 5 components

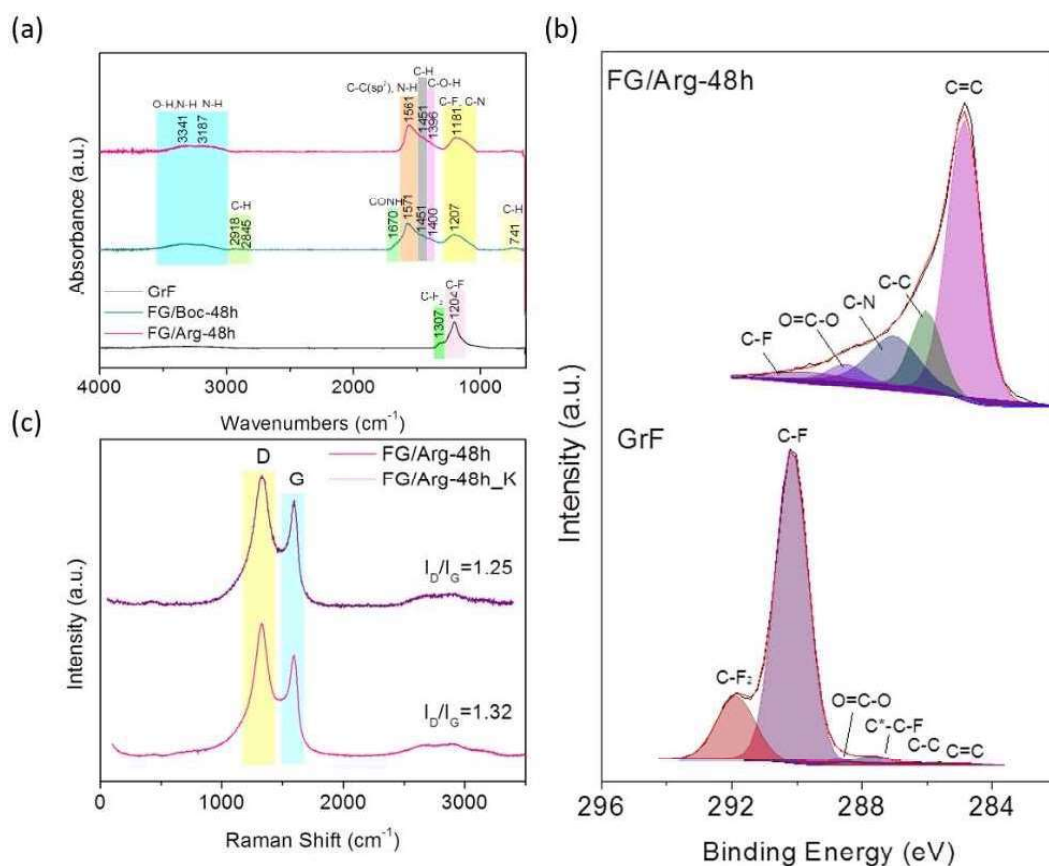


**Figure 2.** (a) FTIR spectra of GrF, FG/Boc-48 h, and FG/Arg-48 h. (b) High-resolution C 1 s XPS spectra of the parent material GrF and final product FG/Arg-48 h. (c) Raman spectra of FG/Arg-48 h and FG/Arg-48 h\_K samples.

**Table 1.** Atomic composition of GrF, FG/Arg-xh (x: 24, 48, and 72 h) and FG/Arg-48 h\_K samples derived from XPS analyses..

Sample	Element content [at%]				C/F
	C	N	O	F	
GrF	44.1	-	0.2	55.7	0.8
FG/Arg-24 h	78.4	10.6	6.0	5.0	15.7
FG/Arg-48 h	76.4	13.7	6.6	3.3	23.2
FG/Arg-72 h	77.2	13.2	6.3	3.3	23.4
FG/Arg-48_K	77.9	13.6	6.5	2.0	39.0

for the derivatives FG/Arg-xh (x: 24, 48, 72 h) and FG/Arg-48 h\_K. The presence of a C–C ( $sp^2$ ) bond was denoted by the peak located at around 284.81 eV, while the presence of C–C ( $sp^3$ ), C–N, C\*–C–F, O=C–O, C–F, and  $CF_2$  bonds was implied by the peaks centered around 285.97, 287.17, 287.84, 288.61, 289.87, and 291.83 eV, respectively. XPS spectra of all the samples are shown in Figure S3. As the reaction time was increased, the atomic percentage of C–F decreased, reaching a value of 4.3 at 48 h, before remaining constant with further increases of time. This C–F content was lower for the sample prepared in the presence of potassium carbonate. The atomic percentage of C atoms bound in C=C ( $sp^2$ ) was maximum at 24 h and then decreased with increasing time, whereas C atoms bound in C–C ( $sp^3$ ) showed the inverse trend. Similar trends were observed for the sample prepared in the presence of potassium carbonate. Values for the content of C atoms participating in C–N and O=C–O groups indicative of FD were maximum for the sample prepared at 48 h (Table 2).

To estimate FD of the graphene derivatives, we combined results from thermogravimetric analysis (TGA) and XPS data. TGA of Arg as well as derivative thermogravimetry (DTG) graphs

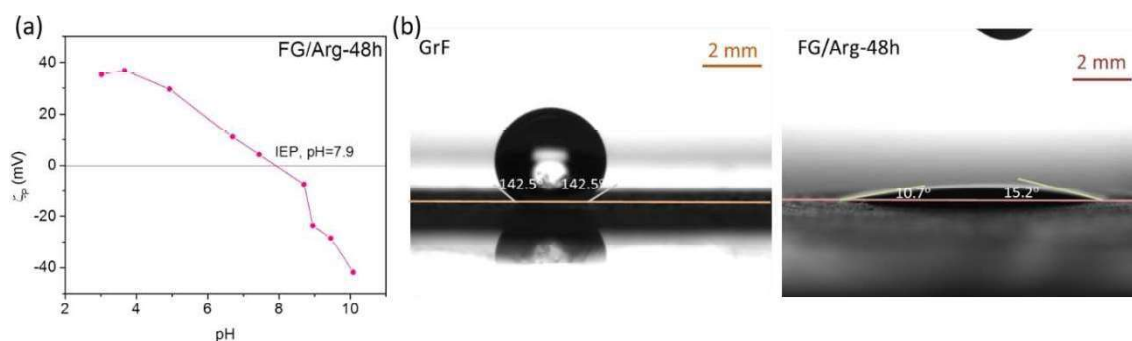
of all the samples are presented in Figure S4a,b. An example of the FD calculations is presented in the Supporting Information. For samples prepared at 24, 48, and 72 h, the corresponding FDs reached 2.9, 3.7, and 3.3, respectively. FD of FG/Arg-48 h\_K was 3.5. The FD, low content of F atoms, and high content of  $sp^2$  C atoms may indicate reasonable conductivity of the graphene with grafted Arg.

Raman spectra of the samples confirmed formation of the functionalized graphene derivative. Two prominent and rather wide D ( $1332\text{ cm}^{-1}$ ) and G ( $1595\text{ cm}^{-1}$ ) bands were present in the spectra. A high intensity ratio  $I_D/I_G \approx 1.32$  ( $> 1$ ) for FG/Arg-48 h reflected the high FD due to the presence of  $sp^3$  hybridized carbon atoms.<sup>122,231</sup> Nevertheless, carbon  $sp^2$  hybridized atoms constituted a dominant fraction, giving rise to an intense G peak. It should be noted that the parent material GrF is a Raman-silent material.<sup>132</sup> The  $I_D/I_G$  ratio increased with increasing FD (Figures 2c and S5). The sample FG/Arg-48 h had the highest FD (3.7) as well as the highest  $I_D/I_G$  ratio (1.32). The slightly lower  $I_D/I_G$  ratio for the FG/Arg-48 h\_K sample could reflect the role of the pore-forming agent, which may etch the less ordered carbon phase, increasing the  $sp^2$  content in the sample.

When the covalently functionalized derivatives were dispersed in water, a zwitterionic network was formed, as shown by zeta potential  $\zeta_p$  measurements as a function of pH (Figure 3a). The FG/Arg-48 h sheets in an aqueous environment were positively charged (up to +36.8 mV) due to protonation of the amino groups (pH 3.0–8.0). The isoelectric point (IEP) of FG/Arg-48 h was estimated to be around 8 (7.9), shifted from the isoelectric point of Arg (10.8). This pronounced shift of IEP can be considered indirect proof of Arg grafting via the

**Table 2.** Atomic percentage (at%) of characteristic groups in FG/Arg-xh derivatives and the parent GrF obtained from deconvolution of high-resolution C 1 s core level XPS spectra.

Sample	Group content [at%]						
	C–C ( $sp^2$ ) $\approx 284.81\text{ eV}$	C–C ( $sp^3$ ) $\approx 285.97\text{ eV}$	C–N $\approx 287.17$	C*–C–F $\approx 287.84\text{ eV}$	O=C–O $\approx 288.61\text{ eV}$	C–F $\approx 289.87\text{ eV}$	$CF_2$ $\approx 291.83\text{ eV}$
GrF	0.7	1.1	–	3.2	0.8	74.6	19.6
FG/Arg-24 h	62.5	14.1	13.7	–	4.1	5.6	–
FG/Arg-48 h	58.4	15.6	17.3	–	4.4	4.3	–
FG/Arg-72 h	56.9	18.1	16.5	–	4.2	4.3	–
FG/Arg-48_K	55.9	20.1	17.2	–	4.3	2.5	–


**Figure 3.** (a)  $\zeta_p$ -potential curve of an FG/Arg-48 h aqueous dispersion versus pH. (b) Water droplet contact angle measurements of GrF and FG/Arg-48 h.

guanidine group. Above this  $\text{pH} \approx 8$ , the  $\zeta\text{p}$  values became negative (up to  $-41.8$  mV).

Both FG and graphene are hydrophobic materials, whereas graphene with grafted Arg is hydrophilic and highly water dispersible. The hydrophilicity of the graphene derivatives was studied by water droplet contact angle measurements. Figure 3b shows there was a sharp change in the hydrophilicity upon Arg functionalization of the hydrophobic parent GrF, with a decrease in the water droplet contact angle from  $142.5^\circ$  for GF to  $10.7$  and  $15.2^\circ$  for FG/Arg-48 h. The high wettability of Arg functionalized graphene verifies the effective functionalization of hydrophobic GrF. The contact angles of all the samples prepared for different reaction times are presented in Figure S6.

The SSA of FG/Arg-48 h and FG/Arg-48 h\_K was determined by  $\text{N}_2$  adsorption/desorption measurements (Figure 4a) together with their corresponding pore size distribution (PSD) characteristics (Figure 4b). Adsorption/desorption isotherms of all the samples with PSD characteristics are shown in Figures S7 and S8, respectively. The Brunauer-Emmett-Teller (BET) surface areas of FG/Arg-24 h, FG/Arg-48 h, and FG/Arg-72 h were  $61$ ,  $29$ , and  $34$   $\text{m}^2\text{g}^{-1}$ , respectively. The relatively small surface areas of the graphene derivatives may be because in the dried samples, the functionalized graphene sheets were closely associated with each other, whereas this behavior was unlikely to occur in

an aqueous dispersion.<sup>[23,33]</sup> It is worth noting that the SSA decreased with increasing FD. The open isotherm of FG/Arg-48 h\_K indicates slow desorption kinetics. We performed additional measurements with prolonged equilibration times (from 10 s used for all other measurements to 60 s, Figure S9). Although the equilibration time was extended considerably, the shape of isotherm remained the same. This confirms slow desorption kinetics, which may originate from the co-existence of micropores observed only in FG/Arg-48 h\_K. Micropores may have been introduced by the release of  $\text{CO}_2$  and etching from the potassium ions since the potassium carbonate is present during the material synthesis. The size of the micropores ( $\approx 1.5$  nm) was sufficient to accommodate electrolyte ions, which is advantageous for supercapacitor electrode materials.

Scanning (SEM) and transmission electron microscopy (TEM) were employed to investigate the morphological characteristics of graphene derivatives prepared using different reaction times and with/without potassium carbonate. SEM images (Figure S10) showed the presence of platy, thin flakes of functionalized graphene with lateral sizes not exceeding  $1$   $\mu\text{m}$ , providing evidence of satisfactory separation of the sheets. The absence of charging during the SEM imaging implied that the graphene-based sheets were electrically conductive. TEM evaluation of the FG/Arg-48 h\_K sample (Figure 5a) after being

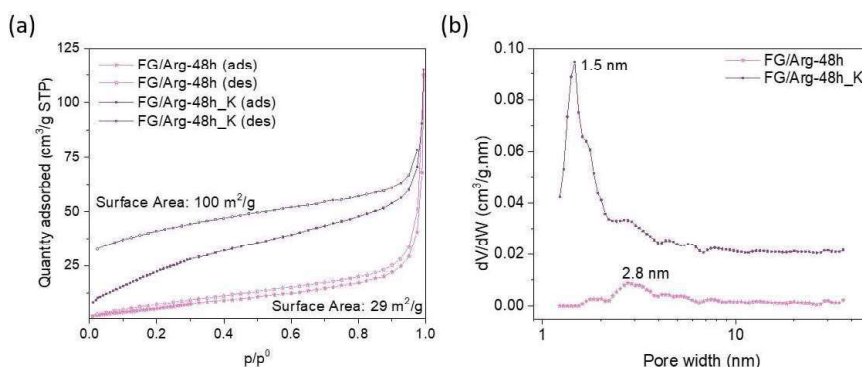


**Figure 4.** (a)  $\text{N}_2$  adsorption/desorption isotherms obtained at  $-196$   $^\circ\text{C}$  for FG/Arg-48 h and FG/Arg-48 h\_K samples. (b) Pore size distributions of FG/Arg-48 h and FG/Arg-48 h\_K samples.

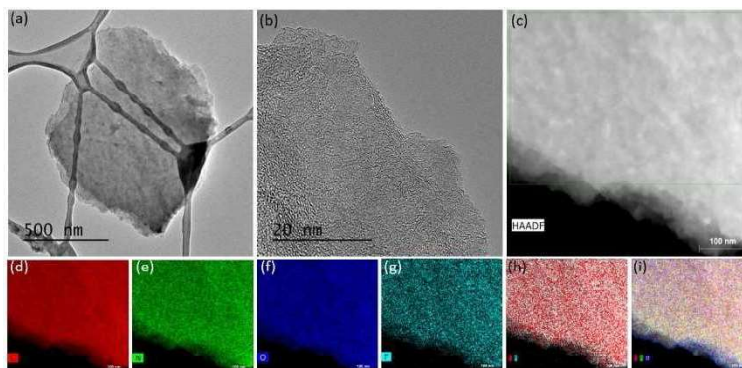


**Figure 5.** (a) TEM and (b) HRTEM micrographs of a FG/Arg-48 h\_K sample. (c) Dark-field HRTEM image of FG/Arg-48 h\_K and corresponding EDS chemical mapping: (d) carbon map, (e) nitrogen map, (f) oxygen map, (g) fluorine map, (h) carbon-fluorine map, and (i) carbon-nitrogen-oxygen overall map. (c–i) Scale bars: 100 nm.

dispersed in ethanol and then dried showed thin, almost transparent, flakes indicative of exfoliated materials. TEM images of all samples are illustrated in Figure S11. The edges of the FG/Arg-48 h\_K sheets in high-resolution (HR)TEM images (Figure 5b) were almost transparent, indicative of few-layer graphene. A dark-field HRTEM image of a FG/Arg-48 h\_K flake is presented in Figure 5c. The corresponding energy-dispersive X-ray spectroscopy (EDS) elemental mapping of this flake revealed homogeneous grafting of functional groups throughout the surface of the flake. Potassium was completely removed during thermal treatment with hydrochloric acid. It should be stressed the high density of functional groups were distributed uniformly across the surface without areas that were more or less densely functionalized (Figures 5d–i). This homogeneity is a major advantage of FG chemistry compared to GO chemistry.

The atomic force microscopy (AFM) image in Figure 6a,b shows a typical FG/Arg-48 h\_K flake and corresponding height profile. The lateral size of the flake was around 0.8  $\mu\text{m}$  and the corresponding height profile ranged from 3.9 to 11.5 nm. Assuming that the thickness of double-sided functionalized graphene with Arg was approximately 0.93 nm, the number of

FG/Arg layers was estimated as ranging from 4 to 12, implying few-layer graphene. The few-layer graphene structure would be detrimental to its capacitive performance in aqueous electrolytes because it was extensively hydrated due to its high hydrophilicity attributed to Arg functionalities. A snapshot from molecular dynamics (MD) calculations (Figure 6c) illustrates the packing of double-sided functionalized FG with Arg. It was observed that arginines easily form a network of intermolecular hydrogen bonds between the layers (on average 7 H-bonds per 10 surface groups). Moreover, the material contains several intramolecular hydrogen bonds (5 intralayer H-bonds per 10 Arg groups), which may improve the final stability and structural rigidity of FG/Arg.

Figure 7a plots a set of cyclic voltammograms (CVs) recorded in 1 M  $\text{H}_2\text{SO}_4$  (at a constant scan rate of  $50 \text{ mV s}^{-1}$ ) for samples prepared with different reaction times. The potential window was fixed at 1 V to prevent the electrolysis of water. As can be seen, the CV curves featured blunt and slanted profiles with small broad redox peaks located at around 0.45 V. The deviation from the ideal rectangular shape can be explained in terms of electron spin resonance (ESR; finite resistance of the

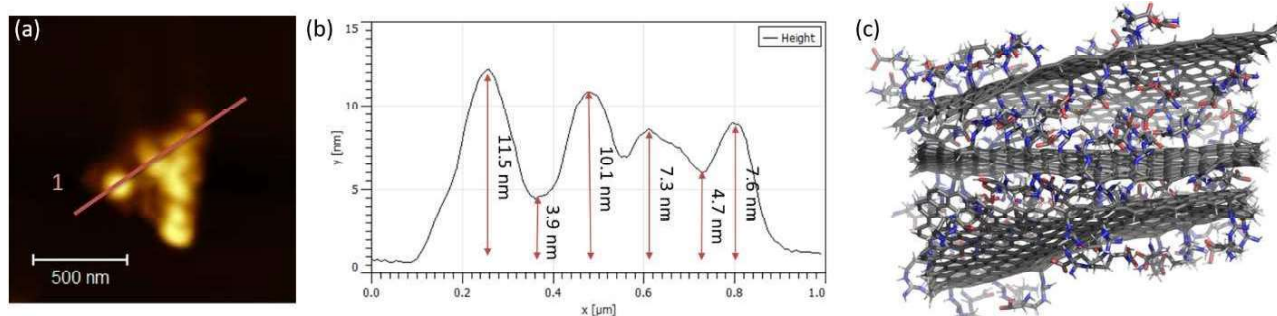


**Figure 6.** (a) AFM image of a representative flake and (b) corresponding height profile in direction 1. (c) Snapshot from MD simulations showing double-sided functionalized FG with Arg (solvent is not shown for clarity).

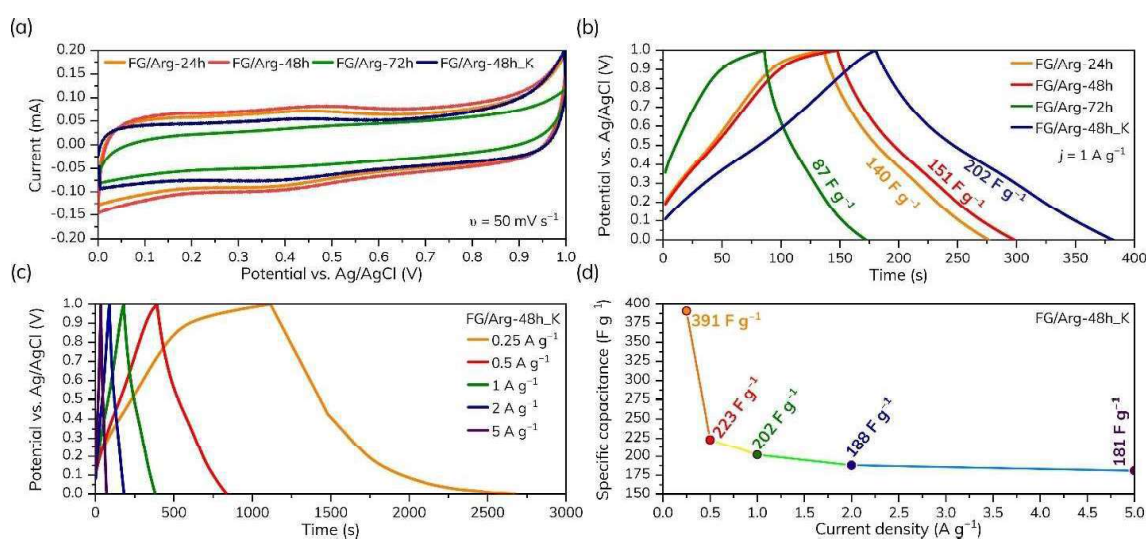


**Figure 7.** (a) CVs of graphene derivatives modified with Arg prepared using different reaction times. (b) GCD profiles of the prepared materials. (c) GCD profiles of FG/Arg-48 h\_K recorded at current densities ranging from 0.25 to  $5 \text{ A g}^{-1}$ . (d) Corresponding specific capacitance vs. current density profile.

electrode material) and electron paramagnetic resonance (EPR; ohmic conduction across the capacitor via the electrolyte), as explained by Boonpakdee et al.,<sup>[34]</sup> while the redox response of the system reflects the presence of oxygen-containing groups<sup>[35,36]</sup> as proved by the XPS and FTIR analysis. The CV results showed that the highest current response was obtained with the sample prepared for 48 h of synthesis. Such current enhancement is connected with a higher FD because the presence of amino groups from Arg can significantly improve the electrochemical performance, especially the conductivity.<sup>[37,38]</sup> To enhance the capacitance performance of the FG/Arg-48 h sample, we prepared a sample with increased SSA and a microporous structure using potassium carbonate, as described in the previous section. As expected, such surface size enhancement decreased the FD (from 3.7 to 3.5) and affected the current response of the FG/Arg-48 h\_K sample. However, a high SSA together with the high level of surface functionalization are still able to improve the capacitive performance of FG/Arg-48 h\_K sample as obvious from galvanostatic charge/discharge (GCD) records (Figure 7b). Figure 7c shows GCD profiles of the “activated” sample recorded at current densities ranging from 0.25 to 5 A g<sup>-1</sup>. The corresponding specific capacitance versus current density profile (Figure 7d) revealed the highest value of specific capacitance at 0.25 A g<sup>-1</sup> (391 F g<sup>-1</sup>). In the FG/Arg-48 h\_K sample, the pore size was around 1.5 nm. Such a pore size enables sulfate ions to interact with the surface and pores of the FG/Arg-48 h\_K sample, especially at a low current density, resulting in high capacitance.

Nyquist and Bode representations of impedance spectroscopy were used to provide further insights into the performance of the tested samples (Figure 8a,b). The absence of a semicircle in the high-frequency region of the Nyquist plot (Figure 8a) indicated the low resistivity of all the tested materials, in agreement with the enhanced conductivity described above. This was accompanied by a low value of ESR, particularly for the FG/Arg-48 h\_K sample, as shown in Figure 8a. The slope of the impedance curve of 45° corresponded

to diffusion-controlled Warburg impedance and reflected the frequency dependence of ion diffusion in the electrolyte to the electrode surface.<sup>[39,40]</sup> It is important to note that the impedance response showed a significantly shortened path for materials prepared at 24–48 h than at 72 h, indicating efficient ion transfer to the electrode surface. Further, the vertical line visible at low frequencies in the Nyquist plot indicated the capacitive behavior of the tested material. The FG/Arg-48 h\_K sample showed a more vertical curve to the y-axis compared to the other samples, indicating that its behavior was close to that of an ideal capacitor (Figure 8a). Bode analysis in the mHz region revealed that the phase angle was -85° for the FG/Arg-48 h\_K sample, as shown in Figure 8b, which is close to the value of -90° indicative of an ideal capacitor.<sup>[41]</sup> The shape of the curves in both impedance representations suggested interaction of ions at high-energy carbon sites (e.g., defects or functional groups) as well as diffusion of adsorbed electroactive species over the pore walls.<sup>[42]</sup>

A symmetric supercapacitor with 1 M H<sub>2</sub>SO<sub>4</sub> as supporting electrolyte was assembled to evaluate the performance of the arginine-based graphene derivative (the cell assembly is shown in the inset of Figure 9c). Figure 9a,b shows the GCD response of FG/Arg-48 h\_K in a two-electrode setup for current densities from 0.1 to 5 A g<sup>-1</sup>. It can be seen that the shape of the GCD curves became more symmetrical, suggesting enhanced diffusion of the ions inside the electrochemical system. Such an observation was also reflected by the perfectly stable capacitive response across the wide range of current densities. Figure 9c shows the extraordinary life-time stability of FG/Arg-48 h\_K, that is, capacitance retention of 82.3% after 30000 GCD cycles. The results from both the three- and two-electrode systems confirmed that FG modified with Arg may be an excellent candidate for supercapacitor applications.

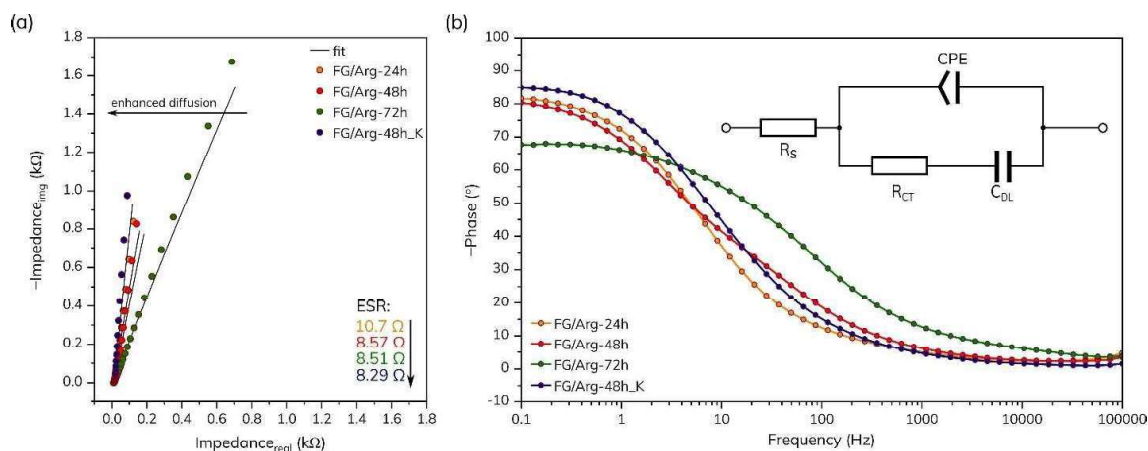


**Figure 8.** (a) Nyquist plots of graphene derivatives modified with Arg prepared using different reaction times. (b) Bode representation of impedance data of all the derivatives; the inset shows the electrical circuit used for data fitting.



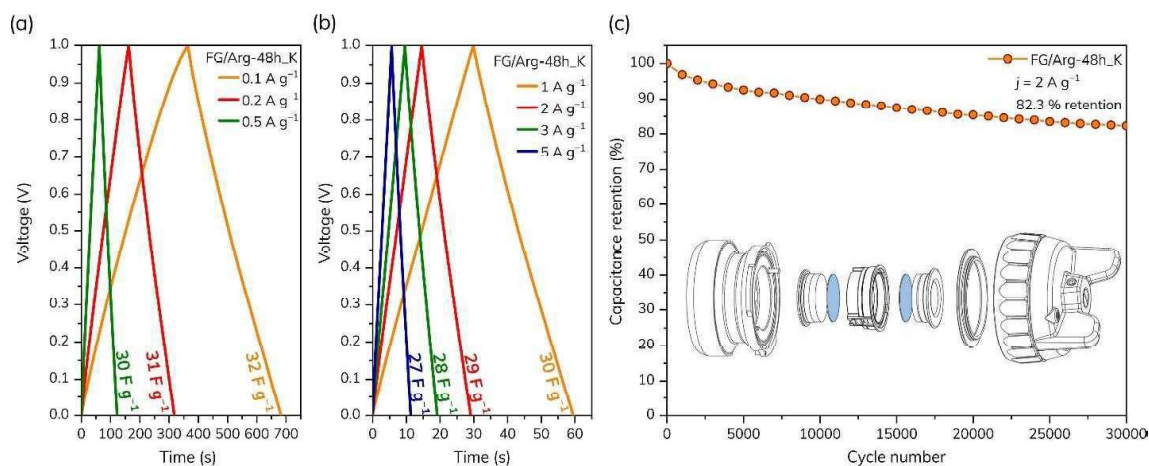


**Figure 9.** GCD profiles of FG/Arg-48 h\_K recorded at current densities ranging from (a) 0.1–0.5 A g<sup>-1</sup> and (b) 1–5 A g<sup>-1</sup>. (c) Capacitance retention of FG/Arg-48 h\_K after 30000 GCD cycles.

## Conclusions

We report the successful covalent grafting of arginine onto a graphene surface by reaction of Boc-protected arginine with fluorographene. Arginine was grafted via its guanidine group homogeneously on both sides of graphene with around 3.7% maximum functionalization degree. This method of arginine grafting leaves both the C and N amino acid termini freely available for further chemical derivatization and introduces hydrophilic and zwitterionic groups onto a conductive graphene surface. Optimization of the composition, functionalization degree, and conductivity of the material was accomplished by monitoring the impact on capacitance performance. The best-performing sample was treated in situ with potassium carbonate, creating hierarchical micro/mesoporosity and tripling the specific surface area. This had a direct effect of boosting the capacitive performance ( $\approx 390 \text{ F g}^{-1}$  at a current density of  $0.25 \text{ A g}^{-1}$ ) because microporosity affords numerous sites for electrolyte ions adsorption, whereas mesoporosity offers ion diffusion paths and facilitates charge propagation. The principal advantage of this material was demonstrated by the durability of the assembled supercapacitor. After numerous ( $\approx 30000$ ) charging/discharging cycles under typical operation conditions, the capacitance retention was around 82.3%. Therefore, as well as being eco-friendly, the material exhibited outstanding sustainability with promising properties for supercapacitor materials. Moreover, adopting the strategy of successful covalent grafting of small molecules on the surface of graphene lays the ground for the development of similar energy storage systems with significantly improved electrochemical performance in terms of capacitance, as well as lifetime stability of these derivatives in both aqueous and organic electrolytes.

## Experimental Section

### Reagents and materials

Graphite fluoride (GrF) (C/F 1:1.1), a Kaiser test kit, and Boc-Arg-OH (Boc) were purchased from Sigma-Aldrich. Acetone (pure), ethanol (absolute), *N,N*-dimethylformamide (DMF), and potassium carbonate were purchased from Penta. Hydrochloric acid (35%) and sulfuric acid (96%) were bought from Lachner. All reagents were used as received without further purification. All stock solutions were prepared with ultrapure water ( $18 \text{ M}\Omega \text{ cm}^{-1}$ ). The Kaiser test protocol is described in the work of Kaiser et al.<sup>[43]</sup> and recently by Soriano and Cárdenas.<sup>[44]</sup>

### Synthesis of Boc- and Arg-functionalized FG

First, 200 mg of GrF was dispersed in 10 mL of DMF and subjected to ultrasonication for 10 min (Bandelin Sonoplus, type UW 3200, probe VS70T). The flask containing the dispersion was then sonicated in a sonication bath for 2.5 h (Bandelin Sonorex, DT255H type, frequency 35 kHz, power 640 W, effective power 160 W). Next, 1.76 g of Boc-Arg-OH was added to the flask and the mixture was sonicated for a further 1 h. Afterwards, the reagents were heated under stirring at 125 °C for  $x=24, 48,$  or 72 h. The black product was separated by centrifugation and was purified by repeated centrifugal washings with DMF, water, and ethanol. The purified product (FG/Boc-*x*h) was transferred to a flask to which were added 20 mL hydrochloric acid ( $\approx 5.7 \text{ M}$ ) and around 3.75 mL acetone. The mixture was heated under stirring at 100 °C for 1 h to remove the Boc protecting group. Finally, the black product was isolated by centrifugation and purified by successive centrifugal washings with water, acetone, and ethanol. The purified product was labeled FG/Arg-*x*h.

### Synthesis of Boc- and Arg-functionalized FG in the presence of potassium carbonate

First, 200 mg of GrF was dispersed in 10 mL of DMF and then subjected to ultrasonication for 10 min (Bandelin Sonoplus, type UW 3200, probe VS70T). The flask containing the dispersion was subsequently sonicated in a sonication bath for 2.5 h (Bandelin Sonorex, DT255H type, frequency 35 kHz, power 640 W, effective power 160 W). Next, 1.76 g of Boc-Arg-OH was added to the flask

and the mixture was sonicated for a further 1 h. Afterwards, 0.44 g of potassium carbonate in 2 mL of water was added and the mixture was sonicated for a further 15 min. Subsequently, the reagents were heated under stirring at 125 °C for 48 h. The black product was separated by centrifugation and was purified by repeated centrifugal washings with DMF, water, and ethanol. The purified product (FG/Boc-48 h\_K) was then transferred to a flask to which were added 20 mL hydrochloric acid ( $\approx 5.7$  M) and around 3.75 mL acetone. The mixture was heated under stirring at 100 °C for 1 h to remove the Boc protecting group. Finally, the black product was isolated by centrifugation and was purified by successive centrifugal washings with water, acetone, and ethanol. The purified product was labeled FG/Arg-48 h\_K.

### Characterization techniques

FTIR spectra were recorded on an iS5 FTIR spectrometer (Thermo Nicolet) using the Smart Orbit ZnSe ATR accessory. Briefly, a droplet of an ethanolic dispersion of the test material was placed on a ZnSe crystal and left to dry to form a film. Spectra were acquired by summing 100 scans obtained using N<sub>2</sub> gas flow through the ATR accessory. ATR and baseline correction were applied to the collected spectra.

UV/Vis absorption spectra were collected on a SPECORD S600 UV-vis spectrophotometer (Analytikjena) over the range 230–900 nm. During the Kaiser test, around 5 mg of the FG/Arg-48 h sample was placed in a test tube and then three solutions were added in the following order: (A) 75  $\mu$ L of solution I (I: 10 g phenol dissolved in 20 mL ethanol), (B) 100  $\mu$ L of solution II (II: 2 mL of an aqueous solution of 1 mM KCN dissolved in 98 mL of pyridine), and (C) 75  $\mu$ L of solution III (III: 1.0 g of ninhydrine dissolved in 20 mL of ethanol). The test tube was incubated in a heating oil bath at 100 °C for 7 min and then removed. Next, 4.8 mL of ethanol was added to reach a final volume of 5 mL. A deep blue supernatant appeared and was separated by centrifugation and then transferred to a UV/Vis cuvette (100-QS, Suprasil, 10 mm purchased from Fischer Scientific). Finally, the UV/Vis absorption spectrum was recorded. An intense peak centered at around 583 nm was detected, verifying the presence of a primary amine group in the sample FG/Arg-48 h. For comparison, a reference Kaiser test was performed in the absence of FG/Arg-48 h, which generated a colorless solution. Further Kaiser test was performed in presence of FG/Boc-48 h ( $\approx 4$  mg) where the supernatant was also colorless (Figure S1).

XPS was employed with a PHI VersaProbe II (Physical Electronics) spectrometer using an AlK $\alpha$  source (15 kV, 50 W). Samples were deposited onto a silicon holder as an ethanol-based slurry, which was left to dry prior to measurement. The obtained data were evaluated and deconvoluted with the MultiPak (Ulvac - PHI, Inc.) software package. Spectral analysis included a Shirley background subtraction and peak deconvolution employing mixed Gaussian–Lorentzian functions.

Water droplet contact angle measurements were performed in a drop shape analyzer (DSA30S, Krüss, GmbH).

Raman spectra were collected using a DXR Raman spectroscope (Thermo Scientific) equipped with a laser operating at wavelength of 633 nm.

Zeta-potential ( $\zeta$ p) measurements were performed with a Malvern ZetaSizer Nano instrument on aqueous dispersions of around 0.03 mg mL<sup>-1</sup>.

Thermal decomposition of the samples was investigated using TGA and DTG (SDT 650, TA Instruments, USA) with a sample mass of 5–10 mg. All measurements were carried out in a N<sub>2</sub> atmosphere with

a flow rate of 100 mL min<sup>-1</sup>. The heating rate was set at 5 °C min<sup>-1</sup>, starting from 40 up to 1000 °C.

Surface area and pore size analyses were performed by N<sub>2</sub> adsorption/desorption measurements at –196 °C on a volumetric gas adsorption analyzer (3Flex, Micromeritics, USA) up to 0.965 p/p<sup>0</sup>. Prior to the analysis, the sample was degassed under high vacuum (10<sup>-4</sup> Pa) at 130 °C for 12 h, whereas high-purity (99.999%) N<sub>2</sub> and He gases were used for the measurements. The BET surface area was determined with respect to Rouquerol criteria<sup>[45]</sup> for the N<sub>2</sub> isotherm. The pore size distribution was analyzed by the N2-NLDFT 77-carbon slit pore kernel.

The samples were analyzed by SEM using a Hitachi SU6600 instrument (Hitachi, Japan) with an accelerating voltage of 5 kV. For these analyses, a drop of a dispersion of the material in ethanol was placed on a copper grid with a carbon film and dried at room temperature.

TEM images in the Supporting Information were obtained with a JEOL JEM 2100 instrument at an accelerating voltage of 200 kV. The samples were dispersed in ethanol and sonicated for 5 min. A drop of the dispersion was placed on a copper grid with a holey carbon film and dried at room temperature. STEM-HAADF (high-angle annular dark-field imaging) analyses for elemental mapping of the products was performed with a FEI Titan HRTEM microscope operated at 80 kV. Figure 5a was also obtained with FEI Titan HRTEM. For these analyses, a droplet of a dispersion of the material in ethanol with concentration of around 0.1 mg mL<sup>-1</sup> was deposited onto a carbon-coated copper grid and dried.

AFM images were obtained in the amplitude-modulated semi-contact mode on an NT-MDT NTegra system equipped with a VIT–P AFM probe and using freshly cleaved muscovite mica as a substrate.

### Electrochemical measurements

Three-electrode measurements were performed using a Metrohm Autolab PGSTAT128 N instrument (Metrohm Autolab B.V., Netherlands) equipped with NOVA software (version 1.11.2). Sulfuric acid with concentration  $c=1$  M was used as a supporting electrolyte. Electrochemical impedance spectroscopy (EIS) was carried out by applying an AC voltage with 5 mV amplitude and frequency range of 0.01 Hz to 100 kHz at open-circuit potential (OCP). A modified Randles circuit was used for fitting all the obtained data.

A three-electrode system was used to obtain initial information about the electrochemical behavior of the studied sample. A platinum wire electrode was used as the auxiliary electrode, whereas a Ag/AgCl electrode was used as the reference electrode. A modified glassy carbon electrode (GCE) served as the working electrode. A well homogenized dispersion of the sample in deionized water ( $c\approx 2$  mg mL<sup>-1</sup>) was prepared, and then 10  $\mu$ L of the dispersion was drop-cast onto the surface of the GCE and left to dry at room temperature. A thin film of the sample was formed on the electrode. According to this procedure, small deviations in mass at such low concentrations and volumes can result into different masses deposited on the GCE. Furthermore, the GCE surface is fully exposed to the electrolyte and therefore possible mass losses to the electrolyte cannot be estimated. For this reason the y-axis in Figure 7a is not normalized as specific current (mA g<sup>-1</sup>), but only current is reported. The CV curves were used in order to gain better understanding of the operation mechanism, such as the presence of the redox peaks, which are not visible in the GCD curves.

Two-electrode measurements were carried out using a BCS-810 battery tester (BioLogic Company, Seyssinet-Pariset, France) driven by BT-Lab software (version 1.65). A well homogenized dispersion (concentration 5 mg mL<sup>-1</sup>) of the sample in DI water was drop-cast onto a gold electrode (diameter 18 mm) to achieve at least 1.8 mg cm<sup>-2</sup> loading, then dried under an IR-lamp, followed by additional water removal in a desiccator for 2 h. Two electrodes with nearly identical loadings of the material were used to assemble a symmetrical electrochemical cell (EI-CELL GmbH, Germany) using a Whatman glass microfiber membrane (thickness 0.26 mm) as separator and 100 µL of 1 M sulfuric acid as electrolyte.

The specific capacitance  $C_s$  was calculated from GCD profiles using the following Equation (1):

$$C_s \text{ [F g}^{-1}\text{]} = \frac{I \times \Delta t}{m \times \Delta V} \quad (1)$$

where  $I$  is the applied current [A],  $\Delta t$  is the discharge time [s],  $m$  is the mass of total electrode material [g] (on both electrodes in a two-electrode system), and  $\Delta V$  is the potential window [V].

### Theoretical calculations

MD simulations were carried out in Gromacs 5.0 software<sup>[46]</sup> using the Amber99 force field.<sup>[47]</sup> Aromatic carbons in the graphene layer were modeled as uncharged LJ spheres using the modified Cheng and Steele parameters for graphitic carbons.<sup>[48]</sup> The dimensions of graphene were assumed to be approximately 4×4 nm with a functionalization degree of 3.5%. In the initial geometry, three sheets of FG/Arg were placed in the middle of a square box ( $a = 7.5$  nm) and solvated with TIP4P water.<sup>[49]</sup> Periodic boundary conditions were applied in all directions. First, the system was minimized and thermalized at 300 K under the NpT ensemble. This was followed by a 30 ns production run under the NVT ensemble. The Lennard–Jones (LJ) potential was used for atomic interactions. Long-range electrostatic interactions were treated by the particle-mesh Ewald (PME) technique. Cut-off distances for LJ interactions and the real space term of the PME were set to 1 nm. Temperature and pressure were maintained using the V-rescale thermostat<sup>[50]</sup> and Berendsen barostat with isotropic scaling (1 bar),<sup>[51]</sup> respectively. Hydrogen atoms were constrained by the LINCS algorithm.<sup>[52]</sup> The Newtonian equations of motion were integrated with a 2 fs time step.

### Acknowledgements

We acknowledge financial support from the ERDF/ESF project "Nano4Future" of the Ministry of Education, Youth, and Sports of the Czech Republic (CZ.02.1.01/0.0/0.0/16\_019/0000754) and an ERC project (683024) as part of the H2020 program. V.Š. thanks the Internal Student Grant Agency of Palacký University in Olomouc, Czech Republic (IGA\_PrF\_2021\_031). R.Z. and A.B. acknowledge funding from the Czech Science Foundation, project GA CR – EXPRO, 19-27454X. The authors also acknowledge partial support provided by the Research Infrastructure NanoEnvicZ project funded by the Ministry of Education, Youth and Sports of the Czech Republic (No. LM2018124). We thank Mgr. Jana Stráská, Dr. Eirini Ioannou, Dr. Martin Petr, and Dr. Zuzana Chaloupková for TEM, SEM, XPS, and Raman measurements.

### Conflict of Interest

The authors declare no conflict of interest.

**Keywords:** arginine · fluorographene · graphene · supercapacitor · ultracapacitor

- [1] G. Luderer, M. Pehl, A. Arvesen, T. Gibon, B. L. Bodirsky, H. S. de Boer, O. Fricko, M. Hejazi, F. Humpenöder, G. Iyer, S. Mima, I. Mouratiadou, R. C. Pietzcker, A. Popp, M. van den Berg, D. van Vuuren, E. G. Hertwich, *Nat. Commun.* **2019**, *10*, 5229.
- [2] Y. Luo, C. Yang, Y. Tian, Y. Tang, X. Yin, W. Que, *J. Power Sources* **2020**, *450*, 227694.
- [3] M. Sethi, U. S. Shenoy, D. K. Bhat, *J. Alloys Compd.* **2021**, *854*, 157190.
- [4] J. Acharya, T. H. Ko, M.-K. Seo, M.-S. Khil, H.-Y. Kim, B.-S. Kim, *ACS Appl. Mater. Interfaces* **2020**, *3*, 7383.
- [5] J. Han, Y. Ping, S. Yang, Y. Zhang, L. Qian, J. Li, L. Liu, B. Xiong, P. Fang, C. He, *Diamond Relat. Mater.* **2020**, *109*, 108044.
- [6] N. Kamboj, T. Purkait, M. Das, S. Sarkar, K. S. Hazra, R. S. Dey, *Energy Environ. Sci.* **2019**, *12*, 2507.
- [7] C. Liu, Z. Yu, D. Neff, A. Zhamu, B. Z. Jang, *Nano Lett.* **2010**, *10*, 4863.
- [8] A. K. Geim, K. S. Novoselov, *Nat. Mater.* **2007**, *6*, 183.
- [9] J.-U. Lee, D. Yoon, H. Cheong, *Nano Lett.* **2012**, *12*, 4444.
- [10] A. Emadi, B. Honarvar, M. Emadi, M. Nafar, *Russ. J. Appl. Chem.* **2020**, *93*, 1160.
- [11] L. Hou, C. Kong, Z. Hu, Y. Yang, H. Wu, Z. Li, X. Wang, P. Yan, X. Feng, *Appl. Surf. Sci.* **2020**, *508*, 145192.
- [12] D. M. El-Gendy, N. A. A. Ghany, E. E. F. El Sherbini, N. K. Allam, *Sci. Rep.* **2017**, *7*, 43104.
- [13] L. Deng, C. Zhou, Z. Ma, G. Fan, *J. Colloid Interface Sci.* **2020**, *561*, 416.
- [14] X. Zhou, T. Meng, F. Yi, D. Shu, D. Han, Z. Zhu, A. Gao, C. Liu, X. Li, K. Yang, H. Yi, *J. Power Sources* **2020**, *475*, 228554.
- [15] Q. Wang, H. Gao, C. Zhao, H. Yue, G. Gao, J. Yu, Y.-U. Kwon, Y. Zhao, *Electrochim. Acta* **2021**, *369*, 137700.
- [16] Y. Yang, W. Ma, H. Zhu, H. Meng, C. Wang, F. Ma, Z. Hu, *New J. Chem.* **2020**, *44*, 16821.
- [17] A. B. Bourlino, A. Bakandritsos, N. Liaros, S. Couris, K. Safarova, M. Otyepka, R. Zbořil, *Chem. Phys. Lett.* **2012**, *543*, 101.
- [18] A. B. Bourlino, K. Safarova, K. Siskova, R. Zbořil, *Carbon* **2012**, *50*, 1425.
- [19] K. E. Whitener, R. Stine, J. T. Robinson, P. E. Sheehan, *J. Phys. Chem. C* **2015**, *119*, 10507.
- [20] M. Medved, G. Zoppellaro, J. Ugoletti, D. Matochová, P. Lazar, T. Pospíšil, A. Bakandritsos, J. Tuček, R. Zbořil, M. Otyepka, *Nanoscale* **2018**, *10*, 4696.
- [21] D. Matochová, M. Medved, A. Bakandritsos, T. Steklý, R. Zbořil, M. Otyepka, *J. Phys. Chem. Lett.* **2018**, *9*, 3580.
- [22] A. Bakandritsos, D. D. Chronopoulos, P. Jakubec, M. Pykal, K. Čépe, T. Steriotis, S. Kalytchuk, M. Petr, R. Zbořil, M. Otyepka, *Adv. Funct. Mater.* **2018**, *28*, 1801111.
- [23] E. C. Vermisoglou, P. Jakubec, A. Bakandritsos, M. Pykal, S. Talande, V. Kupka, R. Zbořil, M. Otyepka, *Chem. Mater.* **2019**, *31*, 4698.
- [24] K. Hou, P. Gong, J. Wang, Z. Yang, Z. Wang, S. Yang, *RSC Adv.* **2014**, *4*, 56543.
- [25] A. R. Rafieerad, A. R. Bushroa, A. Amiri, K. Kalaiselvam, K. Vellamy, J. Vadivelu, *J. Hazard. Mater.* **2018**, *360*, 132.
- [26] D. Chen, Q. Chen, T. Liu, J. Kang, R. Xu, Y. Cao, M. Xiang, *RSC Adv.* **2019**, *9*, 20149.
- [27] C. J. Pandian, R. Palanivel, *J. Exp. Nanosci.* **2016**, *11*, 1193.
- [28] K. Manzoor, M. Ahmad, S. Ahmad, S. Ikram, *RSC Adv.* **2019**, *9*, 7890.
- [29] X. Li, G. Jiang, X. Shen, G. Li, *ACS Sustainable Chem. Eng.* **2020**, *8*, 1899.
- [30] T. Nakajima, V. Gupta, Y. Ohzawa, H. Groult, Z. Mazej, B. Žemva, *J. Power Sources* **2004**, *137*, 80.
- [31] J. Zhu, H. Zhang, R. Chen, Q. Liu, J. Liu, J. Yu, R. Li, M. Zhang, J. Wang, *J. Colloid Interface Sci.* **2019**, *543*, 192.
- [32] M. Zhang, Y. Ma, Y. Zhu, J. Che, Y. Xiao, *Carbon* **2013**, *63*, 149.
- [33] A. Bakandritsos, M. Pykal, P. Błoński, P. Jakubec, D. D. Chronopoulos, K. Poláková, V. Georgakilas, K. Čépe, O. Tomanec, V. Ranc, A. B. Bourlino, R. Zbořil, M. Otyepka, *ACS Nano* **2017**, *11*, 2982.
- [34] D. Boonpakdee, C. F. Guajardo Yévenes, W. Surareungchai, C. La-orakiat, *J. Mater. Chem. A* **2018**, *6*, 7162.



- [35] Y. J. Oh, J. J. Yoo, Y. I. Kim, J. K. Yoon, H. N. Yoon, J.-H. Kim, S. B. Park, *Electrochim. Acta* **2014**, *116*, 118.
- [36] Y.-H. Lee, K.-H. Chang, C.-C. Hu, *J. Power Sources* **2013**, *227*, 300.
- [37] M. Yu, Z. Wang, H. Zhang, P. Zhang, T. Zhang, X. Lu, X. Feng, *Nano Energy* **2019**, *65*, 103987.
- [38] M. Yang, Z. Zhou, *Adv. Sci.* **2017**, *10*.
- [39] L. Zhang, G. Shi, *J. Phys. Chem. C* **2011**, *115*, 17206.
- [40] Y. Wang, Z. Shi, Y. Huang, Y. Ma, C. Wang, M. Chen, Y. Chen, *J. Phys. Chem. C* **2009**, *113*, 13103.
- [41] J. Zhang, X. S. Zhao, *ChemSusChem* **2012**, *5*, 818.
- [42] A. Eftekhari, *ACS Sustainable Chem. Eng.* **2019**, *7*, 3692.
- [43] E. Kaiser, R. L. Colescott, C. D. Bossinger, P. I. Cook, *Anal. Biochem.* **1970**, *34*, 595.
- [44] M. L. Soriano, S. Cárdenas, *J. Carbon Res.* **2019**, *5*, 68.
- [45] J. Rouquerol, F. Rouquerol, P. Llewellyn, G. Maurin, K. S. W. Sing, *Adsorption by Powders and Porous Solids: Principles, Methodology and Applications*, Elsevier Science, **2013**.
- [46] D. Van Der Spoel, E. Lindahl, B. Hess, G. Groenhof, A. E. Mark, H. J. C. Berendsen, *J. Comput. Chem.* **2005**, *26*, 1701.
- [47] W. D. Cornell, P. Cieplak, C. I. Bayly, I. R. Gould, K. M. Merz, D. M. Ferguson, D. C. Spellmeyer, T. Fox, J. W. Caldwell, P. A. Kollman, *J. Am. Chem. Soc.* **1995**, *117*, 5179.
- [48] A. Cheng, W. A. Steele, *J. Chem. Phys.* **1990**, *92*, 3858.
- [49] W. L. Jorgensen, J. Chandrasekhar, J. D. Madura, R. W. Impey, M. L. Klein, *J. Chem. Phys.* **1983**, *79*, 926.
- [50] G. Bussi, D. Donadio, M. Parrinello, *J. Chem. Phys.* **2007**, *126*, 014101.
- [51] H. J. C. Berendsen, J. P. M. Postma, W. F. van Gunsteren, A. DiNola, J. R. Haak, *J. Chem. Phys.* **1984**, *81*, 3684.
- [52] B. Hess, H. Bekker, H. J. C. Berendsen, *J. Comput. Chem.* **1997**, *18*, 1463.

---

Manuscript received: May 18, 2021  
Revised manuscript received: June 18, 2021  
Accepted manuscript online: July 20, 2021  
Version of record online: August 18, 2021

Article

# New Limits for Stability of Supercapacitor Electrode Material Based on Graphene Derivative

Veronika Šedajová<sup>1,2,†</sup>, Petr Jakubec<sup>1,\*,†</sup>, Aristides Bakandritsos<sup>1</sup> , Václav Ranc<sup>1</sup>   
and Michal Otyepka<sup>1,2,\*</sup>

<sup>1</sup> Regional Centre of Advanced Technologies and Materials, Faculty of Science, Palacký University, Šlechtitelů 27, 78371 Olomouc, Czech Republic; veronika.sedajova@upol.cz (V.Š.); a.bakandritsos@upol.cz (A.B.); vaclav.ranc@upol.cz (V.R.)

<sup>2</sup> Department of Physical Chemistry, Faculty of Science, Palacký University, 17. Listopadu 1192/12, 77900 Olomouc, Czech Republic

\* Correspondence: p.jakubec@upol.cz (P.J.); michal.otyepka@upol.cz (M.O.); Tel.: +420-585-634-474 (P.J. & M.O.)

† These authors contributed equally to this work.

Received: 29 July 2020; Accepted: 28 August 2020; Published: 31 August 2020



**Abstract:** Supercapacitors offer a promising alternative to batteries, especially due to their excellent power density and fast charging rate capability. However, the cycling stability and material synthesis reproducibility need to be significantly improved to enhance the reliability and durability of supercapacitors in practical applications. Graphene acid (GA) is a conductive graphene derivative dispersible in water that can be prepared on a large scale from fluorographene. Here, we report a synthesis protocol with high reproducibility for preparing GA. The charging/discharging rate stability and cycling stability of GA were tested in a two-electrode cell with a sulfuric acid electrolyte. The rate stability test revealed that GA could be repeatedly measured at current densities ranging from 1 to 20 A g<sup>-1</sup> without any capacitance loss. The cycling stability experiment showed that even after 60,000 cycles, the material kept 95.3% of its specific capacitance at a high current density of 3 A g<sup>-1</sup>. The findings suggested that covalent graphene derivatives are lightweight electrode materials suitable for developing supercapacitors with extremely high durability.

**Keywords:** graphene acid; supercapacitor; pseudocapacitance; cycling stability

## 1. Introduction

There is tremendous interest in developing different kinds of power supplies owing to the escalating consumption of energy and the need for (mobile) energy storage [1]. Energy devices with high power and energy densities are increasingly important in fields such as industry, the automotive sector and energy supplies, e.g., for portable and medical devices [2]. Supercapacitors (also known as ultracapacitors) offer a higher power density than batteries and a higher energy density than conventional capacitors [3]. These attributes, together with high stability and rather low costs, make them suitable candidates for energy storage devices. Based on their charge storage mechanism, they can be divided into two main classes: electrochemical double-layer capacitors (EDLCs), where the main contribution to the overall capacitance comes from the charge accumulated at the electrode/electrolyte interface [4], and pseudocapacitors, where the charge storage mechanism is driven by fast and reversible faradaic (redox) reactions [5]. Pseudocapacitive materials with a typical faradaic response are able to store more energy (per mole of material) than EDLCs since redox processes occur both at the surface and in the interior of the electrodes. The capacitance of pseudocapacitors can be up to 100 times higher than that of EDLCs [6]. Since the intrinsic properties of redox-active

materials can significantly influence both capacitance and rate performance, the selection of a suitable material is of paramount importance.

Common materials that undergo faradaic responses include conventional transition metal oxides, such as  $\text{RuO}_2$  [7,8],  $\text{MnO}_2$  [9–12] and  $\text{Co}_3\text{O}_4$  [13,14] and various conducting polymers [15–18]. However, these compounds often fail to meet the necessary criteria for practical applications, such as low costs and stability during life cycling [19]. By contrast, carbon-based materials offer the advantages of reasonable prices and a suitable capacitive response. Moreover, the surface of carbon derivatives can be easily modified by different functional groups [20,21]. Such modifications can boost the electrochemical stability as well as capacitive performance. For example, porous carbon has been modified with nitrogen- [22–24], oxygen- [25–27] and phosphorus-containing functional groups [28,29]. As oxygen-containing groups often occur in carbon materials [30], their use may offer a promising strategy for improving the capacitive performance. The insertion of oxygen-containing groups can have positive effects on a material's wettability and pseudocapacitive behavior. In particular, the wettability of the material by an electrolyte increases, and the pore volume becomes more accessible to electrolytes. Therefore, the electrostatic interactions between the electrode and electrolyte ions spread over a larger surface, enhancing the capacitance [21]. Oxygen-containing functionalities may also be involved in fast redox reactions, which can enhance the overall capacitance by the pseudocapacitance contribution [31]. However, it should be noted that some disadvantages counteract the benefits of introducing oxygen-containing groups. The most commonly occurring shortcomings include potential organic electrolyte decomposition, high self-discharge rates, increased leakage current and decreased conductivity [32].

Attention has been paid to optimizing carbon-based materials and improving their lifetime stability. For instance, Cao et al. studied graphene derivatives prepared at different temperatures containing different amounts of oxygen-containing functional groups. The best sample displayed a life cycle stability of 10,000 cycles, with capacitance retention of 98% [33]. Cherusseri et al. showed that oxygen-containing functional groups in hierarchically mesoporous carbon nanopetal based electrodes significantly improved their lifetime stability, reaching 28,900 cycles [34]. Chen et al. investigated the influence of oxygen-containing groups on the supercapacitive performance of nitrogen-doped graphene. Their derivatives exhibited good lifetime stability over 5000 cycles, with capacitive retention of 86.36% and 91.14% [35]. The importance of oxygen-containing functional groups was also shown for graphene modified with triethanolamine by Song et al. The lifetime cyclic stability reached 10,000 cycles, with capacitance retention of 91.7% [36]. However, since supercapacitor devices need to withstand a huge number of charge/discharge cycles, there is scope for further improvements.

In the present study, we investigated the pseudocapacitive behavior of graphene acid (GA) [37] as a potential supercapacitor electrode material with a particular focus on synthesis reproducibility, i.e., batch-to-batch variability and life cycle stability. GA is a conductive, hydrophilic graphene derivative that is well-endowed with oxygen-containing carboxyl groups homogeneously distributed over the graphene surface [37]. GA can be used as a promising material in electrochemical sensing [38], catalysis [39–41] and electrocatalysis [42]. Its properties as an electrode supercapacitor material were tested in a neutral salt environment together with cyanographene [38]. Here, we provide a significantly more interesting look at a pseudocapacitive behavior of GA obtained in  $1 \text{ mol L}^{-1}$  sulfuric acid. A comparison of the properties of three independent GA batches showed the high reproducibility of its synthesis. We also demonstrated that it had very large specific capacitance retention after 60,000 cycles (95.3%) recorded at a high current density of  $3 \text{ A g}^{-1}$  in a two-electrode cell, suggesting that electrodes based on GA may offer outstanding rate stability. These findings place covalent graphene derivatives bearing oxygen-containing functional groups at the forefront for achieving high-durability eco-friendly electrode materials (without the presence of any heavy-metal elements) that can be used in supercapacitors.

## 2. Materials and Methods

### 2.1. Reagents and Materials

Graphite fluoride (>61 wt % F), sodium cyanide (p.a.  $\geq 97\%$ ), *N,N*-dimethylformamide ( $\geq 98\%$ ), sodium sulfate (p.a.  $\geq 99\%$ ) and potassium hydroxide (BioXtra  $\geq 85\%$ ) were purchased from Sigma-Aldrich (St. Louis, MO, USA). Nitric acid (AnalaPure 65%) and sulfuric acid (p.a. 96%) were obtained from Lach-Ner. Acetone (pure) and ethanol (absolute) were purchased from Penta, Czech Republic. All chemicals were used as delivered without any further purification. Ultrapure water ( $18 \text{ M}\Omega \text{ cm}^{-1}$ ) was used for the preparation of all aqueous electrolyte solutions.

### 2.2. Synthesis of Graphene Acid

GA was synthesized from cyanographene similarly to a previously published method [37]. Briefly, graphite fluoride (120 mg) was dispersed in 15 mL *N,N*-dimethylformamide (DMF) and stirred for 2 days under a nitrogen atmosphere. Next, the mixture was sonicated for 4 h and then left under stirring overnight. Afterwards, 800 mg of NaCN was added, and the mixture was heated at  $130 \text{ }^\circ\text{C}$  for 72 h with a condenser and under stirring with a Teflon coated magnetic bar (400 rpm). At the end of the reaction, the reaction flask was left to cool down, and then washing steps were performed using a variety of solvents covering an extensive polarity window (DMF, acetone, ethanol, hot water, cool water and acidified water—3% solution of HCl). Materials were separated from the solvents using centrifugation (centrifuge Sigma 4-16K, Sigma Laborzentrifugen GmbH, Osterode am Harz, Germany) at 10,000 RCF. The final (pure) cyanographene was subjected to hydrolysis to obtain GA [37]. Concentrated nitric acid (65%) was added to a suspension of cyanographene in water under stirring in a ratio to obtain a 25% concentration. The mixture was heated at  $100 \text{ }^\circ\text{C}$  for 24 h with a condenser and under stirring with a Teflon coated magnetic bar (400 rpm). The final product was left to cool down, and washing steps with cold water, hot water and acidified water were performed until precipitation of the product ceased. GA was separated from the solvents using centrifugation at 20,000 RCF.

### 2.3. Characterization Techniques

X-ray diffraction (XRD) measurements were recorded using X'Pert PRO MPD diffractometer (PANalytical) in the Bragg–Brentano geometry. A Co X-ray tube (iron filtered Co  $K\alpha$  radiation with  $\lambda = 0.178901 \text{ nm}$ ), fast X'Celerator detector, and programmable divergence and diffracted beam antiscatter slits were equipped. Fourier transform infrared (FTIR) spectra were measured on an iS5 FTIR spectrometer (Thermo Scientific Nicolet) using the Smart Orbit ZnSe ATR accessory. A drop of an ethanolic dispersion of the material was placed on a ZnSe crystal and left to dry to form a film at ambient temperature. Spectra were recorded by summing 50 scans acquired while nitrogen gas flowed through the ATR accessory. Baseline correction was used on the collected spectra. Raman spectra were recorded on a DXR Raman microscope using a diode laser with a 633 nm excitation line. X-ray photoelectron spectroscopy (XPS) was performed on a PHI VersaProbe II (Physical Electronics) spectrometer using an Al  $K\alpha$  source (15 kV, 50 W). The MultiPak (ULVAC–PHI Inc., Kanagawa, Japan) software package was used for evaluation of the obtained data. High-resolution transmission electron microscopy (HRTEM) images including STEM-HAADF (scanning transmission electron microscopy-high-angle annular dark-field imaging) analyses for elemental mapping of the products were acquired with a FEI Titan HRTEM microscope using an operating voltage of 200 kV. For these analyses, a droplet of a dispersion of the material in ultrapure  $\text{H}_2\text{O}$  with a concentration of  $0.1 \text{ mg mL}^{-1}$  was deposited onto a carbon-coated copper grid and dried. Atomic force microscopy (AFM) images were obtained on an NTEGRA Spectra instrument (NT-MDT, Moscow, Russia) in tapping mode using NSG30 probes. In total,  $5 \text{ }\mu\text{L}$  of an ethanolic dispersion ( $c = 1 \text{ mg/L}$ ) of the analyzed nanomaterial was deposited on a  $\text{SiO}_2$  wafer and left to dry for 30 min, and then the sample was immediately scanned by AFM. Pore size and surface area analyses (Brunauer, Emmett and Teller; BET) were carried out using a volumetric gas adsorption analyzer (3Flex, Micromeritics, Norcross, USA) at  $-196 \text{ }^\circ\text{C}$  and up to

0.9626 bar. The sample was degassed under high vacuum conditions for 24 h at room temperature using high-purity gases (N<sub>2</sub> and He). Conductivity measurements were performed using an Ossila four-point probe system operating over a current range of ±10 nA to ±150 mA (voltage range ±100 μV to ±10 V). The parameters used for the obtained results were as follows: range max 2000 μA; 8192 points per sample; target current was set to 0.5 mA, with a maximum voltage of 1 V with 0.1 V increments; 50 repeats were measured. A fluorine-doped tin oxide (FTO) substrate (1.5 cm × 2.5 cm) was modified with the sample by drop-casting, i.e., a 150 μL drop of a powder suspension (5 g L<sup>-1</sup>) was coated onto the substrate in the center and dried using an infrared light lamp (Helago, Parchim, Germany) to form a thin film, with a diameter of 11.8 mm and a thickness of 4 μm. During the measurement, the four probes were placed carefully on top of the dried film, centered and pressed slightly in order not to touch the FTO substrate.

#### 2.4. Electrochemical Measurements

A MetrohmAutolab PGSTAT128N instrument (MetrohmAutolab B.V., Netherlands) controlled with the NOVA software package (version 1.11.2) was used for complex characterization of GA in a three-electrode setup. A BCS-810 battery tester (BioLogic Company, Seyssinet-Pariset, France) controlled with BT-Lab software (version 1.63) was used for two-electrode cell experiments. Sulfuric acid (*c* = 1 mol L<sup>-1</sup>) was used as a supporting electrolyte unless otherwise stated. All experiments were carried out at room temperature (22 ± 2 °C).

The three-electrode system consisted of a glassy carbon electrode (GCE) serving as the working electrode, a platinum wire electrode as a counter electrode and an Ag/AgCl (3 M KCl) electrode as a reference electrode. Electrochemical impedance spectroscopy (EIS) spectra were recorded using a 5 mV amplitude. All EIS spectra were recorded over the frequency range of 0.1 Hz to 10 kHz at open circuit potential (OCP). The GCE was modified as follows: a 10 μL drop of a powder suspension (2 mg mL<sup>-1</sup>) was coated onto the surface of the GCE electrode and allowed to dry at ambient temperature to form a thin film.

For the two-electrode system, a symmetrical supercapacitor device was constructed according to the following protocol. Briefly, the active material was homogeneously dispersed in ultrapure water (~5 mg mL<sup>-1</sup>) and sonicated for 1 h. Next, 300 μL of the dispersion was drop-coated onto the surface of a gold disk electrode (diameter 18 mm) and dried under an infrared light lamp in a desiccator to achieve a mass loading of at least 1.2 mg cm<sup>-2</sup>. For assembly of the supercapacitor device, two gold disk electrodes with the same loading of active material were placed in an insulator sleeve (EL-Cell insulator sleeve, EL-Cell GmbH, Hamburg, Germany) using Whatman glass microfiber filter paper with a thickness of 0.26 mm as a separator. The separator membrane was soaked with 100 μL of electrolyte. Stainless steel plungers were used to press the electrodes, and the whole device was tightened and connected.

In the three-electrode setup, the specific capacitance of the active material (*C<sub>s</sub>*, F g<sup>-1</sup>) was calculated from the galvanostatic charging/discharging (GCD) curves as follows (Equation (1)):

$$C_s = \frac{2i_m}{(V_f - V_i)^2} \int_{V_i}^{V_f} V dt \quad (1)$$

where *i<sub>m</sub>* represents the current density in A g<sup>-1</sup>, “Vdt” is the integrated area under the discharge curves and *V<sub>f</sub>* and *V<sub>i</sub>* are the final and initial values of the potential range (V), respectively.

In the two-electrode setup, the specific capacitance of the cell (*C<sub>s</sub>*, F g<sup>-1</sup>) was calculated using Equation (2):

$$C_s = \frac{I \times \Delta t}{m \times \Delta V} \quad (2)$$

where *C<sub>s</sub>* is the gravimetric capacitance of the electrode (F g<sup>-1</sup>), *I* is the discharge current (A), *Δt* is the discharge time (s), *ΔV* is the potential window and *m* is the total mass of both electrodes (g).



### 3. Results and Discussion

The Bragg diffraction of GA displayed two broad peaks centered at  $29^\circ$  and  $50^\circ$  corresponding to the diffraction of the (0 0 2) and (1 0 1) planes (Figure 1a). The intense broad peak recorded at  $29^\circ$  related to a  $d$ -space value of 0.3579 nm, which was slightly higher than the equivalent value for the graphite structure (inset of Figure 1a). Such peaks suggest an amorphous structure containing stacked sheets with short-range order [43]. A Raman spectrum of GA revealed two peaks in the range of 1000 to  $1800\text{ cm}^{-1}$ . The D-band at  $1336\text{ cm}^{-1}$  originated from a breathing mode of  $\kappa$ -point phonons of  $A_{1g}$  symmetry, whereas the G-band at  $1605\text{ cm}^{-1}$  originated from the first-order scattering of  $E_{2g}$  phonons by  $sp^2$  carbon domains. The higher intensity of the D-band ( $I_D/I_G$  ratio of 1.69) indicated atomic-scale defects, such as vacancies and grain boundaries [44,45], which commonly appear in highly functionalized graphene derivatives [46–48]. An XPS survey spectrum (Figure 1c) showed the dominant presence of C (76.7 at. %) and O (18.0 at. %), followed by N (3.5 at. %) and F (1.8 at. %) elements. The fluorine content probably originated from the graphite fluoride precursor, whereas the nitrogen content may have originated from unreacted nitrile groups, as cyanographene is a reaction intermediate of GA [37]. The deconvoluted C 1s XPS spectrum of GA (Figure 1d) exhibited six symmetric peaks corresponding to carbon atoms in different functional groups. The first two peaks located at 284.75 eV and 286.75 eV were assigned to  $sp^2$  C=C and  $sp^3$  C-C bonds, respectively, whereas the peaks located at 287.80, 288.84, 286.99 and 290.03 eV were attributed to carbon involved in C-O, O=C-O, C-N and C-F covalent bonds, respectively. The deconvoluted O 1s XPS spectrum (Figure 1e) exhibited two symmetrical peaks located at 531.62 and 533.32 eV, which were attributed to oxygen in C=O and C-OH covalent bonds, respectively. Therefore, the XPS analysis confirmed that GA contained a high content of oxygen-containing carboxyl functional groups, as supported by FTIR measurements (Figure S1) and in agreement with the literature [37]. BET measurements revealed the specific surface area of  $18.6\text{ m}^2\text{ g}^{-1}$  (Figure S4) with an average pore size of approximately 6.2 nm in diameter. It should be noted that the specific surface area in the dry state was low due to the tendency for restacking of individual sheets of graphene functionalized by hydrophilic groups [37,49].

The structural properties and composition of GA were further evaluated by microscopic methods. HRTEM indicated the layered nature of GA, with thin flakes of micrometer-scale lateral size (Figure 2a). Selected area electron diffraction (SAED) analysis displayed two well-developed rings, confirming the graphitic nature of GA with the presence of the (0 0 2) and (1 0 1) planes (Figure 2b). HRTEM imaging was also employed to provide more detailed information about the structure and topography of the chemical element composition (Figure 2c–e). Dark-field HRTEM images were used for energy dispersive X-ray spectroscopy (EDS) chemical mapping of carbon, oxygen, fluorine and nitrogen (Figure 2d,e), which all showed a homogeneous distribution over the surface, confirming the homogeneous surface functionalization of graphene. The energy-dispersive X-ray (EDS) spectrum of GA acquired during HRTEM analysis (Figure 2f) showed dominant peaks for C and O and small peaks for N, F, Na and Ca. The last two elements probably originated from metal ion impurities present in the water used for the sample preparation, as XPS did not detect these metal elements. An AFM image of a GA flake and the corresponding height profile are shown in Figure S3a,b, respectively. A structural model of GA is shown Figure 2g. All the obtained data corroborated that the GA sample could be considered a layered system with a homogeneous distribution of all tested elements over the surface. The findings confirmed that GA is a graphene derivative homogeneously functionalized by oxygen-containing carboxyl groups, in agreement with previous reports [37].

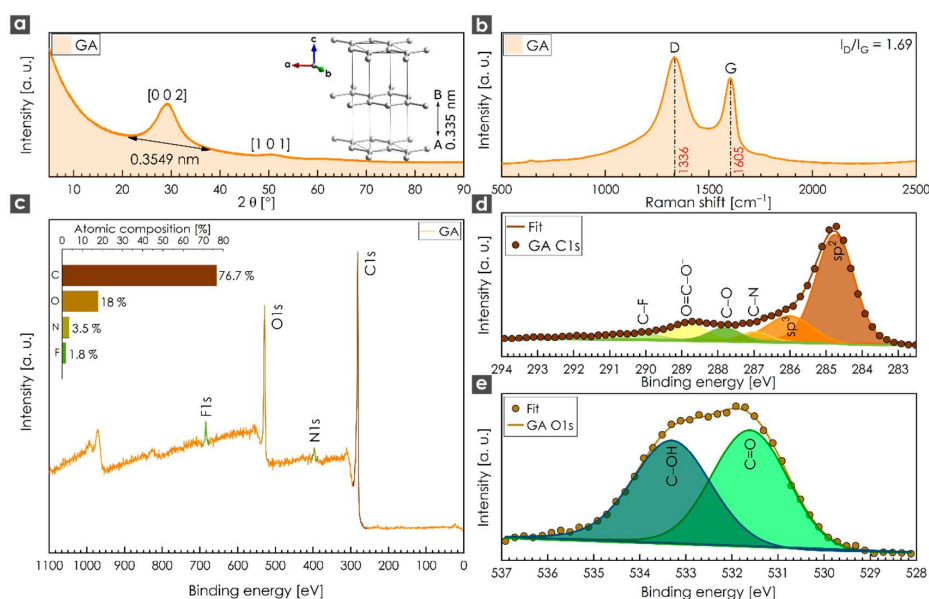


**Figure 1.** (a) X-ray diffraction (XRD) of graphene acid (GA); inset: crystal structure of graphite (hexagonal P 63 mc,  $a$ : 2.456 Å,  $b$ : 2.456 Å,  $c$ : 6.696 Å) obtained from the American Mineralogist Crystal Structure Database (database code: amcsd 0011247). The crystal structure was visualized with the program VESTA (version 3.4.7), developed by Koichi Momma and Fujio Izumi [50]. (b) Raman spectrum of GA with corresponding  $I_D/I_G$  ratio; (c) X-ray photoelectron spectroscopy (XPS) survey spectrum and elemental composition (inset) of GA; (d) XPS spectra of C 1s and (e) O 1s derived from the GA sample.

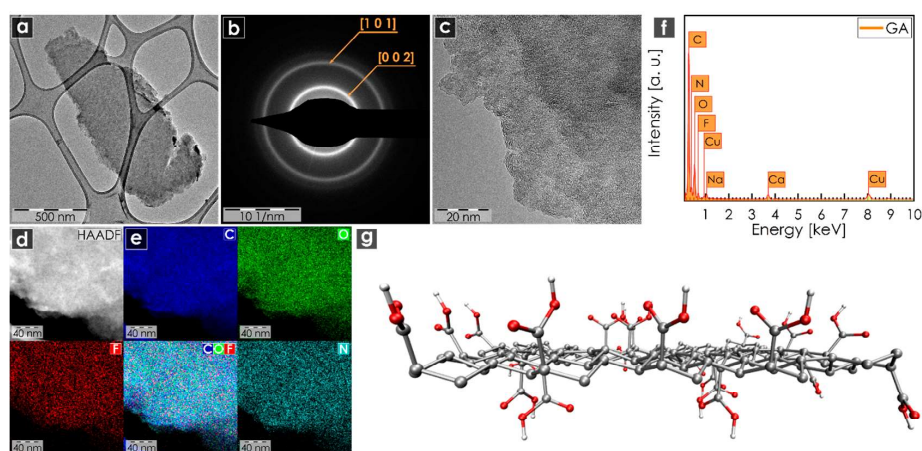


**Figure 2.** (a) High-resolution TEM (HRTEM) image of a GA sample; (b) selected area electron diffraction (SAED) analysis of a GA sample; (c) high-magnification HRTEM image of a GA sample; (d) dark-field HRTEM image used for EDS chemical mapping; (e) EDS elemental mapping of GA sample (on a Cu grid), including carbon, oxygen, fluorine and nitrogen atoms; (f) energy-dispersive X-ray (EDAX) spectrum of a GA sample; (g) optimized structure of GA. The molecular structure of GA was visualized using VMD software (version 1.9.3) [51]. Scale bars were unified from the graphical point of view in order to possess better visibility.

The reproducibility of chemical syntheses is important for practical applications, especially in nanomaterial chemistry. Thus, we prepared and tested three independent batches of GA. Both Raman and XPS spectroscopy confirmed minimal changes in chemical composition among the different batches (Figure S2a,b). The high reproducibility of GA synthesis was also corroborated by the results of electrochemical experiments, as described below.

### Electrochemical Performance of Graphene Acid

A three-electrode setup including a reference electrode is able to describe the electrochemical behavior of a tested material more properly than a two-electrode cell can [52,53]. However, a two-electrode setup is closer to the operational conditions of real capacitor devices. Thus, we decided to use a three-electrode setup first to obtain an insight into the electrode/electrolyte behavior of the tested GA. Figure 3a shows a cyclic voltammetry (CV) response of GA in the presence of three different electrolytes over the potential range of 0.0 to 1.0 V at a constant scan rate of 20 mV s<sup>-1</sup>. Sulfuric acid has the ability to boost the current (capacitive) performance compared to a neutral or alkaline electrolyte of the same ionic strength [54]. The recorded CV scan of GA exhibited distortion of the “ideal” rectangular shape, with a pair of redox peaks located at 0.4–0.45 V. The slight potential separation (<0.1 V) between the anodic and cathodic peak potentials suggests that the electrochemical response of GA could be considered a highly reversible system accompanied by minimal or no structural changes. Such behavior is expected for a system containing oxygen-containing functional groups, as shown above for GA. Oxygen-containing functional groups could enhance capacitive performance; they increased the interaction of the tested material with the electrolyte and made the surface more accessible for ion-exchange reactions. Moreover, fast redox reactions of carbon surface functionalities may introduce an extra capacitance (pseudocapacitive effect) and boost the overall performance [31]. This pseudocapacitive effect was apparent in the CV and could be attributed to the presence of oxygen-containing groups (FTIR spectra of GA—Figure S1). The absence of redox peaks in the neutral or base-derived solutions could be attributed to the lack of protons in these electrolytes (the absence of H<sup>+</sup> prevents the undergoing of the redox reaction of oxygen-containing functional groups). As the sweep rate was increased (Figure 3b), both the anodic and cathodic peak currents exhibited a significant shift, reflecting the ohmic contribution. During a linear scan of a constant rate, the current can be expressed according to a power law as follows (Equation (3)):

$$i = av^b \quad (3)$$

where  $i$  is the current,  $a$  and  $b$  are adjustable values and  $v$  is the scan rate. Thus, the  $b$  factor can be obtained from the slope of a linear fit when  $\log i$  is plotted against  $\log v$  at a fixed potential. A value of  $b = 0.5$  indicates the current is controlled by semi-infinite diffusion processes, whereas  $b = 1$  indicates that the current is surface-controlled (influenced by capacitive or nondiffusive processes) [55,56]. As shown in Figure 3c, the  $b$  factor was close to 1 (data for both the anodic and cathodic current peaks were collected at a constant potential of 0.4 V), suggesting strong surface-associated processes. The ratio between the surface-associated processes (e.g., redox reactions) and diffusion-controlled processes (e.g., EDLC contribution) was further evaluated using Trasatti’s method [57] (a detailed methodology description can be found in the Supplementary Materials, Figure S6). As expected, the presence of oxygen-containing functional groups on the surface of GA reflected the high portion of the pseudocapacitive mechanism (55.9%). Since GA has the structure of layered graphene, the contribution from the EDLC mechanism (44.1%) was apparent as well. Figure 3d shows GCD curves recorded at current densities ranging from 0.5 to 10 A g<sup>-1</sup>. Their symmetric quasitriangular shape suggests the presence of redox-active material as well as a satisfactory capacitive response of GA, even at high current densities. In addition, three samples of GA were synthesized and tested to investigate the reproducibility of the synthesis (Figure 3e). The standard deviation of the results was found to be smaller than 10% (current densities ranging from 0.5 to 5 A g<sup>-1</sup>), suggesting the practical applicability of the GA sample. A small deflection was observed at the highest current density of 10 A g<sup>-1</sup>, for which the standard deviation was found to be 13%. A maximum specific capacitance ( $C_{sp}$ ) of 111 F g<sup>-1</sup> (average for the three independent syntheses of the GA sample (S.D. 5.3%)) was obtained at a current density of 0.5 A g<sup>-1</sup>. The obtained results show that GA is a very competitive material comparable to previously published reports (Table S1 and Figure S5 in the Supplementary Materials). EIS was also employed to evaluate the GA sample based on a modified Frumkin–Melik–Gaykazyan circuit (inset of Figure 3i). The suitability of this circuit for analyzing the EIS spectra was reflected in the

good error of fit (Figure 3i). One can see from the magnified region of the Nyquist plot (Figure 3g) that in the high-frequency region, the EIS spectrum of GA did not exhibit a significant semicircle, indicating a small value of charge transfer resistance,  $R_{ct}$ . According to the data fit, the  $R_{ct}$  was around  $1.06 \Omega$ . Such findings predict good conductivity for the GA sample. We also employed the four-point probe method to test the conductivity of GA. The obtained data confirmed a high conductivity for GA at  $8.174 \times 10^3 \text{ Sm}^{-1}$  and a rather low value of resistivity at  $1.229 \times 10^{-4} \Omega \text{ m}$  (sheet resistance  $30.74 \Omega \text{ square}^{-1}$ ). An almost vertical line in the low-frequency region of the Nyquist plot (Figure 3f) indicated the nearly ideal capacitive response of GA, which could be attributed to fast ion diffusion [58]. The slight deflection from the parallel line was assigned to redox reactions of the oxygen-containing functional groups [5]. A Bode representation for a GCE modified with GA is depicted in Figure 3h. As can be seen, when the frequency decreased, the phase angle reflected a change from a resistive to a fully capacitive response in the mHz region (phase angle:  $\sim -84^\circ$ ). It should be noted that a phase angle close to  $-90^\circ$  indicates an almost ideal capacitor.

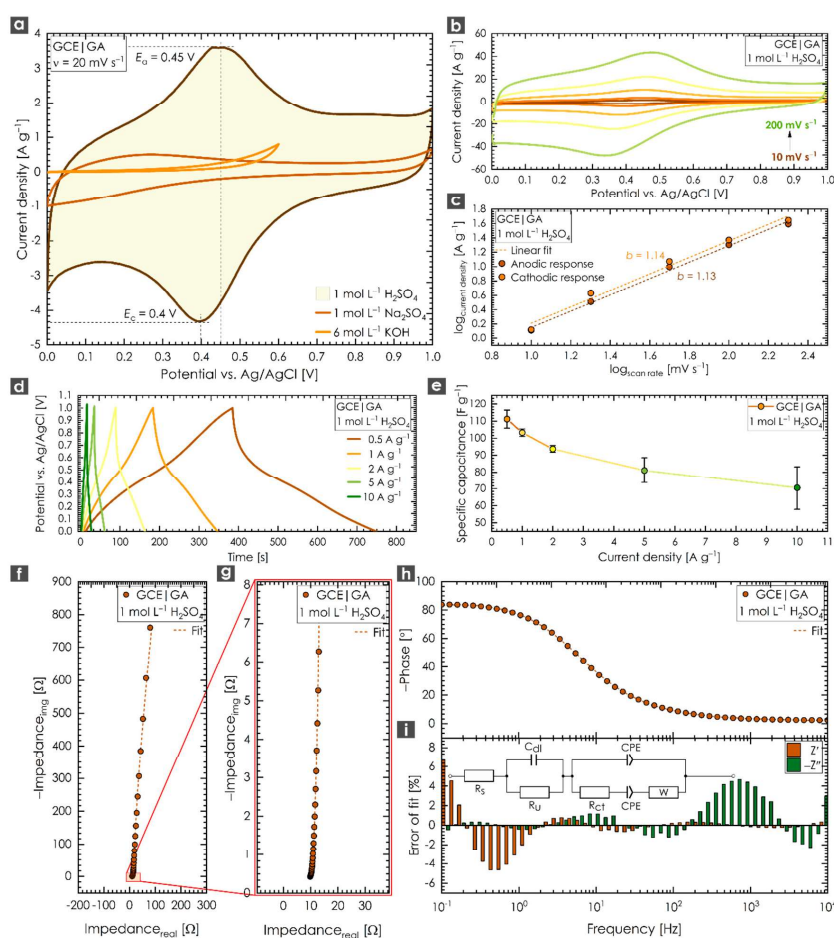


**Figure 3.** (a) Cyclic voltammetry (CV) response of a glassy carbon electrode (GCE) modified with GA in different electrolytes recorded at a constant scan rate of  $20 \text{ mV s}^{-1}$ ; (b) CVs for a GCE modified with GA at different potential scan rates ranging from  $10$  to  $200 \text{ mV s}^{-1}$ ; (c) calculation of  $b$  factor from a linear fit when  $\log i$  is plotted against  $\log v$ ; (d) galvanostatic charging/discharging (GCD) response of a GCE modified with GA recorded at different current densities ranging from  $0.5$  to  $10 \text{ A g}^{-1}$ ; (e) specific capacitance evolution with increasing current density ( $0.5$  to  $10 \text{ A g}^{-1}$ ) for three independent syntheses of GA; (f) Nyquist plot of a GCE modified with GA; (g) magnified high-frequency region of the Nyquist plot for a GCE modified with GA; (h) Bode representation of a GCE modified with GA; (i) the error of fit for the equivalent circuit used; inset: a modified Frumkin–Melik–Gaykazyan circuit. All measurements were performed in  $1 \text{ mol L}^{-1} \text{ H}_2\text{SO}_4$  unless otherwise stated.

To further assess the feasibility of GA for actual applications, a symmetric capacitor using  $1 \text{ mol L}^{-1}$   $\text{H}_2\text{SO}_4$  as the electrolyte was assembled. To avoid any capacitance interferences or boosting effects originating from binders or different additives, we used an aqueous suspension of GA. Figure 4a shows the GCD response of GA in the two-electrode configuration recorded at current densities ranging from 1 to  $20 \text{ A g}^{-1}$ . As expected, all the GCD curves were more symmetrical compared to those of the three-electrode setup, suggesting the reduced influence of ion diffusion as well as satisfactory capacitive behavior. Faster ion diffusion is also demonstrated in Figure 4b, which shows a slow decline in the specific capacitance response across a wide range of current densities. Based on these observations, we also performed a rate stability test (Figure 4c) to evaluate the capacitance stability of the GA system. After 10 repeated GCD tests over a range of current densities from 1 to  $20 \text{ A g}^{-1}$ , the capacitive response remained stable. Hence, it was possible to select a relatively high current density ( $3 \text{ A g}^{-1}$ ) and cycle the system during a long-term experiment. The results confirmed the remarkable stability of GA after 60,000 cycles, with specific capacitance retention of 95.3% (Figure 4d). In practical applications, a single supercapacitor is not able to meet all the energy and power requirements. Therefore, two cells were connected in series (to boost the voltage range) or in parallel (to increase the energy storage density), as illustrated in Figure 4e. The GCD test recorded at  $2 \text{ A g}^{-1}$  revealed that the voltage window could easily be increased up to 2 V for two cells connected in series compared to a single supercapacitor operating at 1 V. On the other hand, connecting supercapacitors in parallel could enhance the energy storage density twice as well. To demonstrate that GA can be used as a candidate for supercapacitor applications, two cells were connected in series and used to power a red light-emitting diode. After charging the system to 2 V, the LED was illuminated without any obvious fading effects, as shown in Figure 4f (Figure 4f (left) shows the open circuit without the presence of GA-based supercapacitors, whereas Figure 4f (right) illustrates the closed circuit with fully charged GA-based supercapacitors).

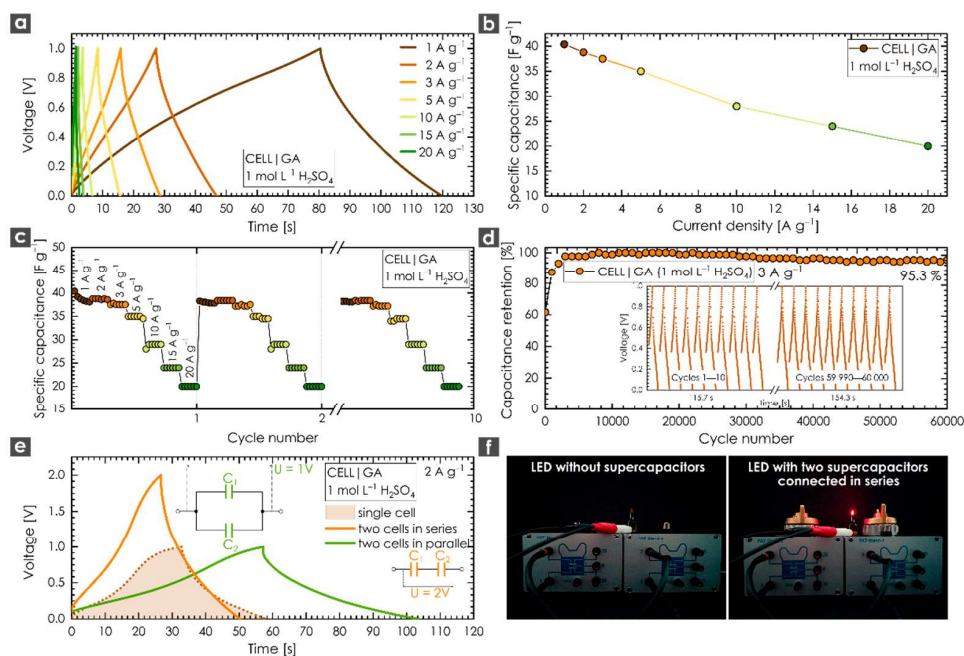


**Figure 4.** (a) GCD response of GA in a two-electrode configuration recorded at current densities ranging from 1 to  $20 \text{ A g}^{-1}$ ; (b) decrease in the specific capacitance of GA with increasing current density; (c) rate stability test of GA recorded at current densities ranging from 1 to  $20 \text{ A g}^{-1}$ ; (d) cycling stability of GA after 60,000 cycles; inset shows first and last 10 cycles in a potential difference of 1 V (recorded from  $-0.35 \text{ V}$  to  $0.65 \text{ V}$ ); (e) response of two supercapacitor cells equipped with GA connected in series or in parallel; (f) LED test of two supercapacitor cells equipped with GA connected in series. All measurements were performed in  $1 \text{ mol L}^{-1} \text{ H}_2\text{SO}_4$ .

#### 4. Conclusions

GA is a graphene derivative prepared from fluorographene that offers a promising stable electrode material for supercapacitors. GA is well-equipped with oxygen-containing groups and exhibited an encouraging pseudocapacitive response in 1 mol L<sup>-1</sup> sulfuric acid. By prepared three independent GA samples, we showed the high reproducibility of its synthesis and electrochemical performance. Owing to the unique features of its surface chemistry, GA exhibited good performance as a pseudocapacitive material, having an enormous rate and lifetime stability. GA could be cycled at least 10 times at various current densities without any capacitance loss. Such an attribute was accompanied by an enormous specific capacitance retention after 60,000 cycles (95.3%) recorded at a reasonably high current density of 3 A g<sup>-1</sup> in a two-electrode cell system. The obtained results demonstrate that GA is a suitable candidate for preparing supercapacitors with exceptional lifetime stability. Generally, covalent graphene derivatives with selected functional groups should be considered a potentially important class of supercapacitor electrode materials.

**Supplementary Materials:** The following are available online at <http://www.mdpi.com/2079-4991/10/9/1731/s1>. Figure S1: Fourier transform infrared (FTIR) spectrum of graphene acid; Figure S2: Comparison of (a) Raman and (b) X-ray photoelectron spectroscopy (XPS) spectra of graphene acid from three independent syntheses; Figure S3: (a) Atomic force microscopy (AFM) image of graphene acid and its corresponding high profile (b). Figure S4 BET measurement of graphene acid with corresponding pore distribution (inset of Figure S4), Figure S5 Ragone plot showing energy and power density of GA, commercial graphene and other comparable published materials. Specific capacitance was recalculated using the same metrics and formulas as in described in the main text of the manuscript, preferably from discharging time of GCD profiles. Energy density and power density values were calculated using the following equations:  $E = (Cs \times 0.5 \times \Delta V^2)/3.6$ ;  $P = 3600 \times (E/\Delta t)$ , where E is the energy density (Wh kg<sup>-1</sup>), P is the power density (W kg<sup>-1</sup>), Cs has the meaning of specific capacitance (F g<sup>-1</sup>),  $\Delta V$  is the voltage window (V) and  $\Delta t$  is the discharge time (s). Figure S6 (a) Dependence of q on  $v^{-1/2}$ , (b) dependence of  $q^{-1}$  on  $v^{1/2}$  for GA in 1 mol L<sup>-1</sup> sulphuric acid electrolyte. (c) bar chart of the contribution of pseudocapacitance (PC) and electrochemical double-layer capacitance (EDLC) to the total capacitance. Table S1: Comparison of specific capacitance, energy density, power density, cyclic stability and capacitance retention in GA, commercial graphene from Ossila and other published comparable materials

**Author Contributions:** Conceptualization, P.J. and M.O.; investigation, V.Š., A.B. and V.R.; writing—original draft preparation, V.Š., P.J., A.B., V.R. and M.O.; writing—review and editing, V.Š., P.J., A.B., V.R. and M.O.; visualization, P.J.; supervision, P.J. and M.O. All authors have read and agreed to the published version of the manuscript.

**Funding:** The authors acknowledge support from the Internal Student Grant Agency of Palacký University in Olomouc, Czech Republic (IGA\_PrF\_2020\_022) and funding from an ERC Consolidator Grant from H2020 (no. 683024) and from the Ministry of Education, Youth and Sports of the Czech Republic via the Operational Programme “Research, Development and Education”—European Regional Development Fund (project no. CZ.02.1.01/0.0/0.0/16\_019/0000754; CZ.1.05/2.1.00/19.0377).

**Acknowledgments:** We gratefully thank K. Štymplová, J. Stráská, O. Tomanec, T. Steklý and J. Pauswang for their expert assistance with the synthesis and material characterization.

**Conflicts of Interest:** The authors declare no conflict of interest.

#### References

1. Lewis, N.S.; Nocera, D.G. Powering the planet: Chemical challenges in solar energy utilization. *Proc. Natl. Acad. Sci. USA* **2006**, *103*, 15729–15735. [[CrossRef](#)]
2. Pomerantseva, E.; Bonaccorso, F.; Feng, X.; Cui, Y.; Gogotsi, Y. Energy storage: The future enabled by nanomaterials. *Science* **2019**, *366*, eaan8285. [[CrossRef](#)] [[PubMed](#)]
3. Raymundo-Piñero, E.; Leroux, F.; Béguin, F. A High-Performance Carbon for Supercapacitors Obtained by Carbonization of a Seaweed Biopolymer. *Adv. Mater.* **2006**, *18*, 1877–1882. [[CrossRef](#)]
4. Salunkhe, R.R.; Lee, Y.-H.; Chang, K.-H.; Li, J.-M.; Simon, P.; Tang, J.; Torad, N.L.; Hu, C.-C.; Yamauchi, Y. Nanoarchitected Graphene-Based Supercapacitors for Next-Generation Energy-Storage Applications. *Chem. Eur. J.* **2014**, *20*, 13838–13852. [[CrossRef](#)] [[PubMed](#)]
5. Wang, G.; Zhang, L.; Zhang, J. A review of electrode materials for electrochemical supercapacitors. *Chem. Soc. Rev.* **2012**, *41*, 797–828. [[CrossRef](#)]

6. Conway, B.E.; Birss, V.; Wojtowicz, J. The role and utilization of pseudocapacitance for energy storage by supercapacitors. *J. Power Sources* **1997**, *66*, 1–14. [[CrossRef](#)]
7. Zhai, S.; Wang, C.; Karahan, H.E.; Wang, Y.; Chen, X.; Sui, X.; Huang, Q.; Liao, X.; Wang, X.; Chen, Y. Nano-RuO<sub>2</sub>-Decorated Holey Graphene Composite Fibers for Micro-Supercapacitors with Ultrahigh Energy Density. *Small* **2018**, *14*, 1800582. [[CrossRef](#)]
8. Han, Z.J.; Pineda, S.; Murdock, A.T.; Seo, D.H.; Ostrikov, K.; Bendavid, A. RuO<sub>2</sub>-coated vertical graphene hybrid electrodes for high-performance solid-state supercapacitors. *J. Mater. Chem. A* **2017**, *5*, 17293–17301. [[CrossRef](#)]
9. Wang, J.-G.; Kang, F.; Wei, B. Engineering of MnO<sub>2</sub>-based nanocomposites for high-performance supercapacitors. *Prog. Mater. Sci.* **2015**, *74*, 51–124. [[CrossRef](#)]
10. Kang, J.; Hirata, A.; Kang, L.; Zhang, X.; Hou, Y.; Chen, L.; Li, C.; Fujita, T.; Akagi, K.; Chen, M. Enhanced Supercapacitor Performance of MnO<sub>2</sub> by Atomic Doping. *Angew. Chem. Int. Ed.* **2013**, *52*, 1664–1667. [[CrossRef](#)]
11. Chen, S.; Zhu, J.; Wu, X.; Han, Q.; Wang, X. Graphene Oxide–MnO<sub>2</sub> Nanocomposites for Supercapacitors. *ACS Nano* **2010**, *4*, 2822–2830. [[CrossRef](#)] [[PubMed](#)]
12. Gu, T.; Wei, B. High-performance all-solid-state asymmetric stretchable supercapacitors based on wrinkled MnO<sub>2</sub>/CNT and Fe<sub>2</sub>O<sub>3</sub>/CNT macrofilms. *J. Mater. Chem. A* **2016**, *4*, 12289–12295. [[CrossRef](#)]
13. Shi, Z.; Xing, L.; Liu, Y.; Gao, Y.; Liu, J. A porous biomass-based sandwich-structured Co<sub>3</sub>O<sub>4</sub>@Carbon Fiber@Co<sub>3</sub>O<sub>4</sub> composite for high-performance supercapacitors. *Carbon* **2018**, *129*, 819–825. [[CrossRef](#)]
14. Liao, Q.; Li, N.; Jin, S.; Yang, G.; Wang, C. All-Solid-State Symmetric Supercapacitor Based on Co<sub>3</sub>O<sub>4</sub> Nanoparticles on Vertically Aligned Graphene. *ACS Nano* **2015**, *9*, 5310–5317. [[CrossRef](#)] [[PubMed](#)]
15. Wang, J.; Wang, J.; Kong, Z.; Lv, K.; Teng, C.; Zhu, Y. Conducting-Polymer-Based Materials for Electrochemical Energy Conversion and Storage. *Adv. Mater.* **2017**, *29*, 1703044. [[CrossRef](#)] [[PubMed](#)]
16. Meng, Q.; Cai, K.; Chen, Y.; Chen, L. Research progress on conducting polymer based supercapacitor electrode materials. *Nano Energy* **2017**, *36*, 268–285. [[CrossRef](#)]
17. Jyothibas, J.P.; Lee, R.-H. Green synthesis of polypyrrole tubes using curcumin template for excellent electrochemical performance in supercapacitors. *J. Mater. Chem. A* **2020**, *8*, 3186–3202. [[CrossRef](#)]
18. Jiang, H.; Cai, X.; Qian, Y.; Zhang, C.; Zhou, L.; Liu, W.; Li, B.; Lai, L.; Huang, W. V<sub>2</sub>O<sub>5</sub> embedded in vertically aligned carbon nanotube arrays as free-standing electrodes for flexible supercapacitors. *J. Mater. Chem. A* **2017**, *5*, 23727–23736. [[CrossRef](#)]
19. Augustyn, V.; Simon, P.; Dunn, B. Pseudocapacitive oxide materials for high-rate electrochemical energy storage. *Energy Environ. Sci.* **2014**, *7*, 1597. [[CrossRef](#)]
20. Hao, L.; Li, X.; Zhi, L. Carbonaceous Electrode Materials for Supercapacitors. *Adv. Mater.* **2013**, *25*, 3899–3904. [[CrossRef](#)]
21. Yan, J.; Wang, Q.; Wei, T.; Fan, Z. Recent Advances in Design and Fabrication of Electrochemical Supercapacitors with High Energy Densities. *Adv. Energy Mater.* **2014**, *4*, 1300816. [[CrossRef](#)]
22. Li, B.; Dai, F.; Xiao, Q.; Yang, L.; Shen, J.; Zhang, C.; Cai, M. Nitrogen-doped activated carbon for a high energy hybrid supercapacitor. *Energy Environ. Sci.* **2016**, *9*, 102–106. [[CrossRef](#)]
23. Hou, J.; Cao, C.; Idrees, F.; Ma, X. Hierarchical Porous Nitrogen-Doped Carbon Nanosheets Derived from Silk for Ultrahigh-Capacity Battery Anodes and Supercapacitors. *ACS Nano* **2015**, *9*, 2556–2564. [[CrossRef](#)] [[PubMed](#)]
24. Lin, T.; Chen, I.-W.; Liu, F.; Yang, C.; Bi, H.; Xu, F.; Huang, F. Nitrogen-doped mesoporous carbon of extraordinary capacitance for electrochemical energy storage. *Science* **2015**, *350*, 1508–1513. [[CrossRef](#)] [[PubMed](#)]
25. Yuan, C.; Liu, X.; Jia, M.; Luo, Z.; Yao, J. Facile preparation of N- and O-doped hollow carbon spheres derived from poly(o-phenylenediamine) for supercapacitors. *J. Mater. Chem. A* **2015**, *3*, 3409–3415. [[CrossRef](#)]
26. Raj, C.J.; Rajesh, M.; Manikandan, R.; Yu, K.H.; Anusha, J.R.; Ahn, J.H.; Kim, D.-W.; Park, S.Y.; Kim, B.C. High electrochemical capacitor performance of oxygen and nitrogen enriched activated carbon derived from the pyrolysis and activation of squid gladius chitin. *J. Power Sources* **2018**, *386*, 66–76. [[CrossRef](#)]
27. Zhao, G.; Chen, C.; Yu, D.; Sun, L.; Yang, C.; Zhang, H.; Sun, Y.; Besenbacher, F.; Yu, M. One-step production of O-N-S co-doped three-dimensional hierarchical porous carbons for high-performance supercapacitors. *Nano Energy* **2018**, *47*, 547–555. [[CrossRef](#)]

28. Nasini, U.B.; Bairi, V.G.; Ramasahayam, S.K.; Bourdo, S.E.; Viswanathan, T.; Shaikh, A.U. Phosphorous and nitrogen dual heteroatom doped mesoporous carbon synthesized via microwave method for supercapacitor application. *J. Power Sources* **2014**, *250*, 257–265. [[CrossRef](#)]
29. Yu, X.; Kang, Y.; Park, H.S. Sulfur and phosphorus co-doping of hierarchically porous graphene aerogels for enhancing supercapacitor performance. *Carbon* **2016**, *101*, 49–56. [[CrossRef](#)]
30. Yang, F.; Ma, X.; Cai, W.-B.; Song, P.; Xu, W. Nature of Oxygen-Containing Groups on Carbon for High-Efficiency Electrocatalytic CO<sub>2</sub> Reduction Reaction. *J. Am. Chem. Soc.* **2019**, *141*, 20451–20459. [[CrossRef](#)]
31. Calvo, E.G.; Rey-Raap, N.; Arenillas, A.; Menéndez, J.A. The effect of the carbon surface chemistry and electrolyte pH on the energy storage of supercapacitors. *RSC Adv.* **2014**, *4*, 32398–32404. [[CrossRef](#)]
32. Pandolfo, A.G.; Hollenkamp, A.F. Carbon properties and their role in supercapacitors. *J. Power Sources* **2006**, *157*, 11–27. [[CrossRef](#)]
33. Cao, H.; Peng, X.; Zhao, M.; Liu, P.; Xu, B.; Guo, J. Oxygen functional groups improve the energy storage performances of graphene electrochemical supercapacitors. *RSC Adv.* **2018**, *8*, 2858–2865. [[CrossRef](#)]
34. Cherusseri, J.; Kar, K.K. Hierarchically mesoporous carbon nanopetal based electrodes for flexible supercapacitors with super-long cyclic stability. *J. Mater. Chem. A* **2015**, *3*, 21586–21598. [[CrossRef](#)]
35. Chen, Y.; Yan, Q.; Zhang, S.; Lu, L.; Xie, B.; Xie, T.; Zhang, Y.; Wu, Y.; Zhang, Y.; Liu, D. Buffering agents-assisted synthesis of nitrogen-doped graphene with oxygen-rich functional groups for enhanced electrochemical performance. *J. Power Sources* **2016**, *333*, 125–133. [[CrossRef](#)]
36. Song, B.; Sizemore, C.; Li, L.; Huang, X.; Lin, Z.; Moon, K.; Wong, C.-P. Triethanolamine functionalized graphene-based composites for high performance supercapacitors. *J. Mater. Chem. A* **2015**, *3*, 21789–21796. [[CrossRef](#)]
37. Bakandritsos, A.; Pykal, M.; Błoński, P.; Jakubec, P.; Chronopoulos, D.D.; Poláková, K.; Georgakilas, V.; Čépe, K.; Tomanec, O.; Ranc, V.; et al. Cyanographene and Graphene Acid: Emerging Derivatives Enabling High-Yield and Selective Functionalization of Graphene. *ACS Nano* **2017**, *11*, 2982–2991. [[CrossRef](#)]
38. Heng Cheong, Y.; Nasir, M.Z.M.; Bakandritsos, A.; Pykal, M.; Jakubec, P.; Zbořil, R.; Otyepka, M.; Pumera, M. Cyanographene and Graphene Acid: The Functional Group of Graphene Derivative Determines the Application in Electrochemical Sensing and Capacitors. *ChemElectroChem* **2019**, *6*, 229–234. [[CrossRef](#)]
39. Blanco, M.; Mosconi, D.; Tubaro, C.; Biffis, A.; Badocco, D.; Pastore, P.; Otyepka, M.; Bakandritsos, A.; Liu, Z.; Ren, W.; et al. Palladium nanoparticles supported on graphene acid: A stable and eco-friendly bifunctional C–C homo- and cross-coupling catalyst. *Green Chem.* **2019**, *21*, 5238–5247. [[CrossRef](#)]
40. Blanco, M.; Mosconi, D.; Otyepka, M.; Medved', M.; Bakandritsos, A.; Agnoli, S.; Granozzi, G. Combined high degree of carboxylation and electronic conduction in graphene acid sets new limits for metal free catalysis in alcohol oxidation. *Chem. Sci.* **2019**, *10*, 9438–9445. [[CrossRef](#)]
41. Reuillard, B.; Blanco, M.; Calvillo, L.; Coutard, N.; Ghedjatti, A.; Chenevier, P.; Agnoli, S.; Otyepka, M.; Granozzi, G.; Artero, V. Noncovalent Integration of a Bioinspired Ni Catalyst to Graphene Acid for Reversible Electrocatalytic Hydrogen Oxidation. *ACS Appl. Mater. Interfaces* **2020**, *12*, 5805–5811. [[CrossRef](#)] [[PubMed](#)]
42. Seelajaroen, H.; Bakandritsos, A.; Otyepka, M.; Zbořil, R.; Sariciftci, N.S. Immobilized Enzymes on Graphene as Nanobiocatalyst. *ACS Appl. Mater. Interfaces* **2020**, *12*, 250–259. [[CrossRef](#)] [[PubMed](#)]
43. Si, Y.; Samulski, E.T. Exfoliated Graphene Separated by Platinum Nanoparticles. *Chem. Mater.* **2008**, *20*, 6792–6797. [[CrossRef](#)]
44. Eckmann, A.; Felten, A.; Mishchenko, A.; Britnell, L.; Krupke, R.; Novoselov, K.S.; Casiraghi, C. Probing the Nature of Defects in Graphene by Raman Spectroscopy. *Nano Lett.* **2012**, *12*, 3925–3930. [[CrossRef](#)]
45. Johra, F.T.; Lee, J.-W.; Jung, W.-G. Facile and safe graphene preparation on solution based platform. *J. Ind. Eng. Chem.* **2014**, *20*, 2883–2887. [[CrossRef](#)]
46. Knirsch, K.C.; Schäfer, R.A.; Hauke, F.; Hirsch, A. Mono- and Ditopic Bisfunctionalization of Graphene. *Angew. Chem. Int. Ed.* **2016**, *55*, 5861–5864. [[CrossRef](#)]
47. Vecera, P.; Chacón-Torres, J.C.; Pichler, T.; Reich, S.; Soni, H.R.; Görling, A.; Edelthammer, K.; Peterlik, H.; Hauke, F.; Hirsch, A. Precise determination of graphene functionalization by in situ Raman spectroscopy. *Nat. Commun.* **2017**, *8*, 15192. [[CrossRef](#)]
48. Englert, J.M.; Vecera, P.; Knirsch, K.C.; Schäfer, R.A.; Hauke, F.; Hirsch, A. Scanning-Raman-Microscopy for the Statistical Analysis of Covalently Functionalized Graphene. *ACS Nano* **2013**, *7*, 5472–5482. [[CrossRef](#)]



49. Vermisoglou, E.C.; Jakubec, P.; Bakandritsos, A.; Pykal, M.; Talande, S.; Kupka, V.; Zbořil, R.; Otyepka, M. Chemical Tuning of Specific Capacitance in Functionalized Fluorographene. *Chem. Mater.* **2019**, *31*, 4698–4709. [[CrossRef](#)]
50. Momma, K.; Izumi, F. VESTA 3 for three-dimensional visualization of crystal, volumetric and morphology data. *J. Appl. Cryst.* **2011**, *44*, 1272–1276. [[CrossRef](#)]
51. Humphrey, W.; Dalke, A.; Schulten, K. VMD: Visual molecular dynamics. *J. Mol. Graph.* **1996**, *14*, 33–38. [[CrossRef](#)]
52. Stoller, M.D.; Ruoff, R.S. Best practice methods for determining an electrode material's performance for ultracapacitors. *Energy Environ. Sci.* **2010**, *3*, 1294. [[CrossRef](#)]
53. Noori, A.; El-Kady, M.F.; Rahmanifar, M.S.; Kaner, R.B.; Mousavi, M.F. Towards establishing standard performance metrics for batteries, supercapacitors and beyond. *Chem. Soc. Rev.* **2019**, *48*, 1272–1341. [[CrossRef](#)] [[PubMed](#)]
54. Andreas, H.A.; Conway, B.E. Examination of the double-layer capacitance of an high specific-area C-cloth electrode as titrated from acidic to alkaline pHs. *Electrochim. Acta* **2006**, *51*, 6510–6520. [[CrossRef](#)]
55. Kong, L.; Zhang, C.; Wang, J.; Qiao, W.; Ling, L.; Long, D. Free-Standing T-Nb<sub>2</sub>O<sub>5</sub>/Graphene Composite Papers with Ultrahigh Gravimetric/Volumetric Capacitance for Li-Ion Intercalation Pseudocapacitor. *ACS Nano* **2015**, *9*, 11200–11208. [[CrossRef](#)]
56. Augustyn, V.; Come, J.; Lowe, M.A.; Kim, J.W.; Taberna, P.-L.; Tolbert, S.H.; Abruña, H.D.; Simon, P.; Dunn, B. High-rate electrochemical energy storage through Li<sup>+</sup> intercalation pseudocapacitance. *Nat. Mater.* **2013**, *12*, 518–522. [[CrossRef](#)]
57. Spinolo, G.; Ardizzone, S.; Trasatti, S. Surface characterization of Co<sub>3</sub>O<sub>4</sub> electrodes prepared by the sol-gel method. *J. Electroanal. Chem.* **1997**, *423*, 49–57. [[CrossRef](#)]
58. He, Y.; Yang, X.; An, N.; Wang, X.; Yang, Y.; Hu, Z. Covalently functionalized heterostructured carbon by redox-active *p*-phenylenediamine molecules for high-performance symmetric supercapacitors. *New J. Chem.* **2019**, *43*, 1688–1698. [[CrossRef](#)]



© 2020 by the authors. Licensee MDPI, Basel, Switzerland. This article is an open access article distributed under the terms and conditions of the Creative Commons Attribution (CC BY) license (<http://creativecommons.org/licenses/by/4.0/>).

P a l a c k ý   U n i v e r s i t y   O l o m o u c

Faculty of Science

Department of Physical Chemistry



## **Chemical functionalization of graphene**

PRESENTATION OF DOCTORAL THESIS

Author: Mgr. Veronika Šedajová

Supervisor: Aristeidis Bakandritsos, Ph.D.

Study programme:

Field of study:

Form of study:

P 1417 Chemistry

Physical Chemistry

Full-time study

Olomouc 2022

Author's first name and surname: Veronika Šedajová

Supervisor: Aristeidis Bakandritsos, Ph.D.

Reviewers:

doc. Ing. Grażyna Simha Martynková, Ph.D.

Ing. Tomáš Zedníček, Ph.D.

Spyros Yannopoulos, Ph.D.

Place and date of the defence:

A place where the dissertation and opinions will be available at least 14 days before the defence:

**List of publications to which the author of this doctoral thesis has contributed as main author or co-author during her doctoral studies (2018 - 2022):**

- (1) Petr, M.; Jakubec, P.; Ranc, V.; Šedajová, V.; Langer, R.; Medved', M.; Błoński, P.; Kašík, J.; Kupka, V.; Otyepka, M.; Zbořil, R. Thermally Reduced Fluorographenes as Efficient Electrode Materials for Supercapacitors. **Nanoscale** 2019, 11 (44), 21364–21375. <https://doi.org/10.1039/C9NR07255A>.  
a. IF=7.8
- (2) Zaoralová, D.; Hrubý, V.; Šedajová, V.; Mach, R.; Kupka, V.; Ugolotti, J.; Bakandritsos, A.; Medved', M.; Otyepka, M. Tunable Synthesis of Nitrogen Doped Graphene from Fluorographene under Mild Conditions. **ACS Sustain. Chem. Eng.** 2020, 8 (12), 4764–4772. <https://doi.org/10.1021/acssuschemeng.9b07161>.  
a. IF=8.2, back cover
- (3) Šedajová, V.; Jakubec, P.; Bakandritsos, A.; Ranc, V.; Otyepka, M. New Limits for Stability of Supercapacitor Electrode Material Based on Graphene Derivative. **Nanomaterials** 2020, 10 (9), 1731. <https://doi.org/10.3390/nano10091731>.  
a. IF=5
- (4) Chalmpes, N.; Bourlinos, A. B.; Šedajová, V.; Kupka, V.; Moschovas, D.; Avgeropoulos, A.; Karakassides, M. A.; Gournis, D. Hypergolic Materials Synthesis through Reaction of Fuming Nitric Acid with Certain Cyclopentadienyl Compounds. **C** 2020, 6 (4), 61. <https://doi.org/10.3390/c6040061>.
- (5) Jakubec, P.; Bartusek, S.; Dvořáček, J. J.; Šedajová, V.; Kupka, V.; Otyepka, M. Flax-Derived Carbon: A Highly Durable Electrode Material for Electrochemical Double-Layer Supercapacitors. **Nanomaterials** 2021, 11 (9), 2229. <https://doi.org/10.3390/nano11092229>.  
a. IF=5
- (6) Chalmpes, N.; Asimakopoulos, G.; Baikousi, M.; Moschovas, D.; Avgeropoulos, A.; Bourlinos, AB; Šedajová, V.; Bakandritsos, A.; Gournis, D.; Karakassides, MA. Fast and Direct Microwave Synthesis of Carbon from Bovine Blood Waste: A Feedstock Material for Extractive Metallurgy, Carbon Dots Production and Graphite Synthesis. **J. Nanotechnol. Res.** 2021, 3, 011-028. <https://doi.org/10.26502/jnr.2688-85210021>
- (7) Vermisoglou, E. C.; Jakubec, P.; Bakandritsos, A.; Kupka, V.; Pykal, M.; Šedajová, V.; Vlček, J.; Tomanec, O.; Scheibe, M.; Zbořil, R.; Otyepka, M. Graphene with Covalently Grafted Amino Acid as a Route Toward Eco-Friendly and Sustainable Supercapacitors. **ChemSusChem** 2021, 14 (18), 3904–3914. <https://doi.org/10.1002/cssc.202101039>.  
a. IF=8.9

- (8) Saini, H.; Srinivasan, N.; Šedajová, V.; Majumder, M.; Dubal, D. P.; Otyepka, M.; Zbořil, R.; Kurra, N.; Fischer, R. A.; Jayaramulu, K. Emerging MXene@Metal–Organic Framework Hybrids: Design Strategies toward Versatile Applications. **ACS Nano** 2021, 15 (12), 18742–18776. <https://doi.org/10.1021/acsnano.1c06402>.  
a. IF=15.9, cover
- (9) Obratsov, I.; Bakandritsos, A.; Šedajová, V.; Langer, R.; Jakubec, P.; Zoppellaro, G.; Pykal, M.; Presser, V.; Otyepka, M.; Zbořil, R. Graphene Acid for Lithium-Ion Batteries—Carboxylation Boosts Storage Capacity in Graphene. **Adv. Energy Mater.** 2022, 12 (5), 2103010. <https://doi.org/10.1002/aenm.202103010>.  
a. IF=29.4
- (10) Dědek, I.; Kupka, V.; Jakubec, P.; Šedajová, V.; Jayaramulu, K.; Otyepka, M. Metal-Organic Framework/Conductive Polymer Hybrid Materials for Supercapacitors. **Appl. Mater. Today** 2022, 26, 101387. <https://doi.org/10.1016/j.apmt.2022.101387>.  
a. IF=10
- (11) Šedajová, V.; Bakandritsos, A.; Błoński, P.; Medved', M.; Langer, R.; Zaoralová, D.; Ugolotti, J.; Dzibelová, J.; Jakubec, P.; Kupka, V.; Otyepka, M. Nitrogen Doped Graphene with Diamond-like Bonds Achieves Unprecedented Energy Density at High Power in a Symmetric Sustainable Supercapacitor. **Energy Environ. Sci.** 2022, 15 (2), 740–748. <https://doi.org/10.1039/D1EE02234B>.  
a. IF=38.5
- (12) Hrubý, V.; Zdražil, L.; Dzibelová, J.; Šedajová, V.; Bakandritsos, A.; Lazar, P.; Otyepka, M. Unveiling the True Band Gap of Fluorographene and Its Origins by Teaming Theory and Experiment. **Appl. Surf. Sci.** 2022, 587, 152839. <https://doi.org/10.1016/j.apsusc.2022.152839>.  
a. IF=6.7
- (13) Asimakopoulos, G.; Moschovas, D.; Avgeropoulos, A.; Bourlinos, A.B.; Tantis, I.; Šedajová, V.; Tomanec, O.; Salmas, C.E.; Gournis, D.; Karakassides, M.A. From Waste Tea to Carbon Rocket Fuels through a Piranha Solution-Mediated Carbonization Treatment **J. Nanotechnol. Res.** 2022, 4, 31. <https://doi.org/10.26502/jnr.2688-85210029>
- (14) Chaloupková, Z.; Medříková, Z.; Král, M.; Šedajová, V.; Ranc, V.; Label-free determination of PSA and freePSA using MA-SERS. **Front. Anal. Sci.** 2022, 2, 847730. <https://doi.org/10.3389/frans.2022.847730>

- (15) Panáček, D.; Zdražil, L.; Langer, M.; Šedajová, V.; Baďura, Z.; Zoppellaro, G.; Yang, Q.; Nguyen, P.E.; Álvarez, R.; Hrubý, V.; Kolařík, J.; Chalmes, N.; Bourlinos, A.B.; Zbořil, R.; Merkoçi, A.; Bakandritsos, A.; Otyepka, M. Graphene Nanobeacons with High-Affinity Pockets for Combined, Selective, and Effective Decontamination and Reagentless Detection of Heavy Metals **Small** 2022, 18, 2201003. <https://doi.org/10.1002/sml.202201003>  
a. IF=13.3
- (16) A. Inman, V. Šedajová, K. Matthews, J. Gravlin, J. Busa, C. E. Shuck, A. VahidMohammadi, A. Bakandritsos, M. Shekhirev, M. Otyepka and Y. Gogotsi, **J. Mater. Res.** Shear delamination of multilayer MXenes. Just accepted. <https://doi.org/10.1557/s43578-022-00690-3>.  
a. IF=2.9

## Table of contents

1	INTRODUCTION.....	8
1.1	Graphene.....	9
1.1	Functionalization of graphene .....	11
1.1.1	Non-covalent approaches .....	12
1.1.2	Covalent approaches .....	13
1.2	Fluorographene.....	14
1.3	Graphene derivatives in electrochemical applications - supercapacitors .....	15
2	AIM OF THE THESIS.....	17
3	RESULTS AND DISCUSSION .....	18
3.1	Nitrogen Doped Graphene with Diamond-like Bonds Achieves Unprecedented Energy Density at High Power in a Symmetric Sustainable Supercapacitor .....	18
	Introduction .....	18
	Results .....	19
	Conclusions .....	24
3.2	Graphene with Covalently Grafted Amino Acid as a Route Toward Eco-Friendly and Sustainable Supercapacitors.....	25
	Introduction .....	25
	Results .....	25
	Conclusions .....	29
3.3	New Limits for Stability of Supercapacitor Electrode Material Based on Graphene Derivative .....	30
	Introduction .....	30
	Results .....	31
	Conclusions .....	34
4	SUMMARY .....	35
5	ZÁVĚR.....	36
6	REFERENCES.....	37





# 1 INTRODUCTION

It has been almost twenty years since the discovery of graphene. Nevertheless, graphene and its derivatives are still being intensively studied and investigated throughout the scientific world. With such promising properties, a broad portfolio of synthetic procedures, applications and/or theoretical studies was already published. However, there are still many possible ways to expand knowledge in this exciting field.

Graphene, as one atom thick carbon layer with  $sp^2$  hybridization, honeycomb lattice, and aromatic network, comes with relatively low reactivity of graphene itself. Moreover, combined with graphene's zero band gap and hydrophobicity, these facts spurred the research directions towards graphene derivatives with non-zero band gap with tunable functional groups.

Fluorographene (exfoliated graphite fluoride) is a graphene derivative having a fluorine atom bonded on every carbon. Its rich chemistry provides an easy pathway to prepare homogeneously and highly chemically functionalized graphene derivatives because the fluorographene's reactivity is much higher than graphene's.

Within this work, new ways of chemical functionalization of graphene were pursued with a focus on tuning the materials' properties toward energy storage applications. The aim was to yield highly conductive functionalized graphene derivatives, which will preferably have redox-active groups grafted or nitrogen atoms introduced into the graphenic lattice to improve their properties.

Firstly, nitrogen superdoped graphene was synthesized with diamond-like interlayer bonds with exceptionally high mass density. Secondly, amino-acid functionalized, as well as carboxyl group functionalized, graphene derivatives were prepared via the intense study and tailored synthetic protocols utilizing the fluorographene chemistry.

In the frame of this thesis, all materials were utilized in the energy storage field application as highly stable and exceptionally performing supercapacitor active electrode materials.

## 1.1 Graphene

Graphene, a two-dimensional carbon-based material, is a one-atom thin single layer of graphite. It was first predicted theoretically in 1947<sup>1</sup> and experimentally prepared during the next 50 years<sup>2,3</sup>. In 2004, Geim and Novoselov published their breakthrough re-discovery and characterization of graphene<sup>4</sup>. It disproved the long-standing claim that strictly 2D crystals can not be thermodynamically stable – therefore exist<sup>5,6</sup>. Alongside graphene, the boron nitride was another example of stable 2D material<sup>7</sup>. The years of 2004 and 2005 started incredible research interest in novel low-dimensional materials due to their very intriguing properties and promising applicability.

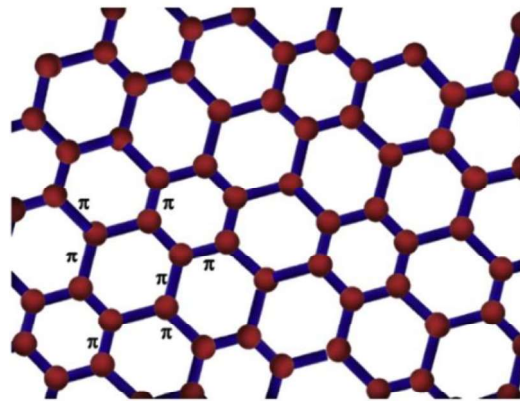


Figure 1 The schematic representation of a graphene's structure. Adapted from ref<sup>8</sup>

Graphene consists of units of six  $sp^2$ -carbon atoms tightly bonded in hexagonal, honeycomb-like rings, forming a conductive network thanks to the delocalized electrons in  $\pi$ - orbitals (Figure 1). This electron cloud, perpendicular to the graphene layer, is the reason behind the exceptional electrical conductivity but also the chemical inertness of the graphene<sup>9</sup>. Such properties offer a possibility of multiple applications in the fields of electronics, sensors, biosystems, or as protective layers against corrosions. The crystallographic studies revealed two sublattices, A and B, in the graphene structure, as shown in Figure 2.

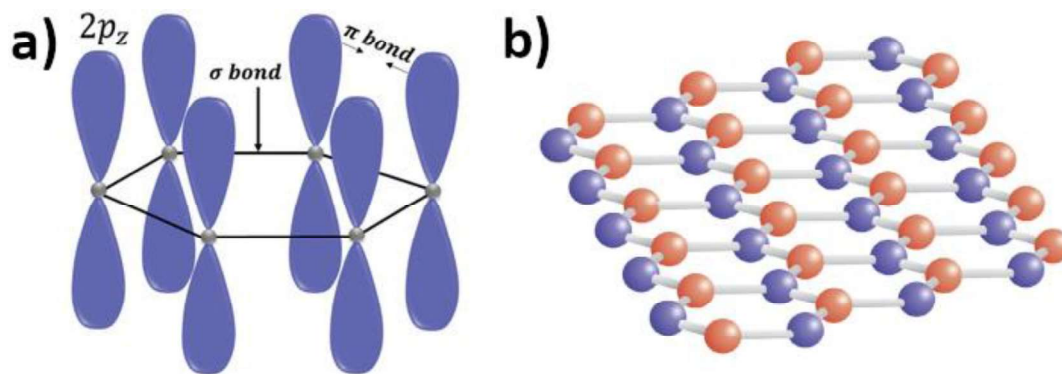


Figure 2 a) The schematic showing  $p_z$ -orbitals of graphene with  $\sigma$ - and  $\pi$ - bonds. Adapted from ref<sup>10</sup>. b) Crystallographic sublattices A (red atoms) and B (blue atoms). Adapted from ref<sup>11</sup>

Most of the materials have some defects: including graphene. During synthesis and preparation of graphene, there are always defects, such as vacancies, different edge configurations, or impurities, which all alter its properties. Defects change graphene's chemical and electronic properties since they act as centres of activity. Targeted interactions on the defects can lead to the proper identification of the defects<sup>12</sup> and toward the modification of the electronic structure of graphene.<sup>8,12–26</sup>

The above-listed properties suggest that graphene is a two-dimensional material with extraordinary properties. However, a few obstructive properties have an immense negative impact on the direct application potential. Zero band-gap, dispersibility and self-aggregation are all among these undesirable properties. The direct use of graphene in semiconductor passive parts is disallowed due to the zero band gap, a significant flaw in the electronics world. Pristine graphene is hydrophobic and can be dispersed only in solvents with high surface tension<sup>27</sup>, insoluble in most traditional solvents and self-aggregating due to  $\pi$ - $\pi$  interactions, disrupting the ease of processing dispersions of graphene mainly for scale-up synthesis and usage.

Identifying tailored procedures to overcome these bottlenecks of pure graphene monolayers is a crucial step toward wide graphene use in daily life. The facilitation of multifunctional applications of graphene is of immense interest due to its exciting properties and potential to replace some of the critical elements, environmentally non-friendly elements and compounds or to replace current technologies already at their fundamental limit (like Si-based technology). Functionalization of graphene is a solution to graphene's issues.

## 1.1 Functionalization of graphene

Functionalization of graphene or its derivatives via different methods and approaches is a vital way to increase the competitive strength of graphene in many applications since functionalization causes the opening of a band-gap, better dispersibility, reduces the re-stacking of graphene sheets. Moreover, functionalization is a way of imprinting desired properties in the graphene based materials.

Covalent attachment or non-covalent interactions of various foreign compounds, atoms or molecules lead to a precisely controlled functionalization of a graphene single or multi-layers. Because the functionalized derivatives overcome the pristine graphene's struggles, they are widely used and precisely designed and synthesized in order to fit perfectly and exhibit extraordinary performance in the desired application, preferably better than current technologies.

This theoretical introduction will focus on the chemical functionalization of pure graphene and fluorographene, the latter as the main subject of the experimental part, excluding the functionalization of graphene oxide. The graphene oxide is a non-stoichiometric graphene derivative with various oxygen-bearing moieties, enabling a wide window of possible functionalities. However, the major disadvantage of graphene oxide is the presence of many different functional groups, including peroxides, carboxyls, hydroxyls, and epoxy groups. Such a variety causes low selectivity and non-specific interactions for any possible compounds used for functionalization because they can react with the different types of functionalities. Moreover, the functionalization of graphene oxide yields low conducting materials because the many moieties already disrupt the  $sp^2$  conductive network of the parent graphene oxide. Thus, the functionalization of graphene oxide will not be discussed in detail.<sup>24</sup>

Thanks to their unique and tunable properties, functionalized graphene derivatives are utilized in various applications (Figure 3), including catalysis<sup>28</sup>, water remediation<sup>29,30</sup>, bio-applications<sup>31</sup>, sensing<sup>32-34</sup>, hydrogen storage<sup>35</sup> or the field of energy storage<sup>36,37</sup>, closely related to the research done within this thesis.

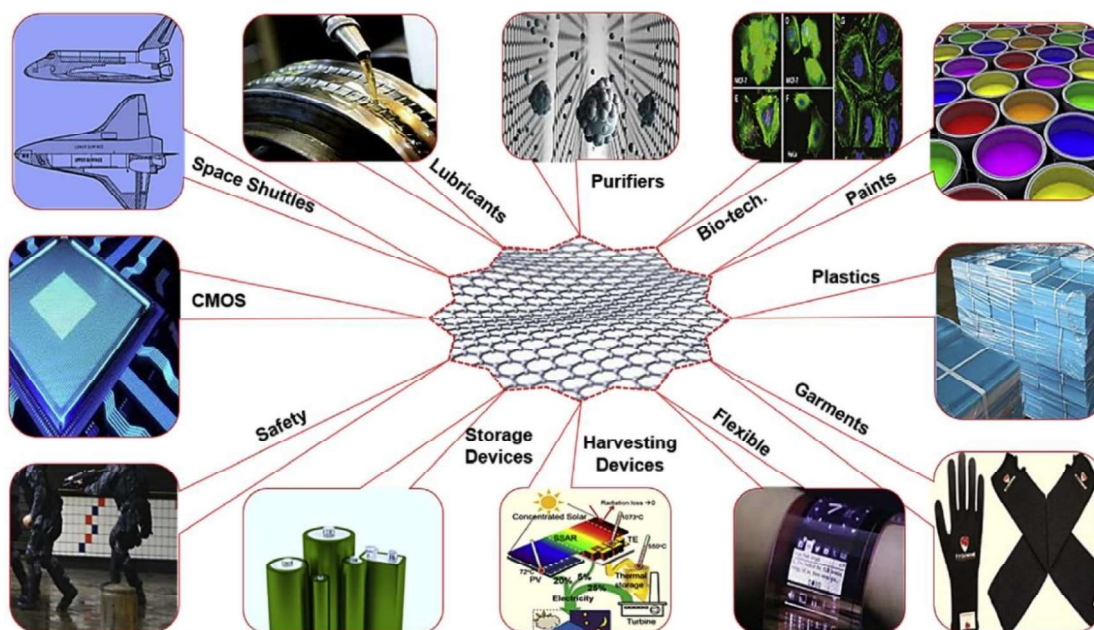


Figure 3 Schematic representation of the broad portfolio of the possible application utilizing functionalized graphene derivatives. Adapted from ref<sup>8</sup>

### 1.1.1 Non-covalent approaches

Non-covalent functionalization is an elegant way to improve graphene's intrinsic properties while retaining most features like pristine structure. It usually utilizes different types of non-covalent interactions, such as electrostatic or  $\pi$ -interactions, which offer effective synthetic methods for attaching functional groups without disrupting the conducting electronic network.<sup>16</sup> The  $\pi$ -interaction term encapsulates various attractive forces and also repulsive forces. Understanding which of them would prevail and would be beneficial during the preparation of non-covalently functionalized materials is crucial for designing synthetic pathways. (Figure 4).

- Hydrogen- $\pi$ -interaction
- $\pi$ - $\pi$ -interaction
- Cation- $\pi$ -interaction
- Anion- $\pi$ -interaction
- Other graphene-ligand interactions

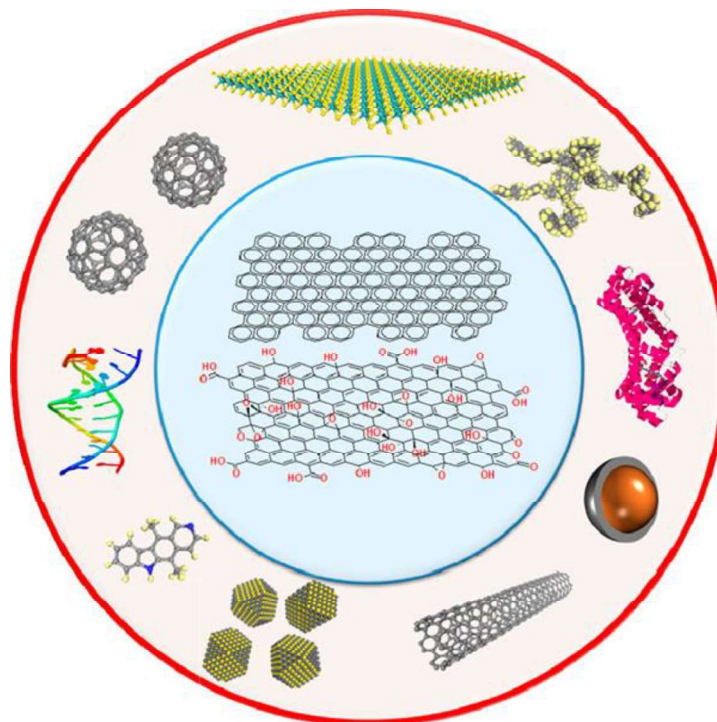


Figure 4 Schematic representation of a non-covalent functionalization of graphene and graphene oxide. Adapted from ref<sup>38</sup>.

### 1.1.2 Covalent approaches

Covalently grafted electron-donating or electron-withdrawing groups significantly alter graphene's electronic structure,  $\pi$ - $\pi$  conjugation system, and open its band gap. Moreover, the attachment considerably increases the dispersibility in commonly used solvents which is also connected to less re-stacking.<sup>23</sup> The advantage of the covalently functionalized graphene derivatives is their stability in different environments since the covalent bond is hardly broken and the possibility of the solid attachment of various functional groups.<sup>11,39</sup> Since several mechanisms allow for covalent attachment of groups onto the graphenic surface, the suitable one for every possible group can be chosen, each with its unique application potential. In order to covalently graft moieties on the low-reactive graphene flakes, there are synthetic pathways for preparing the derivatives directly from pristine graphene:<sup>12,19,20,23,40</sup>

- Nucleophilic addition:
- Cycloaddition: [2+1] cycloaddition, [2+2] cycloaddition, [3+2] cycloaddition, [4+2], mostly known as Diels-Alder, cycloaddition
- Radical reactions

- Substitution reaction
- Rearrangement

## 1.2 Fluorographene

Fluorographene, sometimes so-called “2D-teflon”, is a stoichiometric graphene derivative with a fluorine atom bonded to every carbon atom in a graphene-like structure. With a  $C_1F_1$  composition, it can exist in four different conformations – the most stable chair, followed by armchair, boat, and zig-zag. Both top-bottom and bottom-up synthetic approaches yield different compositions of fluorographene, resulting in varying properties depending on the coverage of fluorine ad-atoms.

Because the covalent attachment of fluorine atoms to the carbon atoms disrupts the  $\pi$ -conjugated system, fluorographene is the thinnest known insulator with a recently accurately theoretically calculated and experimentally verified (by means of DRIFT) bandgap of 5.7 eV.<sup>41</sup>

Moreover, the exceptional strength of the C-F bond is usually beneficial in the means of thermal stability and chemical inertness – therefore, the “nickname” 2D-Teflon. However, contrary to Teflon, fluorographene offers a plethora of possible reactions (Figure 5) thanks to the fluorine vacancies, partial positive charge on the carbanion and resulting nucleophilic substitution on such region in the fluorographene’s structure.<sup>42–44</sup>

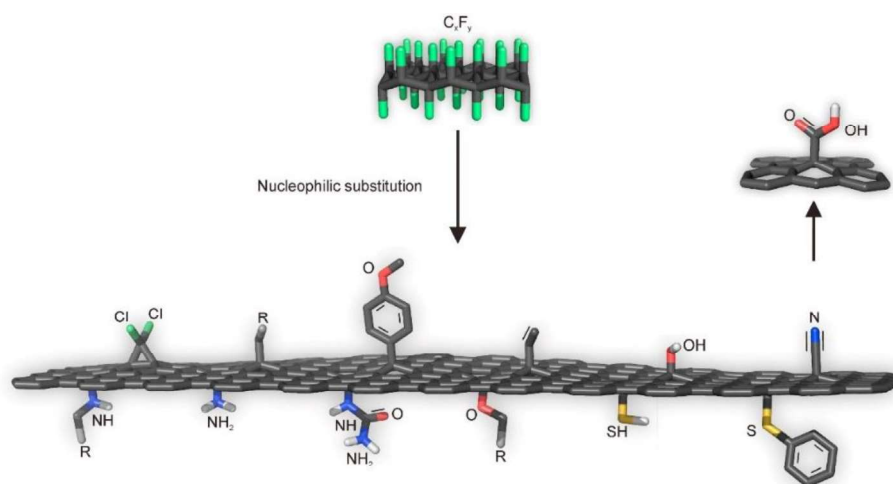


Figure 5 Examples of possible graphene derivatives synthesized via fluorographene chemistry. Adapted from ref<sup>45</sup>.

### 1.3 Graphene derivatives in electrochemical applications - supercapacitors

Graphene derivatives, thanks to their exceptional properties, found an application in many fields, as described thoroughly in many reports in the literature. One of the most promising fields is energy storage because carbon-based materials present a lightweight, conductive, cheap, stable and eco-friendly alternative to currently widely used technologies.

Inherent from graphene itself, graphene derivatives usually possess a large surface area and, depending on the degree of functionalization, also a substantial conductivity. The theoretical capacitance of graphene should reach up to  $550 \text{ F g}^{-1}$ .<sup>46</sup> However, most of the reports utilizing pure graphene/reduced graphene oxide do not exhibit such a high value, probably due to the restacking of the sheets and low wettability by the electrolyte. Therefore, both in-plane (heteroatom doping) and out-of-plane (functional groups) functionalization of graphene is very beneficial for increasing the surface area available for contact with electrolytes, as shown in Figure 6. Moreover, a possible introduction of redox-active molecules can boost the performance with pseudocapacitance contribution for the already inherent double-layer capacitance.

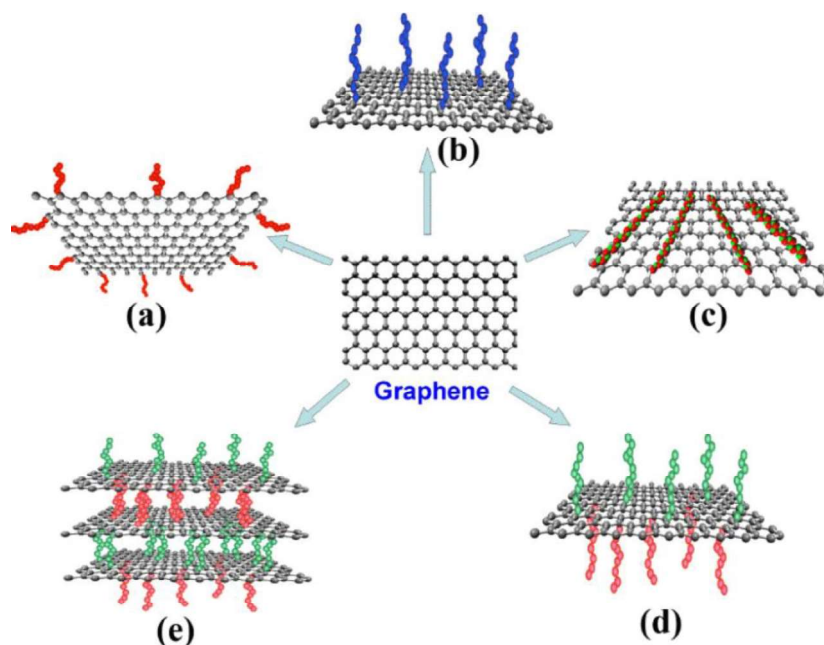


Figure 6 Overview of possible functionalization of graphene, such as a) on edge, b) – d) on the basal plane, and e) stacked into a layered structure. Adapted from ref<sup>47</sup>.

Fluorographene offers rich chemistry, yielding well-defined graphene derivatives with a low amount of residual fluorine and high functionalization degree. Since these



derivatives contain both conductive  $sp^2$  conjugated network and  $sp^3$  carbon bearing the functional groups, they offer precise tweaking of their conductivity.<sup>37,42,43,48</sup> Therefore, we can assume that fluorographene is a perfect precursor for synthesizing a broad portfolio of conductive, precisely tailored, functionalized derivatives with controlled properties and structure. These derivatives are forming a potentially large emerging new class of covalently functionalized graphene-based materials that offer very promising properties and performance for their application in the energy storage field.

## 2 AIM OF THE THESIS

This doctoral thesis aims to develop new covalently functionalized graphene derivatives, via fluorographene chemistry, with tailored properties targeting specific applications. As described previously, fluorographene offers higher reactivity than graphene. Thus, it enables a broad portfolio of possible reactions, yielding different graphene derivatives. Exploiting this chemistry, nitrogen-doped graphene, amino acid functionalized graphene, and graphene acid were prepared, characterized, and studied as active electrode materials in electrochemical energy storage applications, especially supercapacitors.

The aims of this thesis involve the in-depth description of the pathways to yield the three different graphene derivatives, their characterization, and their physicochemical and electrochemical properties:

- Firstly, a highly nitrogen doped graphene derivative (GN3) was prepared, further characterized, and used in energy storage application.
- Secondly, a new amino acid functionalized material was prepared and used as active electrode material in a sustainable supercapacitor.
- Lastly, an application study of highly functionalized graphene derivatives, graphene acid, was conducted to evaluate its performance as a supercapacitor focusing on the intrinsically good properties of graphene acid for utilization in energy storage.

This thesis provides an example of two strategies for precise designing and preparing chemically functionalized graphene derivatives for targeted use in the energy storage field. The tunable and efficient grafting of carefully selected moieties enabled a better performance than state-of-the-art in terms of energy content, power density or stability upon charging/discharging.

## 3 RESULTS AND DISCUSSION

This thesis's discussion comprises four publications dealing with functionalized graphene derivatives utilized in energy storage applications. The author of this thesis contributed as a first author in two of those publications<sup>49,50</sup> and as a co-author in the third one<sup>51</sup>.

### 3.1 Nitrogen Doped Graphene with Diamond-like Bonds Achieves Unprecedented Energy Density at High Power in a Symmetric Sustainable Supercapacitor

*Text adapted from*

- Šedajová, V.; Bakandritsos, A.; Błoński, P.; Medved', M.; Langer, R.; Zaoralová, D.; Ugolotti, J.; Džibelová, J.; Jakubec, P.; Kupka, V.; Otyepka, M. *Nitrogen Doped Graphene with Diamond-like Bonds Achieves Unprecedented Energy Density at High Power in a Symmetric Sustainable Supercapacitor*. *Energy Environ. Sci.* 2022, 15 (2), 740–748. <https://doi.org/10.1039/D1EE02234B>.

#### Introduction

Supercapacitors belong to the portfolio of energy storage devices with their extraordinary qualities, like fast charging/discharging and very long cycle-life.<sup>52</sup> Unfortunately, the energy density of the best existing supercapacitors (their amount of stored energy) is at low values. Commercial supercapacitors have cell-level specific energies (and energy densities) of 10 Wh kg<sup>-1</sup> (5-8 Wh L<sup>-1</sup>)<sup>53,54</sup>. In comparison, lead-acid batteries offer 20-35 Wh kg<sup>-1</sup> (40-80 Wh L<sup>-1</sup>)<sup>55</sup>, with the state-of-the-art Li-ion batteries achieving ~150 Wh kg<sup>-1</sup> (~250 Wh L<sup>-1</sup>).<sup>56,57</sup> However, the disadvantages of Li-ion batteries are well known, such as long charging/discharging times and short life cycle due to the irreversible processes during cycling. Identification of electrode materials with substantially improved energy densities combined with long life and high power is necessary to utilize the benefits of supercapacitors in a broader range of applications. Moreover, reducing our dependence on critical resources, increasing sustainability, and decreasing our carbon footprint are widely discussed targets. The replacement of metal atoms in electrode materials with earth-abundant, non-metallic elements, such as carbon, fits perfectly within the goals of the Green Deal.

Energy density is a crucial parameter in energy storage devices, making it a high priority target to improve<sup>53–55,58–61</sup>. The highest energy density reported to date was obtained using electrodes consisting of bilayers of exfoliated graphene-mediated hydrogen iodide-reduced graphene oxide (EGM-GO)<sup>62</sup> with a mass density of *ca.* 1 g cm<sup>-3</sup> exhibiting capacitance 203 F cm<sup>-3</sup> and, at that time, the record energy density of 113 Wh L<sup>-1</sup> at 0.9 kW L<sup>-1</sup> (current density 1 A g<sup>-1</sup>). Within this work, we reported a novel carbon-based electrode material, GN3, with an unprecedented mass density of 2.8 g cm<sup>-3</sup>. Its excellent ability to host ions surpasses commercially used porous materials (S.A. > 2000 m<sup>2</sup> g<sup>-1</sup>). GN3, with its extraordinary properties, achieved an energy density of 200 Wh L<sup>-1</sup> at a power density of 2.6 kW L<sup>-1</sup>, corresponding to improvements of 74% and 190%, respectively, over the previous record.<sup>62</sup>

## Results

Therefore, we experimentally and theoretically investigated a reaction of few-layered fluorographene with sodium azide. Sodium azide has a double role as a defluorinating and doping agent (introducing different configurations of nitrogen atoms inside the graphenic lattice). The functionalization increases the polarity and hydrophilicity of the carbon surface and creates vacancies, as previously studied through reactions of fluorographene with other nitrogen-containing nucleophiles.<sup>63–65</sup> Exfoliated fluorographene was subjected to a reaction with NaN<sub>3</sub> in dimethylformamide at 130 °C, yielding nitrogen-superdoped graphene (Figure 7). XPS revealed a significant decrease in the atomic content of 4h byproduct, followed by almost complete defluorination after 72h. Moreover, the GN3 material's N content reached 16.1 at.% after the reaction also reflected in the C1s deconvolutions. The carbon atoms, initially bonded with fluorine (binding energies above 289.5 eV), were transformed during the synthesis into aromatic *sp*<sup>2</sup> carbons (284.7 eV, 45%), non-functionalized *sp*<sup>3</sup> carbons (285.5 eV, 25%), and nitrogen bonded carbons (286.6 eV, 19%), respectively. The other components are related to the residual amounts of fluorine (the non-reactive CF<sub>2</sub> species on the edges) and carbon atoms bonded to oxygen (coming from the environment).

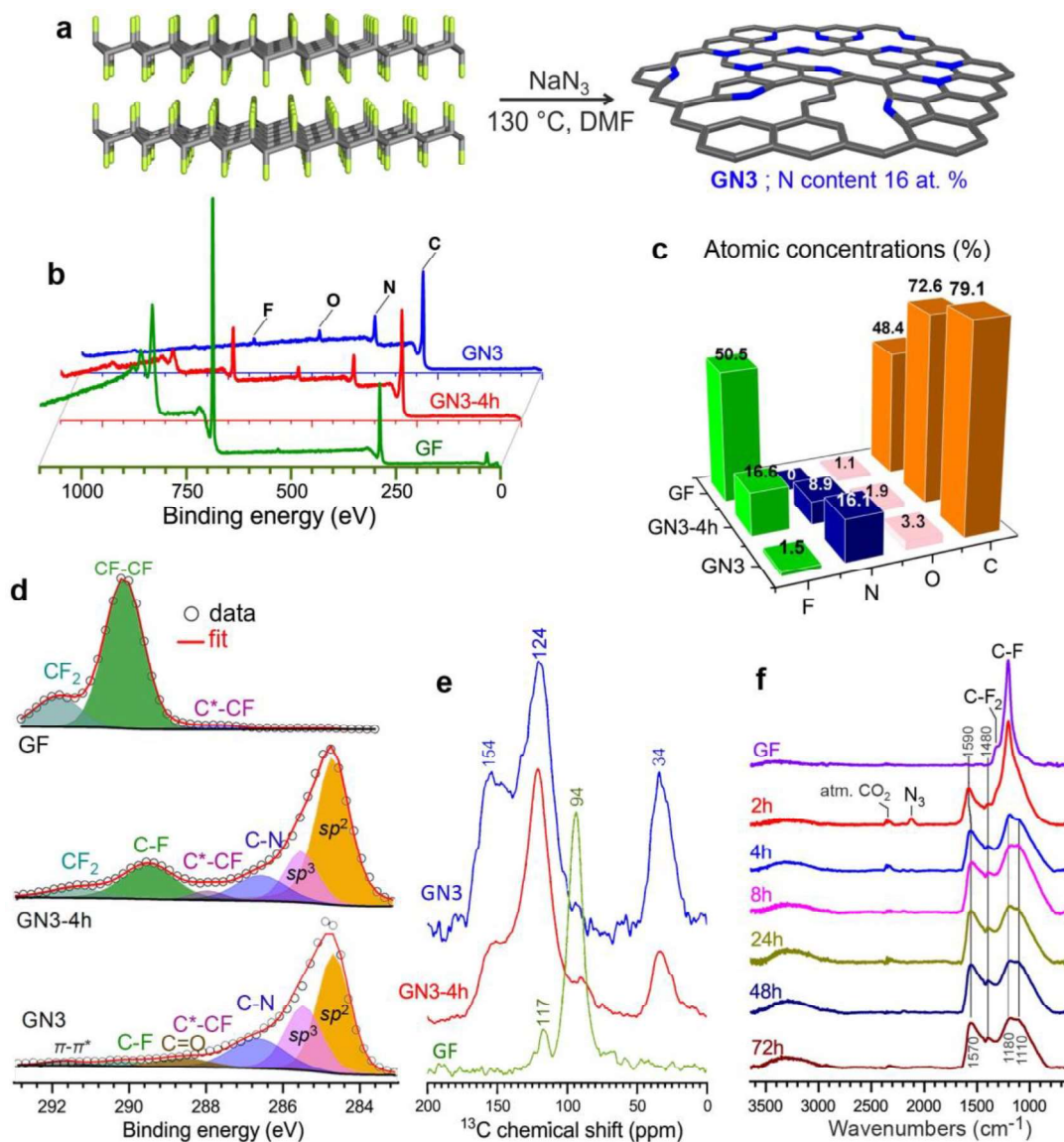


Figure 7 (a) Schematic depiction of the synthesis of GN3. (b)-(d) XPS characterization and deconvolutions. (e) CP MAS  $^{13}\text{C}$  solid-state NMR and (f) FT-IR spectra of starting product, byproducts, and final material.

The  $^1\text{H}\rightarrow^{13}\text{C}$  CP MAS solid-state NMR spectra (Figure 7) showed peaks at 34 ppm typical for non-functionalized and non-nitrogen bonded  $sp^3$  carbons in diamond and diamond-like carbon materials.<sup>66</sup> This peak was more intense in the spectrum of GN3 final material than in the GN3-4h intermediate, indicating that these  $sp^3$  carbons were formed as the reaction progressed. Moreover, the presence of a  $\pi$ -conjugated aromatic network and aromatic  $>\text{C}=\text{N}$  moieties (pyridinic and pyrrolic)<sup>66,67</sup> was confirmed by the peaks centered at 124 and 154 ppm, respectively.

The FTIR technique provided thorough insights into the reaction mechanism; specifically, the bands of the CF and  $\text{CF}_2$  groups of GF ( $1200$  and  $1305\text{ cm}^{-1}$ ,

respectively) were progressively replaced with bands at 1580 and 1210  $\text{cm}^{-1}$  (characteristic of aromatic carbon rings<sup>68</sup>), indicating the defluorination and formation of an  $sp^2$  network (Figure 7). Additional aromatic-ring vibrations, corresponding to the band at 1400  $\text{cm}^{-1}$ , can be assigned to a heteroatom substitution (e.g., with pyridinic nitrogens<sup>68,69</sup>), as suggested using theoretical calculations.<sup>70,71</sup>

The high-resolution transmission electron microscopy (HR-TEM) revealed that the nature of the GN3 structure is indeed 2D sheets with a very holey design, as shown in Figure 8. EDXS elemental mapping with high-angle annular dark-field scanning transmission electron microscopy (HAADF-STEM, Figure 8) showed that the GN3 sheets are densely and homogeneously doped with nitrogen atoms inside the graphenic lattice.

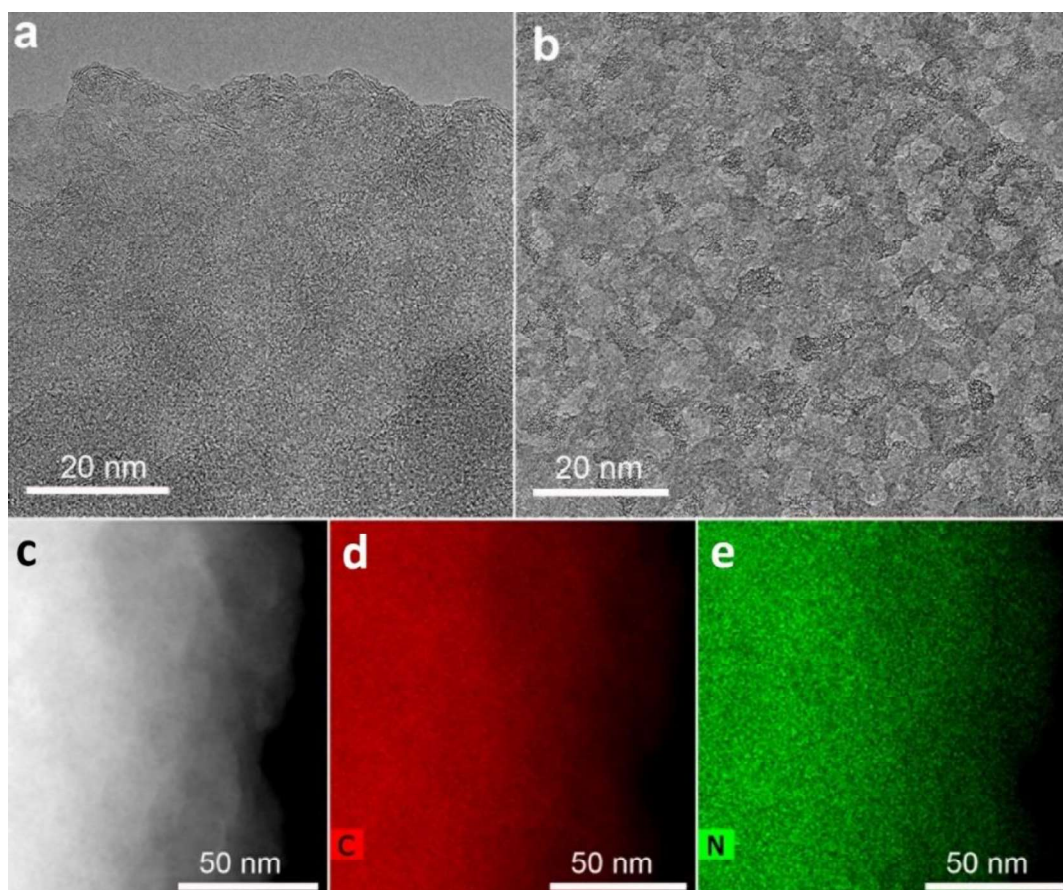


Figure 8 HR-TEM images of the GN3 material alongside the EDS mapping of carbon and nitrogen.

Pasted films of GN3 material with additives (polymer binder PTFE at 10%wt; conductive additive TimCal at 5%wt.) were prepared via the Dr. Blade technique by pasting homogeneous slurries on Al foil for density measurements and preparation

of supercapacitor electrodes. Thickness measurements using SEM<sup>49</sup> and digital micrometer (Figure 9) showed that pressing the film between two metallic plates for 1 min at 80 kN caused bed consolidation of the material, increasing the mass density of the material to 2.75 g cm<sup>-3</sup> compared to 0.5 g cm<sup>-3</sup> before pressing.

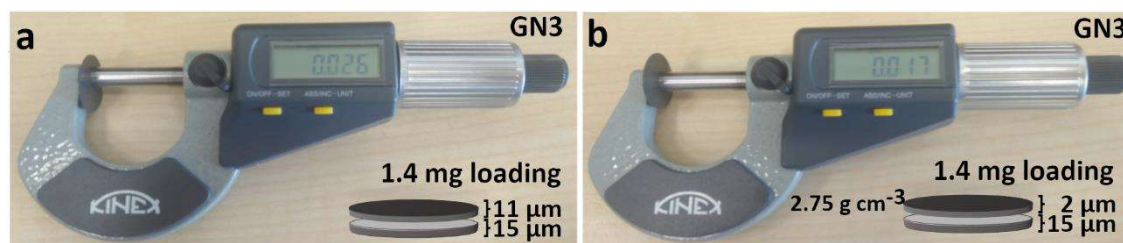


Figure 9 Photos of a digital micrometer with GN3 electrodes before and after pressing at 80 kN for 1 minute.

All the above-mentioned properties predetermined the GN3 material to be superior in energy storage applications, especially in supercapacitors. Briefly, the electrochemical properties of GN3 were studied in a symmetric system in an organic electrolyte (1-ethyl-3-methylimidazolium tetrafluoroborate EMIM-BF<sub>4</sub> with 1,1,2,2-tetrafluoroethyl-2,2,3,3-tetrafluoropropyl ether TTE in a 9:1 ratio).

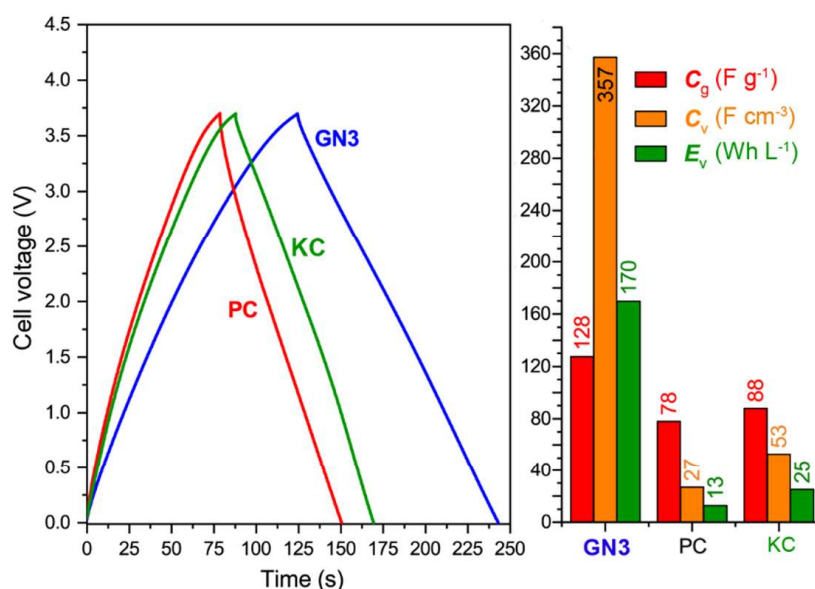


Figure 10 Comparison of (a) GCD curves and (b) energy storage values at 2 A g<sup>-1</sup> of the GN3 material with porous carbons.

Moreover, as proper benchmark materials, the carbons PC and KC<sup>72</sup> were tested under identical conditions. GN3 material had a significantly better discharging time (Figure 10) than PC and KC. Despite the dramatic difference in the BET surface area of the GN3 materials and the very porous carbon materials, GN3 exhibited superior performance in both volumetric and gravimetric terms, dominating mainly the volumetric values owing to its high mass density.

Volumetric performance is crucial for devices in the portable energy storage landscape;<sup>53,55,58,59,62,73</sup> when both high energy and high power density are desirable at the same time. The former directly affects the amount of energy that can be stored, while the latter allows for fast charging and discharging. Energy density is the usual weak point of supercapacitors, whereas high power densities are one of their benefits, which must be preserved. The GN3 cell (Figure 11) demonstrated ground-breaking performance by delivering simultaneously ultrahigh energy density and power density, especially when its energy density was *ca.* 200 Wh L<sup>-1</sup> at a power of 2.6 kW L<sup>-1</sup> and 143 Wh L<sup>-1</sup> at 52 kW L<sup>-1</sup>. In order to compare our results with the current state of the art, we had selected top-performing materials from the field, as can be found in Figure 11 (when the same sets of equations and metrics were used in all cases<sup>62</sup>).

Lastly, the GN3 cell could also be operated at commercially relevant mass loadings of up to 10 mg cm<sup>-2</sup>, demonstrating 99% retention of low-mass loading capacitance at a temperature of 38 °C, which is in the range typically used to evaluate energy storage devices,<sup>74-77</sup>.

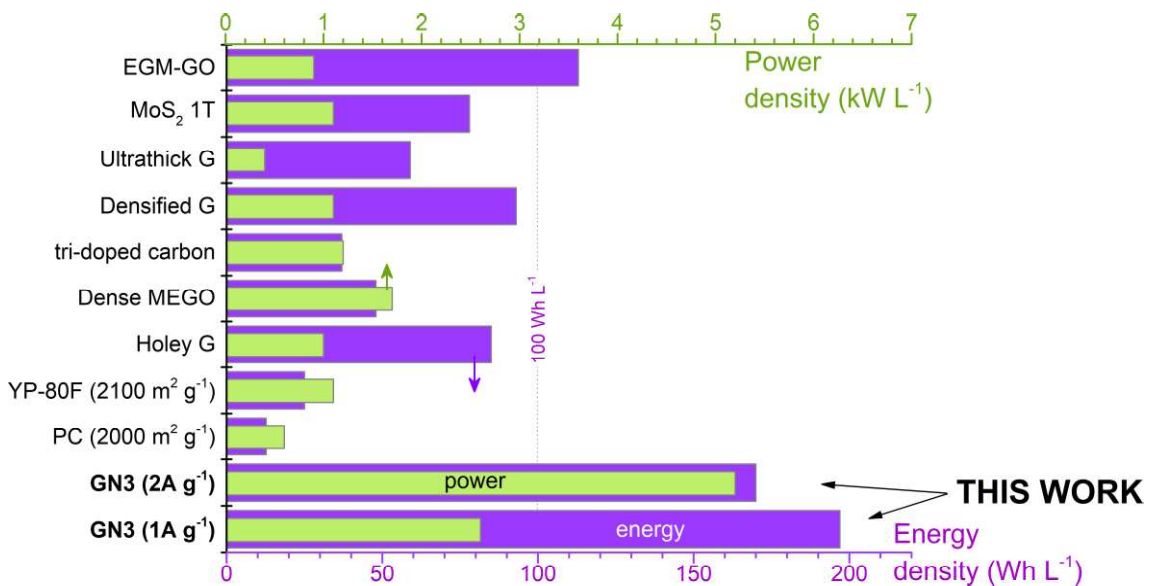


Figure 11 State-of-the-art comparison of the previously published report and this work's results.



## Conclusions

In the frame of this work, we have reported a new class of carbon-based materials featuring nitrogen-doped graphene with diamond tetrahedral bonds for high energy density supercapacitor electrodes. The new materials are prepared by utilizing radical-based FG chemistry, allowing the beneficial combination of  $sp^2$  and  $sp^3$  carbon bonds in the same network alongside very high nitrogen doping and vacancies. This hybrid carbon achieves a mass density of  $2.8 \text{ g cm}^{-3}$  while maintaining efficient charge transport, ion penetration, diffusion, and storage, even at commercial level mass loading. Specifically, its energy density was approximately  $200 \text{ Wh L}^{-1}$  at  $2.6 \text{ kW L}^{-1}$  and  $143 \text{ Wh L}^{-1}$  at  $52 \text{ kW L}^{-1}$ , well above the state-of-the-art literature reports.

## 3.2 Graphene with Covalently Grafted Amino Acid as a Route Toward Eco-Friendly and Sustainable Supercapacitors

*Text adapted from*

- Vermisoglou, E. C.; Jakubec, P.; Bakandritsos, A.; Kupka, V.; Pykal, M.; Šedajová, V.; Vlček, J.; Tomanec, O.; Scheibe, M.; Zbořil, R.; Otyepka, M. *Graphene with Covalently Grafted Amino Acid as a Route Toward Eco-Friendly and Sustainable Supercapacitors. ChemSusChem* 2021, 14 (18), 3904–3914. <https://doi.org/10.1002/cssc.202101039>.

### Introduction

As mentioned above, direct covalent functionalization of graphene is hard to achieve. Fluorographene chemistry circumvents this obstacle, enabling a broad portfolio of graphene derivatives to be synthesized with covalently attached functional groups. The starting material, graphite fluoride, is well abundant (production in tons) because of its use industrially as a lubricant.

This presented work reported a synthesis of zwitterionic arginine-functionalized FG (FG/Arg). The guanidino functional group on arginine acted as a nucleophile and caused grafting on FG through the nucleophilic attack. The initiation is known to be caused by the electrophilic radical centres at the defect sites of FG.<sup>78,79</sup> Employment of tert-butoxycarbonyl (Boc) protected Arg was necessary in order to protect the amino acid from the random attachment of the arginine onto FG. Afterwards, the arginine already covalently grafted on the FG was deprotected from the Boc group.

These presented findings showed that this strategy of covalent functionalization of graphene tuned three key factors important in energy storage application - conductivity, FD, and porosity.<sup>80</sup> The synthesized material represents eco-friendly Arg-functionalized graphene that could be used as an efficient supercapacitor in aqueous electrolytes.

### Results

The reaction leading to the covalent functionalization of FG with Arg is shown in Figure 12. First, the FG reacted through nucleophilic attack with the primary guanidino amine of Boc-Arg-OH, followed by the deprotection of FG/Boc with hydrochloric acid under heating.

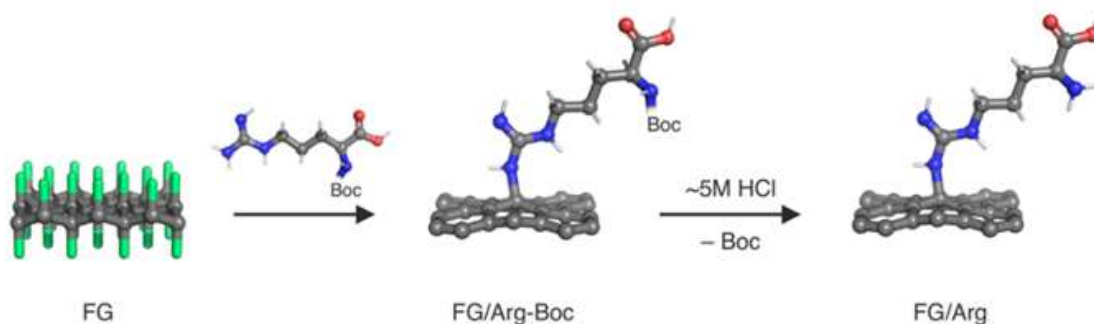


Figure 12 Scheme illustrating FG reaction with Boc-Arg-OH, followed by removal of the Boc protecting group, resulting in the FG/Arg product. Colour coding is as follows: carbon – grey; fluorine – green; nitrogen – blue; oxygen – red.

FTIR measurements confirmed the successful removal of the Boc-protecting group and the presence of a free out-of-plane amino group in the final product (Figure 2), as well as provided direct evidence for the functionalization of FG with Arg. The spectrum of FG/Boc-48h shows the distinctive band of N-H stretching vibrations at  $3187\text{ cm}^{-1}$ , attributed to the secondary amine. The FG/Arg-48h product exhibited the O-H vibration (broad band below  $3500\text{ cm}^{-1}$ ), directly overlapping with a second N-H stretching vibration band attributed to the deprotected primary amine.<sup>81,82</sup> Boc protecting group in the deprotected product was proved by the two weak bands at  $\sim 2800\text{-}2950\text{ cm}^{-1}$ , attributed to C-H stretching vibrations of present methyls.<sup>81</sup>

The byproducts and final products were evaluated by XPS to compare the atomic ratios. The results showed a significant loss of F atoms with time up to 48 h (decrease from 55.7 at.% of fluorine to 3.2 at.%), which was further reduced by adding the potassium carbonate (2 at.% of fluorine). The complete atomic composition of the FG/Arg-48h product is 76.4 at.% of carbon, 13.7 at.% of nitrogen, 6.6 at.% of oxygen and 3.3 at.% of fluorine, respectively.

High-resolution C 1s XPS spectra of the parent material and the covalently functionalized graphene derivative FG/Arg-48h are presented in Figure 13. The deconvolution the C1s region of both materials resulted in the evident differences of the deconvoluted components: C-C ( $\text{sp}^2$ ), C-C ( $\text{sp}^3$ ), C-N, C\*-C-F, O=C-O, C-F and  $\text{CF}_2$ . As the reaction time increased, the area percentage of C-F decreased, reaching a value of 4.3% in the C 1s area in sample treated for 48 h, before remaining constant with further time increases.

The formation of the functionalized graphene derivative was further proved by means of Raman spectroscopy. Two characteristic bands D ( $1332\text{ cm}^{-1}$ ) and G ( $1595\text{ cm}^{-1}$ ) bands were present in the spectra of both prepared samples. The FG/Arg-48h exhibited a ratio  $I_D/I_G$  of 1.32 ( $>1$ ), reflecting the high FD as well as the presence of  $\text{sp}^3$  hybridized carbon atoms.<sup>80,83</sup>

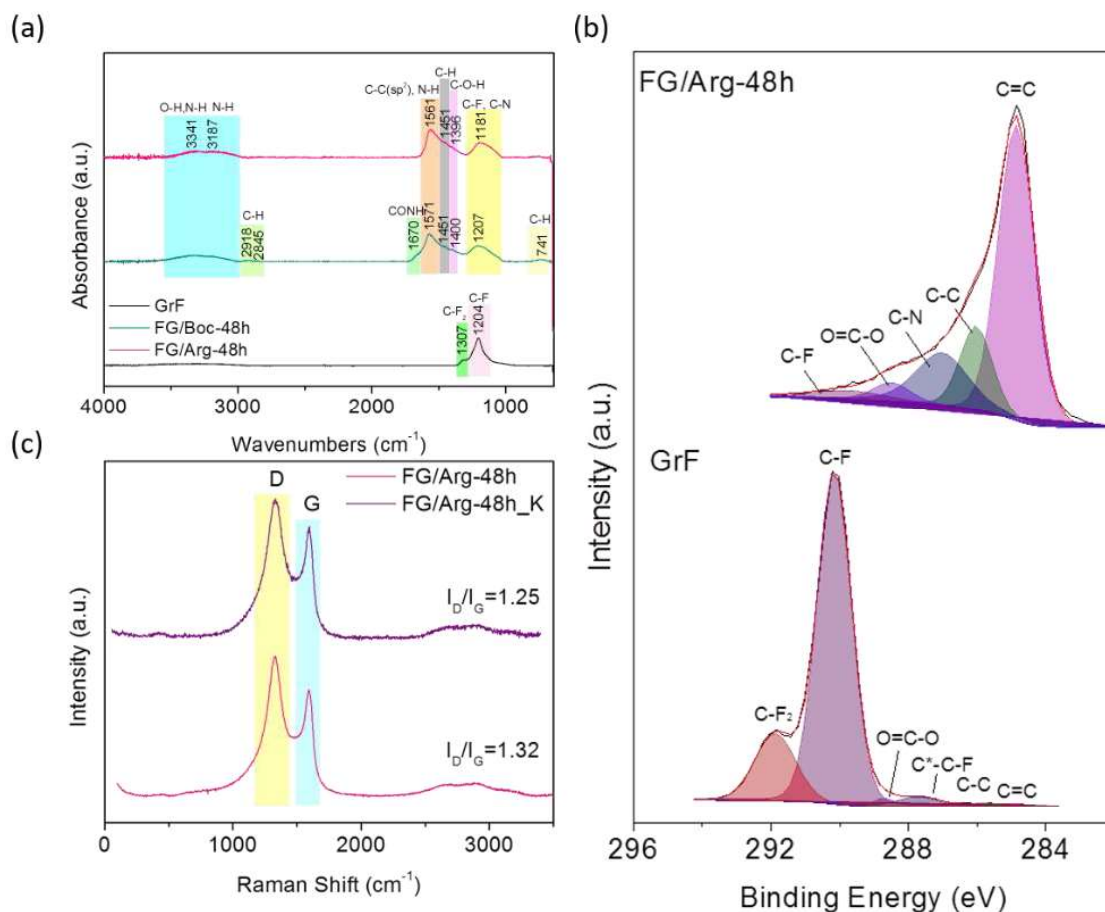


Figure 13 (a) FTIR spectra of GrF, FG/Boc-48h and FG/Arg-48h. (b) High resolution C1s XPS spectra of the parent material GrF and final product FG/Arg-48h. (c) Raman spectra of FG/Arg-48h and FG/Arg-48h\_K samples.

TEM techniques (Figure 14) revealed thin flakes, indicative of exfoliated materials, of FG/Arg-48h\_K sample. The edges of the FG/Arg-48h\_K sheets in HR-TEM images were almost transparent, indicating that this material's thickness is only a few graphenic layers. Elemental mapping of FG/Arg-48h\_K (Figure 14d-i) revealed homogeneous grafting of functional groups throughout the flake's surface. Potassium was removed entirely during thermal treatment with hydrochloric acid. As evident, a high density of functional groups was distributed uniformly across the surface of the graphene flakes. This homogeneity in distribution and the precise type of covalently

grafted functional groups are significant advantages of FG chemistry compared to GO chemistry.

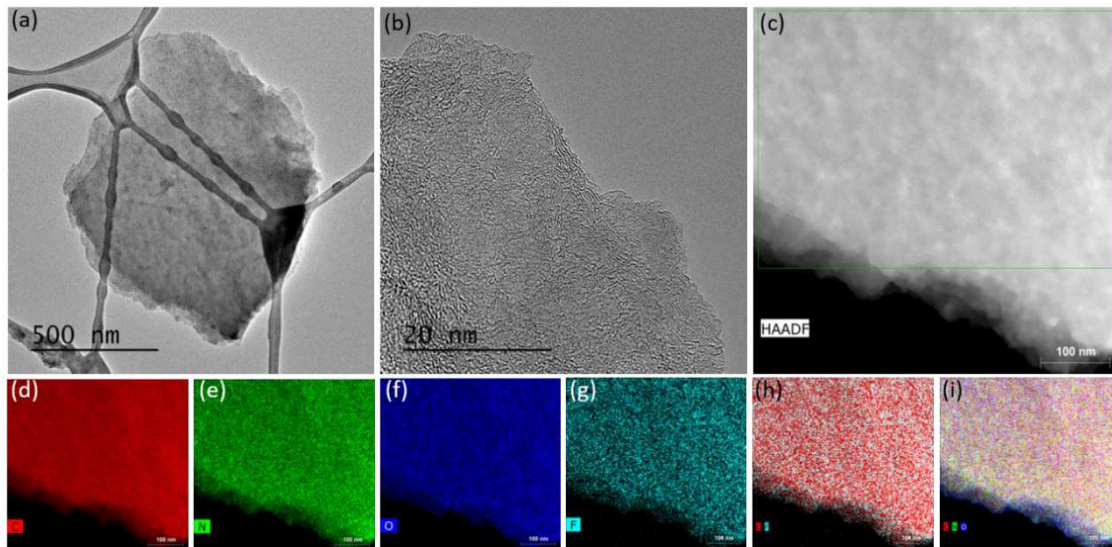


Figure 14 (a) TEM and (b) HRTEM images of a FG/Arg-48h\_K sample. (c) Dark field HRTEM image of FG/Arg-48h\_K and corresponding chemical mapping: (d) carbon map, (e) nitrogen map, (f) oxygen map, (g) fluorine map, (h) carbon-fluorine map, and (i) carbon-nitrogen-oxygen combined map.

In order to enhance the double-layer capacitance component of the FG/Arg-48h sample, the sample with increased SSA and a microporous structure was prepared using potassium carbonate, as described in the previous section.

A symmetric supercapacitor in a two-electrode setup with 1 M  $\text{H}_2\text{SO}_4$  as an electrolyte was assembled to evaluate the performance of the FG/Arg-48h\_K sample. Figure 15 shows the GCD profiles of FG/Arg-48h\_K using current densities from 0.1  $\text{A g}^{-1}$  to 5  $\text{A g}^{-1}$ . It can be seen that the shape of the GCD curves is significantly more symmetrical, suggesting enhanced diffusion of the ions inside the electrochemical cell. The rate test revealed outstanding stability of the capacitive response across the wide range of current densities. Moreover, the life-time stability test confirmed the stability of the FG/Arg-48\_K sample, resulting in capacitance retention of 82.3 % after 30,000 GCD cycles.

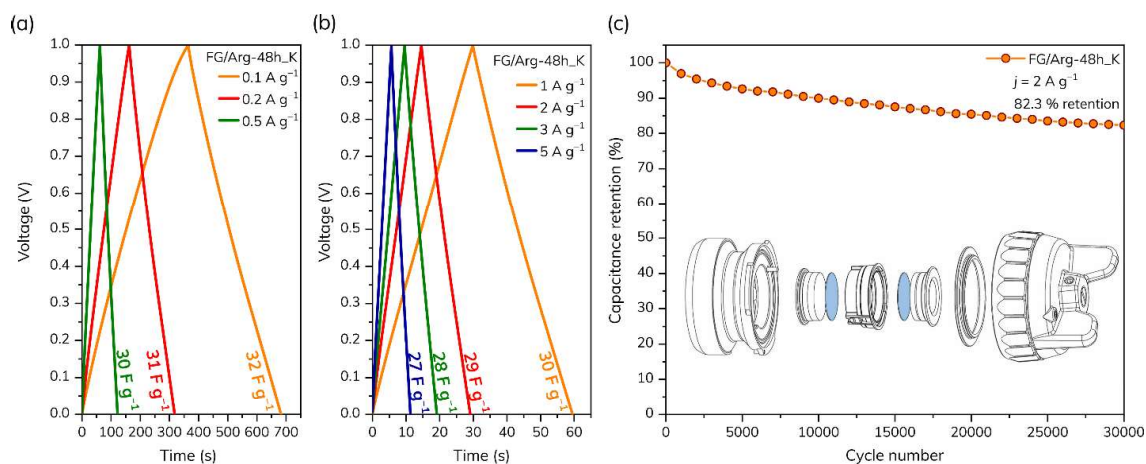


Figure 15 (a), (b) GCD profiles of FG/Arg-48h\_K recorded at different current densities. (c) Stability of FG/Arg-48h\_K after 30,000 GCD cycles.

## Conclusions

This presented work reported a successful synthesis of covalently functionalized graphene derivative with arginine to a graphene surface by reacting arginine was grafted via its guanidine group homogeneously on both sides of graphene (3.7 % functionalization degree). The best performing sample in supercapacitor application was treated with a pore-forming agent, potassium carbonate, directly boosting the capacitive performance ( $\sim 390 \text{ F g}^{-1}$  at a current density of  $0.25 \text{ A g}^{-1}$ ). After 30,000 charging/discharging cycles at a current density of  $2 \text{ A g}^{-1}$ , the capacitance retained over 80 %. Therefore, as well as being eco-friendly, the material exhibited outstanding sustainability with promising properties for supercapacitor materials. Moreover, adopting the strategy of successful covalent grafting of particular functional groups on the surface of graphene paves the way for the development of energy storage devices with significantly improved electrochemical performance and stability.

### 3.3 New Limits for Stability of Supercapacitor Electrode Material Based on Graphene Derivative

*Text adapted from*

- Šedajová, V.; Jakubec, P.; Bakandritsos, A.; Ranc, V.; Otyepka, M. *New Limits for Stability of Supercapacitor Electrode Material Based on Graphene Derivative. Nanomaterials* 2020, 10 (9), 1731. <https://doi.org/10.3390/nano10091731>.

#### Introduction

Carbon-based materials' surface is prone to be functionalized via different routes to graft various functional groups, as discussed previously in this thesis. Our group reported that such modifications boost electrochemical stability, capacitive performance, and rate performance<sup>84,85</sup>. As oxygen-containing groups are present in most carbon-based materials due to the reactions in the air atmosphere, targeted utilization would offer a promising strategy for improving the capacitive performance. The insertion of oxygen-containing groups positively affects a material's wettability, hydrophilicity, and pseudocapacitive behaviour. Thanks to the oxygen functionalities, the material is less restacked due to electrostatic interactions; increased wettability enhances the contact between the active material and electrolyte<sup>86</sup>. Oxygen-containing functionalities are usually involved in fast redox reactions, increasing the pseudocapacitance contribution<sup>87</sup>. However, it is of high importance that the oxygen-containing groups would be covalently attached in a stable form, such as carboxylic groups, to prevent possible decomposition, high self-discharge rates, or increased leakage current<sup>88</sup>.

The presented studies investigated the pseudocapacitive behaviour of graphene acid (GA)<sup>89</sup> as a supercapacitor electrode material<sup>50</sup>. GA is a highly conductive, hydrophilic graphene derivative, functionalized with carboxyl groups, which are homogeneously dispersed among the graphene surface<sup>89</sup>. GA was already employed with excellent results in electrochemical sensing<sup>90</sup>, catalysis<sup>91–93</sup> and electrocatalysis<sup>94</sup>.

This paper focused on describing the pseudocapacitive behaviour of GA in an acidic electrolyte in supercapacitor application. Contrary to most published reports, we showed the excellent reproducibility of the synthesis, with variations in the individual measurements. The graphene acid was tremendously stable, exhibiting 95% specific capacitance retention after 60,000 cycles in a two-electrode cell and high rate stability.

These findings again show that covalently functionalized graphene derivatives provide a solution for supercapacitor metal-free electrode materials.

## Results

Graphene acid was synthesized based on an already published report<sup>95</sup>. However, we decided to repeat the synthesis three times and perform a thorough characterization, focusing on the reproducibility of the synthesis. The XRD showed two broad peaks at 29° and 50°, corresponding to the (0 0 2) and (1 0 1) planes, respectively, characteristic for stacked sheets with short-range order in amorphous structure<sup>96</sup>. The d-space value of 0.3579 nm, calculated from the 29° peak, is slightly higher than the one of graphite (inset of Figure 16 (a)). A Raman spectrum of GA revealed two well-known peaks, D-band related to defects and vacancies and G-band related to the aromatic sp<sup>2</sup> structure.<sup>97,98</sup> The I<sub>D</sub>/I<sub>G</sub> ratio of 1.69 confirms the suggested structure of GA, with out-of-plane functionalities, but retaining the sp<sup>2</sup> structure responsible for the conductivity, which was noted in previously highly functionalized graphene derivatives.<sup>37,51,84,85,99</sup>

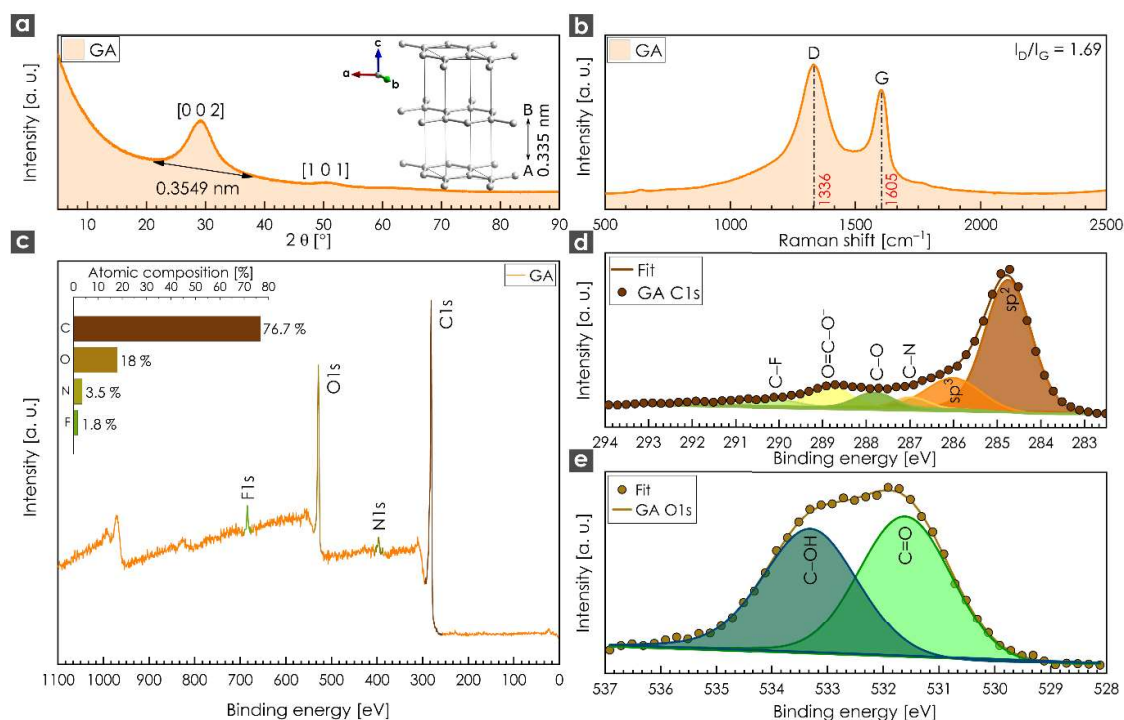


Figure 16 Structural characterization of GA material, (a) XRD and (b) Raman spectra. (c)-(e) XPS evaluation of GA.

An XPS survey spectrum (Figure 16) revealed the atomic composition as follows: carbon (76.7 at. %), oxygen (18.0 at. %), followed by N (3.5 at. %) and F (1.8



at. %). Both carbon and oxygen deconvolution confirmed the presence of the carboxylic groups, as well as the FT-IR spectrum with a band located at around  $1600\text{ cm}^{-1}$ , usually attributed to the carbon-oxygen vibration in carboxylic groups.<sup>50,95</sup>

Microscopic methods further evaluated the structural properties and composition of GA (Figure 17), showing the layered structure of GA, with thin graphenic sheets and lateral size of units of a micrometre. HAADF-HRTEM was used to investigate the elemental distribution of the graphene derivative, showing that the oxygen functional groups are homogeneously dispersed across the surface, further confirming GA well-defined nature. Based on the characterization techniques, the optimized GA structure model was designed.

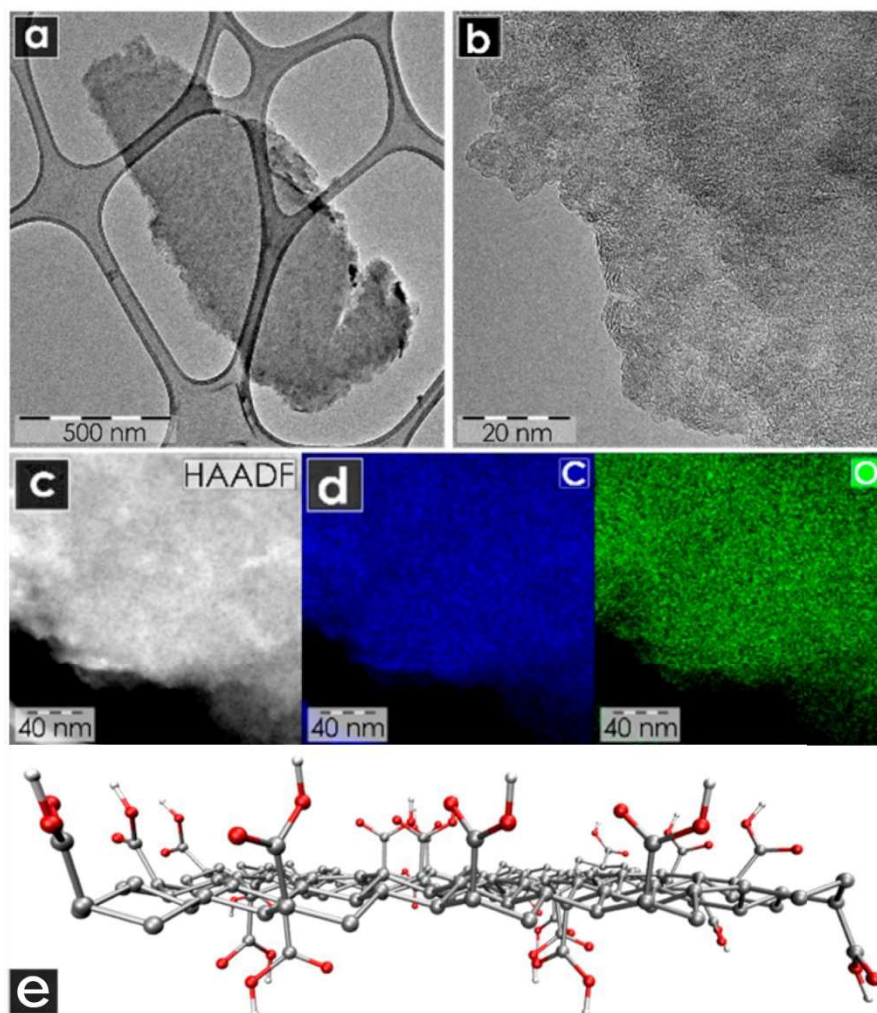


Figure 17 (a), (b) HRTEM images of GA. (c)-(d) HAADF image and corresponding elemental mapping of carbon and oxygen. (e) Structural GA model.

Electrochemical testing of a material can be performed in a three- or two-electrode system, whereas the two electrode system is much closer to the real

operational conditions of commercial supercapacitors. We first evaluated the GA in a three-electrode system; however, more importantly, we tested its performance in a two-electrode symmetric system to assess the feasibility of GA.

We have assembled a symmetric supercapacitor with  $1 \text{ mol L}^{-1} \text{ H}_2\text{SO}_4$  as the electrolyte. Additive-free, drop-casted electrodes were used, further highlighting the high conductivity of GA and the simplicity of the electrode preparation. The charging and discharging responses of GA were recorded at a range of 1 to  $20 \text{ A g}^{-1}$ , showing linear response (contrary to the three-electrode system) since the two electrode system operates differently with the voltage<sup>100</sup>.

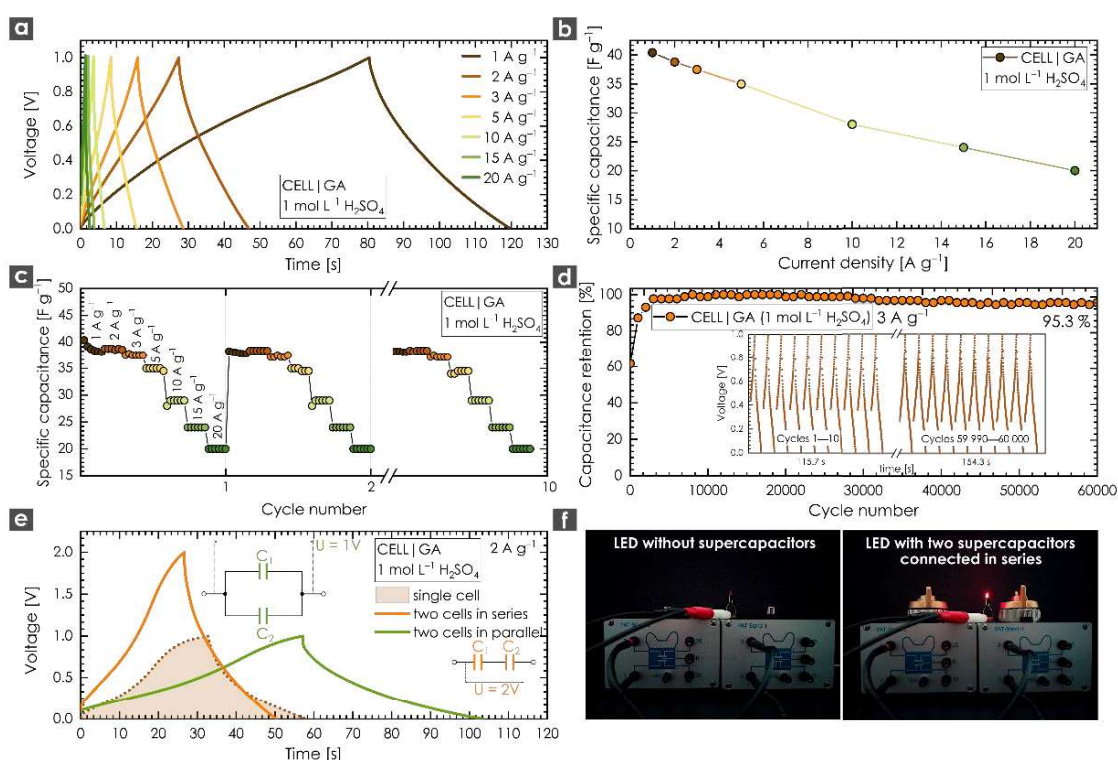


Figure 18 (a) GCD profiles of GA in a two-electrode system, (b) the dependence of capacitance vs current density. (c) Rate and (d) cycling stability test. (e),(f) Supercapacitors with GA electrodes connected in parallel and series, showing increased values as well as lighted up 2V LED diode.

The GA exhibited excellent rate stability, as well as remarkable cycling stability at  $3 \text{ A g}^{-1}$  current density (Figure 18). Such stability for a carbon-based material is significantly important precedence for its wide use since commercial supercapacitors endure many charge/discharge cycles. In real-life applications, supercapacitors are usually connected in parallel (to increase the capacitance – alias the amount of stored energy) or in series (to increase the voltage window). Two supercapacitors with GA as electrode material were successfully tested in both configurations, exhibiting the

expected electrochemical behaviour. Moreover, we conducted the LED test, where the two cells assembled with GA electrodes and sulphuric acid electrolyte lighted up 2V LED without fast fading.

## **Conclusions**

Graphene acid is a covalently functionalized graphene derivative prepared from fluorographene, offering a very stable electrode material for supercapacitors with promising performance. The oxygen-containing functional groups offer a high pseudocapacitive response in a sulphuric acid electrolyte without compromising the stability of the system. Both rate and cycling stability tests revealed the extraordinary performance of GA, demonstrating the high feasibility of GA for supercapacitor applications.

## 4 SUMMARY

This doctoral thesis focused on the synthesis and characterization of covalently functionalized graphene derivatives, using fluorographene as starting material. The physicochemical and electrochemical properties of the developed materials were evaluated in order to understand their function as electrode materials in electric double-layer capacitors (supercapacitors). The type of the covalently attached functional groups and/or nitrogen doping critically affects their overall properties, enabling their efficient use in supercapacitors and improving their operation.

Within the frame of this thesis, fluorographene chemistry was used to circumvent graphene's low reactivity during direct functionalization. The pathways using exfoliated graphite fluoride yielded chemically functionalized graphene derivatives, with nitrogen doping and with covalently attached amino acid and carboxylic groups.

Firstly, nitrogen superdoped (16 at.%) graphene was synthesized with diamond-like interlayer bonds with exceptionally high mass density. This material, when used as electrode in a symmetric supercapacitor device operating with an ionic liquid, presented a ground-breaking volumetric energy density compared to the state-of-the-art materials and commercially used high surface area carbons.

Secondly, amino-acid functionalized graphene derivatives were prepared with optimized porous structure using a pore-forming agent and applied as supercapacitor electrodes. The final device benefited from the covalently grafted functional groups, which provided redox processes during charging and discharging. Moreover, the use of eco-friendly electrolyte further increased the feasibility of the whole device.

Lastly, the highly carboxylated graphene derivative was subjected to an in-depth characterization, emphasizing the synthesis reproducibility in terms of stability of the electrochemical properties. Remarkably, the graphene acid exhibited exceptional life-cycle stability in an acidic electrolyte in supercapacitor application.

The materials and the synthetic procedures reported in this thesis show new ways to develop covalent graphene derivatives, which can offer interesting properties in technologically important areas, as in electrochemical energy storage and in particular in supercapacitors. These reported designs pave the way for new, specifically tailored properties of graphene derivatives for desired applications.

## 5 ZÁVĚR

Tato disertační práce byla zaměřena na syntézu a charakterizaci kovalentně funkcionalizovaných derivátů grafenu s využitím fluorografenu jako výchozího materiálu. Vlastnosti a benefity prezentovaných materiálů byly zkoumány a testovány pro jejich aplikaci jako elektrodových materiálů na poli ukládání energie v superkondenzátorech. Functionalizace a dusíkový doping kladně ovlivňují jejich chování, a proto zlepšují jejich výkon v zařízeních.

V rámci této práce byla využita fluorografenová chemie k překonání nízké reaktivity grafenu při jeho přímé funkcionalizaci. Syntetické procesy využily exfoliovaný grafit fluorid pro přípravu chemicky funkcionalizovaných derivátů grafenu s dopováním dusíkem a s kovalentně připojenými aminokyselinami a karboxylovými skupinami.

Prvně byl syntetizován dusíkem superdopovaný (16 at.%) grafen s mezivrstevnými vazbami podobnými diamantu s mimořádně vysokou hustotou. Tento materiál, v symetrickém zařízení za použití iontové kapaliny jako elektrolytu, představuje průlom v objemovém ukládání energie ve srovnání s dříve publikovanými výsledky.

Následně byly připraveny deriváty grafenu funkcionalizované aminokyselinami, které byly dále optimalizovány pomocí pórotvorného činidla a využity jako aktivní materiál v superkondenzátorech. Finální zařízení benefitovalo právě z kovalentně navázaných funkčních skupin, které zajišťovaly redoxní procesy v superkondenzátoru. Použití ekologického elektrolytu navíc dále zvýšilo relevantnost, udržitelnost a možnost komerčního využití celého zařízení.

Jako poslední byl v rámci práce charakterizován vysoce karboxylovaný derivát grafenu s důrazem na reprodukovatelnost syntézy. Grafenová kyselina vykazovala výjimečnou cyklickou stabilitu v kyselém elektrolytu a našla opět využití v superkondenzátorech.

Materiály a syntetické postupy uvedené v této práci ukazují nové cesty pro vývoj kovalentních derivátů grafenu. Ty byly přesně navrženy tak, aby poskytovaly výjimečné a excelentní vlastnosti v technologicky důležitých oblastech, s důrazem na použití v aplikacích pro ukládání energie, zejména v superkondenzátorech.

## 6 REFERENCES

- 1 P. R. Wallace, *Phys. Rev.*, 1947, **71**, 622–634.
- 2 C. Oshima and A. Nagashima, *J. Phys. Condens. Matter*, 1997, **9**, 1–20.
- 3 A. E. Karu and M. Beer, *J. Appl. Phys.*, 1966, **37**, 2179–2181.
- 4 K. S. Novoselov, A. K. Geim, S. V. Morozov, D. Jiang, Y. Zhang, S. V. Dubonos, I. V. Grigorieva and A. A. Firsov, *Science*, 2004, **306**, 666–669.
- 5 L. D. Landau, *Phys. Z. Sowjetunion*, 1937, **11**, 26–35.
- 6 R. Peierls, *Ann. Inst. Henri Poincaré*, 1935, **5**, 177–222.
- 7 K. S. Novoselov, D. Jiang, F. Schedin, T. J. Booth, V. V. Khotkevich, S. V. Morozov and A. K. Geim, *Proc. Natl. Acad. Sci.*, 2005, **102**, 10451–10453.
- 8 K. R. Nandanapalli, D. Mudusu and S. Lee, *Carbon*, 2019, **152**, 954–985.
- 9 Y. Gogotsi and V. Presser, *Carbon Nanomaterials*, CRC Press, 2013th edn., 2013.
- 10 H. A. Hafez, S. Kovalev, K.-J. Tielrooij, M. Bonn, M. Gensch and D. Turchinovich, *Adv. Opt. Mater.*, 2020, **8**, 1900771.
- 11 M. I. Katsnelson, *Mater. Today*, 2007, **10**, 20–27.
- 12 D. W. Boukhvalov and M. I. Katsnelson, *Nano Lett.*, 2008, **8**, 4373–4379.
- 13 G. Yang, D. Bao, H. Liu, D. Zhang, N. Wang and H. Li, *J. Inorg. Organomet. Polym. Mater.*, 2017, **27**, 1129–1141.
- 14 G. Bottari, M. Ángeles Herranz, L. Wibmer, M. Volland, L. Rodríguez-Pérez, D. M. Guldi, A. Hirsch, N. Martín, F. D’Souza and T. Torres, *Chem. Soc. Rev.*, 2017, **46**, 4464–4500.
- 15 M. S. Chang, Y. S. Kim, J. H. Kang, J. Park, S. J. Sung, S. H. So, K. T. Park, S. J. Yang, T. Kim and C. R. Park, *Chem. Mater.*, 2017, **29**, 307–318.
- 16 V. Georgakilas, M. Otyepka, A. B. Bourlinos, V. Chandra, N. Kim, K. C. Kemp, P. Hobza, R. Zboril and K. S. Kim, *Chem. Rev.*, 2012, **112**, 6156–6214.
- 17 A. Hirsch, J. M. Englert and F. Hauke, *Acc. Chem. Res.*, 2013, **46**, 87–96.
- 18 P. Arranz-Mascarós, M. L. Godino-Salido, R. López-Garzón, C. García-Gallarín, I. Chamorro-Mena, F. J. López-Garzón, E. Fernández-García and M. D. Gutiérrez-Valero, *ACS Omega*, 2020, **5**, 18849.
- 19 T. Kuila, S. Bose, A. K. Mishra, P. Khanra, N. H. Kim and J. H. Lee, *Prog. Mater. Sci.*, 2012, **57**, 1061–1105.
- 20 J. Zhang, K. Hu, Q. Ouyang, Q. Gui and X. Chen, *Front. Mater. Sci.*, 2020, **14**, 198–210.
- 21 P. Arranz-Mascarós, M. L. Godino-Salido, R. López-Garzón, C. García-Gallarín, I. Chamorro-Mena, F. J. López-Garzón, E. Fernández-García and M. D. Gutiérrez-Valero, *ACS Omega*, 2020, **5**, 18849–18861.
- 22 J. Park and M. Yan, *Acc. Chem. Res.*, 2013, **46**, 181–189.
- 23 C. K. Chua and M. Pumera, *Chem. Soc. Rev.*, 2013, **42**, 3222–3233.
- 24 W. Yu, L. Sisi, Y. Haiyan and L. Jie, *RSC Adv.*, 2020, **10**, 15328–15345.
- 25 G. Bottari, M. Á. Herranz, L. Wibmer, M. Volland, L. Rodríguez-Pérez, D. M. Guldi, A. Hirsch, N. Martín, F. D’Souza and T. Torres, *Chem. Soc. Rev.*, 2017, **46**, 4464–4500.
- 26 V. V. Shnitov, M. K. Rabchinskii, M. Brzhezinskaya, D. Yu. Stolyarova, S. V. Pavlov, M. V. Baidakova, A. V. Shvidchenko, V. A. Kislenko, S. A. Kislenko and P. N. Brunkov, *Small*, 2021, **17**, 2104316.
- 27 Y. Hernandez, V. Nicolosi, M. Lotya, F. M. Blighe, Z. Sun, S. De, I. T. McGovern, B. Holland, M. Byrne, Y. K. Gun’Ko, J. J. Boland, P. Niraj, G. Duesberg, S. Krishnamurthy, R. Goodhue, J. Hutchison, V. Scardaci, A. C. Ferrari and J. N. Coleman, *Nat. Nanotechnol.*, 2008, **3**, 563–568.

- 28D. Haag and H. H. Kung, *Top. Catal.*, 2014, **57**, 762–773.
- 29K. Christian Kemp, H. Seema, M. Saleh, N. H. Le, K. Mahesh, V. Chandra and K. S. Kim, *Nanoscale*, 2013, **5**, 3149–3171.
- 30N. Baig, Ihsanullah, M. Sajid and T. A. Saleh, *J. Environ. Manage.*, 2019, **244**, 370–382.
- 31S. Kumar and K. Chatterjee, *ACS Appl. Mater. Interfaces*, 2016, **8**, 26431–26457.
- 32N. M. Nurazzi, N. Abdullah, S. Z. N. Demon, N. A. Halim, A. F. M. Azmi, V. F. Knight and I. S. Mohamad, *Nanotechnol. Rev.*, 2021, **10**, 330–369.
- 33X. Tang, M. Debliquy, D. Lahem, Y. Yan and J.-P. Raskin, *Sensors*, 2021, **21**, 1443.
- 34N. Alzate-Carvajal and A. Luican-Mayer, *ACS Omega*, 2020, **5**, 21320–21329.
- 35V. Jain and B. Kandasubramanian, *J. Mater. Sci.*, 2020, **55**, 1865–1903.
- 36H. Huang, H. Shi, P. Das, J. Qin, Y. Li, X. Wang, F. Su, P. Wen, S. Li, P. Lu, F. Liu, Y. Li, Y. Zhang, Y. Wang, Z.-S. Wu and H.-M. Cheng, *Adv. Funct. Mater.*, 2020, **30**, 1909035.
- 37A. Bakandritsos, P. Jakubec, M. Pykal and M. Otyepka, *FlatChem*, 2019, **13**, 25–33.
- 38V. Georgakilas, J. N. Tiwari, K. C. Kemp, J. A. Perman, A. B. Bourlinos, K. S. Kim and R. Zboril, *Chem. Rev.*, 2016, **116**, 5464–5519.
- 39K. P. Loh, Q. Bao, P. K. Ang and J. Yang, *J. Mater. Chem.*, 2010, **20**, 2277–2289.
- 40D. W. Boukhvalov and M. I. Katsnelson, 2009.
- 41V. Hrubý, L. Zdražil, J. Dzibelová, V. Šedajová, A. Bakandritsos, P. Lazar and M. Otyepka, *Appl. Surf. Sci.*, 2022, **587**, 152839.
- 42R. Langer, D. Zaoralová, M. Medved', P. Banáš, P. Błoński and M. Otyepka, *J. Phys. Chem. C*, 2019, **123**, 27896–27903.
- 43M. Dubecký, E. Otyepková, P. Lazar, F. Karlický, M. Petr, K. Čépe, P. Banáš, R. Zbořil and M. Otyepka, *J. Phys. Chem. Lett.*, 2015, **6**, 1430–1434.
- 44M. Medved', G. Zoppellaro, J. Ugolotti, D. Matochová, P. Lazar, T. Pospíšil, A. Bakandritsos, J. Tuček, R. Zbořil and M. Otyepka, *Nanoscale*, 2018, **10**, 4696–4707.
- 45D. D. Chronopoulos, A. Bakandritsos, M. Pykal, R. Zbořil and M. Otyepka, *Appl. Mater. Today*, 2017, **9**, 60–70.
- 46J. Xia, F. Chen, J. Li and N. Tao, *Nat. Nanotechnol.*, 2009, **4**, 505–509.
- 47L. Dai, *Acc. Chem. Res.*, 2013, **46**, 31–42.
- 48R. A. Borse, M. B. Kale, S. H. Sonawane and Y. Wang, *Adv. Funct. Mater.*, 2022, **32**, 2202570.
- 49V. Šedajová, A. Bakandritsos, P. Błoński, M. Medved', R. Langer, D. Zaoralová, J. Ugolotti, J. Dzibelová, P. Jakubec, V. Kupka and M. Otyepka, *Energy Environ. Sci.*, 2022, **15**, 740–748.
- 50V. Šedajová, P. Jakubec, A. Bakandritsos, V. Ranc and M. Otyepka, *Nanomaterials*, 2020, **10**, 1731.
- 51E. C. Vermisoglou, P. Jakubec, A. Bakandritsos, V. Kupka, M. Pykal, V. Šedajová, J. Vlček, O. Tomanec, M. Scheibe, R. Zbořil and M. Otyepka, *ChemSusChem*, 2021, **14**, 3904–3914.
- 52A. S. Aricò, P. Bruce, B. Scrosati, J.-M. Tarascon and W. van Schalkwijk, *Nat. Mater.*, 2005, **4**, 366–377.
- 53W. Gu and G. Yushin, *Wiley Interdiscip. Rev. Energy Environ.*, 2014, **3**, 424–473.
- 54Q. Wang, J. Yan and Z. Fan, *Energy Environ. Sci.*, 2016, **9**, 729–762.
- 55Y. Gogotsi and P. Simon, *Science*, 2011, **334**, 917–918.
- 56J. W. Choi and D. Aurbach, *Nat. Rev. Mater.*, 2016, **1**, 16013.
- 57P. Albertus, S. Babinec, S. Litzelman and A. Newman, *Nat. Energy*, 2018, **3**, 16–21.
- 58P. Simon and Y. Gogotsi, *Acc. Chem. Res.*, 2013, **46**, 1094–1103.

- 59 H. Li, Y. Tao, X. Zheng, J. Luo, F. Kang, H.-M. Cheng and Q.-H. Yang, *Energy Environ. Sci.*, 2016, **9**, 3135–3142.
- 60 D. Yu, K. Goh, H. Wang, L. Wei, W. Jiang, Q. Zhang, L. Dai and Y. Chen, *Nat. Nanotechnol.*, 2014, **9**, 555–562.
- 61 R. Weber, M. Genovese, A. J. Louli, S. Hames, C. Martin, I. G. Hill and J. R. Dahn, *Nat. Energy*, 2019, **4**, 683–689.
- 62 Z. Li, S. Gadipelli, H. Li, C. A. Howard, D. J. L. Brett, P. R. Shearing, Z. Guo, I. P. Parkin and F. Li, *Nat. Energy*, 2020, **5**, 160–168.
- 63 D. Zaoralová, V. Hrubý, V. Šedajová, R. Mach, V. Kupka, J. Ugolotti, A. Bakandritsos, M. Medved' and M. Otyepka, *ACS Sustain. Chem. Eng.*, 2020, **8**, 4764–4772.
- 64 G. Zoppellaro, A. Bakandritsos, J. Tuček, P. Błoński, T. Susi, P. Lazar, Z. Bad'ura, T. Steklý, A. Opletalová, M. Otyepka and R. Zbořil, *Adv. Mater.*, 2019, **31**, 1902587.
- 65 Y. Liu, Y. Shen, L. Sun, J. Li, C. Liu, W. Ren, F. Li, L. Gao, J. Chen, F. Liu, Y. Sun, N. Tang, H.-M. Cheng and Y. Du, *Nat. Commun.*, 2016, **7**, 1–9.
- 66 A. S. Mazur, M. A. Vovk and P. M. Tolstoy, *Fuller. Nanotub. Carbon Nanostructures*, 2020, **28**, 202–213.
- 67 R. L. Johnson, J. M. Anderson, B. H. Shanks and K. Schmidt-Rohr, *Chem. Mater.*, 2014, **26**, 5523–5532.
- 68 D. W. Mayo, in *Course Notes on the Interpretation of Infrared and Raman Spectra*, eds. D. W. Mayo, F. A. Miller and R. W. Hannah, John Wiley & Sons, Inc., 2004, pp. 101–140.
- 69 J. Senthilnathan, C.-C. Weng, J.-D. Liao and M. Yoshimura, *Sci. Rep.*, 2013, **3**, srep02414.
- 70 A. Bakandritsos, R. G. Kadam, P. Kumar, G. Zoppellaro, M. Medved', J. Tuček, T. Montini, O. Tomanec, P. Andrášková, B. Drahoš, R. S. Varma, M. Otyepka, M. B. Gawande, P. Fornasiero and R. Zbořil, *Adv. Mater.*, 2019, **31**, 1900323.
- 71 P. Lazar, R. Mach and M. Otyepka, *J. Phys. Chem. C*, 2019, **123**, 10695–10702.
- 72 L. Weinstein and R. Dash, *Mater. Today*, 2013, **16**, 356–357.
- 73 H. Jin, X. Feng, J. Li, M. Li, Y. Xia, Y. Yuan, C. Yang, B. Dai, Z. Lin, J. Wang, J. Lu and S. Wang, *Angew. Chem. Int. Ed.*, 2019, **58**, 2397–2401.
- 74 R. Weber, M. Genovese, A. J. Louli, S. Hames, C. Martin, I. G. Hill and J. R. Dahn, *Nat. Energy*, 2019, **4**, 683–689.
- 75 X. Lin, M. Salari, L. M. R. Arava, P. M. Ajayan and M. W. Grinstaff, *Chem. Soc. Rev.*, 2016, **45**, 5848–5887.
- 76 L. Timperman, H. Galiano, D. Lemordant and M. Anouti, *Electrochem. Commun.*, 2011, **13**, 1112–1115.
- 77 J. Alvarado, M. A. Schroeder, M. Zhang, O. Borodin, E. Gobrogge, M. Olguin, M. S. Ding, M. Gobet, S. Greenbaum, Y. S. Meng and K. Xu, *Mater. Today*, 2018, **21**, 341–353.
- 78 M. Medved', G. Zoppellaro, J. Ugolotti, D. Matochová, P. Lazar, T. Pospíšil, A. Bakandritsos, J. Tuček, R. Zbořil and M. Otyepka, *Nanoscale*, 2018, **10**, 4696–4707.
- 79 D. Matochová, M. Medved', A. Bakandritsos, T. Steklý, R. Zbořil and M. Otyepka, *J. Phys. Chem. Lett.*, 2018, **9**, 3580–3585.
- 80 E. C. Vermisoglou, P. Jakubec, A. Bakandritsos, M. Pykal, S. Talande, V. Kupka, R. Zbořil and M. Otyepka, *Chem. Mater.*, 2019, **31**, 4698–4709.
- 81 A. R. Rafieerad, A. R. Bushroa, A. Amiri, K. Kalaiselvam, K. Vellasamy and J. Vadivelu, *J. Hazard. Mater.*, 2018, **360**, 132–140.
- 82 D. Chen, Q. Chen, T. Liu, J. Kang, R. Xu, Y. Cao and M. Xiang, *RSC Adv.*, 2019, **9**, 20149–20160.



- 83 A. Bakandritsos, D. D. Chronopoulos, P. Jakubec, M. Pykal, K. Čépe, T. Steriotis, S. Kalytchuk, M. Petr, R. Zbořil and M. Otyepka, *Adv. Funct. Mater.*, 2018, **28**, 1801111.
- 84 K. Jayaramulu, M. Horn, A. Schneemann, H. Saini, A. Bakandritsos, V. Ranc, M. Petr, V. Stavila, C. Narayana, B. Scheibe, Š. Kment, M. Otyepka, N. Motta, D. Dubal, R. Zbořil and R. A. Fischer, *Adv. Mater.*, 2021, **33**, 2004560.
- 85 E. C. Vermisoglou, P. Jakubec, A. Bakandritsos, M. Pykal, S. Talande, V. Kupka, R. Zbořil and M. Otyepka, *Chem. Mater.*, 2019, **31**, 4698–4709.
- 86 J. Yan, Q. Wang, T. Wei and Z. Fan, *Adv. Energy Mater.*, 2014, **4**, 1300816.
- 87 E. G. Calvo, N. Rey-Raap, A. Arenillas and J. A. Menéndez, *RSC Adv*, 2014, **4**, 32398–32404.
- 88 A. G. Pandolfo and A. F. Hollenkamp, *J. Power Sources*, 2006, **157**, 11–27.
- 89 A. Bakandritsos, M. Pykal, P. Błoński, P. Jakubec, D. D. Chronopoulos, K. Poláková, V. Georgakilas, K. Čépe, O. Tomanec, V. Ranc, A. B. Bourlinos, R. Zbořil and M. Otyepka, *ACS Nano*, 2017, **11**, 2982–2991.
- 90 Y. Heng Cheong, M. Z. M. Nasir, A. Bakandritsos, M. Pykal, P. Jakubec, R. Zbořil, M. Otyepka and M. Pumera, *ChemElectroChem*, 2019, **6**, 229–234.
- 91 M. Blanco, D. Mosconi, C. Tubaro, A. Biffis, D. Badocco, P. Pastore, M. Otyepka, A. Bakandritsos, Z. Liu, W. Ren, S. Agnoli and G. Granozzi, *Green Chem.*, 2019, **21**, 5238–5247.
- 92 M. Blanco, D. Mosconi, M. Otyepka, M. Medved', A. Bakandritsos, S. Agnoli and G. Granozzi, *Chem. Sci.*, 2019, **10**, 9438–9445.
- 93 B. Reuillard, M. Blanco, L. Calvillo, N. Coutard, A. Ghedjatti, P. Chenevier, S. Agnoli, M. Otyepka, G. Granozzi and V. Artero, *ACS Appl. Mater. Interfaces*, 2020, **12**, 5805–5811.
- 94 H. Seelajaroen, A. Bakandritsos, M. Otyepka, R. Zbořil and N. S. Sariciftci, *ACS Appl. Mater. Interfaces*, 2020, **12**, 250–259.
- 95 A. Bakandritsos, M. Pykal, P. Błoński, P. Jakubec, D. D. Chronopoulos, K. Poláková, V. Georgakilas, K. Čépe, O. Tomanec, V. Ranc, A. B. Bourlinos, R. Zbořil and M. Otyepka, *ACS Nano*, 2017, **11**, 2982–2991.
- 96 Y. Si and E. T. Samulski, *Chem. Mater.*, 2008, **20**, 6792–6797.
- 97 A. Eckmann, A. Felten, A. Mishchenko, L. Britnell, R. Krupke, K. S. Novoselov and C. Casiraghi, *Nano Lett.*, 2012, **12**, 3925–3930.
- 98 F. T. Johra, J.-W. Lee and W.-G. Jung, *J. Ind. Eng. Chem.*, 2014, **20**, 2883–2887.
- 99 A. Bakandritsos, D. D. Chronopoulos, P. Jakubec, M. Pykal, K. Čépe, T. Steriotis, S. Kalytchuk, M. Petr, R. Zbořil and M. Otyepka, *Adv. Funct. Mater.*, 2018, **28**, 1801111–1801111.
- 100 Y. Gogotsi and P. Simon, *Science*, 2011, **334**, 917–918.